

ABSTRACT

SULLIVAN, IAN. Structural, Optical and Photoelectrochemical Properties of Novel Metal Oxide Semiconductors. (Under the Direction of Paul A. Maggard).

This dissertation describes the structural, optical and photoelectrochemical properties of polycrystalline films of Cu(I) based metal oxide semiconductors through the use of materials' characterization techniques. The research described is primarily concentrated on Cu(I) based metal oxide semiconductors, including copper tantalates ($\text{Cu}_5\text{Ta}_{11}\text{O}_{30}$ and $\text{Cu}_2\text{Ta}_4\text{O}_{11}$), as well as optical and structural properties of other Cu(I) oxides including Cu_2O , copper delafossites, and copper vandates and niobates. These materials are light absorbing semiconductors and differ from other widely studied semiconductors due to their *p*-type conductivity. These materials produce cathodic photocurrents, and are suitable for the reduction of protons to H_2 gas, or possibly for the reduction of CO_2 to fuel sources such as methanol or methane.

Chapter 1 is a broad overview of how electronic and optical properties can affect the overall efficiency of both *n*-type and *p*-type semiconductors. Chapter 2 describes the structural, optical, and photoelectrochemical properties of $\text{Cu}_5\text{Ta}_{11}\text{O}_{30}$ polycrystalline films as they are heated in air. Chapter 3 describes the synthesis of $\text{Cu}_5\text{Ta}_{11}\text{O}_{30}$ nanoparticles, sensitization with Zn-porphyrin based dyes, and photophysical properties for use as a *p*-DSSC. Chapter 4 describes an investigation into the photoelectrochemical properties of $\text{Cu}_2\text{Ta}_4\text{O}_{11}$ polycrystalline films, and its relationship to other Cu(I) based semiconductors, including $\text{Cu}_5\text{Ta}_{11}\text{O}_{30}$, $\text{Cu}_3\text{Ta}_7\text{O}_{19}$, and CuNb_3O_8 . Chapter 5 focuses on general trends in the optical and structural properties in several classes of Cu(I) based metal oxides. Lastly, Chapter 6 is a summary of the research and gives insight to future directions of Cu(I) based materials for use in solar energy harvesting.

© Copyright 2015 Ian Sullivan

All Rights Reserved

Structural, Optical, and Photoelectrochemical Properties of Novel Metal Oxide
Semiconductors

by
Ian Sullivan

A dissertation submitted to the Graduate Faculty of
North Carolina State University
in partial fulfillment of the
requirements for the degree of
Doctor of Philosophy

Chemistry

Raleigh, North Carolina

2016

APPROVED BY:

Dr. Paul A. Maggard
Committee Chair

Dr. James D. Martin

Dr. Elena Jakubikova

Dr. Walter W. Weare

DEDICATION

I would like to dedicate my dissertation to Leanna. Without her love and support I would not be the chemist or man I am today.

BIOGRAPHY

Ian Sullivan was born in Point Pleasant, NJ and attended Point Pleasant Borough High School, where his interest in chemistry took hold. Ian attended Rutgers University for part of his undergraduate education, and finished his Bachelors of Science at Georgian Court University. He then worked for a startup company, Liquid Light Inc. where he investigated the electrochemical reduction of CO₂ using a pyridinium catalyst. Afterwards, he joined the Maggard group at North Carolina State University and investigated semiconducting metal oxides for use in solar water splitting and solar energy harvesting.

ACKNOWLEDGMENTS

There are many people who have helped and guided me on my academic career, and without this help I would not have been able to accomplish my goal of earning a Ph.D. in chemistry. I would first like to thank my advisor Paul A. Maggard for his guidance in my research and teaching me what an excellent scientist should be. I thank my group members Dr. Nacole King, Dr. Lan Luo, Jonathan Boltersdorf, Brandon “B-Dog” Zoellner, and Zahir Sohag for their friendship, help, and intellectual input into my research. I thank my friends Tom Chase, Chris Brackett, Eric Goggins, Lance Wilson, Dan Frasco, Chris Tichnell, Blake Paris and the rest of the drinking crew for the many fun times had in Raleigh. I thank Frank Zappa, whose music made lab work much more enjoyable. I would also like to thank my family and friends for their encouragement and support throughout my life and career. Saving the best for last, I would like to thank my parents Sean and Sandi, my brother Kevin, and Leanna Meyer for their continued love and support, which has helped me in more ways than they can imagine.

TABLE OF CONTENTS

LIST OF TABLES	vi
LIST OF FIGURES	viii
CHAPTER 1: Introduction	1
References	10
CHAPTER 2: Cu-Deficiency in the <i>p</i>-Type Semiconductor $\text{Cu}_{5-x}\text{Ta}_{11}\text{O}_{30}$: Impact on its Crystalline Structure, Surfaces, and Photoelectrochemical Properties	15
References	35
CHAPTER 3: Photo-Injection of High Potential Holes into $\text{Cu}_5\text{Ta}_{11}\text{O}_{30}$ Nanoparticles by Porphyrin Dyes	51
References	74
CHAPTER 4: Flux-Mediated Syntheses, Structural Characterization, and Low-Temperature Polymorphism of the <i>p</i>-Type Semiconductor $\text{Cu}_2\text{Ta}_4\text{O}_{11}$	85
References	102
CHAPTER 5: Conclusions	116
References	122
APPENDICES	128
APPENDIX A	129
APPENDIX B	139
APPENDIX C	159

LIST OF TABLES

Table 2.1. Calculated unit cell volumes after heating $\text{Cu}_{5-x}\text{Ta}_{11}\text{O}_{30}$ in air at three different temperatures and heating times.....	39
Table 2.2. Selected Rietveld refinement parameters for $\text{Cu}_{3.2(1)}\text{Ta}_{11}\text{O}_{30}$	39
Table 2.3. Selected interatomic distances and bond angles for the Cu-deficient $\text{Cu}_{3.2(1)}\text{Ta}_{11}\text{O}_{30}$, and the corresponding differences compared to those in $\text{Cu}_5\text{Ta}_{11}\text{O}_{30}$	40
Table 3.1. Short circuit current, open circuit potential, fill factor and light conversion efficiency of D1 and D2	75
Table 4.1. Selected Rietveld Refinement Data for $\alpha\text{-Cu}_2\text{Ta}_4\text{O}_{11}$	102
Table 4.2. Selected Interatomic Distances for the Symmetry-Inequivalent Metal Sites in $\alpha\text{-Cu}_2\text{Ta}_4\text{O}_{11}$ from the powder Rietveld refinement at 298 K.....	103
Table 5.1. Reported Bandgap Sizes, Photocurrents, Stability, and Coordination of Cu(I) in the Cu(I) Oxides.....	119
Table 6.1 The direct ($n = 2$) and indirect ($n = 1/2$) band gaps were obtained from Tauc plots of $(F(R) \times hv)^n$ vs. hv (eV).....	191
Table A1. Unit cell volumes calculated from lattice parameters of heated films of $\text{Cu}_{5-x}\text{Ta}_{11}\text{O}_{30}$	127
Table A2. Refined atomic coordinates and isotropic displacement parameters (\AA^2) and site shifts in the atomic positions (Δ_{pos}) of $\text{Cu}_{3.1(1)}\text{Ta}_{11}\text{O}_{30}$, compared to the previously reported $\text{Cu}_5\text{Ta}_{11}\text{O}_{30}$	128
Table A3. The results of Curie-Weiss fits to magnetic susceptibility measurements for $\text{Cu}_5\text{Ta}_{11}\text{O}_{30}$ and the Cu-deficient $\text{Cu}_{5-x}\text{Ta}_{11}\text{O}_{30}$ after heating to 250 °C, 350 °C and 450 °C..	129
Table B1. Table of Parameters Determined in the Efficiency Calculations.....	152
Table C1. The atomic positions, Isotropic Displacement Parameters (\AA), and Wyckoff sites for the refined structure of $\alpha\text{-Cu}_2\text{Ta}_4\text{O}_{11}$ at 298 K.....	159
Table C2. Lattice Constant Refinements $\text{Cu}_2\text{Ta}_4\text{O}_{11}$ in the temperature range of 223 K to 723 K. The lattice constants of powder X-ray samples at the temperature 223 K and 298 K	

were refined and indexed using a monoclinic Cc unit cell, powder samples at 523 K, 623 K, and 723 K were refined and indexed using a rhombohedral $R\bar{3}c$ unit cell.....160

LIST OF FIGURES

- Figure 1.3.** Effects of doping an intrinsic semiconductor (a), *p*-type (b) and *n*-type (d). Band bending in *p*-type (c) and *n*-type (e) semiconductors after equilibration with a redox mediator. 13
- Figure 1.6.** Energy and band diagrams of *n*-type (left) and *p*-type (right) dye sensitized solar cells. 14
- Figure 2.1.** SEM images of $\text{Cu}_5\text{Ta}_{11}\text{O}_{30}$ before heating (a,b), after heating to 350 °C for 60 min (c,d), and after heating to 550 °C for 60 min (e,f). 41
- Figure 2.2.** The powder X-ray diffraction patterns for $\text{Cu}_5\text{Ta}_{11}\text{O}_{30}$ without oxidation (a), heated in air to 550 °C for 3 h (b), to 550°C for 12 h (c), to 650°C for 3 h (d), and to 750 °C for 3 h (e) 441
- Figure 2.3.** Detailed XPS scans of Cu *2p* core levels for $\text{Cu}_5\text{Ta}_{11}\text{O}_{30}$ heated to increasing temperatures, indicating only Cu(II) at the surface at 350 °C and above (left). 43
- Figure 2.4.** Rietveld refinement results for powder X-ray diffraction data on $\text{Cu}_5\text{Ta}_{11}\text{O}_{30}$ after heat it in air to 450 °C for 3 h. The observed profile is indicated by circles and the calculated profile by the solid line. Bragg peak positions are indicated by vertical tics, and the difference is shown at the bottom 44
- Figure 2.5.** Polyhedral structural model $\text{Cu}_{3,2(1)}\text{Ta}_5\text{O}_{11}$, with the unit cell (outlined) on the left, and a local structural view on the right. Selected atom types are labeled, and the coordinate system is drawn at the bottom. 45
- Figure 2.6.** Polyhedral views of the local coordination environments of each of the three types of Ta sites in $\text{Cu}_{3,2(1)}\text{Ta}_5\text{O}_{11}$. Atom types are labeled, and the *c*-axis is vertical in each. 45
- Figure 2.7.** Linear sweep voltammetry under chopped irradiation (upper) and chronoamperometry (lower; -0.2 applied bias) of films heated to 350 °C (a-b), 450 °C (c-d) and 550 °C (e-f). for 15 min (black), 30 min (red) and 60 min (blue), in a 0.5M Na_2SO_4 solution at a pH of ~6.5. 46
- Figure 2.8.** UV-Vis DRS of films before heating (blue), heated to 350 °C (black), 450 °C (red), 550 °C (green), and after soaking a heated film in 6 M HCl (yellow) to dissolve the CuO surface islands. Inset: Films of $\text{Cu}_5\text{Ta}_{11}\text{O}_{30}$ before (a) and after (b) heating. 46
- Figure 2.9.** Comparison of the linear sweep voltammetry under chopped irradiation (upper) and chronoamperometry (lower; applied bias of -0.2 V) of polycrystalline *p*-type Cu_2O and $\text{Cu}_{5-x}\text{Ta}_{11}\text{O}_{30}$ (heated to 350 °C for 3 h in air) photoelectrodes. 47

- Figure 2.10.** Detail XPS scans of the Cu 2*p* core levels for Cu₅Ta₁₁O₃₀ with no heat treatment (a), after heating to 450 °C for 60 min in air (b), and after chronoamperometry measurements for 1000 s (c)..... 47
- Figure 2.11.** Calculated densities-of-states for Cu₅Ta₁₁O₃₀ (A; upper) and Cu_{3.2(1)}Ta₁₁O₃₀ (B; lower) with the individual atomic-orbital contributions projected out and the Fermi level (*E_f*) labeled..... 48
- Figure 2.12.** Calculated electron-density plots for the Cu/TaO₆ layer (~50% Cu vacancies) of Cu_{3.2(1)}Ta₁₁O₃₀ at the highest energies of the valence band edge (upper; blue shading) and lowest energies of the conduction band edge (lower; red shading). Atom types and Cu-vacancy sites are labeled..... 49
- Figure 2.13.** Structural view of the Cu(I)/TaO₆ layer in Cu_{3.2(1)}Ta₅O₁₁. Three symmetry-equivalent Cu-migration pathways are labeled within the unit cell by dashed arrows, and four individual Cu-migration steps are illustrated and labeled as 0 (start), 2, 4, 6, and 8 (finish) . 50
- Figure 2.14.** Polyhedral models of the crystal morphologies of Cu₅Ta₁₁O₃₀ (hexagonal crystal system), with the major crystal facets labeled..... 51
- Figure 3.1.** Representative HR-TEM of NP–Cu₅Ta₁₁O₃₀ where a quasi-spherical distribution of particles with sizes of (15 ± 5) nm can be observed. **Inset:** Size distribution obtained by DLS of NP–Cu₅Ta₁₁O₃₀ dispersed in an ethanol solution..... 76
- Figure 3.2. a)** Absorption spectrum of NP–Cu₅Ta₁₁O₃₀ in ethanol at a concentration of 0.75 mg/mL. **Inset:** Absorption onset value of the first direct allowed transition for NP–Cu₅Ta₁₁O₃₀ (red line) and 99% confident bands (blue line). **b)** Mott-Schottky plot of NP–Cu₅Ta₁₁O₃₀..... 77
- Figure 3.3.** Molecular structures of the dyes **D1** and **D2** in their acid forms. Molecular structures of dyes **D1E** and **D2E**, in their ester forms, are shown in the Supporting Information. 78
- Figure 3.4.** Cyclic voltammogram of **a) D1E** and **b) D2E** in DMF/CIO₄TBA with a Pt working electrode, a Pt counter electrode and an Ag wire as the reference electrode. 78
- Figure 3.5.** Diagram depicting the reduction potentials for the ground and the lowest excited singlet states of **D1** and **D2**, the NP–Cu₅Ta₁₁O₃₀ conduction band energy (CB), and the NP–Cu₅Ta₁₁O₃₀ valence band energy (VB). 79
- Figure 3.6.** Absorption (solid lines) and emission (dashed lines) spectra of **D1** (panel a) and **D2** (panel b) before (red line) and after (black line) attachment to the NP–Cu₅Ta₁₁O₃₀ nanoparticles. Emission spectra were taken with excitation at 540 nm..... 80

Figure 3.7. Difference absorption spectra **a)** (D1^{•-}- D1) and **c)** (D2^{•-}- D2) obtained by spectroelectrochemistry. Decay-associated-spectra in ethanol solution measured by fs transient absorption after excitation at 428 nm for **b)** D1-NP-Cu₅Ta₁₁O₃₀ and **d)** D2-NP-Cu₅Ta₁₁O₃₀. 81

Figure 3.8. Linear sweep voltammograms of **D1** (black lines) and **D2** (red lines) in dark (dotted lines) and under AM 1.5 G irradiation (solid lines) with sweep rate of 10 mV·s⁻¹. .. 884

Figure 4.1. The Rietveld refinement pattern of the monoclinic α -Cu₂Ta₄O₁₁ at 298 K under flowing nitrogen. The observed intensities are indicated in blue (+), calculated intensities in green, the difference pattern is indicated by light blue, and the peak positions of α -Cu₂Ta₄O₁₁ in the monoclinic Cc space group are indicated by the blue tick marks. Impurities of Ta₂O₅ were masked as indicated by the purple lines. 104

Figure 4.2. A crystal structure of α -Cu₂Ta₄O₁₁ at 298 K in the monoclinic Cc space group along the ac direction of the unit cell, outline in blue. The Cu and O atoms are in blue and red, respectively. The Ta cation and polyhedra are shown in tan 105

Figure 4.3. A crystal structure of a layer of edge-sharing TaO₇ in the pentagonal bipyramid layer of the monoclinic α -Cu₂Ta₄O₁₁ a) a view of the edge sharing of Ta cations along the ab plane with the unit cell outline in a blue dashed line, black line indicates the distortion of Ta₂ into an octahedra in the edge-shared tantalate layer b-d) the local coordination environment of Ta₃, Ta₁ and Ta₂, respectively. 106

Figure 4.4. A crystal structure of a layer of edge-sharing TaO₇ in the pentagonal bipyramid layer of the rhombohedral β -Cu₂Ta₄O₁₁ a) a view of the edge sharing of Ta cations along the ab plane with the unit cell outline in a blue dashed line b) a smaller segment from the uppermost three Ta cations, the grey arrows indicate the out-of-center displacement of Ta due to repulsions from nearest neighbor cations a local view of the Ta cations from the small segments (c-e) for Ta cations labeled 1, 2, and 3 respectively. 107

Figure 4.5. The powder X-ray diffraction patterns of α -Cu₂Ta₄O₁₁ in an inert atmosphere with i) the simulated XRD of α -Cu₂Ta₄O₁₁ from the Rietveld refinement, ii-vi) the experimental powder XRD patterns heated at 223 K, 273 K, 523 K, 623 K, and 723 K, and vii) the simulated XRD pattern of β -Cu₂Ta₄O₁₁ at room temperature. 108

Figure 4.6. The Tauc plots of the UV-vis diffuse reflectance data for the monoclinic α -Cu₂Ta₄O₁₁ showing indirect (n = 1/2; orange) and direct (n = 2; green) band gap transitions. 109

Figure 4.7. The linear sweep voltammetry scans of the polycrystalline monoclinic α -Cu₂Ta₄O₁₁ films annealed under vacuum at 773 K for 3 h (red), and heated in air to 523 K (blue), and 623 K (green) for 3 h each. 110

Figure 4.8. The linear sweep voltammetry scans of the polycrystalline monoclinic α - $\text{Cu}_2\text{Ta}_4\text{O}_{11}$ films heated to 523 K for 3 h (red), 523 K with CuO on surface (blue), and 623 K for 3 h.....	111
Figure 4.9. The plots of electron density for the monoclinic α - $\text{Cu}_2\text{Ta}_4\text{O}_{11}$ with the orbital contributions in the A) valence band with electron density contributions in blue shading and in the B) conduction band with electron density contributions in tan shading.....	11115
Figure 5.1. SEM images of copper oxide extrusion in (a,b) Cu_3VO_4 , (c,d) CuNb_3O_8 , and (e,f) $\text{Cu}_5\text{Ta}_{11}\text{O}_{30}$. Figures (a,b) adapted from ref. 68 with permission of The Royal Society of Chemistry. Figures (c,d) and (e,f) reprinted with permission from refs. 65 and 87. Copyright 2014 American Chemical Society.	121
Figure 5.2. Preferential copper migration through the crystallites of $\text{Cu}_5\text{Ta}_{11}\text{O}_{30}$ (a), and copper migration within the channels along the [100] and [010] directions (b). Reprinted with permission from ref. 87. Copyright 2014 American Chemical Society.	121
Figure 6.1. Band positions of various copper oxides compared to the redox potentials of water and CO_2 . Bands have been shifted to reflect positions at pH 0 for comparison.	125
Figure A1. Powder XRD patterns of $\text{Cu}_5\text{Ta}_{11}\text{O}_{30}$ films before heating (a), heated to 350 °C for 15 min (b), 30 min (c) and 60 min (d); heated to 450 °C for 15 min (e), 30 min (f) and 60 min (g); and heated to 550 °C for 15 min (h), 30 min (i) and 60 min (j).....	130
Figure A2. Powder XRD patterns of $\text{Cu}_5\text{Ta}_{11}\text{O}_{30}$ films before heating (a), heated to 350 °C for 15 min (b), 30 min (c) and 60 min (d); heated to 450 °C for 15 min (e), 30 min (f) and 60 min (g); and heated to 550 °C for 15 min (h), 30 min (i) and 60 min (j).....	131
Figure A3. UV-Vis absorption of CuO dissolved in HCl/ H_2O solution and a heated film of $\text{Cu}_5\text{Ta}_{11}\text{O}_{30}$ with CuO surface islands soaked in a similarly prepared solution.....	132
Figure A4. Temperature-dependent magnetic susceptibility of $\text{Cu}_5\text{Ta}_{11}\text{O}_{30}$ that was heated in air at 450 °C for 3 h.	133
Figure A5. Calculated electron-density plots for $\text{Cu}_{3.2(1)}\text{Ta}_{11}\text{O}_{30}$ (~50% Cu vacancies) at the highest energies of the valence band edge (upper; blue shading) and lowest energies of the conduction band edge (lower; red shading). Atom types are labeled.	134
Figure A6. Powder XRD pattern of the electrodeposited Cu_2O polycrystalline film (upper), and the calculated theoretical pattern (lower) with Miller indices labeled.	135
Figure A7. Detailed XPS scans of Ta 4 <i>f</i> (left) and O 2 <i>p</i> (right) core levels for $\text{Cu}_5\text{Ta}_{11}\text{O}_{30}$ heated to increasing temperatures. The Ta 4 <i>f</i> _{7/2} doublet is the red and green fit and the 4 <i>f</i> _{5/2} doublet is the blue and yellow fit (right).....	136

Figure A8. Detailed XPS scans of the Ta 4 <i>f</i> core levels for Cu ₅ Ta ₁₁ O ₃₀ with no heat treatment (a), after heating to 450 °C for 1 h in air (b), and after chronoamperometry measurements for 1000 s (c). The Ta 4 <i>f</i> _{7/2} doublet is the red and green fit and the 4 <i>f</i> _{5/2} doublet is the blue and yellow fit.	137
Figure B1. Representative HR-TEM images of NP-Cu ₅ Ta ₁₁ O ₃₀	139
Figure B2. ¹ H-NMR of 1 in CDCl ₃	141
Figure B3. ¹ H-NMR of 2 in CDCl ₃	14143
Figure B4. ¹ H-NMR of 3 in CDCl ₃	143
Figure B5. ¹ H-NMR of D1E in DMSO-d ₆	144
Figure B6. ¹ H-NMR of D1 in DMSO-d ₆	145
Figure B7. ¹ H-NMR of D2E in DMSO-d ₆	146
Figure B8. ¹ H-NMR of D2 in DMSO-d ₆ /D ₂ O.	147
Figure B9. Absorption spectra in ethanol for: a) D1-Cu ₅ Ta ₁₁ O ₃₀ (black line) and b) D2-NP-Cu ₅ Ta ₁₁ O ₃₀ (red line).	148
Figure B10. Absorption spectra (solid lines) and emission spectra upon 560 nm excitation (dash lines) in ethanol for D1E-NP-Cu ₅ Ta ₁₁ O ₃₀ (red) and D1E (black).	149
Figure B11. Decay-associated-spectra in ethanol measured by fs transient absorption upon excitation at a) 426 nm and b) 560 nm for D1E-NP-Cu ₅ Ta ₁₁ O ₃₀	150
Figure B12: Power-voltage (P-V) curves and fill factor (ff) plots for Dye-1 (top) and Dye-2 (bottom) on nanoparticle Cu ₅ Ta ₁₁ O ₃₀ films.	151
Figure B13. Control i-v curves for Cu ₅ Ta ₁₁ O ₃₀ nanoparticle films without dye.	15152
Figure B14. Particle size distributions of Cu ₂ O (red) and Ta ₂ O ₅ (blue) nanoparticle precursors and Cu ₅ Ta ₁₁ O ₃₀ nanoparticle product (black).	153
Figure B15. UV-Vis of suspended Cu ₂ O (red), Ta ₂ O ₅ (green) and Cu ₅ Ta ₁₁ O ₃₀ (black) nanoparticles.	154
Figure B16. FESEM image of an annealed film of Cu ₅ Ta ₁₁ O ₃₀ nanoparticles in solution with elemental mapping of Cu and Ta (right). Inset: EDS spectrum of the area.	155

Figure B17. Powder X-ray diffraction pattern of the $\text{Cu}_5\text{Ta}_{11}\text{O}_{30}$ film (upper), and comparison to a calculated pattern based on the known crystalline structure of $\text{Cu}_5\text{Ta}_{11}\text{O}_{30}$ (lower)..... 156

Figure C1. The Rietveld refinement pattern of the monoclinic $\alpha\text{-Cu}_2\text{Ta}_4\text{O}_{11}$ at 223 K under flowing nitrogen. The observed intensities are indicated in blue (+), calculated intensities in green, the difference pattern is indicated by light blue, and the peak positions of $\alpha\text{-Cu}_2\text{Ta}_4\text{O}_{11}$ in the monoclinic Cc space group are indicated by the blue tick marks. Impurities of Ta_2O_5 were masked as indicated by the purple lines..... 161

Figure C2. A) The crystal structure of a unit cell of $\alpha\text{-Cu}_2\text{Ta}_4\text{O}_{11}$ along the *ac* direction showing the coordination of TaO_6 and TaO_7 polyhedra in the distorted tantalate layer to the TaO_6 octahedra in the alternating layer with the unit cell outlined in dashed blue line. B-E) Local coordination environment of Ta1, Ta2, Ta3, and Ta4 cations with the interatomic distances shown. The Ta cations and polyhedra are shown in tan, and the O atoms are shown in red. 16162

Figure C3. A) The crystal structure of $\alpha\text{-Cu}_2\text{Ta}_4\text{O}_{11}$ along the *ab* direction of the layer of linearly coordinated Cu cations bridged to the TaO_6 octahedra with the unit cell outlined in a blue dashed line. B-C) The local coordination environments of Ta4 and the symmetry inequivalent Cu(I) cations are shown with the interatomic distances displayed. The Ta cations and polyhedra are shown in tan, the Cu and O atoms are shown in blue and red, respectively..... 163

Figure C4. Figures adapted from Jahnberg indicating the relationship between the phase transition from a monoclinic to a rhombohedral unit cells A) 3 monoclinic unit cells stacked on top of each other outlined in the dashed line along the *ab* plane and B) the hexagonal unit cell outlined in the solid line. C) a single monoclinic unit cell outlined in a dashed line along the *bc* plane with the β angle shown in relation to the [001] of the rhombohedral unit cell. D) the *ab* plane of the monoclinic unit cell outlined in a dashed line in relation to the [100] direction of a hexagonal unit cell outlined in a solid line. The equations [1] to [3] reported from Ercit et. al 164

Figure C5. Chronoamperometric scans of the monoclinic $\alpha\text{-Cu}_2\text{Ta}_4\text{O}_{11}$ polycrystalline films that were annealed under vacuum at 500 °C for 3 h a) not heated in air b) heated in air at 250 °C for 3 h, c) heated in air 350 °C. 165

Figure C6. The powder X-ray diffraction patterns of $\text{Cu}_2\text{Ta}_4\text{O}_{11}$ before and after heating in air after photoelectrochemical measurements i) simulated XRD of $\alpha\text{-Cu}_2\text{Ta}_4\text{O}_{11}$ ii) before heating iii) after heating at 250 °C, iv) after heating at 350 °C, v) after heating at 450 °C vi) simulated XRD of the rhombohedral $\beta\text{-Cu}_2\text{Ta}_4\text{O}_{11}$ 166

Figure C7. The calculated band structure diagram of $\alpha\text{-Cu}_2\text{Ta}_4\text{O}_{11}$ with contributions from the valence and conduction band in blue and tan respectively. The indirect and direct band gap transitions are indicated with a black arrow..... 167

Figure C8. The calculated densities-of-states for α -) with the partial densities-of-states from Cu, Ta, and O indicated in blue, tan, and red. The total densities of states are indicated in black..... 168

CHAPTER 1: Introduction

This chapter has been adapted from a manuscript prepared for publication.

Ian Sullivan, Brandon Zoellner, and Paul A. Maggard*

North Carolina State University Department of Chemistry, Raleigh, North Carolina 27695-8204

The world's energy consumption was estimated to be 13.5 TW in 2001, and has been predicted to double to 27 TW by 2050.¹ A majority of this energy is fossil fuel based and results in the emission of greenhouse gasses. In 2013, 81% of the US energy consumption was fossil fuel based, including petroleum-based products, coal, and natural gas.² While the demand for energy is growing, an attractive alternate source of energy is the Sun. The energy from sunlight incident upon the Earth's surface in one hour can theoretically power all of the energy supply needed by the world.³ To harness this energy, the sunlight needs to be absorbed and converted into either electrical or chemical energy for storage. Semiconducting materials are excellent candidates for this application as they have the ability to absorb light and directly convert it to electrical power which can either be stored in batteries, or used to split water or reduce carbon dioxide to fuel sources.

Copper(I)-based metal oxides are promising materials as *p*-type semiconductors for solar energy applications. These materials have a wide range of bandgap sizes, ranging from as low as ~1.3 eV to greater than 3.0 eV, enabling their potential use in various types of solar energy harvesting. They also exhibit high charge carrier mobility as compared to other *p*-type materials, such as NiO, as well as relatively better stability compared to III-V or II-VI semiconductors, for example, *p*-GaAs or CdS. The *p*-type nature of these materials also

allows them to facilitate redox chemistry that *n*-type semiconductors are not suitable for, such as CO₂ reduction.^{4,5} The goal of this dissertation is to understand the structural and optical properties of new types of Cu(I) based metal oxide semiconductors, including Cu₂O, the copper delafossites, and the group-V copper oxides, and how these properties effect photoelectrochemical performance and efficiency when used in solar energy harvesting.

Background

Much research in solar energy and artificial photosynthesis has been focused on the use of metal oxides such as TiO₂, ZnO, Fe₂O₃, and ZrO₂.⁶ There are many different configurations in which these catalysts can be used to produce chemical or electrical energy from sunlight, such as suspended particle photocatalysis, as photoelectrodes for photoelectrochemical (PEC) water splitting, photovoltaics, or as a component in dye sensitized solar cells (DSSC).^{7,8} These metal oxides are examples of *n*-type semiconductors and are typically used as photoanodes in PEC cells, or for transport of electrons in DSSCs and PV cells. Many commonly studied *n*-type semiconductors are also wide band gap materials, with bandgap sizes greater than 3.0 eV, which limits their light absorption to the UV region.⁹ Another common limitation for smaller bandgap metal oxides is that they commonly suffer from low charge carrier mobility, as is the case for α -Fe₂O₃.¹⁰ As with all electrochemical systems, there must take place two reactions: oxidation and reduction. The *n*-type semiconductors are typically used for oxidation of water, whereas the *p*-type semiconductors are used for the reduction of water or CO₂.¹¹ For instance in water splitting, water is oxidized to oxygen gas at the photoanode, and the protons from this reaction are reduced to H₂ at the photocathode. While much research has been in the area of the oxidation/*n*-type metal oxides, the reduction/*p*-type side has shown much less progress.

Herein, research is described on Cu(I)-based metal oxides which show promise as *p*-type materials for solar energy conversion through water or CO₂ reduction, or as photovoltaic materials.

Photoelectrochemical and Photovoltaic Overview

There are several requirements necessary for a material to be an effective semiconductor for solar energy harvesting.¹⁴ The ability to absorb a large fraction of visible light in the solar spectrum, stability against degradation, low cost, and non-toxicity are some of the required characteristics. Other electronic characteristics of the semiconductor also determine how it will function and how efficient it will be, including its space-charge width, conductivity and charge carrier mobility. Depending on how the bands of a semiconductor bend at the heterojunction or surface-electrolyte interface determines whether the material is *n*-type (upward band bending) or *p*-type (downward band bending).¹⁵ Shown in Figure 1.1 is an illustration of the electronic energy levels of an *n*-type semiconductor (b,c) and *p*-type semiconductor (d,e). As with all semiconductors, the conduction and valence bands are in a flat-band state before the equilibration of the Fermi levels at the surface-electrolyte interface (Figure 1.1 b,d). The majority carriers for *n*-type semiconductors are electrons (e⁻) that diffuse from the space charge layer to the back contact. The minority carrier, holes (h⁺), will travel to the surface/electrolyte interface.¹¹ For an oxidation reaction to occur, the valence band of *n*-type photoelectrodes must be lower in energy (more positive) than the redox potential of interest, for instance the oxidation of water to O₂ (1.23 V vs. SHE). Well-known examples of *n*-type semiconductors are TiO₂ and α -Fe₂O₃.^{9,16} In *p*-type semiconductors, the opposite is true; downward band bending is present, and electrons, which are the minority charge carrier, will travel to the surface-electrolyte interface for reduction while the hole

majority carriers will travel to the back contact. For a *p*-type metal oxide to be effective, the conduction band must be higher in energy (more negative) than the redox potential of interest, for example H⁺/H₂ in proton reduction (0.0 V vs. SHE).¹⁷ For further information on band bending, extensive reviews can be found in the literature.^{18–20}

While an effective semiconductor can absorb light and excite an electron from the valence band to the conduction band, the charge carriers must be able to travel to the surface/electrolyte interface, and back contact allowing a current to flow. Charge carrier mobility is also another important characteristic in semiconductors. The larger the charge carrier mobility, the higher conductivity can be achieved in that material, allowing for diffusion of charge carriers to the surfaces and driving the redox chemistry and allowing current to flow. These are related in the Equation 1:

$$\sigma = ne\mu \quad (1)$$

where σ is the conductivity (S•cm⁻¹), n is the number of charge carriers per unit volume (cm⁻³), e is the elementary charge (C), and μ is the mobility of the charge carrier (cm²V⁻¹s⁻¹). The mobility is also related to the effective mass, m^* (kg), shown in equation 2:

$$m^* = \frac{e\tau_s}{\mu} \quad (2)$$

where τ_s is the mean scattering time (s). In this relationship the effective mass is inversely proportional to the mobility *i.e.* larger effective mass results in less mobility. The effective mass is related to the band dispersion in *k*-space, shown in Equation 3:

$$m^* = \hbar^2 \left(\frac{\partial^2 E}{\partial k^2} \right)^{-1} \quad (3)$$

where \hbar is the reduced Planck's constant, E is energy, and k is a wave vector in k-space. Thus for semiconductors with large band dispersion, this will yield a reduced effective mass and a higher conductivity.

The physical thickness of a semiconducting film is an important factor as there is a tradeoff between the absorption coefficient and the charge carrier diffusion length. The charge carrier diffusion coefficient is given by Equation 4:

$$D_n = \frac{k_B T}{e} \mu_n \quad D_p = \frac{k_B T}{e} \mu_p \quad (4)$$

where D is the diffusion coefficient (cm^2s^{-1}) of the charge carrier in n or p -type semiconductors, k_B is Boltzmann's constant ($\text{eV}\cdot\text{K}^{-1}$), T is absolute temperature (K), e is the elementary charge, and μ is the mobility of the charge carrier.¹¹ The diffusion coefficient is a relative measure of how far the charge carriers will diffuse when excited by a photon. The absorption coefficient is given by Equation 5:

$$\alpha = \frac{1}{d} \ln \frac{I_o}{I} \quad (5)$$

where α is the absorption coefficient (cm^{-1}), d is the thickness of the semiconductor sample (cm), I is the incident light intensity (W), and I_o is the transmitted light intensity. Ideally the charge carrier mobility is on the order of the absorption coefficient, and if there is a large difference between the two, higher recombination rates will most likely occur. For instance, $\alpha\text{-Fe}_2\text{O}_3$ is an n -type semiconductor with a band gap of ~ 2.0 eV, a diffusion coefficient of ~ 0.01 cm^2s^{-1} , and a hole diffusion length of 2-4 nm. Due to the low diffusion coefficient and short hole diffusion length, there is a relatively higher probability that the excited charge carriers will not reach the surface/electrolyte interface before recombining. This has been cited as the main reason for the limited performance of $\alpha\text{-Fe}_2\text{O}_3$ as a viable photoanode for water oxidation.¹⁰

In DSSC photovoltaics, a wide band gap semiconductor ($E_g > 3.0$ eV) acts as a charge transport layer and is sensitized by a molecular dye, or by quantum dots,^{21,22} yielding light absorption into the visible-light range. The valence and conduction band positions relative to the energy levels of the dye molecule and redox mediator are of great importance as this will limit (thermodynamically) the maximum efficiency of the solar cell.⁷ Figure 1.2 illustrates the ideal energy levels of the conduction and valence band, as compared with the dye molecule and redox mediator energy levels for a *p*-type DSSC. In step 1, light excites an electron from the HOMO of the dye to the LUMO. In step 2, hole-injection into the valence band of the semiconductor occurs, leaving a reduced dye. In step 3, the dye should then transfer the electron to the redox mediator (M). The positive charge from the initial hole-injection is collected at the counter electrode and oxidizes the redox mediator in step 4. The initial states are thus regenerated. Ideally, the excited electron in the dye does not relax back to the ground state before hole injection (step 5) or recombine with the hole in the valence band (step 6). The valence band should be lower in energy than the LUMO of the dye molecule, but higher in energy than the HOMO, allowing hole-injection into the semiconductor. The conduction band should be sufficiently high enough in energy to not participate in any of these photoelectrochemical steps.²³ The reduction potential of the redox mediator should be lower in energy than the LUMO of the dye molecule, allowing electrons to reduce the mediator. Research into new combinations of metal-oxide semiconductors, dyes and redox mediators can be found in the recent literature.²¹⁻²⁷

Photovoltaic solar cells (PV cells) are based on heterojunctions of *p*-type and *n*-type materials (*p-n* junctions). These can be composed of single elements (*p*-Si and *n*-Si), metal chalcogenides, metal oxides, or a combination thereof. As the fermi levels of the *p* and *n*

materials equilibrate band bending occurs, resulting in a built-in potential at the interface. This governs the maximum photovoltage of the device and determines the efficiency of the cell. Many different parameters govern the efficiency of the PV cell, including bandgap size, band alignment, and resistivity.²⁸

For both DSSCs and PV cells, the overall efficiency is given by Equation 6:

$$\eta = V_{oc} I_{sc} \frac{FF}{I_c} \quad (6)$$

where η is efficiency, V_{oc} is the open circuit voltage (V), I_{sc} is the short circuit current (A), FF is the fill factor, and I_c is the power of incident light (W/cm^2). The fill factor is given by Equation 7:

$$FF = \frac{I_{sc} V_{oc}}{I_{mp} V_{mp}} \quad (7)$$

where I_{mp} and V_{mp} are the current and voltage at maximum power, respectively. The efficiency can be calculated from values found in current density-potential curves (j-v curves).^{28,29}

Benefits of Cu(I)-Mixed Metal Oxides

Recently, many ternary metal oxides comprised of a Cu(I)-based valence band, and combined with another metal M^{n+} (e.g. Nb(V), Ta(V), and V(V)) based conduction band, have been investigated as alternative *p*-type oxides. Depending on the energy of the conduction band, bandgap sizes as low as ~ 1.0 eV and up to >3.0 eV can be attained. The ability to tune such a material can tailor specific needs of Z-scheme tandem solar cells³⁰, or multi-junction photovoltaic cells allowing for absorption of a wide range of wavelengths, larger photocurrents, and maximum efficiency.

Another advantage of mixed-metal oxides is the potential stabilization of the material. As previously described, Cu_2O will self-reduce under irradiation in aqueous solution. This is

due to the excitation of an electron from the copper $3d^{10}$ valence band to the primarily copper $4s$ conduction band.³¹ Adding another metal with unfilled d orbitals allows for electrons to be excited into the M^{n+} -based conduction band, and help inhibit the reduction of Cu(I). The investigation of the electronic properties of $Cu_5Ta_{11}O_{30}$ and $Cu_2Ta_4O_{11}$ gives insight into the stabilization of Cu(I) based materials, by allowing electrons to be excited from the Cu $3d^{10}$ based valence band into the Ta $5d^0$ based conduction band.

Outline of Original Research

The structural and optical properties of metal oxide semiconductors play an important role in the photoelectrochemical performance of polycrystalline films, DSSCs, and PV cells. Chapter 2 describes the investigation of these characteristics in the p -type semiconductor $Cu_5Ta_{11}O_{30}$. Through the use of XRD, SEM imaging, XPS, and Rietveld refinements, it was found that increased photocurrents could be achieved by heating the material in air, allowing for CuO to form at the surface and forming a type-II heterojunction. Chapter 3 describes the synthesis, characterization and use of $Cu_5Ta_{11}O_{30}$ nanoparticles in a p -DSSC. By decreasing the size of the particles, quantum confinement occurs and the band gap increases, from 2.6 eV to 3.0 eV. The band positions were found to be at the correct energy levels to be used with Zn-based porphyrin dyes to be used in a DSSC.

From the previous research on the structural, optical and photoelectrochemical properties of $Cu_5Ta_{11}O_{30}$, a similar approach was used to determine the photoelectrochemical properties of $Cu_2Ta_4O_{11}$ polycrystalline films in Chapter 4. It was found that heating this material in air also induces surface changes, increased light absorption and increased cathodic photocurrents. Similarly increased photocurrents due to the formation of a favorable band offset was determined by addition of CuO nanoparticles to the surface of $Cu_2Ta_4O_{11}$.

Chapter 5 describes trends in the structural and optical properties of several different Cu(I) based metal oxides including the group-V Cu(I) metal oxides (vanadates, niobates and tantalates), and Cu(I) delafossites, including both the above thesis research and recent research found in the literature. Chapter 6 is a summary of the overall research conclusions and describes how the structural and optical properties of mixed metal oxides can be tuned to increase their efficiency and overall photocurrents.

REFERENCES

- (1) Lewis, N. S.; Nocera, D. G. Powering the Planet: Chemical Challenges in Solar Energy Utilization. *PNAS* **2006**, *103* (43), 15729–15735.
- (2) U.S. DOE. Annual Energy Outlook 2015. **2015**, 154.
- (3) Tsao, J.; Lewis, N.; Crabtree, G. Solar FAQs. *US Dep. Energy* **2006**, 1–24.
- (4) Flynn, C. J.; Oh, E. E.; Mccullough, S. M.; Call, R. W.; Donley, C. L.; Lopez, R.; Cahoon, J. F. Hierarchically-Structured NiO Nanoplatelets as Mesoscale P-Type Photocathodes for Dye-Sensitized Solar Cells. *J. Phys. Chem. C* **2014**, *118* (26), 14177–14184.
- (5) Halmann, M. Photoelectrochemical Reduction of Aqueous Carbon Dioxide on P-Type Gallium Phosphide in Liquid Junction Solar Cells. *Nature* **1978**, *275*, 115–116.
- (6) Osterloh, F. E. Inorganic Nanostructures for Photoelectrochemical and Photocatalytic Water Splitting. *Chem. Soc. Rev.* **2013**, *42* (6), 2294–2320.
- (7) O'Regan, B.; Gratzel, M. A Low-Cost, High-Efficiency Solar Cell Based on Dye-Sensitized Colloidal TiO₂ Films. *Nature* **1991**, *353*, 737–740.
- (8) Osterloh, F. E. Inorganic Materials as Catalysts for Photochemical Splitting of Water. *Chem. Mater.* **2008**, *20* (1), 35–54.
- (9) Fujishima, A.; Honda, K. Electrochemical Photolysis of Water at a Semiconductor Electrode. *Nature* **1972**, *238*, 37–38.
- (10) Qin, D.; Tao, C.; In, S.; Yang, Z.; Mallouk, T. E.; Bao, N.; Grimes, C. A. Facile Solvothermal Method for Fabricating Arrays of Vertically Oriented α -Fe₂O₃ Nanowires and Their Application in Photoelectrochemical Water Oxidation. *Energy Fuels* **2011**, *25* (11), 5257–5263.
- (11) Memming, R. *Semiconductor Electrochemistry*; Wiley-VCH: Weinheim, 2000.
- (12) Jara, D. H.; Yoon, S. J.; Stamplecoskie, K. G.; Kamat, P. V. Size-Dependent Photovoltaic Performance of CuInS₂ Quantum Dot-Sensitized Solar Cells. *Chem. Mater.* **2014**, *26* (24), 7221–7228.
- (13) Santra, P. K.; Nair, P. V.; George Thomas, K.; Kamat, P. V. CuInS₂-Sensitized Quantum Dot Solar Cell. Electrophoretic Deposition, Excited-State Dynamics, and Photovoltaic Performance. *J. Phys. Chem. Lett.* **2013**, *4* (5), 722–729.
- (14) Lewis, N. S. Light Work with Water. *Nature* **2001**, *414* (6864), 589–590.

- (15) Rajeshwar, K. Fundamentals of Semiconductor Electrochemistry and Photoelectrochemistry. *The encyclopedia of electrochemistry*; 2003; pp 1–53.
- (16) Townsend, T. K.; Sabio, E. M.; Browning, N. D.; Osterloh, F. E. Photocatalytic Water Oxidation with Suspended α -Fe₂O₃ Particles-Effects of Nanoscaling. *Energy Environ. Sci.* **2011**, *4* (10), 4270.
- (17) Walter, M. G.; Warren, E. L.; McKone, J. R.; Boettcher, S. W.; Mi, Q.; Santori, E. A.; Lewis, N. S. Solar Water Splitting Cells. *Chem. Rev.* **2010**, *110* (11), 6446–6473.
- (18) Zhang, Z.; Yates, J. T. Band Bending in Semiconductors: Chemical and Physical Consequences at Surfaces and Interfaces. *Chem. Rev.* **2012**, *112* (10), 5520–5551.
- (19) Gomes, W. P.; Cardon, F. Electron Energy Levels in Semiconductor Electrochemistry. *Prog. Surf. Sci.* **1982**, *12* (2), 155–215.
- (20) Gelderman, K.; Lee, L.; Donne, S. W. Flat-Band Potential of a Semiconductor : Using the Mott–Schottky Equation. *J. Chem. Educ.* **2007**, *84* (4), 685–688.
- (21) Kamat, P. V. Quantum Dot Solar Cells. The Next Big Thing in Photovoltaics. *J. Phys. Chem. Lett.* **2013**, *4* (6), 908–918.
- (22) Kamat, P. V. Quantum Dot Solar Cells. Semiconductor Nanocrystals as Light Harvesters. *J. Phys. Chem. C* **2008**, *112* (48), 18737–18753.
- (23) Odobel, F.; Pellegrin, Y. Recent Advances in the Sensitization of Wide-Band-Gap Nanostructured P-Type Semiconductors. Photovoltaic and Photocatalytic Applications. *J. Phys. Chem. Lett.* **2013**, *4* (15), 2551–2564.
- (24) Bachmeier, A.; Hall, S.; Ragsdale, S. W.; Armstrong, F. A. Selective Visible-Light-Driven CO₂ Reduction on a P-Type Dye-Sensitized NiO Photocathode. *J. Am. Chem. Soc.* **2014**, *136* (39), 13518–13521.
- (25) Lee, M. M.; Teuscher, J.; Miyasaka, T.; Murakami, T. N.; Snaith, H. J. Efficient Hybrid Solar Cells Based on Meso-Superstructured Organometal Halide Perovskites. *Science*. **2012**, *338* (6107), 643–647.
- (26) Sherman, B. D.; Ashford, D. L.; Lapidus, A. M.; Sheridan, M. V.; Wee, K.-R.; Meyer, T. J. Light-Driven Water Splitting with a Molecular Electroassembly-Based Core/Shell Photoanode. *J. Phys. Chem. Lett.* **2015**, *6* (16), 3213–3217.
- (27) Snaith, H. J. Perovskites: The Emergence of a New Era for Low-Cost, High-Efficiency Solar Cells. *J. Phys. Chem. Lett.* **2013**, *4* (21), 3623–3630.

- (28) Gray, J. L. The Physics of the Solar Cell. In *Handbook of Photovoltaic Science and Engineering, Second Edition*; Luque, A., Hegedus, S., Eds.; 2011.
- (29) Green, M. A. Solar Cell Fill Factors: General Graph and Empirical Expressions. *Solid State Electron.* **1981**, *24* (8), 788–789
- (30) Gratzel, M. Photoelectrochemical Cells. *Nature* **2001**, *414*, 338–344.
- (31) Meyer, B. K.; Polity, A.; Reppin, D.; Becker, M.; Hering, P.; Klar, P. J.; Sander, T.; Reindl, C.; Benz, J.; Eickhoff, M.; et al. Binary Copper Oxide Semiconductors: From Materials towards Devices. *Phys. Status Solidi B* **2012**, *249* (8), 1487–1509.

Figures

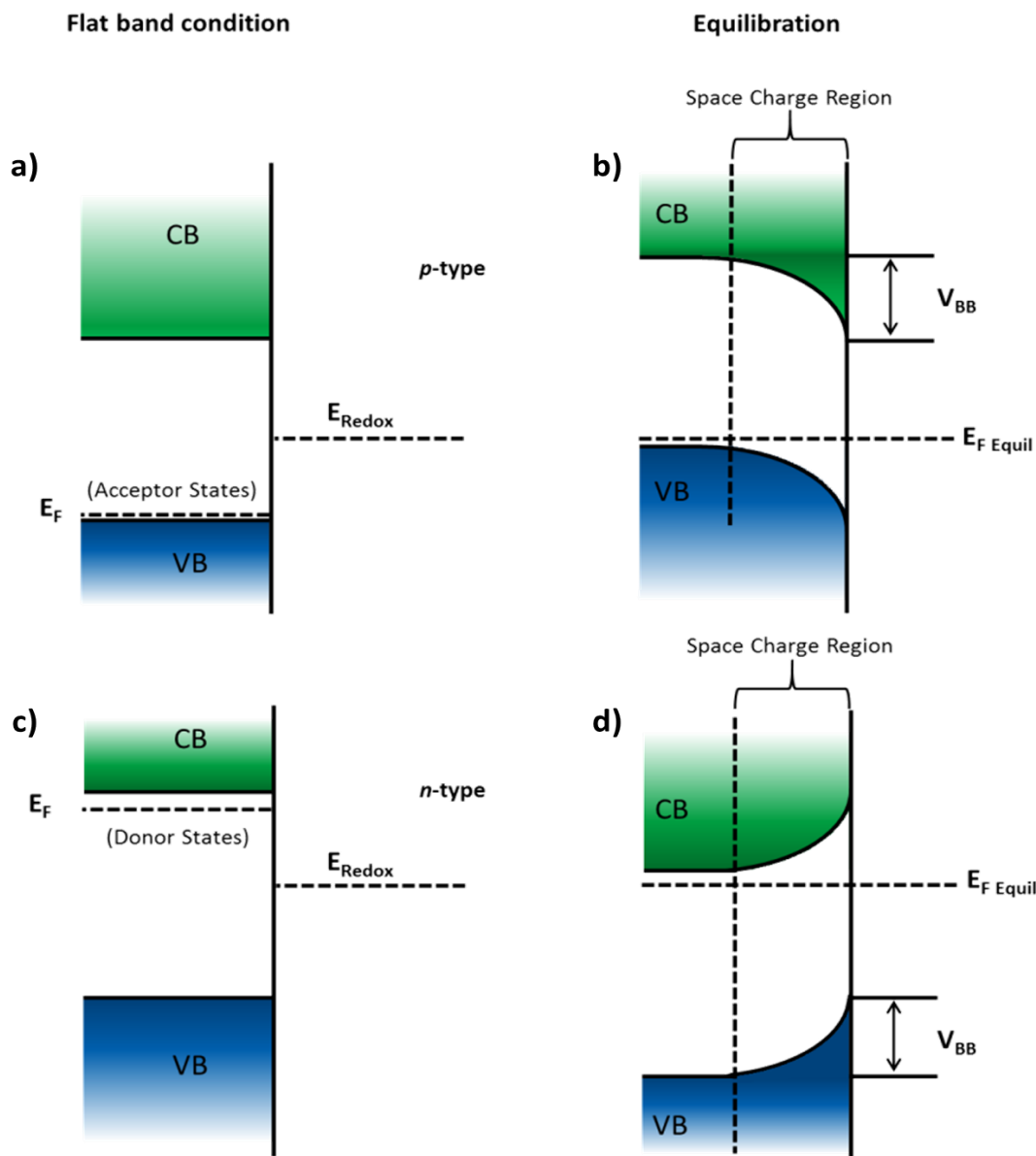


Figure 1.1. Valence and conduction bands before equilibration for a *p*-type semiconductor (a) and *n*-type semiconductor (c). After equilibration, downward band bending is present for *p*-type semiconductors (b) and upward band bending for *n*-type semiconductors (d). The diagrams from left to right are drawn to the same relative potential scale. CB, conduction band; VB, valence band; E_f , Fermi level; E_{Redox} , redox potential of the electrolyte; V_{BB} , band bending potential.¹⁸

DSSC Band and Energy Levels

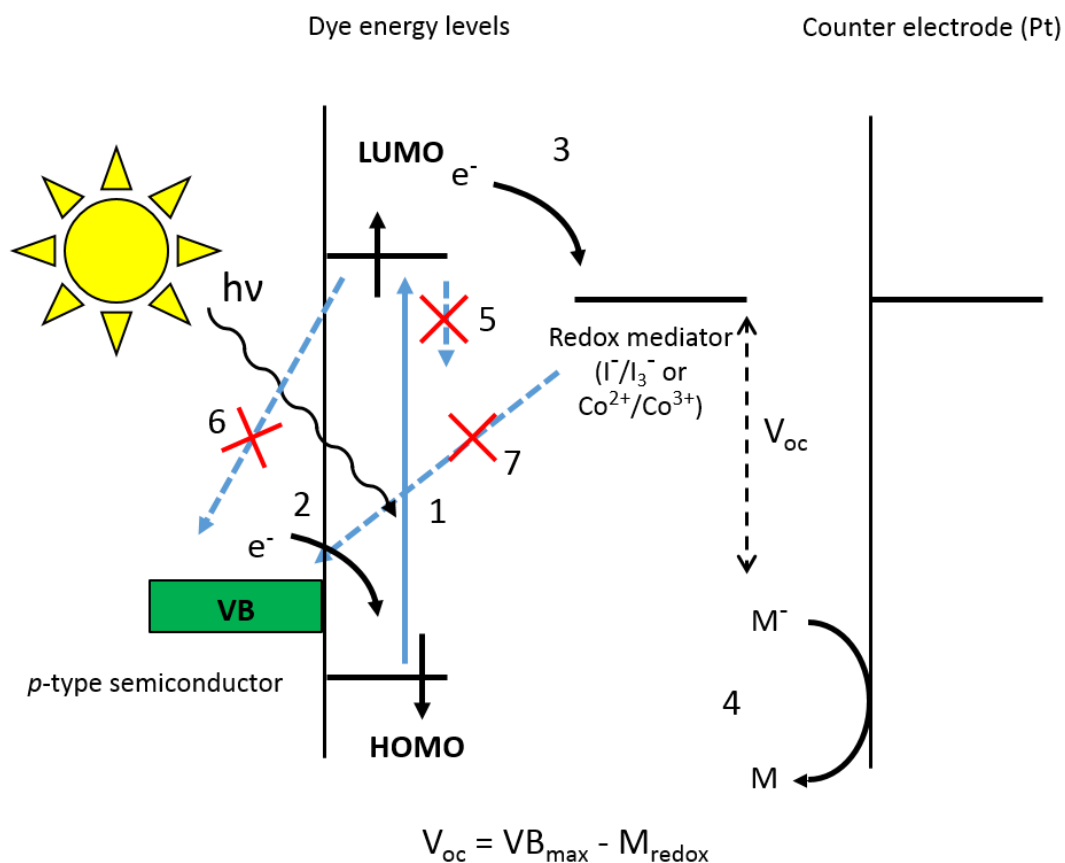


Figure 1.2. Energy levels required for *p*-DSSC. The dye absorbs light and an electron is promoted to an excited state (1), hole injection should then occur between the dye and *p*-type semiconductor (2). The dye is now in a reduced state and should transfer an electron to the redox mediator (3). The redox mediator must then travel to the counter electrode and be oxidized by holes from the semiconductor (4). Other processes such as relaxation of the electron from the LUMO to the HOMO (5) or recombination of the excited dye (6) or redox mediator (7) will diminish the efficiency of the *p*-DSSC.²³

CHAPTER 2: Cu-Deficiency in the *p*-Type Semiconductor $\text{Cu}_{5-x}\text{Ta}_{11}\text{O}_{30}$: Impact on its Crystalline Structure, Surfaces, and Photoelectrochemical Properties

Based on a journal article published in Chemistry of Materials

Chem. Mater. **2014**, 26, 6711-6721.

Ian Sullivan,^a Prangya P. Sahoo,^a Lindsay Fuoco,^a Andy S. Hewitt,^b Sean Stuart,^b Daniel Dougherty^b and Paul A. Maggard^{a,*}

^a Department of Chemistry, North Carolina State University, Raleigh, NC 27695-8204.

^b Department of Physics, North Carolina State University, Raleigh, NC 27695-8204.

The research presented here is a combination of work from all of the authors. The author of this dissertation contributed to the flux synthesis and powder XRD characterization of $\text{Cu}_5\text{Ta}_{11}\text{O}_{30}$, powder XRD lattice refinements, interpretation of XPS data, SEM imaging, UV-DRS measurements, and fabrication and photoelectrochemical measurements of polycrystalline $\text{Cu}_5\text{Ta}_{11}\text{O}_{30}$ photocathodes.

ABSTRACT

The *p*-type semiconductor $\text{Cu}_5\text{Ta}_{11}\text{O}_{30}$ has been investigated for the effect of Cu extrusion on its crystalline structure, surface chemistry, and photoelectrochemical properties. The $\text{Cu}_5\text{Ta}_{11}\text{O}_{30}$ phase was prepared in high purity using a CuCl-mediated flux synthesis route, followed by heating the products in air from 250 °C to 750 °C in order to investigate the effects of its reported film preparation conditions as a *p*-type photoelectrode. At 650 °C and higher temperatures, $\text{Cu}_5\text{Ta}_{11}\text{O}_{30}$ is found to decompose into CuTa_2O_6 and Ta_2O_5 . At lower temperatures of 250 °C to 550 °C, nanosized and/or amorphous $\text{Cu}^{\text{II}}\text{O}$ surface islands and a Cu-deficient crystalline structure, i.e., $\text{Cu}_{5-x}\text{Ta}_{11}\text{O}_{30}$ ($x \sim 1.8(1)$ after 450 °C for 3h in air) is found by electron microscopy and Rietveld structural refinement results, respectively.

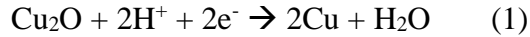
Its crystalline structure exhibits a decrease in the unit cell volume with increasing reaction temperature and time, owing to the increasing removal of Cu(I) ions from its structure. The parent structure of $\text{Cu}_5\text{Ta}_{11}\text{O}_{30}$ is conserved up to ~50% Cu vacancies, but with one notably shorter Cu – O distance (by ~0.26 Å) and concomitant changes in the Ta – O distances within the pentagonal bipyramidal TaO_7 layers (by ~0.29 Å to ~0.36 Å). The extrusion and oxidation of Cu(I) to Cu(II) cations at its surfaces is found by X-ray photoelectron spectroscopy, while magnetic susceptibility data are consistent with the oxidation of Cu(I) within its structure, as given by $\text{Cu}^{\text{I}}_{(5-2x)}\text{Cu}^{\text{II}}_x\text{Ta}_{11}\text{O}_{30}$. Polycrystalline films of $\text{Cu}_{5-x}\text{Ta}_{11}\text{O}_{30}$ were prepared under similar conditions by sintering, followed by heating in air at temperatures of 350 °C, 450 °C, and 550 °C, each for 15 min, 30 min, and 60 min. An increasing amount of copper deficiency in the $\text{Cu}_{5-x}\text{Ta}_{11}\text{O}_{30}$ structure and $\text{Cu}^{\text{II}}\text{O}$ surface islands are found to result in significant increases in its *p*-type visible-light photocurrent at up to -2.5 mA/cm² (radiant power density of ~500 mW/cm²). Electronic structure calculations show that an increase in Cu vacancies shifts the Fermi level to lower energies, resulting in the depopulation of primarily Cu $3d^{10}$ -orbitals as well as O $2p$ orbitals. Thus, these findings help shed new light on the role of Cu-deficiency and $\text{Cu}^{\text{II}}\text{O}$ surface islands on the *p*-type photoelectrode films for solar energy conversion systems.

INTRODUCTION

The discovery and development of visible-light-absorbing semiconductors can address a critical barrier in achieving efficient systems for the conversion of sunlight to chemical or electrical energy.^{1,2} Recently, Cu(I)-containing semiconductors have demonstrated a significant and rapidly growing potential in this area.³⁻¹⁶ The majority of simple metal-oxides have large bandgap sizes and absorb in the ultraviolet and higher

energies (i.e. $E_g > 3.0$ eV), while most Cu(I)-containing oxides are able to absorb far into the visible region owing to the formation of a higher-energy valence band comprised of the Cu $3d^{10}$ orbitals. For example, an increasing Cu(I) content has been shown to significantly decrease the bandgap size by as much as ~ 2.6 eV in the $\text{Li}_{1-x}\text{Cu}_x\text{Nb}_3\text{O}_8$,¹² $\text{Cu}_{3x}\text{La}_{1-x}\text{Ta}_7\text{O}_{19}$,¹⁴ and other similar solid solutions.⁵ Further, Cu(I)-containing oxides are also typically *p*-type semiconductors and exhibit suitable band energies for the reduction of water or carbon dioxide to chemical fuels such as hydrogen or methanol.

The simplest Cu(I)-oxide, i.e., Cu_2O , is a well-known *p*-type semiconductor that has been intensely investigated for promising applications in solar energy conversion. However, the reduction potential of Cu_2O falls within its band gap, and thus bandgap irradiation thermodynamically drives its self-reduction at the surfaces according to Equation 1.^{17,18}



Much recent research has been directed at the stabilization of Cu_2O by coating its surfaces with other metal oxides.¹⁹ Alternatively, new *p*-type semiconductors within the Cu(I) niobate and Cu(I) tantalate systems have been reported by the Maggard research group, and which exhibit visible-light bandgap sizes ($\sim 1.3 - 2.6$ eV) and large photocurrents ($\sim 1 - 3$ mA/cm²) as polycrystalline photoelectrode films. Light absorption in these semiconductors originates from a bandgap transition primarily between the filled Cu $3d^{10}$ -orbitals and the empty Nb/Ta d^0 -orbitals. Excitation of the electron into the empty Nb/Ta orbitals can thus potentially help to stabilize Cu(I) against its reduction. The Cu(I)-niobate family, including CuNbO_3 ,⁶ $\text{Cu}_2\text{Nb}_8\text{O}_{21}$,¹¹ and CuNb_3O_8 ,^{9,15} exhibits a range of bandgap sizes from ~ 1.4 eV (CuNb_3O_8), to ~ 1.6 eV ($\text{Cu}_2\text{Nb}_8\text{O}_{21}$), to ~ 2.0 eV (CuNbO_3), and all of which have shown significant cathodic photocurrent densities under visible-light irradiation. The Cu(I)-tantalate system

currently includes $\text{Cu}_2\text{Ta}_4\text{O}_{11}$,^{5,20} $\text{Cu}_3\text{Ta}_7\text{O}_{19}$ and $\text{Cu}_5\text{Ta}_{11}\text{O}_{30}$,³ with a relatively smaller range of bandgap sizes from ~2.4 to 2.6 eV. Polycrystalline films of both $\text{Cu}_3\text{Ta}_7\text{O}_{19}$ and $\text{Cu}_5\text{Ta}_{11}\text{O}_{30}$ exhibit high cathodic photocurrents in aqueous solutions under visible-light irradiation.⁸

Interestingly, the highest cathodic photocurrents of the *p*-type Cu(I)-niobate and Cu(I)-tantalate photoelectrode films occur after heating them in air to 350 °C to 550 °C. Under these conditions, the *p*-type CuNb_3O_8 and $\text{Cu}_2\text{Nb}_8\text{O}_{21}$ phases were recently reported to show Cu-site vacancies and the formation of surface nano-islands of CuO, and that correlated with their highest measured photocurrents.^{11,15} However, similar investigations within the Cu(I)-tantalate system have not yet been reported. For example, the $\text{Cu}_5\text{Ta}_{11}\text{O}_{30}$ semiconductor has a bandgap size (i.e., ~2.6 eV) and conduction band potential (i.e., -1.53 V vs. NHE) that satisfies the thermodynamic requirements for the reduction of water into hydrogen. Herein we report on the CuCl-mediated flux synthesis of $\text{Cu}_5\text{Ta}_{11}\text{O}_{30}$ microcrystalline particles, and the impact of heating in air on its bulk crystalline structure, surfaces, and photoelectrochemical properties.

EXPERIMENTAL

A. Synthetic Methods. The synthesis of $\text{Cu}_5\text{Ta}_{11}\text{O}_{30}$ was performed using a molten salt flux method, as previously described.³ Stoichiometric amounts of Cu_2O (Alfa Aesar, 99.99%) and Ta_2O_5 (Alfa Aesar, 99.99%) were combined and mixed with a CuCl flux (Alfa Aesar, 99%), and ground together in an Argon atmosphere into a fine homogenous powder. The mixture was loaded into a fused-silica tube and sealed under vacuum. The mixture was then heated to 900 °C for 24 h. After cooling, the products were washed with concentrated

HCl, concentrated NH₄OH, and deionized water to yield a homogeneous yellow powder that was found to be in high purity according to powder X-ray diffraction (XRD).

B. Characterization. Powder XRD data were taken on an Inel X-ray diffractometer using Cu K α_1 radiation ($\lambda=1.54056 \text{ \AA}$) from a sealed tube X-ray generator (30 mA, 35 kV). A curved position sensitive detector (CPS-120) was used in transmission mode to obtain diffractograms. A sample mass of ~50 mg was placed between two pieces of Scotch tape and rotated between the X-ray beam and detector. Data were collected anywhere from 30-120 min, and plotted using the software program WinPlotr.²¹ Lattice constant refinements were performed using the Rietveld method using whole pattern fitting (WPF) in the software program Jade 9.²² Refined unit cell volumes are given in Table 2.1, and the refined lattice constants are listed in the Supporting Information (Table A1).

A full structure Rietveld refinement was also performed for a Cu-deficient Cu_{5-x}Ta₁₁O₃₀ that had been heated in air at 450 °C for 3h. A powder X-ray diffraction data set for the refinement was collected at room temperature on a Philips X-pert diffractometer with Cu K α radiation over the angular range $10^\circ \leq 2\theta \leq 110^\circ$ with a step width of 0.017°. The diffractometer had been calibrated against a silicon powder (NIST-SRM 640c) standard. The data were analyzed by Le Bail profile analysis and then refined by the Rietveld method as implemented in the JANA2000 program suite.²³ The background was estimated by a Legendre polynomial function consisting of 15 coefficients, and the peak shapes were described by a pseudo-Voigt function with five profile coefficients. The initial unit cell dimensions and atomic coordinates were obtained from the reported structure of Cu₅Ta₁₁O₃₀,³ which crystallizes in the hexagonal crystal system (space group $P\bar{6}2c$, no. 190) with $a = 6.2252(1) \text{ \AA}$, $c = 32.516(1) \text{ \AA}$ and $V = 1091.26(4) \text{ \AA}^3$. There are three symmetry-unique Ta

sites, one Cu site and eight oxygen sites within the unit cell. The background and the peak shape parameters were refined first, followed by the unit cell and zero shift parameters. The scale parameter and atomic coordinates were refined next, beginning with Ta and Cu atoms, and subsequently the O atoms. The atomic displacement parameters were then refined, showing relatively larger values for the Cu site. Several cycles of refinements were carried out that converged to 0.53(1) occupancy for the Cu site, giving a refined composition of $\text{Cu}_{3.2(1)}\text{Ta}_{11}\text{O}_{30}$. The site occupancy of all atomic positions were similarly allowed to refine, but only the Cu site occupancy was found to be less than unity. The final R_p and R_{wp} factors converged to 3.58 % and 4.92 %, respectively. The highest residual electron density peaks were 1.71 and $-2.53 \text{ e}/\text{\AA}^3$, respectively, indicating that the electron density had been properly modeled. Selected refinement parameters and interatomic distances are given in Tables 2 and 3, and the refined atomic coordinates are listed in Table S1 of the Supporting Information.

C. Characterization Techniques. UV-Vis diffuse reflectance spectra (DRS) were taken on a Shimadzu UV-3600 spectrometer with a BaSO_4 background. The reflectance data are plotted as $F(R_\infty)$ versus Energy (eV), where $F(R_\infty) = \frac{(1-R_\infty)^2}{2R_\infty} = \frac{\alpha}{s}$ in the Kubelka-Munk theory of diffuse reflectance which relates reflectance, R , to an absorption coefficient, α , and a scattering coefficient, s . Assuming a constant s value, R can be approximated as proportional to α .²⁴ The bandgap energy is estimated by extrapolating the linear rise in the absorbance that is indicative of the fundamental bandgap transition. Scanning electron microscopy (SEM) was performed on a JEOL JSM-6400F field-emission scanning electron microscope. An acceleration voltage of 10.0 kV was used, and images were collected by an Everhart-Thornley secondary electron detector. Thermogravimetric analyses were taken in

air on a TA Instruments TGAQ50, and the data were plotted as % weight change (grams) versus time at the temperatures of 250 °C, 350 °C and 450 °C.

X-ray photoelectron spectroscopy (XPS) was performed on a Specs hemispherical analyzer, using a Mg K α radiation source (1253.6 eV), and under ultra-high vacuum (UHV) (base pressure $\sim 2 \times 10^{-10}$ mbar). All spectra were calibrated to the C 1s peak binding energy (284 eV).

D. Film Preparation. Polycrystalline films were prepared on TEC-7 fluorine-doped tin oxide (FTO) slides (Pilkington Glass Inc.). The FTO slides were sonicated in deionized water, followed by ethanol, and finally acetone solution for 30 minutes each. An area of 1 cm² was taped off with Scotch tape on the conducting side and the polycrystalline Cu₅Ta₁₁O₃₀ product was deposited using the doctor blade method. A water/tert-butanol solution was used as a dispersant, instead of ethanol reported in prior investigations.⁸ The films were then annealed at 500 °C for 3 h under dynamic vacuum ($P \leq 25$ mtorr). After annealing, the films were heated in air from 350 °C to 550 °C for 15 min, 30 min, or 60 min. For *p*-type Cu₂O, a polycrystalline photoelectrode was electrodeposited on FTO using identical conditions as reported previously.²⁵ Briefly, an FTO slide with a taped-off area of 1cm² was immersed into a plating solution (an aqueous solution of 0.2M CuSO₄ and 3.0M lactic acid) and heated to 60 °C. Next, a -0.6V bias was applied (vs SCE) until a charge of 1.4 C/cm² was achieved. Powder XRD indicated the film was high-purity crystalline Cu₂O (See Supporting Information).

Photoelectrochemical measurements were taken using a custom Teflon-constructed three electrode cell in an aqueous 0.5M Na₂SO₄ electrolyte solution at a pH of ~ 6.5 . The polycrystalline films served as the working electrode, a Pt foil served as the counter electrode

and a saturated calomel electrode (SCE sat. KCl) was used as a reference. All potentials will be referenced to the SCE unless otherwise noted. All solutions were purged with nitrogen gas for 30 min prior to and during the experiments. Linear sweep voltammetry (LSV) measurements were performed within a potential range of 0.100 V to -0.600 V at a scan rate of 25 mV s⁻¹. Chronoamperometric measurements were taken at an applied bias of -0.2 V for 1000 s. A high pressure Xenon lamp (Newport Corporation) was used as a light source. The lamp was fitted with infrared and ultraviolet light cutoff filters (1000 nm > λ > 420 nm). The light source was chopped during the measurements to observe both the dark current and photocurrent. The irradiant power density was measured to be ~500 mW/cm².

E. Electronic Structure Calculations. Electronic band-structure calculations were performed on the geometry-optimized and Cu-deficient Cu_{5-x}Ta₁₁O₃₀ structure ($x = 0, 1$ or 2), using plane-wave density functional theory within the Vienna Ab-Initio Simulation Package (VASP; ver. 4.6).²⁶ The refined crystal structures of Cu₅Ta₁₁O₃₀ and Cu_{3.2(1)}Ta₁₁O₃₀ were utilized in the calculations. The Cu-site vacancies in each (16.7%, 33.3%, and 50%) were modeled using a 2 × 1 × 1 superstructure that enabled a distribution of 1 to 2 Cu vacancies within each of the Cu(I) layers. Within a single unit cell, the migration of a Cu atom between a filled and a vacant site were modeled within both the Cu₅Ta₁₁O₃₀ and Cu_{3.2(1)}Ta₁₁O₃₀ structures. All calculations used the Perdew-Burke-Ernzerhof functional in the generalized gradient approximation,²⁷ and ultrasoft Vanderbilt-type pseudopotentials.²⁸ The Monkhorst-Pack scheme was used for automatic selection of k -points within the Brillouin zone.²⁹

RESULTS AND DISCUSSION

A. Bulk Phase Analysis and Surface Characterization. The CuCl-mediated flux synthesis yielded high purity Cu₅Ta₁₁O₃₀, as confirmed by powder XRD given in the

Supporting Information (Figure A1). The refined lattice constants are consistent with previous reports (Sp. Grp. P-62c; $a = 6.2252(1) \text{ \AA}$ and $c = 32.516(1) \text{ \AA}$). Shown in Figure 2.1, Scanning Electron Microscopy (SEM) images of the products show micron-sized $\text{Cu}_5\text{Ta}_{11}\text{O}_{30}$ crystallites with highly faceted and smooth surfaces, ranging in sizes between ~ 5 to 20 \mu m . The $\text{Cu}_5\text{Ta}_{11}\text{O}_{30}$ crystallites were heated to increasing temperatures in air, at up to $750 \text{ }^\circ\text{C}$, in order to determine its range of stability and the decomposition products. As shown in the powder XRD patterns in Figure 2.2, a Ta_2O_5 impurity begins to appear at $550 \text{ }^\circ\text{C}$ to $650 \text{ }^\circ\text{C}$, before $\text{Cu}_5\text{Ta}_{11}\text{O}_{30}$ then completely decomposes in air to yield CuTa_2O_6 and Ta_2O_5 . Interestingly, Cu(II)-containing impurities could only be detected by powder XRD at $750 \text{ }^\circ\text{C}$, owing to the formation of amorphous and/or nanoparticle CuO phases in very small amounts at the crystallite surfaces (as described below).

When heated at the lower temperatures of $350 \text{ }^\circ\text{C}$ to $550 \text{ }^\circ\text{C}$, the $\text{Cu}_5\text{Ta}_{11}\text{O}_{30}$ products did not exhibit any impurity phases detectable by powder XRD. However, significant shifting of the diffraction peaks to larger 2θ angles was observed. This shifting was most significant for the (0,0,10) peak and other Cu-containing (00*l*) planes. The refined *a*-axis and *c*-axis lattice constant dimensions (and the corresponding unit cell volumes) exhibited a gradual decrease both with temperature and with reaction time, as listed in Tables 1 and S1. At $450 \text{ }^\circ\text{C}$, for example, the *c*-axis dimension decreased from 32.529 \AA (15 min) to 32.295 \AA (60 min), while the unit cell volume decreased from 1093.6 \AA^3 (15 min) to 1091.1 \AA^3 (60 min). By contrast, at $350 \text{ }^\circ\text{C}$ these changes in lattice dimensions were smaller and could only be detected after heating in air for at least 30 min. Shown in Figure 2.1 (c to f) are SEM images for $\text{Cu}_5\text{Ta}_{11}\text{O}_{30}$ crystallites heated in air at $350 \text{ }^\circ\text{C}$ for 60 min and at $550 \text{ }^\circ\text{C}$ for 60 min. Nano-sized surface islands are observed at the sides and on surface steps of the faces of

the hexagonally-shaped particles (e.g., Figure 2.1C), growing in amount and size with increasing temperature and time. These nano-sized islands on the surfaces could be dissolved in acid solutions, and which exhibited a solution UV-Vis absorption spectrum that matched closely with the dissolution of Cu(II) (from CuO; Figure A3 in Supporting Information). Thus, at the lower temperatures, the small surface islands corresponded to nanoparticle and/or amorphous Cu^{II}O species. Formation of these types of surface CuO islands have recently been reported to occur after heating CuNb₃O₈ in air, resulting from the extrusion and disproportionation of Cu(I) cations at the surfaces.¹⁵

B. XPS Measurements. X-ray photoelectron spectroscopy (XPS) measurements were taken on non-heated Cu₅Ta₁₁O₃₀ powders, and Cu₅Ta₁₁O₃₀ samples heated to 350 °C, 450 °C, and 550 °C for 60 min each, and at 650 °C and 750 °C for 3 h each. Detailed photoemission of the Cu core levels are illustrated in Figure 2.3. The Cu 2*p* core-level spectra for the non-heated Cu₅Ta₁₁O₃₀ powder indicated mainly Cu(I) at the surface with minor contributions from Cu(II) as indicated by the higher binding-energy “shake-up” satellites. As the Cu₅Ta₁₁O₃₀ powder is heated in air, the Cu spectra show increasing Cu(II) content, consistent with the picture of Cu(I) migration and oxidation at the surfaces. The Cu(II) shake-up satellites around 940 eV increase in intensity compared to the main 2*p*_{3/2} peak as the powder is heated.³⁰ Since this measurement is particularly surface sensitive, this observation agrees with SEM showing CuO islands near the surface. Additionally, XRD results show this Cu migration with a change in the bulk crystal structure. It is evident that at increased heating temperatures a larger amount of Cu(II) is present at the surface. In addition to Cu oxidation near the surface, XPS observations provided in the Supporting Information show that heating in air result in a partial reduction of Ta(V) to suboxides, similar to effects

seen in annealing studies of Ta₂O₅.³¹ These changes are in part responsible for maintaining charge balance in the crystal during surface modification while annealing.

C. Rietveld Refinement of the Cu_{5-x}Ta₁₁O₃₀ Structure. A powder XRD Rietveld refinement was performed on Cu_{5-x}Ta₁₁O₃₀ after heating in air at 450 °C for 3 h. The overall fit of the structure refinement is plotted in Figure 2.4, and selected refinement parameters are listed in Table 2.2. As shown in Figure 2.5, the structure consists of layers of TaO₇ pentagonal bipyramids, and has been described as part of a family of structures related to the α-U₃O₈ structure type.³² Selected interatomic distances are listed in Table 2.3. This is the only known member of the family that contains alternating single (Ta1) and double layers (Ta2) of the TaO₇ pentagonal bipyramids. Each of these is separated by layers of TaO₆ octahedra (Ta3) and nearly linearly-coordinated Cu(I) cations. The local coordination environments for Ta1, Ta2, and Ta3 are illustrated in Figure 2.6, and their interatomic distances are within similar ranges as previously reported for Cu₅Ta₁₁O₃₀. The overall structure is closely similar to that previously reported for Cu₅Ta₁₁O₃₀, but with a Cu-deficient composition of Cu_{3.2(1)}Ta₁₁O₃₀, consistent with the extrusion of Cu(I) cations from the bulk structure to the surfaces. This is significantly lower than the Cu-site occupancy in the regular Cu₅Ta₁₁O₃₀ structure of 0.833. A full Cu-site occupancy in this structure would yield a composition of Cu₆Ta₁₁O₃₀, but which cannot be prepared owing to the charge-balancing considerations of the Cu(I) and Ta(V) cations.

Compared to Cu₅Ta₁₁O₃₀, the Cu-deficient structure of Cu_{3.2(1)}Ta₁₁O₃₀ exhibits several changes in interatomic distances and angles that result from the decreasing Cu content, tabulated as Δ_{dist}(Å) and Δ_{ang}(°) in Table 3. The Cu – O distances stay relatively unchanged with the exception of a significant contraction in the distance to O8 (by ~0.26Å).

Concomitantly, the Ta3 – O8 distance increases (by $\sim 0.1\text{\AA}$) and the triangular faces of each TaO₆ octahedra rotate the O8 atoms into closer contact with a Cu site. The linearly-coordinated Cu atom has thus formed a shorter distance to a third O8 neighbor, which is consistent with an increase in the oxidation state of Cu(I) to Cu(II), as described below. The other significant contractions occur for the Ta – O4 distances (by $\sim 0.29\text{\AA}$ and $\sim 0.36\text{\AA}$) that are in the equatorial plane of the TaO₇ pentagonal bipyramids. Interestingly, the apical Ta – O distances of the layers of pentagonal bipyramids (Ta1 – O3; Ta2 – O7; Ta2 – O8), which are aligned down the *c*-axis direction, have only changed by a relatively small amount ($< 0.07\text{\AA}$). The large contraction of the *c*-axis dimension is instead the result of decreased bond angles within the layers of TaO₇ pentagonal bipyramids, as illustrated in Figure 2.6 for the double layer (Ta2 – O7 – Ta2 at 154.8°) and single layer (O3 – Ta1 – O3 at 150.6°) local coordination environments. Overall, the single layers decrease in height by $\sim 0.1\text{\AA}$ and the double layers decrease in height by $\sim 0.05\text{\AA}$, while the intervening Cu/TaO₆ layers expand in height by $\sim 0.027\text{\AA}$. Thus, while the cell volume and the *c*-axis dimension both contract, the expansion of the Cu/TaO₆ layers facilitates the easy migration of Cu to the surfaces.

The extrusion of Cu from Cu_{5-x}Ta₁₁O₃₀ at 350 °C to 550 °C is thus found to occur with its oxidation in air to yield surface nanoparticles of cupric oxide, as given by the reaction: $\text{Cu}_5\text{Ta}_{11}\text{O}_{30}(\text{s}) + x/2 \text{O}_2(\text{g}) \rightarrow \text{Cu}_{5-x}\text{Ta}_{11}\text{O}_{30}(\text{s}) + x\text{CuO}(\text{surface})$. From charge balance considerations, the formal oxidation state of copper within Cu_{5-x}Ta₁₁O₃₀ also increases from Cu(I) to Cu(II), as represented by the chemical formula Cu^I_(5-2x)Cu^{II}_xTa₁₁O₃₀. The formation of Cu vacancies is accompanied by the oxidation of Cu(I) to Cu(II) within the structure. Thus, when Cu₅Ta₁₁O₃₀ is heated in air, increasing amounts of both the surface and bulk structure Cu(I) cations are oxidized to Cu(II). This occurs in a 1:1 molar ratio

(surface-to-bulk ratio of Cu(II) cations), as given by the above reaction. Prior reported thermogravimetric analyses on $\text{Cu}_5\text{Ta}_{11}\text{O}_{30}$ and the related $\text{Cu}_3\text{Ta}_7\text{O}_{19}$ showed weight gains that increased with both temperature and time,⁸ and that are consistent with the formation of CuO at the surfaces. The temperature-dependent magnetic susceptibility was measured for the $\text{Cu}_5\text{Ta}_{11}\text{O}_{30}$ compound, both before and after heating it in air at 250 °C, 350 °C and 450 °C. The data could be fit to the Curie-Weiss law ($S = \frac{1}{2}$ for Cu(II)), with the parameters listed in Table S3. The effective magnetic moment of the sample is shown to increase from ~0.10 to 0.13 B.M. at room temperature and 250 °C, to ~0.25 B.M. after heating to 350 °C, and ~0.44 B.M. after heating to 450 °C. These results are consistent with the gradual partial oxidation of Cu(I) to Cu(II) within the structure and at its surfaces.

D. Photoelectrochemical Properties. Polycrystalline films of *p*-type Cu(I) niobates and Cu(I) tantalates have previously been found to exhibit significant increases in their cathodic photocurrents under visible-light irradiation after being heated in air to temperatures between 250 °C and 550 °C for 3h. Examples include polycrystalline films of CuNbO_3 , CuNb_3O_8 , $\text{Cu}_3\text{Ta}_7\text{O}_{19}$ and $\text{Cu}_5\text{Ta}_{11}\text{O}_{30}$.^{6,8,9,11,15} However, there have been no prior investigations of the effects of shorter and varying reaction times of 15 min, 30 min, and 60 min on their photoelectrochemical properties. As described above for $\text{Cu}_5\text{Ta}_{11}\text{O}_{30}$, it has been found that a growing amount of Cu-deficiency results with increasing reaction times and temperatures. Thus, polycrystalline films of $\text{Cu}_5\text{Ta}_{11}\text{O}_{30}$ were prepared and heated in air at 350 °C, 450 °C, and 550 °C for increasing reactions times in order to investigate the effects of increasing Cu deficiency on photoelectrochemical properties.

As shown in Figure 2.7, the cathodic photocurrents of *p*-type $\text{Cu}_{5-x}\text{Ta}_{11}\text{O}_{30}$ polycrystalline films ranged from -0.5 mA/cm² (350 °C) to -2.5 mA/cm² (550 °C), and

significantly increased for films that had been heated to the higher temperatures and longer times. The most significant enhancement of photocurrent with heating time (15 min versus 30 min versus 60 min) was observed for films heated to 350 °C. The films heated to 450 °C exhibited a much smaller enhancement in their photocurrent with increasing heating time beyond 15 min. At 450 °C, The decrease in the unit cell volume and weight gain has nearly reached completion after 15 min, with relatively much smaller changes occurring at 30 min and 60 min. These results are consistent with the largest changes versus time in the amount of Cu-vacancies and Cu^{II}O surface islands when the Cu₅Ta₁₁O₃₀ products at heated to the lower temperature of 350 °C (i.e., 15 min vs 30 min vs 60 min), versus those heated to 450 °C. Conversely, the photocurrent is the highest after 15 min of heating at 550 °C, before then decreasing with an increasing heating time of 30 min and 60 min. At this highest temperature, the Cu(I) cations are extruded and oxidized more rapidly at the surfaces (within 15 min) to produce CuO islands, and which may then further react at the surfaces and degrade the photocurrent response for longer heating times. After heating at these temperatures, the polycrystalline Cu_{5-x}Ta₁₁O₃₀ films change from yellow to black colored, as recorded in the UV-Vis diffuse reflectance spectra shown in Figure 2.8 (and insets a and b). This color change is caused by the formation of CuO at the surfaces, and which has a bandgap size of 1.2 eV. After washing a film in 6M HCl(aq), the absorption from ~1.2 eV to ~2.6 eV is significantly decreased owing to the dissolution of CuO from the surfaces. This confirms the enhancement in the cathodic photocurrent of the films is related to the increasing amount of the *p*-type defects (i.e., Cu vacancies) as well as the CuO surface islands.

For comparison, a polycrystalline *p*-type Cu₂O electrode was prepared according to literature reports²⁵ and its photocurrent was measured under the same conditions as the Cu_{5-x}Ta₁₁O₃₀ films. Plotted in Figure 2.9 are the photocurrent responses versus potential (upper) and time (lower) for the *p*-type Cu₂O film and a Cu_{5-x}Ta₁₁O₃₀ film that had been heated to 350 °C for 3h in air. Across the entire range of applied bias, the photocurrent for Cu_{5-x}Ta₁₁O₃₀ is nearly double the value measured for the Cu₂O film. A number of factors may be responsible, such as a higher hole mobility, higher *p*-type doping, or the CuO surface islands observed for Cu_{5-x}Ta₁₁O₃₀. Another factor is the more efficient charge separation expected from the bandgap transition that occurs between the Cu(3*d*¹⁰) and Ta(5*d*⁰) orbitals that comprise the valence and conduction bands, respectively, as described previously. The chronoamperometric data (i.e., photocurrent versus time) show a photocurrent decay that is similar for both films, and as well, which is similar for all of the Cu_{5-x}Ta₁₁O₃₀ films, as plotted in Figures 2.7 (lower) and Figure 2.9. In *p*-type Cu₂O films, this decay is known to result from the reduction of Cu(I) cations at the surfaces to Cu(s). Powder XRD characterization of the Cu_{5-x}Ta₁₁O₃₀ films indicate that the bulk of it is stable under these different conditions. Shown in Figure 2.10, XPS techniques were used in order to investigate the changes at the surfaces of a Cu_{5-x}Ta₁₁O₃₀ film (heated to 450 °C for 60 min in air) after chronoamperometry measurements for 1000 s. After the photocurrent measurements, the surface still consisted of only the oxidized Cu(II) cations, but no Cu(I) cations or Cu(s). As before, partially reduced Ta is observed by XPS before the photocurrent measurement, (Figure A8 in the Supporting Information). After chronoamperometric measurements, however, the observed spectra of the Ta 4*f* orbitals indicate a fully oxidized Ta species, which is similar to that before heating of the film. Any reduced Ta^{*n*+} cations (i.e., *n* = 3, 4)

should be oxidized back to Ta^{5+} via reaction with water. Further photoelectrochemical investigations are in progress to fully uncover the decay mechanism(s) at the $\text{Cu}_{5-x}\text{Ta}_{11}\text{O}_{30}$ surfaces, and which will be the subject of a separate complete study.

E. Electronic Structure Calculations. The electronic structures of $\text{Cu}_5\text{Ta}_{11}\text{O}_{30}$ and the Cu-deficient $\text{Cu}_{5-x}\text{Ta}_{11}\text{O}_{30}$ were calculated using density-functional theory (DFT) methods within VASP.²⁶ The Cu-deficient structural model was taken from the refined structure of $\text{Cu}_{3.2(1)}\text{Ta}_{11}\text{O}_{30}$, and included Cu vacancies that were varied from 16.7% for $\text{Cu}_5\text{Ta}_{11}\text{O}_{30}$ to 50% for ' $\text{Cu}_3\text{Ta}_{11}\text{O}_{30}$ '. The calculated electronic structure has been previously reported for the $\text{Cu}_5\text{Ta}_{11}\text{O}_{30}$ structure based on DFT methods.^{8,33} For $\text{Cu}_5\text{Ta}_{11}\text{O}_{30}$, the band gap has been found to be determined by the energy difference between its valence band that is comprised primarily of filled Cu $3d^{10}$ orbitals and a conduction band that consists primarily of empty Ta $5d^0$ orbitals, each with some O $2p$ orbital contributions. Shown in Figure 2.11, the calculated electronic densities-of-states plot for ' $\text{Cu}_3\text{Ta}_{11}\text{O}_{30}$ ' is compared to that for $\text{Cu}_5\text{Ta}_{11}\text{O}_{30}$. A larger amount of Cu-vacancies in the former (i.e., ~50%) causes a decrease in the Fermi-level energy (i.e., the highest occupied Kohn-Sham orbital) and a depopulation of the Cu- $3d$ orbitals, in agreement with the oxidation of Cu(I) to Cu(II) throughout the structure. In addition, the Cu- $3d$ orbitals are lowered in energy relative to the O- $2p$ orbitals, and causing the latter to cross the Fermi level and become depopulated by a nearly equal amount. Similar to that recently reported for CuNb_3O_8 ,¹⁵ these O- $2p$ contributions occur over the bridging Cu-O-Ta neighbors when the Cu sites are vacant. Shown in Figure 2.12 is the calculated electron density for the conduction band states (red shading; lower) and valence band states (blue shading, upper) for a layer with Cu vacancies. This layer has relatively larger contributions from the O- $2p$ orbitals than the layers with no Cu vacancies.

This type of electronic perturbation has recently been postulated to lead to a more effective separation of excited electron/hole pairs within these kinds of Cu(I)-containing structures.¹⁵

Electronic structure calculations were also performed in order to understand the Cu-migration pathways that occur preferentially to specific edges of the different crystal morphologies, as observed in Figure 2.1. Within a single Cu/TaO₆ layer, there are three facile and symmetry-equivalent pathways for the migration of the Cu(I) cations between their individual sites, as illustrated and labeled with arrows in Figure 2.13. There are three intermediate atomic positions between neighboring Cu sites that are labeled in Figure 2.13 (labeled 2, 4, and 6), and which represent the migration of Cu from one site to the next (labeled 0 and 8) throughout the structure. Within the structure, each Cu atom has two oxygen neighbors at an interatomic distance of 1.90Å. For the intermediate Cu positions, the Cu – O distances change by relatively small amounts, for example, at position 2 (Cu – O of ~1.7Å and ~2.4Å), position 4 (~1.8Å and ~2.0Å), and position 6 (~2.2Å and ~1.7Å). Total energy calculations on each of these geometry-relaxed intermediate structures show an activation energy ΔE_{act} for Cu-migration between sites (i.e., migration of one vacancy per unit cell) to be in the range change of ~1.35 eV for Cu₅Ta₁₁O₃₀ and ~1.5 eV for ‘Cu₃Ta₁₁O₃₀’. By comparison, the activation energy for vacancy migration in elemental copper has been determined experimentally to be in the range of ~1.0 eV.³⁴ These results are in agreement with facile Cu-vacancy migration, and which becomes easier with higher amounts of Cu-vacancies (and the increased Cu/TaO₆ layer height).

The external crystal morphologies of the most commonly observed (by SEM; See Figure 2.1) single-crystal shapes are modeled in Figure 2.14, showing an example of a hexagonal platelet (left) and a hexagonal rod with tapering at the ends (right). These

morphologies have been modeled using the VESTA software package,³⁵ and can be compared with the SEM images in Figure 2.1. The crystallographic orientation of the Cu/TaO₆ layer (i.e., the directions of facile Cu migration) lies within the *ab* plane of the Cu₅Ta₁₁O₃₀ crystal structure, and is perpendicular to the *c*-axis direction, i.e., the labeled [001] directions. For example, the directions of high Cu mobility are shown as the dashed arrows that are overlaid on top of the hexagonal-platelet crystal morphology in Figure 2.14. Thus, electronic-structure calculations predict that the Cu atoms will most easily migrate and be oxidized to CuO surface islands at the outer edges of these particle morphologies, and not over their hexagonal faces. This observation is confirmed experimentally in Figure 2.1 (c to f).

Interestingly, the excitation of electrons across the band gap results in their delocalization within the layers of edge-shared TaO₇ pentagonal bipyramids that also lie in the *ab* plane of the Cu₅Ta₁₁O₃₀ crystal structure, as shown in Figure A5 and found previously for the related Na₂Ta₄O₁₁ and BiTa₇O₁₉ structures.^{36,37} The delocalized states in these *ab* planes can provide an efficient path for excited electrons that is aligned to allow transfer to the surface CuO islands. The high cathodic photocurrents of the polycrystalline Cu_{5-x}Ta₁₁O₃₀ photoelectrodes are thus found to result from a complex synergistic combination of the crystallographic orientation of the Cu migration pathways, the preferential formation of CuO surface islands on specific crystal facets, and the anisotropy of the electron mobility of the conduction band of the bulk solid.

CONCLUSIONS

Heating *p*-type Cu₅Ta₁₁O₃₀ in air from 250 °C to 750 °C is found to result in significant changes to its crystalline structure and surfaces, resulting in new insights into the

origins of its photoelectrochemical properties. At temperatures of 650 °C and higher, the $\text{Cu}_5\text{Ta}_{11}\text{O}_{30}$ phase decomposes to CuTa_2O_6 and Ta_2O_5 . However, in the lower temperature range of 250 °C to 550 °C, the formation of nanosized and/or amorphous CuO surface islands are observed with increasing temperature and time. These surface changes are correlated with increasing Cu vacancies in the bulk structure, yielding a Cu-deficient $\text{Cu}_{3.2(1)}\text{Ta}_{11}\text{O}_{30}$ composition after heating to 450 °C for 3 h in air. Combined XPS and magnetic susceptibility data show that Cu(I) is oxidized both at the surfaces and within the bulk structure to Cu(II) (in CuO). These changes are shown to lead to the high cathodic photocurrents for polycrystalline $\text{Cu}_5\text{Ta}_{11}\text{O}_{30}$ photoelectrodes under visible-light irradiation. Electronic structure calculations confirm the Fermi level shifts to lower energies with increasing Cu vacancies, resulting in the depopulation of the Cu(I) $3d^{10}$ orbitals and its oxidation to Cu(II) throughout the structure. Further, the CuO islands are shown to preferentially form over specific surfaces which are aligned with the directions of high Cu-mobility within the structure (i.e., within the *ab* plane). The excited electrons in the conduction band are calculated to be delocalized within the TaO_7 -based layers, and which are also oriented within the *ab* plane of the structure. Thus, the CuO nano-islands have the synergistic effect of serving as surface cocatalysts that lead to the increased photocurrents for the reduction of water to hydrogen. This findings shed new light into the origins of the high photocurrents of Cu(I)-niobate and Cu(I)-tantalate films for solar energy conversion applications.

ACKNOWLEDGMENTS

We would like to thank Dr. Chuck Mooney at the Analytical Instrument Facility (AIF) at North Carolina State University for assistance with SEM imaging.

SUPPORTING INFORMATION AVAILABLE

Refined lattice constants and powder X-ray diffraction patterns for $\text{Cu}_{5-x}\text{Ta}_{11}\text{O}_{30}$ after heating in air, atomic coordinates from the X-ray diffraction Rietveld refinement, temperature-dependent magnetic susceptibility data, UV-Vis absorption spectra, detail XPS scans of the Ta $4f$ and O $2p$ core levels after heating and after chronoamperometry measurements, and electron density plots from DFT calculations.

REFERENCES

- (1) Lewis, N.S.; Nocera, G. *Proceedings of the National Academy of Sciences* **2006**, 103, 15729-15735.
- (2) Lewis, N. S. *Nature* **2001**, 414, 589–90.
- (3) Palasyuk, O.; Palasyuk, A.; Maggard, P.A. *J. Solid State Chem.* **2010**, 183, 814-822.
- (4) Joshi, U.; Palasyuk, A.; Arney, D.; Maggard, P.A. *J. Phys. Chem. Lett.* **2010**, 1(18), 2719-2726.
- (5) Palasyuk, O.; Palasyuk, A.; Maggard, P.A. *Inorg. Chem.* **2010**, 49(22), 10571-10578.
- (6) Joshi, U.; Palasyuk, A.; Maggard, P.A. *J. Phys. Chem. C* **2011**, 115(27), 13534-13539.
- (7) Palasyuk, O.; Maggard, P.A. *J. Solid St. Chem.* **2012**, 191, 263-270.
- (8) Fuoco, L.; Joshi, U.; Maggard, P.A. *J. Phys. Chem. C* **2012**, 116(19), 10490-10497.
- (9) Joshi, U.; Maggard, P.A. *J. Phys. Chem. Lett.*, **2012**, 3, 1577-1581.
- (10) Read, C.G.; Park, Y.; Choi, K.-S. *J. Phys. Chem. Lett.* **2012**, 3(14), 1872-1876.
- (11) Choi, J.; King, N.; Maggard, P.A. *ACS Nano*, **2013**, 7, 1699-1708.
- (12) Sahoo, P.P.; Maggard, P.A. *Inorg. Chem.* **2013**, 52, 4443-4450
- (13) Gu, Jing; Wuttig, Anna; Krizan, Jason W.; Hu, Yuan; Detweiler, Zachary M.; Cava, Robert J.; Bocarsly, Andrew B. *J. Phys. Chem. C*, **2013**, 117, 12415-12422.
- (14) Kato, H.; Takeda, A.; Kobayashi, M.; Hara, M.; Kakihana, M. *Catal. Sci. Technol.* **2013**, 3, 3147-3154.
- (15) King, N.; Sahoo, P.P.; Fuoco, L.; Stuart, S.; Dougherty, D.; Liu, Y.; Maggard, P.A. *Chem. Mater.* **2014**, 26(6), 2095-2104.
- (16) Gu, Jing; Yan, Yong, Krizan, Jason W.; Gibson, Quinn D.; Detweiler, Zachary M.; Cava, Robert J.; Bocarsly, Andrew B. *J. Am. Chem. Soc.*, **2014**, 136, 830-833.
- (17) de Jongh, P. E.; Vanmaekelbergh, D.; Kelly, J. J. *J. Electrochem. Soc.* **2000**, 147, 486.
- (18) Ida, S. et al. *J. Am. Chem. Soc.* **2010**, 132, 17343-17345.
- (19) Paracchino, A.; Laporte, V.; Sivula, K.; Gratzel, M.; Thimsen, E. *Nature*, **2011**, 10, 456-461

- (20) King, N.; Sommer, R.; Watkins-Curry, P.; Chan, J.; Maggard, P.A. *Submitted to Cryst. Grow. Des.* **2014**.
- (21) Rodriguez-Carvajal, J.; Roisnel, T. FullProf and WinPLOTOR, Commission For Powder Diffraction, International Union for Crystallography **2004**.
- (22) MDI Jade9 Version 9.0.2.
- (23) Dusek, M.; Petricek, V.; Wunschel, M.; Dinnebier, R.E.; van Smaalen, J. *Appl. Crystallogr.* **2001**, 34, 398-404
- (24) Kubelka, P.; Munk, F. *Z. Tech. Physik* **1931**, 12, 593.
- (25) Septina, W.; Ikeda, S.; Khan, M.A.; Hirai, T.; Harada, T.; Matsumura, T.; Matsumura, M.; Peter, L.M. *Electrochim. Act.* **2011**, 56(13), 4882-4888.
- (26) (a) Kresse, G.; Hafner, G. *Phys. Rev. B* **1993**, 47(1), 558-561; (b) *Ibid*, **1994**, 49(20), 14251-14270; (c) Kresse, G.; Furthmüller J. *Comput. Mat. Sci.* **1996**, 6(1), 15-50; (d) Kresse, G.; Furthmüller J. *Phys. Rev. B* **1996**, 54(16), 11169-11186.
- (27) Perdew, J.P.; Burke, K.; Ernzerhof, M. *Phys. Rev. Lett.* **1996**, 77(18), 3865-3868.
- (28) (a) Vanderbilt, D. *Phys. Rev. B* **1990**, 41(11), 7892-7895; (b) Kresse, G.; Hafner, G. *J. Phys.: Condens. Matter.* **1994**, 6, 8245-8257.
- (29) Monkhorst, H.J.; Pack, J.D. *Phys. Rev. B* **1976**, 13, 5188-5192.
- (30) Biesinger, M.C.; Payne, B.P.; Grosvenor, A.P.; Lau, L.W.M.; Gerson, A.R.; Smart, R.St.C. *Appl. Surf. Sci.* **2010**, 257, 887-898.
- (31) Nowak, A.; Persson, J.; Schmelzer, B.; Szade, J.; Szot, K. *J. Phys. D.: Appl. Phys.* **2014**, 47, 135301-135309.
- (32) Jahnberg, L. *Mat. Res. Bull.* **1981**, 16, 513-518.
- (33) Harb, M.; Masih, D.; Takanabe, K. *Phys. Chem. Chem. Phys.* **2014**, Advance article published on the web: <http://pubs.rsc.org/En/content/articlepdf/2014/cp/c4cp02497d>
- (34) Granato, A.; Hikata, A.; Lücke, K. *Phys. Rev.* **1957**, 108, 1344-1345.
- (35) VESTA 3 for three-dimensional visualization of crystal, volumetric and morphology data; Momma, K.; Izumi, F. *J. Appl. Crystallogr.* **2011**, 44, 1272-1276.
- (36) McLamb, N.; Sahoo, P.P.; Fuoco, L.; Maggard, P.A. *Cryst. Grow. Des.* **2013**, 13, 2322-2326.

(37) Boltersdorf, J.; Wong, T.; Maggard, P.A. *ACS Catal.* **2013**, *3*, 2943-2953.

Table 2.1. Calculated unit cell volumes after heating $\text{Cu}_{5-x}\text{Ta}_{11}\text{O}_{30}$ in air at three different temperatures and heating times.

Time (min)	350 °C Volume (\AA^3)	450 °C Volume (\AA^3)	550 °C Volume (\AA^3)
15	1099.3(4)	1092.5(3)	1093.7(3)
30	1097.0(3)	1091.2(5)	1091.2(4)
60	1095.8(5)	1090.4(5)	1094.7(4)

Table 2.2. Selected Rietveld refinement parameters for $\text{Cu}_{3.2(1)}\text{Ta}_{11}\text{O}_{30}$.

Formula	$\text{Cu}_{3.2(1)}\text{Ta}_{11}\text{O}_{30}$
Formula weight (g/mol)	2673.1
Space group, Z	$P\bar{6}2c$, 2
Radiation	Cu $K\alpha_1 = 1.54051 \text{ \AA}$ $K\alpha_2 = 1.54433 \text{ \AA}$
Crystal system	Hexagonal
$a/\text{\AA}$	6.2359(2)
$c/\text{\AA}$	32.2139(5)
Volume/ \AA^3	1084.87(5)
R_p, R_{wp}	0.0358, 0.0492
2θ (°) range	10–110
No. of unique data	6175

Table 2.3. Selected interatomic distances and bond angles for the Cu-deficient $\text{Cu}_{3.2(1)}\text{Ta}_{11}\text{O}_{30}$, and the corresponding differences compared to those in $\text{Cu}_5\text{Ta}_{11}\text{O}_{30}$.

Atom pair	Distance (Å)	$\Delta_{\text{dist}}(\text{Å})^a$	Atom pair	Distance(Å)	$\Delta_{\text{dist}}(\text{Å})^a$
<u>Ta1, pentagonal bipyramid</u>			<u>Ta2, pentagonal bipyramid</u>		
Ta1 – O1 (×2)	2.00(2)	+0.00	Ta2 – O4	1.73(6)	-0.26
– O1	2.36(6)	-0.06	– O4	2.46(6)	+0.05
– O2 (×2)	2.06(2)	+0.04	– O4	2.34(6)	+0.33
– O3 (×2)	1.94(4)	-0.04	– O5	2.011(4)	+0.01
<u>Ta3, octahedron</u>			– O6	2.00(2)	-0.01
Ta3 – O3 (×3)	2.10(6)	+0.08	– O7	1.94(1)	+0.04
– O8 (×3)	2.05(6)	+0.10	– O8	1.96(4)	-0.09
<u>Cu, linear</u>			<u>Bond Angles (°)</u>		<u>$\Delta_{\text{ang}}(^{\circ})^b$</u>
Cu – O3	1.90(7)	+0.00	O3–Ta1–O3	151.7(5)	-15.0
– O8	1.90(8)	-0.00	Ta2–O7–Ta2	155.1(9)	-11.4
– O8	2.49(5)	-0.26			
– O3	2.76(7)	-0.00			

^a $\Delta_{\text{dist}}(\text{Å})$ is the difference in interatomic distance as compared to that reported for the $\text{Cu}_5\text{Ta}_{11}\text{O}_{30}$ structure;²³ $\Delta_{\text{ang}}(^{\circ})$ is the difference in the bond angles as compared to that in $\text{Cu}_5\text{Ta}_{11}\text{O}_{30}$.

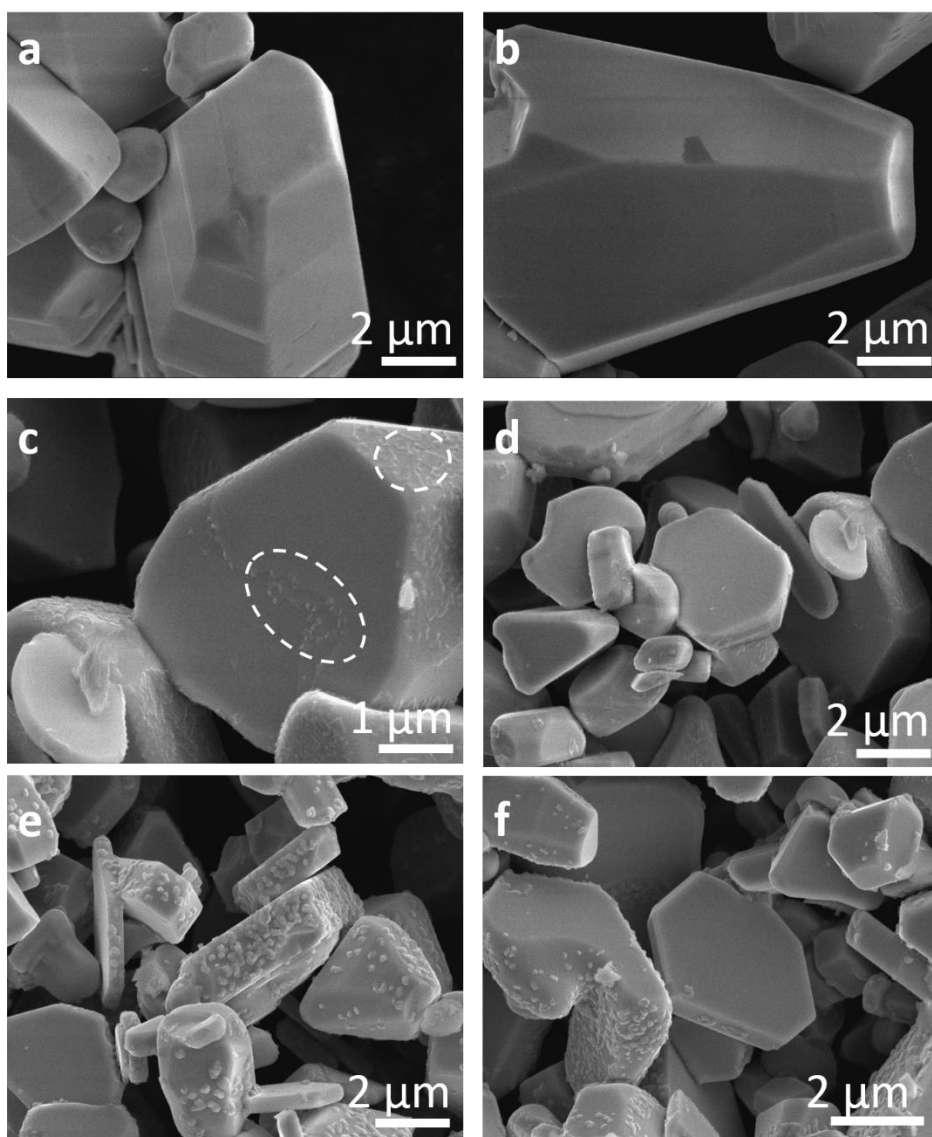


Figure 2.1. SEM images of $\text{Cu}_5\text{Ta}_{11}\text{O}_{30}$ before heating (a,b), after heating to 350 °C for 60 min (c,d), and after heating to 550 °C for 60 min (e,f).

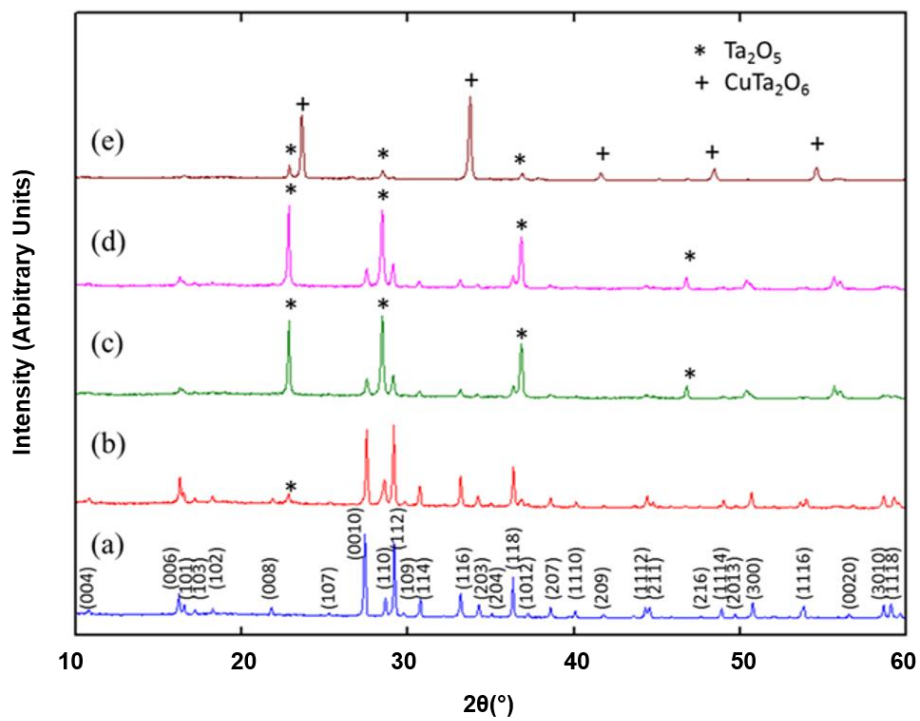


Figure 2.2. The powder X-ray diffraction patterns for $\text{Cu}_5\text{Ta}_{11}\text{O}_{30}$ without oxidation (a), heated in air to 550°C for 3 h (b), to 550°C for 12 h (c), to 650°C for 3 h (d), and to 750°C for 3 h (e).

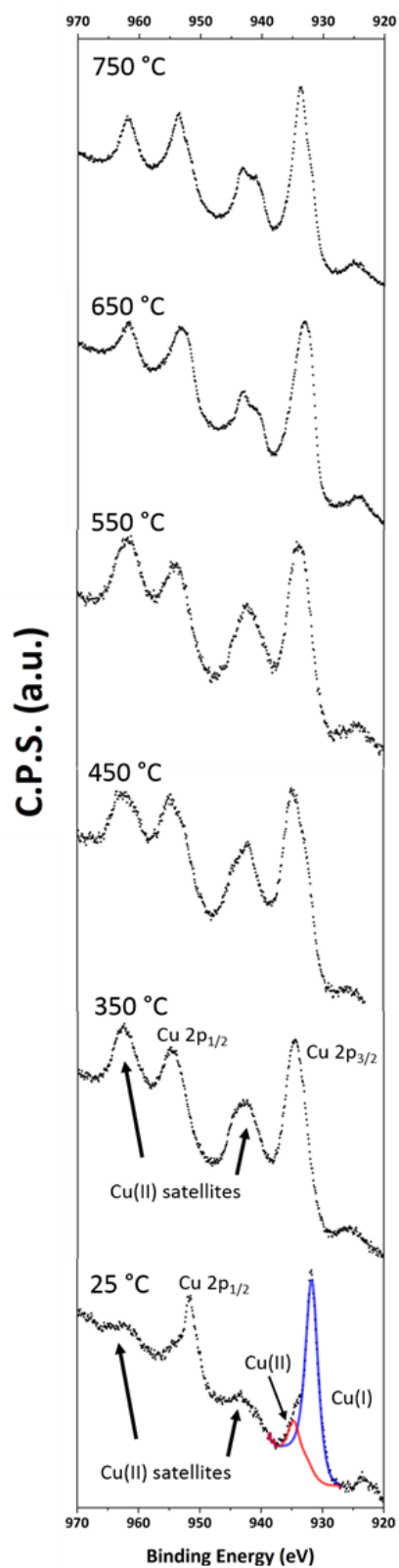


Figure 2.3. Detailed XPS scans of Cu 2p core levels for $\text{Cu}_5\text{Ta}_{11}\text{O}_{30}$ heated to increasing temperatures, indicating only Cu(II) at the surface at 350 °C and above (left).

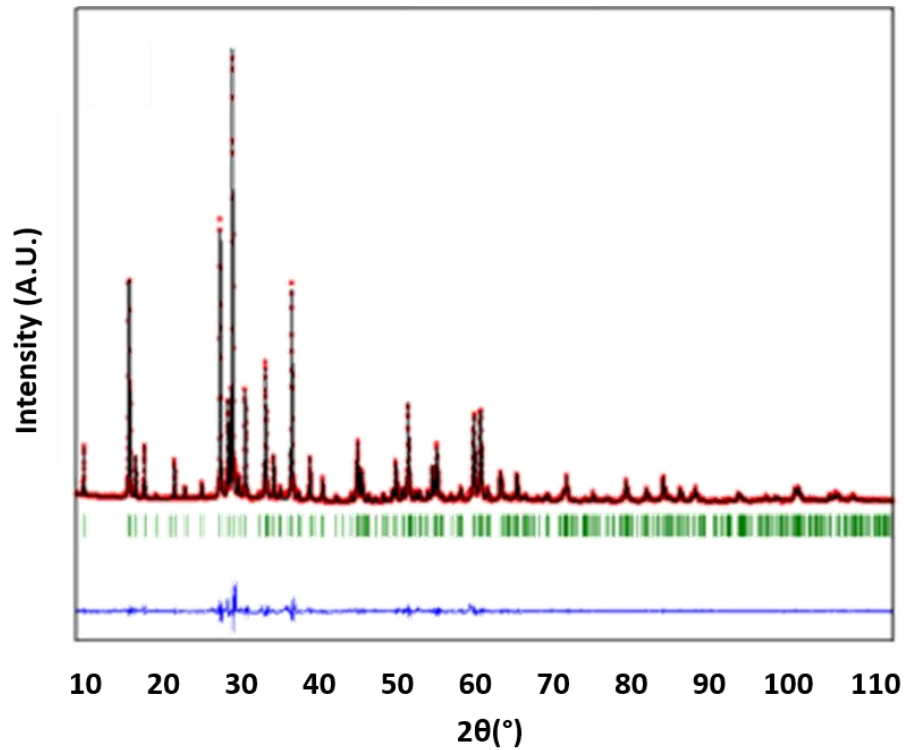


Figure 2.4. Rietveld refinement results for powder X-ray diffraction data on $\text{Cu}_5\text{Ta}_{11}\text{O}_{30}$ after heat it in air to 450 °C for 3 h. The observed profile is indicated by circles and the calculated profile by the solid line. Bragg peak positions are indicated by vertical ties, and the difference is shown at the bottom.

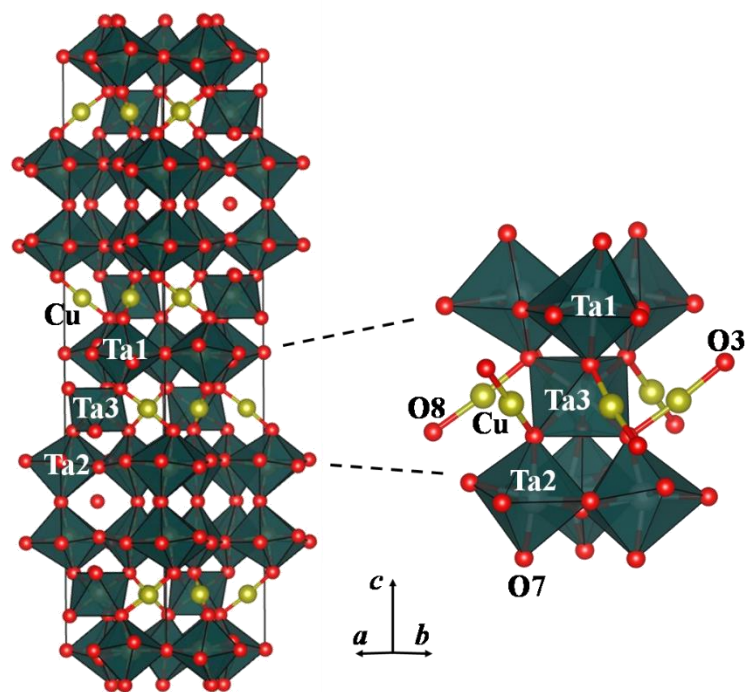


Figure 2.5. Polyhedral structural model $\text{Cu}_{3.2(1)}\text{Ta}_5\text{O}_{11}$, with the unit cell (outlined) on the left, and a local structural view on the right. Selected atom types are labeled, and the coordinate system is drawn at the bottom.

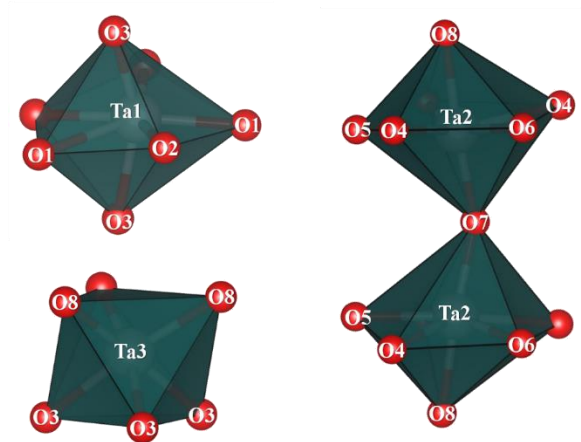


Figure 2.6. Polyhedral views of the local coordination environments of each of the three types of Ta sites in $\text{Cu}_{3.2(1)}\text{Ta}_5\text{O}_{11}$. Atom types are labeled, and the *c*-axis is vertical in each.

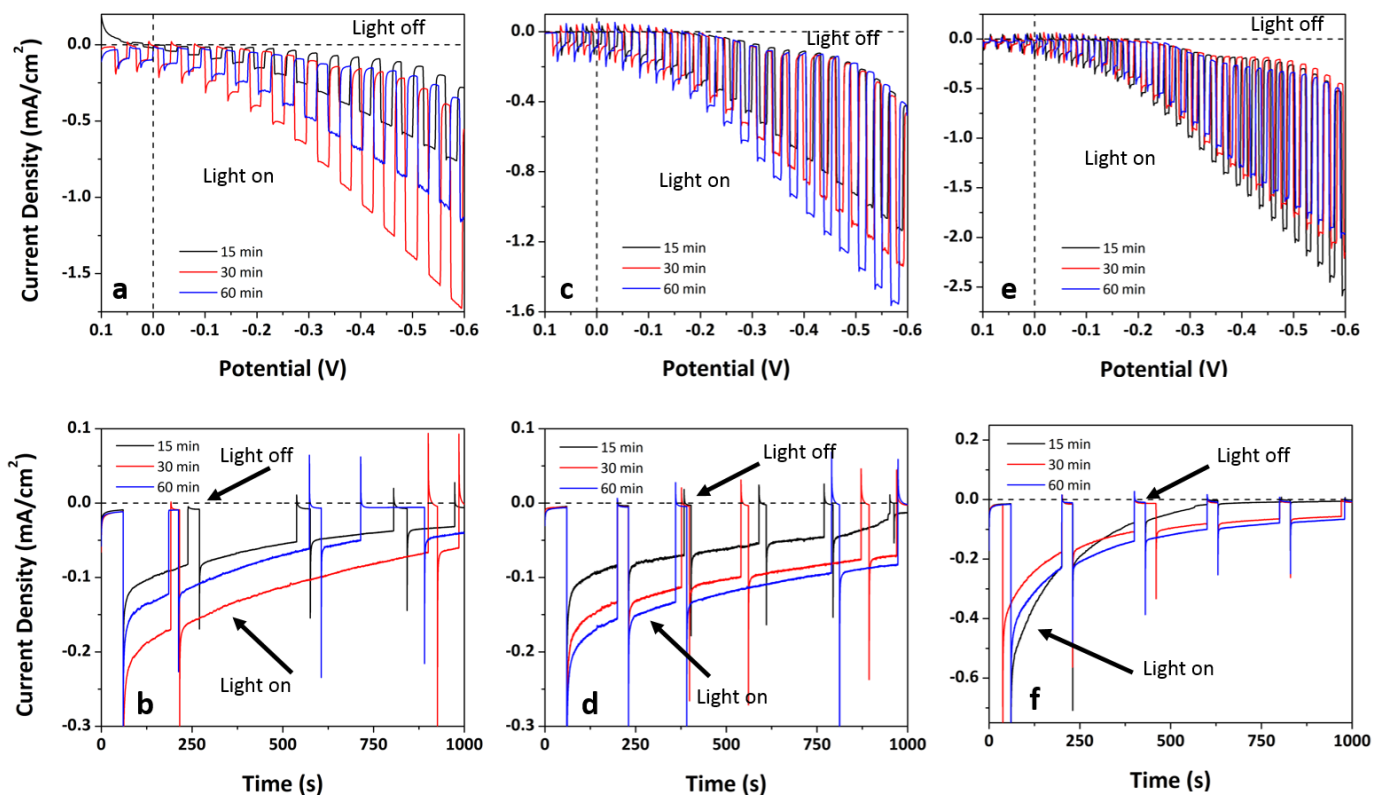


Figure 2.7. Linear sweep voltammetry under chopped irradiation (upper) and chronoamperometry (lower; -0.2 applied bias) of films heated to 350 °C (a-b), 450 °C (c-d) and 550 °C (e-f). for 15 min (black), 30 min (red) and 60 min (blue), in a 0.5M Na₂SO₄ solution at a pH of ~6.5.

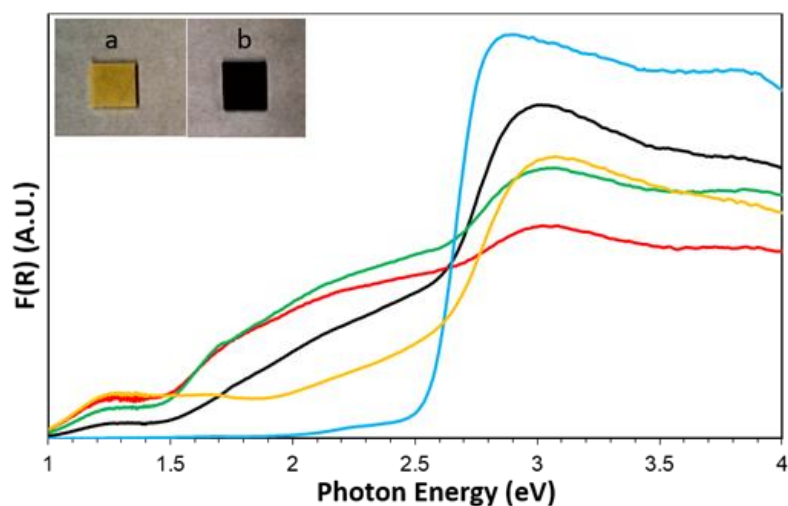


Figure 2.8. UV-Vis DRS of films before heating (blue), heated to 350 °C (black), 450 °C (red), 550 °C (green), and after soaking a heated film in 6 M HCl (yellow) to dissolve the CuO surface islands. Inset: Films of Cu₅Ta₁₁O₃₀ before (a) and after (b) heating.

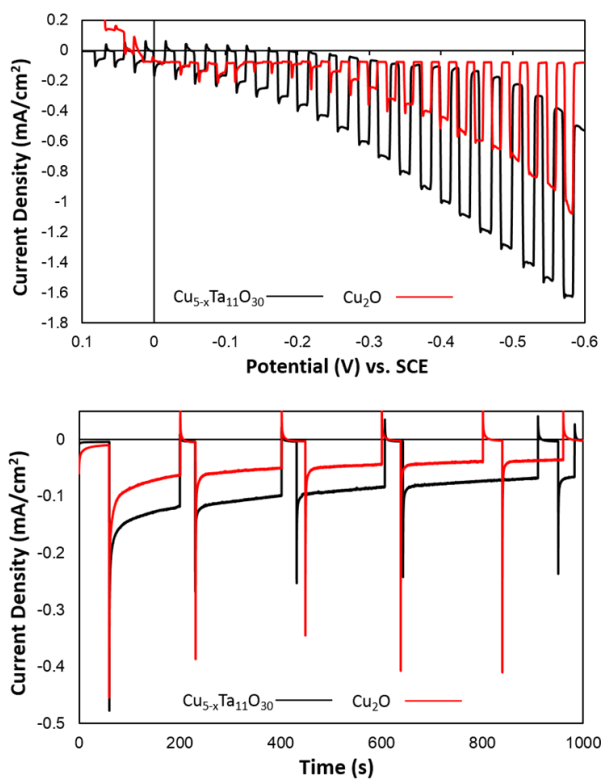


Figure 2.9. Comparison of the linear sweep voltammetry under chopped irradiation (upper) and chronoamperometry (lower; applied bias of -0.2 V) of polycrystalline *p*-type Cu_2O and $\text{Cu}_{5-x}\text{Ta}_{11}\text{O}_{30}$ (heated to 350 °C for 3 h in air) photoelectrodes.

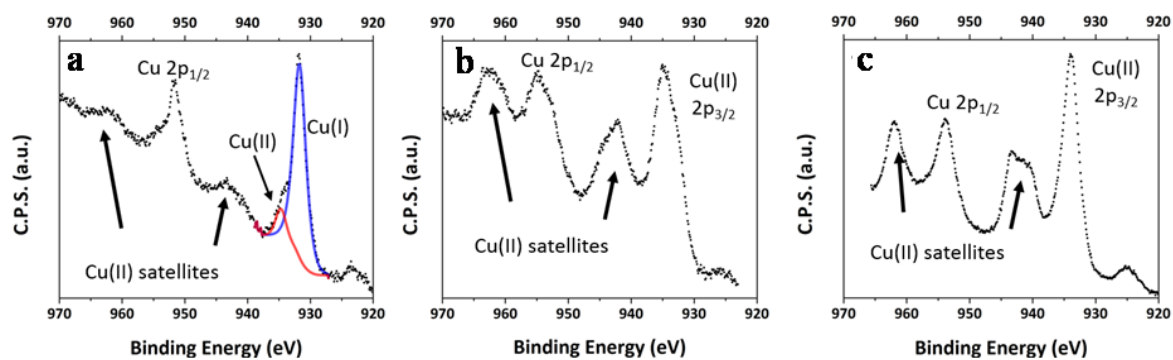


Figure 2.10. Detail XPS scans of the Cu $2p$ core levels for $\text{Cu}_5\text{Ta}_{11}\text{O}_{30}$ with no heat treatment (a), after heating to 450 °C for 60 min in air (b), and after chronoamperometry measurements for 1000 s (c).

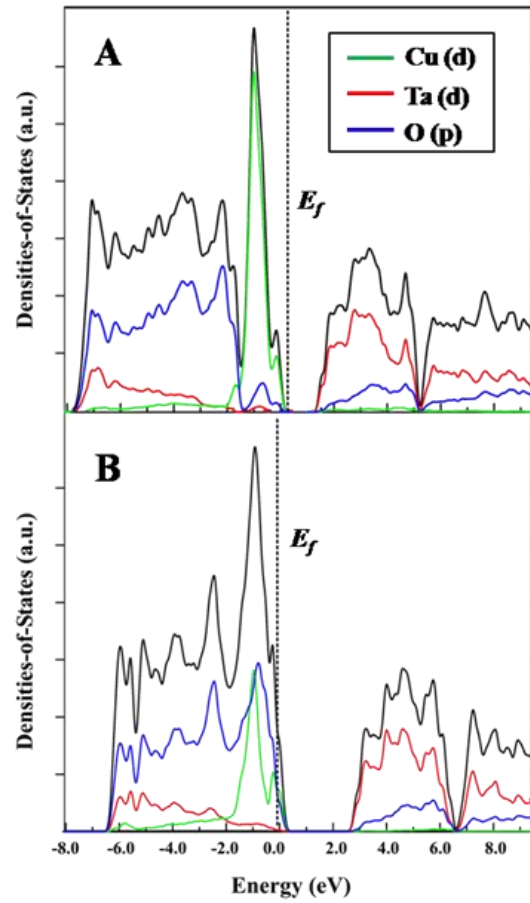


Figure 2.11. Calculated densities-of-states for $\text{Cu}_5\text{Ta}_{11}\text{O}_{30}$ (A; upper) and $\text{Cu}_{3.2(1)}\text{Ta}_{11}\text{O}_{30}$ (B; lower) with the individual atomic-orbital contributions projected out and the Fermi level (E_f) labeled.

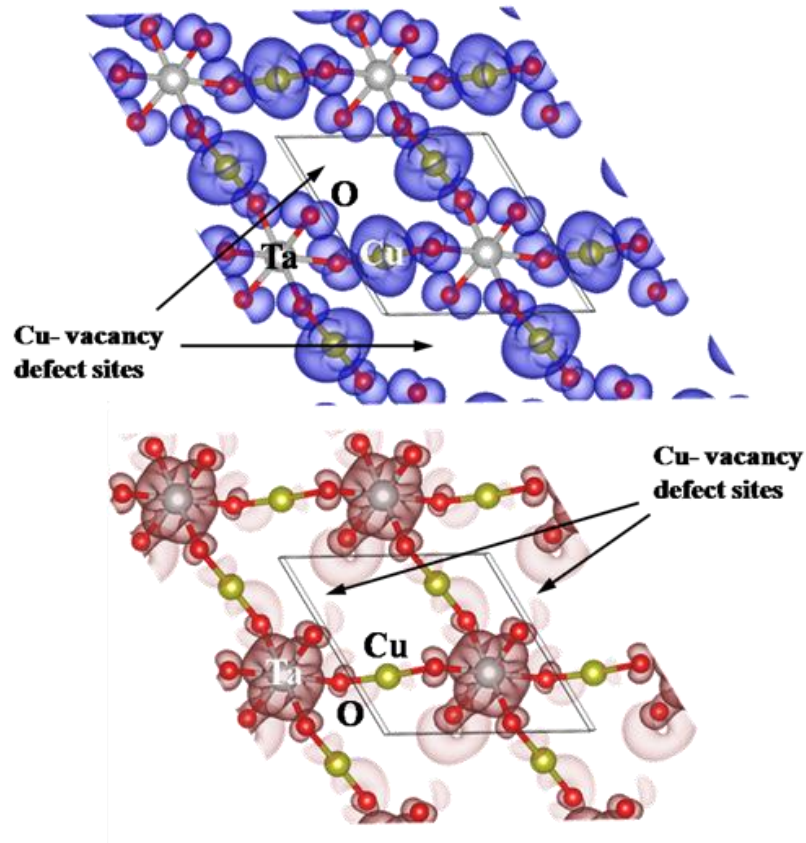


Figure 2.12. Calculated electron-density plots for the Cu/TaO₆ layer (~50% Cu vacancies) of Cu_{3.2(1)}Ta₁₁O₃₀ at the highest energies of the valence band edge (upper; blue shading) and lowest energies of the conduction band edge (lower; red shading). Atom types and Cu-vacancy sites are labeled.

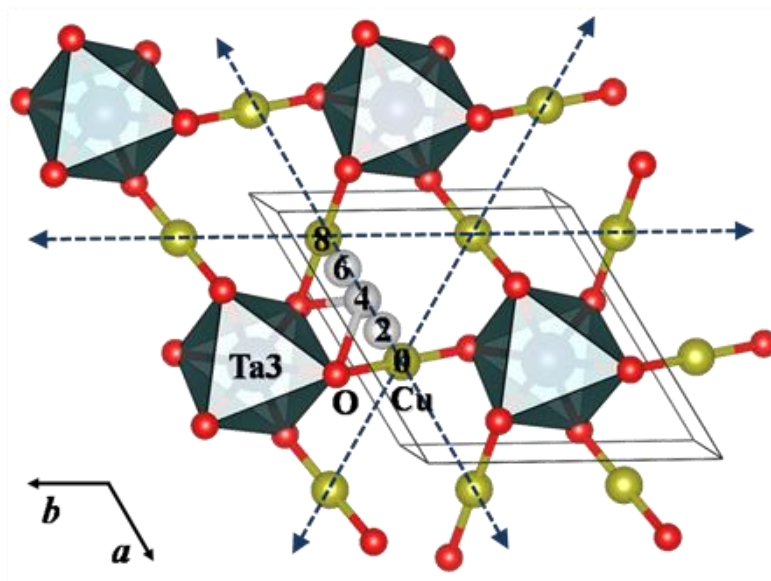


Figure 2.13. Structural view of the Cu(I)/TaO₆ layer in Cu_{3.2(1)}Ta₅O₁₁. Three symmetry-equivalent Cu-migration pathways are labeled within the unit cell by dashed arrows, and four individual Cu-migration steps are illustrated and labeled as 0 (start), 2, 4, 6, and 8 (finish).

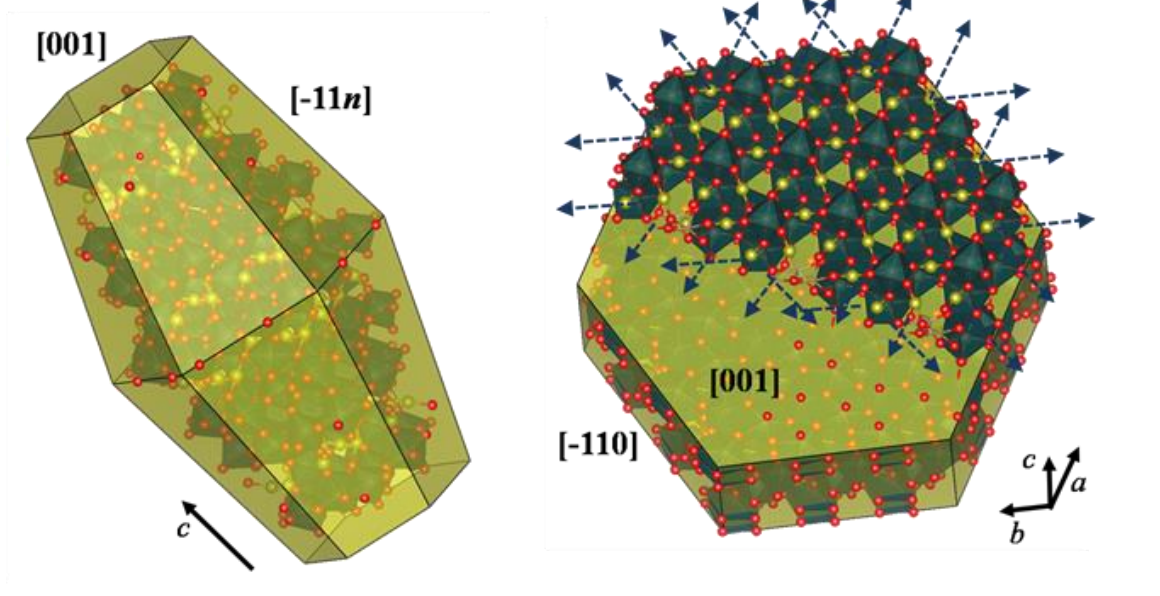


Figure 2.14. Polyhedral models of the crystal morphologies of $\text{Cu}_5\text{Ta}_{11}\text{O}_{30}$ (hexagonal crystal system), with the major crystal facets labeled.

CHAPTER 3: Photo-Injection of High Potential Holes into Cu₅Ta₁₁O₃₀ Nanoparticles by Porphyrin Dyes

Based on a journal article published in the Journal of Physical Chemistry C

J. Phys. Chem. C, **2015**, 119, 21294-21303.

Ian Sullivan,^a Chelsea Brown,^b Manuel J. Llansola-Portoles,^b Miguel Gervaldo,^c Gerdenis Kodis,^b Thomas A. Moore,^b Devens Gust,^b Ana Moore,^b Paul Maggard^a

^a *Department of Chemistry, North Carolina State University, Raleigh, NC 27695-8204 USA*

^b *Department of Chemistry and Biochemistry, Arizona State University, Tempe, AZ 85287-1604 USA*

^c *Departamento de Química, Universidad Nacional de Río Cuarto. Agencia Postal Nro. 3, X5804BYA Río Cuarto, Córdoba, Argentina*

The research presented here is a combination of work from all of the authors. The author of this dissertation contributed to the synthesis of Cu₅Ta₁₁O₃₀ nanoparticles, DLS measurements, XRD measurements, electronic absorption spectroscopy of Cu₅Ta₁₁O₃₀ nanoparticles, Mott-Schottky measurements, and the fabrication and photoelectrochemical measurements of the solar cells.

ABSTRACT

Excited-state hole injection into the valence band of Cu₅Ta₁₁O₃₀ nanoparticles (NP-Cu₅Ta₁₁O₃₀) was investigated through sensitization with zinc porphyrin dyes using simulated solar irradiance. The Cu₅Ta₁₁O₃₀ nanoparticles were prepared by a flux-mediated synthesis and found to have an average particle size of ~10–15 nm by DLS and TEM. The zinc 4-(10,15,20-tris(4-pyridinyl)-porphin-5-yl)phenylphosphonic acid (**D1**) and its analog in which the pyridine groups are methylated (**D2**) were synthesized and found to have excited state reduction potentials appropriate for *p*-type dye sensitization of the nanoparticles. The dye-sensitized NP-Cu₅Ta₁₁O₃₀ exhibited fluorescence quenching consistent with electron transfer

from the NP-Cu₅Ta₁₁O₃₀ to the dye; forward and recombination rates were obtained by transient absorption measurements. Hole injection times of 8 ps and <100 fs were observed for **D1** and **D2**, respectively. Nanoparticulate films of Cu₅Ta₁₁O₃₀ were prepared and evaluated in dye sensitized solar cells (DSSC) under simulated solar irradiance (AM 1.5 G, 100 mW/cm²). Measureable photocurrents with open circuit potentials (V_{oc}) of 200 mV and 110 mV were observed using **D1** and **D2**, respectively.

INTRODUCTION

Anthropogenic activity and especially the massive burning of fossil fuels has a deleterious effect on the global ecosystem.¹ Owing to the magnitude of the solar energy reaching the earth, development of a technology that is capable of efficiently converting sunlight into electricity or highly energetic fuels is an appealing prospect.² In this connection, photoelectrochemical dye-sensitized solar cells (DSSCs) have attracted growing interest since the seminal contribution by Grätzel and O'Regan in 1991.³ Currently, two general classes of DSSC designs can be distinguished. The first (n-DSSC) is based on the sensitization of a wide-band-gap n-type semiconductor oxide (e.g. TiO₂, SnO₂ or ZnO). Photoinduced electron injection from the excited photosensitizer into the oxide conduction band is followed by electron transmission by a conductor through the load and to a non-photochemically active cathode. A mediator in solution transports electrons from the cathode to regenerate the oxidized dye at the photoanode. So far photoconversion efficiencies up to 13% have been achieved.⁴ The second class of DSSC uses a p-type metal oxide such as NiO, Cu(I)-containing oxides, zinc cobalt oxide,⁵ or doped diamond (p-DSSC). In these devices, photoinduced hole injection into the valence band (VB) of the semiconductor of a

photocathode initiates the overall electron flow. Thus far, they have achieved a maximum energy conversion efficiency of around 1.3%.⁶

These same concepts may be used in the design of photoelectrosynthetic systems that use visible light to split water into oxygen and hydrogen, or that produce other fuels or chemicals. Such systems are generally inefficient because of the great challenge of generating the necessary photopotential.⁷ However, if both efficient photocatalytic n-DSSC type anodes and p-DSSC type photocatalytic cathodes were available, one can envision their use in a tandem-type photoelectrosynthetic cell for water splitting.⁸ Such a cell would be based on two-cell configuration,^{9,10} wherein water is oxidized by catalysts at the photoanode and hydrogen is produced by catalysts at the photocathode. In principle, such cells could be very efficient because the overall power conversion efficiency of a tandem cell is higher than the Shockley-Queisser limitation for a single junction cell.¹¹ In a tandem photoelectrosynthetic cell, electron flow is analogous to that in the Z scheme of natural oxygenic photosynthesis, but the thermodynamics are fundamentally different in that a properly designed tandem cell better matches the absorption spectra of the sensitizers to the solar spectrum, thereby nearly doubling the rate of light absorption. Optimally designed sensitizers would cover the solar spectrum from the near UV to about 750 nm for one photoelectrode and from 750 nm to about 1100 nm for the second photoelectrode.¹²

The principle of operation of a *p*-type semiconductor sensitized by organic dyes is illustrated in Scheme 1a. Light excitation (step 1) of the sensitizer (S), forms the excited state (S*), which decays by hole injection into the valence band of the *p*-type semiconductor to form the charge separated state (step 2). In this case, because there is no “wiring” to take the hole or electron away from the interface, they must recombine following step 3. Scheme 1b

illustrates the pathway followed by a hole in a p-DSSC photoelectrochemical cell. Upon light absorption (step 1), the sensitizer excited state (S^*) injects a hole into the valence band of the semiconductor, leading to the reduction of the sensitizer ($S^{\bullet-}$) (step 2). The injected holes diffuse to the back side of the transparent conducting electrode, pass into the external circuit and reach the counter electrode where they oxidize the redox mediator (M/M^+) (step 4). This mediator reacts with the reduced sensitizer to restore the ground state of the sensitizer (step 5).¹³ In a photoelectrosynthetic application, a catalyst may be linked to or otherwise associated with the sensitizer so that useful synthetic chemistry is carried out at each electrode. In this case, an alternative pathway at the photocathode is reduction of the catalyst by the sensitizer excited state followed by hole injection into the semiconductor by the oxidized sensitizer.

In this work, we describe the synthesis and characterization of $Cu_5Ta_{11}O_{30}$ nanoparticles (NP- $Cu_5Ta_{11}O_{30}$) and their ability to accept high-potential holes into their valence band from a photoexcited porphyrin. Such nanoparticles may be suitable candidates for construction of tandem cells. In these cells, the photocathode would take advantage of the well-known high hole mobility of the copper(I)-based semiconductors like Cu_2O ¹⁴ and $CuNb_3O_8$,¹⁵ as compared to the significantly lower charge carrier mobility in the commonly used NiO .¹⁶ However, the main point of this study is to determine the energy levels of the dyes, and band positions of the polycrystalline semiconductor films. These fundamental concepts are the foundation for DSSCs and understanding these concepts will allow future optimization of these types of cells.

EXPERIMENTAL SECTION

Materials. Dichloromethane (anhydrous, 99.5%), anhydrous methanol (99.8%), propionic acid, 4-pyridinecarboxaldehyde, 4-bromobenzaldehyde, triethylamine, diethyl phosphite, zinc acetate dihydrate, iodomethane, bromotrimethylsilane, tetrakis(triphenylphosphine)palladium (0), and ammonium hexafluorophosphate were purchased from Sigma-Aldrich and used without further purification. Pyrrole was purchased from Sigma-Aldrich and distilled prior to use. Silica gel (SiliaFlash F60 40–63 μm) used for column chromatography was purchased from SiliCycle. Dichloromethane, hexane, ethyl acetate, methanol, acetone, tetrahydrofuran, acetonitrile, and chloroform for synthesis and column chromatography were distilled. Toluene and dimethylformamide for synthesis were dried over activated 4 Å molecular sieves. Copper sulfate (anhydrous, 99%), ascorbic acid (99.9%), tantalum pentachloride (99.9%), and copper chloride (99%) were purchased from Alfa Aesar and used without further purification.

Structural Characterization. Mass spectra were obtained with a Bruker Microflex LRF matrix-assisted laser desorption/ionization time-of-flight spectrometer (MALDI-TOF), equipped with a 60 Hz laser, using α -cyano-4-hydroxycinnamic acid (αCN), sinapinic acid (SA), or (1E, 3E)-1,4-diphenylbuta-1,3-diene (DPB) as a matrix. The reported mass is the most abundant isotope observed. Calculated values are listed after the experimental result for comparison. The $^1\text{H-NMR}$ spectra were taken on a Varian spectrometer at 400 MHz. Samples were prepared using deuterated solvents and with 0.03% tetramethylsilane as an internal standard.

Synthesis of Dyes. Scheme S1 shows the synthetic strategy followed for the preparation of the porphyrin sensitizers.

5-(4-Pyridinyl)dipyrromethane (1). Compound **1** was synthesized following a published procedure.¹⁷ Portions of 4-pyridinecarboxaldehyde (2.0 g, 18.7 mmol, 1.8 mL) and pyrrole (18.8 g, 281 mmol, 20 mL) were added to a 100 mL round-bottom flask equipped with an air-cooled condenser. The mixture was purged with argon for 20 min and heated at 85 °C under argon and stirred for 24 h. The resulting dark red solution was first purified using silica gel column chromatography (hexane:ethyl acetate 1:1) and further purified by crystallization from hexane:dichloromethane (DCM). The first crop of crystals was light brown (1.0 g) and the second was brown (1.2 g), giving an overall yield of 2.2 g (1.0 mmol, 53% yield). ¹H-NMR δ ppm (CDCl₃): 8.48 (d, *J* = 6.0 Hz, 2H), 8.16 (s, 2H), 7.12 (d, *J* = 6.0 Hz, 2H), 6.73 (m, 2H), 6.17 (dd, *J* = 2.9, 5.8 Hz, 2H), 5.89 (m, 2H), 5.45 (s, 1H).

5,10,15-Tris(4-pyridinyl)-20-(4-bromophenyl)-porphyrin (2). In a 250 mL round bottom flask was placed **1** (2.0 g, 8.58 mmol), 4-pyridinecarboxaldehyde (0.46 g, 4.29 mmol), and 4-bromobenzaldehyde (0.79 g, 4.29 mmol). Propionic acid (70 mL) was added and the flask was equipped with a condenser. The reaction was refluxed at 140 °C for 45 min and then cooled to room temperature. The propionic acid was removed by distillation under reduced pressure and the mixture was dissolved in DCM. The organic solution was washed with a saturated sodium bicarbonate solution (× 4) to neutralize any remaining acid. The organic layer was dried over Na₂SO₄. The solvent was removed under reduced pressure and the mixture was purified by silica gel column chromatography (4% MeOH:DCM) to yield a purple solid (175 mg, 0.252 mmol, 5.5% yield). ¹H-NMR δ ppm (CDCl₃): 8.99 (d, *J* = 4.0 Hz, 6H), 8.83 (d, *J* = 4.8 Hz, 2H) 8.77 (m, 6H) 8.08 (d, *J* = 4.0 Hz, 6H), 7.99 (d, *J* = 8.2 Hz, 2H), 7.84 (d, *J* = 8.2 Hz, 2H), -2.96 (s, 2H). MALDI-TOF: *m/z* obsd. 695.14 calc. for C₄₁H₂₆BrN₇ 695.14.

4-(10,15,20-Tris(4-pyridinyl)-porphin-5-yl)phenylphosphonic acid diethyl ester (3).

Compound **2** (160 mg, 0.23 mmol) was dissolved in dry toluene (100 mL), triethylamine (20 mL), and diethyl phosphite (0.65 g, 4.60 mmol, 0.6 mL). The solution was purged with argon for 20 min and tetrakis(triphenylphosphine)palladium(0) (53 mg, 0.046 mmol) was added quickly. The reaction was stirred under argon at 80 °C for 18 h. The solvent was removed by distillation under reduced pressure and the mixture was purified using silica gel column chromatography (2% MeOH:18% acetone:DCM). Compound **3** was obtained in 23% yield (40 mg, 0.053 mmol). ¹H-NMR δ ppm (CDCl₃): 9.06 (d, *J* = 5.6 Hz, 6H), 8.85 (m, 8H), 8.33 (dd, *J* = 4.0, 7.9 Hz, 2H), 8.24 (dd, *J* = 7.9, 13.1 Hz, 2H) 8.16 (d, *J* = 5.6 Hz, 6H), 4.40 (m, 4H), 1.53 (t, *J* = 7.1, 7.1 Hz, 6H) -2.89 (s, 2H). MALDI-TOF: *m/z* obsd. 753.27 calc. for C₄₅H₃₆N₇O₃P 753.26.

Zinc 4-(10,15,20-tris(4-pyridinyl)-porphin-5-yl)phenylphosphonic acid diethyl ester (D1E).

In a 100 mL round bottom flask compound **3** (40 mg, 0.053 mmol) and ZnOAc·2H₂O (117 mg, 0.53 mmol) were dissolved in THF (20 mL) and DCM (20 mL). The round bottom flask was equipped with a condenser and the reaction mixture was refluxed at 60 °C for 12 h. The solvent was removed by distillation under reduced pressure. The mixture was redissolved in DCM and washed with H₂O three times. The organic solution was dried over Na₂SO₄ and filtered, and the solvent was removed under reduced pressure. The mixture was purified using silica gel column chromatography (10% MeOH:DCM) to yield a purple solid (14.1 mg, 0.0173 mmol, 32% yield). ¹H-NMR δ ppm (DMSO): 9.01 (d, *J* = 5.6 Hz, 6H), 8.81 (m, 8H), 8.35 (dd, *J* = 3.8, 8.0 Hz, 2H) 8.21 (d, *J* = 5.6 Hz, 6H), 8.14 (dd, *J* = 8.0, 13.0 Hz, 2H) 4.28 (m, 4H), 1.42 (t, *J* = 7.1, 7.1 Hz, 6H). MALDI-TOF: *m/z* obsd. 815.18 calc. for C₄₅H₃₄N₇O₃PZn 815.18.

Zinc 4-(10,15,20-tris(4-pyridinyl)-porphin-5-yl)phenylphosphonic acid (D1). **D1E** (5 mg, 6.1 μmol) was dissolved in chloroform (10 mL) and triethylamine (17 μL). The solution was heated at 60 °C in a flask bearing a condenser and trimethylsilyl bromide (TMS-Br) (14.1 mg, 92.1 μmol , 12 μL) was added. The reaction mixture was refluxed for 18 h. The solvent was removed under reduced pressure and the product was extracted using DCM:H₂O. The organic layer was dried over Na₂SO₄ and filtered, and the solvent was removed by distillation under reduced pressure. The final product was obtained in a 100% yield (5 mg, 6.14 μmol). ¹H-NMR δ ppm (DMSO): 9.14 (s, 6H), 8.90 (m, 4 H), 8.87 (d, $J = 4.7$ Hz, 2H), 8.83 (d, $J = 4.7$ Hz, 2H), 8.43 (s, 6H), 8.28 (dd, $J = 3.3, 8.0$ Hz, 2H), 8.12 (dd, $J = 7.9, 12.8$ Hz, 2H). MALDI-TOF: m/z obsd. 759.15 calc. for C₄₁H₂₆N₇O₃PZn 759.11.

Zinc 4-(10,15,20-tris(4-(N-methylpyridiniumyl)-porphin-5-yl)phenylphosphonic acid diethyl ester (D2E). **D1E** (20 mg, 0.025 mmol) was dissolved in dry dimethylformamide (DMF) (10 mL) and the solution was purged with argon for 10 min. Methyl iodide (5.2 mg, 0.037 mmol, 2.3 μL) was added and the reaction mixture was heated at 100 °C for 1 h, and then cooled to room temperature and stirred for 12 h. The solvent was removed by distillation under reduced pressure and the mixture was extracted using DCM:H₂O. The aqueous layer was removed and concentrated by distillation of the solvent under reduced pressure. Anion exchange with NH₄PF₆ yielded porphyrin with hexafluorophosphate counterions, thus, increasing the solubility of the porphyrin in organic solvents. The mixture was cooled to 0 °C and the product precipitated out of solution. The water was removed by filtration to give a purple solid (21.5 mg, 0.0349 mmol, 100%). ¹H-NMR δ ppm (DMSO): 9.42 (d, $J = 6.3$ Hz, 6H), 9.04 (m, 4H), 8.98 (d, $J = 4.7$ Hz, 2H), 8.92 (m, 8H), 8.35 (dd, $J = 3.7, 7.7$ Hz, 2H),

8.18 (dd, $J = 7.8, 13.0$ Hz, 2H), 4.71 (s, 9H), 4.30 (m, 4H), 1.43 (t, $J = 7.0, 7.0$ Hz, 6H).

MALDI-TOF: m/z obsd. 860.42 calc. for $C_{48}H_{43}N_7O_3PZn^{3+}$ 860.24.

4-(10,15,20-Tris(4-(N-methylpyridiniumyl)-porphin-5-yl)phenylphosphonic acid (7).

D2E (5 mg, 5.8 μ mol) was dissolved in acetonitrile (10 mL) and triethylamine (0.02 mL) and heated to 65 °C. TMS-Br (13.3 mg, 0.087 mmol, 15 μ L) was added and the reaction mixture was refluxed for 12 h. The reaction conditions both cleaved the phosphonate esters and removed the zinc from the macrocycle. A green solid precipitated and the solvent was removed under reduced pressure. The solid was resuspended in H₂O and washed with DCM. The H₂O was then removed under reduced pressure to yield a green solid (5 mg, 5.8 μ mol, 100%). Compound **7** was used immediately to reintroduce the zinc without further purification. MALDI-TOF: m/z obsd. 742.30 calc. for $C_{44}H_{37}N_7O_3P^{3+}$ 742.27.

Zinc 4-(10,15,20-tris(4-(N-methylpyridiniumyl)-porphin-5-yl)phenylphosphonic acid

(D2). In a 50 mL round bottom flask compound **7** (5 mg, 6 μ mol) was dissolved in H₂O (5 mL) and THF (10 mL). ZnOAc·2H₂O (26 mg, 0.119 mmol) was added and the flask was equipped with a condenser. The reaction was refluxed for 2 h. The solvent was removed by distillation under reduced pressure and the mixture was crystallized in H₂O/acetone. The crystals were filtered and rinsed with cold acetone to yield a green solid (5 mg, 6 μ mol, 100%). ¹H-NMR δ ppm (DMSO/D₂O): 9.22 (s, 6H), 9.01 (d, $J = 19.2$ Hz, 8H), 8.80 (s, 6H), 8.20 (m, 4H), 4.65 (s, 9H). MALDI-TOF: m/z obsd. 804.34 calc. for $C_{44}H_{35}N_7O_3PZn^{3+}$ 804.18.

High Resolution Transmission Electron Microscopy. TEM micrographs were collected using a Philips CM200 TEM at 200kV, Cs 1.2 mm, PTP Resolution: 0.25nm

Focused Probe: 0.5nm and Imaging Modes: TEM/STEM. TEM micrographs were analyzed using *Digital Micrograph*TM software.¹⁸

Dynamic Light Scattering. Dynamic light scattering (DLS) data were taken on a Malvern Zetasizer Nano S with the detector 173° from the incident beam and a laser wavelength of 633 nm. Intensity by number was used for expressing the particle size distribution of the dispersion of nanoparticles. The particle size is determined using the velocity of Brownian motion and the Stokes-Einstein equation.

$$d = \frac{kT}{3\pi\eta D} \quad (1)$$

Where d is the hydrodynamic diameter, k is Boltzmann's constant, T is absolute temperature, η is viscosity and D is the translational diffusion coefficient. These measurements were done by placing 5 mL of a dispersion of nanoparticles in ethanol into a disposable plastic cuvette with a path length of 1 cm. The refractive index of Cu₂O (2.94) was used as an approximation of the refractive index of Cu₅Ta₁₁O₃₀, which has not been determined in the literature.¹⁹

Mott-Schottky Measurements. Electrochemical impedance spectroscopy was used to measure the flat-band potentials of nanoparticles of Cu₅Ta₁₁O₃₀, using a frequency of 30 KHz and ac amplitude of 5 mV. Measurements were carried out using a Parstat-2263 potentiostat from Princeton Applied Research. A three necked flask filled with 0.5 M Na₂SO₄ solution (pH 6.5) was purged with N₂ gas 30 min prior to the experiment. A flow of N₂ gas was kept over the headspace to purge any oxygen during the experiment. A film of NP-Cu₅Ta₁₁O₃₀ deposited on fluorine doped tin oxide (FTO, Pilkington TEC-15) served as the working electrode, Pt foil as a counter electrode and a saturated calomel electrode (SCE sat. KCl) as

the reference electrode. The working electrode was made by depositing an ethanol solution of the nanoparticles onto the FTO slides at 70°C in air.

Current-voltage measurements (i-v curves). $\text{Cu}_5\text{Ta}_{11}\text{O}_{30}$ nanoparticle films were deposited on fluorine-doped tin oxide (FTO) slides by a drop cast method and annealed under vacuum at 200 °C for 2 h. The films were then immersed in a 0.1 mM solution of **D1** (methanol) or **D2** (1% methanol in water) overnight, rinsed with ethanol and dried in air. Pt counter electrodes were fabricated by applying a 6 mM solution of H_2PtCl_6 in ethanol to FTO on a glass substrate (1 drop/cm²) and heating to 350 °C in air for 30 min. The working and counter electrodes were sandwiched together with a Parafilm gasket and the redox electrolyte (0.2 M KI and 0.02 M I₂ in ethylene glycol) was introduced by capillary diffusion. Current-voltage experiments were performed using a CH-Instruments CH620a potentiostat under simulated AM 1.5 G irradiation at 100 mW/cm² (Oriel) using a scan rate of 10 mVs⁻¹. Scans were started negative of the open circuit voltage (V_{oc}) and scanned towards the short circuit condition (I_{sc} , $V=0$). The sensitized film served as the working electrode and platinized FTO served as counter and reference electrode.

Steady State Absorption and Fluorescence. Spectra were recorded in 1 cm path length cuvettes with the following spectrophotometers: diode array HP 8452, Shimadzu - UV-IR (2041PC), and Hitachi double beam UV/Vis spectrophotometer (U-2800). Steady-state fluorescence spectra were measured using a Photon Technology International MP-1 spectrometer and corrected for detection system response and excitation source intensity as a function of wavelength. Excitation was provided by a 75 W xenon-arc lamp and single-grating monochromator. Fluorescence was detected at 90° to the excitation beam via a single-

grating monochromator and an R928 photomultiplier tube having S-20 spectral response and operating in the single photon counting mode.

Electrochemical and Spectroelectrochemical experiments. The voltammetric characterization of the redox processes was performed with an Autolab potentiostat-galvanostat (Electrochemical Instruments) in a conventional three-electrode cell. Electrochemical and spectroelectrochemical studies of porphyrins were carried out in anhydrous N,N-dimethylformamide (DMF) deoxygenated solution (argon bubbling), with 0.10 M tetra-*n*-butylammonium perchlorate (TBAClO₄) as supporting electrolyte. For cyclic voltammetry a Pt working electrode, a Pt counter electrode, and a silver wire quasi-reference electrode were used, while for spectroelectrochemistry a Pt mesh was used as working electrode. Absorption spectra of the dyes in the reduced state were obtained by applying a fixed potential at the redox potential of the first cathodic wave. After each voltammetric experiment, ferrocene was added as an internal standard (Fc/Fc⁺ = 0.72 V vs Normal Hydrogen Electrode), and the potential axis was calibrated against the formal potential for the NHE. The Pt working electrode was cleaned between experiments by polishing with 0.3 μm alumina paste followed by solvent rinses.

Time resolved absorption. Transient absorption measurements in the femtosecond to nanosecond window were acquired with a kilohertz pulsed laser source and a pump-probe optical setup. Laser pulses of ca. 100 fs at 800 nm were generated from an amplified, mode-locked titanium sapphire kilohertz laser system (Millennia/Tsunami/Spitfire, Spectra Physics). The laser pulse was divided and part was sent through an optical delay line and focused onto a 3 mm sapphire plate to generate a white light continuum for the probe beam. The rest of the pulse was used to pump an optical parametric amplifier to generate excitation

pulses selected using a mechanical chopper. Polarization of the pump beam was set to the magic angle (54.7°) relative to the probe beam and its intensity was adjusted using a continuously variable neutral density filter. White light generated was compressed by prism pairs (CVI) before passing through the sample. The white light probe was dispersed by a spectrograph (300 line grating) onto a charge-coupled device (CCD) camera (DU420, Andor Tech.). The final spectral resolution was about 2.3 nm for over a nearly 300 nm spectral region. Decay-associated spectra (DAS) were obtained by globally fitting the transient absorption kinetic traces over a selected wavelength region using a parallel kinetic model, equation (2).²⁰

$$\Delta A(\lambda, t) = \sum_{i=1}^n A_i(\lambda) \exp(-t / \tau_i) \quad (2)$$

where $\Delta A(\lambda, t)$ is the observed absorption change at a given wavelength at time delay t and n is the number of kinetic components used in the fitting. A plot of $A_i(\lambda)$ versus wavelength is called a DAS and represents the amplitude spectrum of the i^{th} kinetic component, which has a lifetime of τ_i .

RESULTS AND DISCUSSION

Synthesis and Characterization of NP-Cu₅Ta₁₁O₃₀. Nanoparticulate (NP)-Cu₅Ta₁₁O₃₀ was prepared by a flux-mediated synthesis using Cu₂O nanoparticles, Ta₂O₅ nanoparticles and CuCl, following procedures similar to those used for nanoparticles of the Cu(I)-niobate phases such as Cu₂Nb₈O₂₁.²¹ The Cu₂O and Ta₂O₅ nanoparticles were synthesized following methods reported elsewhere.^{22,23} Both Cu₂O nanoparticles (0.109 g) and Ta₂O₅ nanoparticles (0.390 g) were ground together with a mortar and pestle inside a

glove box, along with 0.250 g of CuCl as the flux.²⁴ In flux synthesis, the inorganic salt is heated to above its melting point and functions as a relatively low-temperature reaction medium for the dissolution of the reactant metal oxides and the formation of high-quality crystals of the product phase. The metal oxide nanoparticles were allowed to react within the molten CuCl flux at this temperature, yielding a better dispersion of the nanoparticles during the reaction. This mixture was placed under vacuum in a fused-silica reaction vessel and then heated at 900°C for 24 h. Afterwards, the powder obtained, which is a mixture of bulk and NP-Cu₅Ta₁₁O₃₀, was sonicated in absolute ethanol for 30 min and the larger particles were removed from the nanoparticle solution by centrifugation via sedimentation at 3000 rpm for 20 min. The yellow supernatant, consisting of the nanoparticles suspended in ethanol, was decanted to produce a yield on the order of ~1% in mass.

The NP-Cu₅Ta₁₁O₃₀ product was characterized by UV-Vis, DLS and HR-TEM. Figure 3.1 shows a representative HR-TEM micrograph of NP-Cu₅Ta₁₁O₃₀ with a narrow size distribution (15 ± 5 nm) having quasi-spherical morphologies, as measured from 50 nanoparticles (Supporting Information, Figure B1). It is noteworthy that the NP-Cu₅Ta₁₁O₃₀ product does not exhibit crystallinity detectable by powder XRD, suggesting either very small crystalline domains or a high amount of amorphous content. Although the nanoparticles show a slight tendency for agglomeration when they are dried, they are stable and remain dispersed for months in an ethanol solution. In order to gain insight into their behavior in ethanol solution, DLS measurements were performed.^{25,26} A size distribution centered on 12 nm (Figure 3.1, inset) was observed. Within the experimental error, the size and distribution of NP-Cu₅Ta₁₁O₃₀ measured by DLS is in good agreement with the HR-TEM images.

The UV-Vis absorption spectrum was recorded in order to compare the absorption of NP-Cu₅Ta₁₁O₃₀ to that of bulk Cu₅Ta₁₁O₃₀. Figure 3.2a shows the UV-Vis absorption spectrum of Cu₅Ta₁₁O₃₀ at a concentration of 0.75 mg/mL in ethanol. The energy gap for NP-Cu₅Ta₁₁O₃₀ was determined using a Tauc plot, (equation (3) ²⁷ and inset in Figure 3.2a), where α is the absorption coefficient, h is Planck's constant, ν represents the frequency of incident light, k is a proportionality constant and E_g is the energy gap.

$$(\alpha h\nu)^2 = k(h\nu - E_g) \quad (3)$$

The energy gap obtained for these NP-Cu₅Ta₁₁O₃₀ is 3.1 ± 0.2 eV, which is significantly larger than the Cu₅Ta₁₁O₃₀ bulk band gap situated at 2.6 eV.²⁸ This result suggests that in NP-Cu₅Ta₁₁O₃₀ the Bohr radius is larger than 7.5 nm; hence our sample is in the quantum confinement regime and the potentials of the conduction and valence bands are shifted from the bulk potentials. In order to determine the new positions of the semiconductor energy levels, Mott-Schottky analyses were performed. In this case, for *p*-type semiconductors the capacitance is related to the flat-band potential (V_{fb}) as given in equation (4).²⁹

$$\frac{1}{c^2} = \left(\frac{2}{e\epsilon_r\epsilon_0 N_A A^2} \right) \bullet \left(-V_0 + V_{fb} - \frac{KT}{e} \right) \quad (4)$$

where c is the capacitance, e is the charge of the electron, ϵ_r is the dielectric constant of the material, ϵ_0 is the permittivity of free space, N_A is the acceptor density, A is the geometrical area of the working electrode, K is Boltzmann's constant, and T is temperature in Kelvin. Plotting the inverse square of capacitance against applied bias yields a straight line, which can be extrapolated to the x -ordinate (V_0) using equation (5).

$$V_0 = V_{fb} - \frac{KT}{e} \quad (5)$$

These data are plotted in Figure 3.2b; the negative slope indicates that the semiconductor is *p*-type. The value obtained for V_0 is 0.625 V, and hence V_{fb} is 0.652 V vs. SCE. Converting from SCE to NHE, the V_{fb} is 0.896 V vs. NHE. The valence band energy, E_v , can be obtained from equation (6),

$$E_v = V_{fb} - kT \cdot \ln\left(\frac{N_A}{N_V}\right) \quad (6)$$

where N_A and N_V are the acceptor level and the densities of states, respectively. The acceptor level, N_A , can be calculated using the second term of the Mott-Schottky equation where:

$$Slope = \frac{-2}{e\epsilon_0\epsilon N_A A^2} \quad (7)$$

Using an N_A of $\sim 10^{16}$ and densities of states of $\sim 10^{19}$, E_v is calculated to be 1.07 V vs. NHE. Thus, the valence band is ~ 200 mV more positive than the oxidation potential of water at pH of 6.5.^{15,28,29}

Synthesis of Dyes. The structures of the dyes used for these studies are shown in Figure 3.3. They were prepared using variations of methods reported in the literature and characterized using NMR, mass spectrometry, and UV-Visible spectroscopy. Details are given in the Experimental Section.

Electrochemical experiments. Cyclic voltammograms for **D1E** and **D2E** were obtained in dimethylformamide containing tetrabutylammonium perchlorate (DMF/ ClO_4TBA) as the supporting electrolyte with a Pt working electrode, a Pt counter electrode and Ag wire as a

reference electrode. Both dyes were expected to have the reduction potential of their first singlet excited state more positive than the valence band of NP-Cu₅Ta₁₁O₃₀.^{30,31} Figure 3.4 shows the CV for a) **D1E** where a reversible porphyrin reduction is observed at -0.41 V vs NHE and b) **D2E** having a quasi-reversible porphyrin reduction at -0.23 V vs NHE. The porphyrin reduction potential of **D2E** is less negative than that of **D1E** due to the presence of the electron-withdrawing alkylated pyridyl groups.

Based on the reduction potentials obtained for the nanoparticles and the dyes, Figure 3.5 depicts the relative energetics of the ground and excited states of the dyes and the conduction band edge (CB) and valence band edge (VB) of NP-Cu₅Ta₁₁O₃₀. The potential for the first reduction ($D/D^{\bullet-}$) of the dye was measured electrochemically as discussed above, and the potential for the reduction of the excited state ($D^*/D^{\bullet-}$) was calculated using the zero-zero optical excitation energy estimated from the absorption spectra for porphyrin **D1** and **D2** attached to nanoparticles, where E_{00} is ~2.0 eV for both, within the experimental error (See Figure B2). As depicted in Figure 3.5, the excited singlets of **D1** and **D2** are thermodynamically capable of photoinjecting a hole into the VB because the position of the VB of NP-Cu₅Ta₁₁O₃₀ is at less positive potentials than the porphyrin dye $D^*/D^{\bullet-}$ levels. In contrast, the conduction band potential of NP-Cu₅Ta₁₁O₃₀ is more negative than the oxidation potential of the excited states of the porphyrins by >1.12 V and >1.30 V for **D1** and **D2**, respectively and thus electron injection from the excited dye into the conduction band of the semiconductor is not thermodynamically possible.

In order to study the photophysical behavior of the systems **D1**-NP-Cu₅Ta₁₁O₃₀ and **D2**-NP-Cu₅Ta₁₁O₃₀, the dyes were attached to the nanoparticles as follows. The dye (**D1** or **D2** in acid form) dissolved in methanol ([dye] ~ 10⁻³ M) was added dropwise into an ethanol

suspension of $\text{Cu}_5\text{Ta}_{11}\text{O}_{30}$ until the mixture reached an absorbance of 0.4 at 560 nm ([dye] $\sim 10^{-5}$ M). The suspension was stirred for 24 h at 40 °C to reach equilibrium conditions. The system **D1E**-NP- $\text{Cu}_5\text{Ta}_{11}\text{O}_{30}$, where **D1** is in ester form was studied as well; results obtained are similar to the **D1**-NP- $\text{Cu}_5\text{Ta}_{11}\text{O}_{30}$ (see Supporting Information).

Absorption and steady-state fluorescence experiments. UV-Vis absorption spectra of **D1**, **D1**-NP- $\text{Cu}_5\text{Ta}_{11}\text{O}_{30}$, **D2**, and **D2**-NP- $\text{Cu}_5\text{Ta}_{11}\text{O}_{30}$ in ethanol were recorded (Figure 3.6). After the dyes were attached to the nanoparticles, a broadening and shifting to longer wavelengths of the Soret and Q-bands was observed for both dyes. This phenomenon is more significant for **D2** than **D1**. Since the experimental conditions are the same, this may be explained by taking into account that **D2** has three positive charges on the methylpyridinium groups and it is possible that (instead of, or in addition to, attaching to the nanoparticles through the phosphonic moiety) **D2** associates with the nanoparticles in a different way. Emission spectra of **D1**, **D1**-NP- $\text{Cu}_5\text{Ta}_{11}\text{O}_{30}$, **D2**, and **D2**-NP- $\text{Cu}_5\text{Ta}_{11}\text{O}_{30}$ in ethanol were taken with excitation at 540 nm. Figure 3.6 (a and b) shows a complete quenching of fluorescence for both dyes when they are attached to NP- $\text{Cu}_5\text{Ta}_{11}\text{O}_{30}$. This fluorescence quenching is consistent with the first excited singlet state of the porphyrins being deactivated by means of electron transfer from the NP- $\text{Cu}_5\text{Ta}_{11}\text{O}_{30}$ VB to the excited dye (hole injection into the VB).

Transient absorption measurements. Transient absorption measurements were done in both systems to investigate the hole injection into the VB of NP- $\text{Cu}_5\text{Ta}_{11}\text{O}_{30}$ by the excited dyes and to determine the injection and recombination rates. The absorption signatures of the reduced dyes **D1** $^{\bullet-}$ and **D2** $^{\bullet-}$ were obtained by spectroelectrochemistry, as is shown in Figures 3.7a and 3.7c, respectively. The difference absorption spectrum for **D1** $^{\bullet-}$ shows

ground-state bleaching of the Q-bands at 560 nm and 610 nm. There is also a broad absorption band at 620–760 nm. The difference absorption spectrum for **D2**^{•-} presents a well-defined ground state bleaching of Q-bands at 560 nm and 610 nm and a broad band at ~620–770 nm.

The decay-associated-spectra (DAS) for **D1**-NP-Cu₅Ta₁₁O₃₀ and **D2**-NP-Cu₅Ta₁₁O₃₀ in ethanol solution measured by fs transient absorption after excitation at 428 nm are shown in Figures 3.7b and 3.7d, respectively. For **D1**-NP-Cu₅Ta₁₁O₃₀, global analysis of the transient absorption gives a satisfactory fit with three decay lifetimes of 0.7 ps, 8 ps and 190 ps (Figure 7b). The 0.7 ps DAS shows a characteristic induced absorption at ~640–740 nm, which corresponds to the **D1** radical anion and therefore can be associated with the decay of the **D1**^{•-}-NP-Cu₅Ta₁₁O₃₀(+) transient. The 8 ps DAS can be attributed to the formation of the **D1**^{•-}-NP-Cu₅Ta₁₁O₃₀(+) state since it shows ground state bleaching of Q-bands and stimulated emission at ~670 nm. The bleaching maxima of the Q-bands are red shifted, probably due to the attachment of **D1** to the nanoparticles. The 190 ps DAS features ground state bleaching of the Q-band maxima that is blue shifted compared to the 0.7 DAS and 8 ps DAS, and therefore can be associated with **D1** molecules that are aggregated and/or not directly attached to the nanoparticles. Due to the high heterogeneity of the system, obtained lifetimes do not correspond to single species. These lifetimes represent an average of the decay of several slightly different species. For **D1**-NP-Cu₅Ta₁₁O₃₀ there is likely some population with very fast formation of charge separate state (<100 fs), this would explain high amplitude of 0.7 ps DAS in such inverted kinetics case, but overall the rate of decay of the charge-separated species is greater than the average effective rate of formation.

For the system **D2**-NP-Cu₅Ta₁₁O₃₀ the global analysis of the transient absorption gives a satisfactory fit with four decay lifetimes of 2.8 ps, 19.6 ps, 277 ps and a nondecaying lifetime on a 1 ns time scale (Figure 3.7d). The 2.8 ps DAS does not show stimulated emission and instead shows **D2** radical-anion induced absorption at ~580–700, and can therefore be associated with the decay of the species **D2**^{•-}-NP-Cu₅Ta₁₁O₃₀(+). The charge separated species is formed in <100 fs, and its rise time is too fast to observe. The other three DAS show ground state bleaching of Q band maxima that is blue shifted compared to the 2.8 ps DAS, and which therefore can be attributed to **D2** that is aggregated and/or not directly attached to the semiconductor surface.

In thermodynamic terms, the more rapid hole injection observed for the **D2** system (as compared to the **D1** case) may be ascribed to the larger energetic driving force for the process, i.e., as shown in Figure 3.5. Alternatively, the driving force for charge recombination is greater for the **D1** system, and thus this rate constant is larger than that for the **D2** case.

DSSC measurements. Cu₅Ta₁₁O₃₀ nanoparticles were deposited on fluorine-doped tin oxide (FTO) slides. Characterization of annealed films by X-ray diffraction (XRD) indicate a phase pure material. Energy dispersive spectroscopy (EDS) as well as elemental mapping both show the presence of Cu and Ta in appropriate ratios (see Supporting Information). Current-potential scans were performed in the dark and under AM 1.5 G irradiation at a scan rate of 10 mV·s⁻¹, starting from negative applied potentials and continuing to the I_{sc} condition. The results are shown in Figure 3.8.

In Figure 3.8, positive current indicates hole injection into the photocathode. In the dark, both dye-nanoparticle systems show negligible current as no hole injection occurs. At suitably

negative applied potentials, somewhat larger currents in the opposite direction are observed. These are likely due to reduction of the redox mediator by the semiconductor. In fact, when no dye is present, much larger currents of this type are observed, and are similar under both dark and light conditions (see Supplementary Information). When light is applied to the electrodes bearing the dye-nanoparticle composites, photoinjection of holes from the dye molecules into the nanoparticles and thence into the circuit is observed (Figure 3.8). As summarized in Table 3.1, open circuit voltages (V_{OC}) of 110 mV and 200 mV were observed for nanoparticles bearing **D2** and **D1**, respectively. Such V_{OC} values are comparable to those observed for NiO (~ 100 mV)¹⁶ and other Cu(I) based p-DSSCs (~ 150 – 300 mV)^{32,33} using the I^-/I_3^- redox mediator. Short circuit currents (I_{SC}) were on the order of a few μA per cm^2 . Table 3.1 also reports the fill factors (ff) and light conversion efficiencies (η), calculated as discussed in the Supporting Information. These results indicate that the dye-nanoparticle composites are indeed capable of light-driven hole injection into an external circuit. SEM images of annealed films indicate growth of the nanoparticles to micron sizes, disrupting the homogeneity of the film; this along with the lack of a suitable blocking layer³⁴ to slow charge recombination cause the low overall efficiency of the cell and differences in current densities. While efficiency in the DSSC is low, further developments in the film making process may increase the overall efficiency.

CONCLUSIONS

The preparation of p-type semiconductor $Cu_5Ta_{11}O_{30}$ nanoparticles (NP- $Cu_5Ta_{11}O_{30}$) with a valence band edge suitable for water oxidation has been described. Two sensitizers, zinc 4-(10,15,20-tris(4-pyridinyl)-porphin-5-yl)phenylphosphonic acid (**D1**) and its analog in which the pyridine groups are methylated (**D2**), were shown to have excited state reduction

potentials that were thermodynamically capable of photoinjecting a hole into the VB of the NP-Cu₅Ta₁₁O₃₀. These sensitizers are not thermodynamically capable of photoinjecting electrons into the CB of the NP-Cu₅Ta₁₁O₃₀. Transient absorption measurements of the **D1**-NP-Cu₅Ta₁₁O₃₀ system show hole injection in 8 ps and very fast recombination in ~700 fs. The **D2**-NP-Cu₅Ta₁₁O₃₀ system shows very fast injection, <100 fs, and slower recombination on the 2.8 ps time scale. DSSC measurements on the NP-Cu₅Ta₁₁O₃₀ sensitized with **D1** and **D2** show significant photocurrent responses under simulated solar irradiance. Taken together, the thermodynamic, spectroscopic, and cathodic i-v measurements lead us to conclude that these systems function by a photoinduced hole injection mechanism. Investigating the use of NP-Cu₅Ta₁₁O₃₀ as a new p-type semiconductor with a VB more positive than the water oxidation potential and extremely negative CB (< -2.0 V vs. NHE) is a step in the development of new materials for p-DSSCs, which could lead to more efficient ways to carry out solar water splitting.

SUPPORTING INFORMATION: Includes HR-TEM and SEM images, EDS and elemental mapping, XRD, DLS, UV-Vis, schematic and details of dye synthesis, ¹H-NMR results, absorption and transient absorption spectra, power-voltage curves and control experiments, and fill factor and efficiency calculations. This material is available free of charge via the Internet at <http://pubs.acs.org>.

Acknowledgements

The work at ASU was supported by the Center for Bio-Inspired Solar Fuel Production, an Energy Frontier Research Center funded by the U.S. Department of Energy, Office of Science, Office of Basic Energy Sciences under Award Number DE-SC0001016 and the Office of Basic Energy Sciences, Division of Chemical Sciences, Geosciences, and Energy

Biosciences, Department of Energy under contract DE-FG02-03ER15393. The work at NCSU was supported by the Research Corporation for Science Advancement (P.M. is a Scialog awardee) and the Department of Chemistry. M.G. gratefully acknowledges financial support from Secyt-UNRC, CONICET and ANPCYT.

REFERENCES

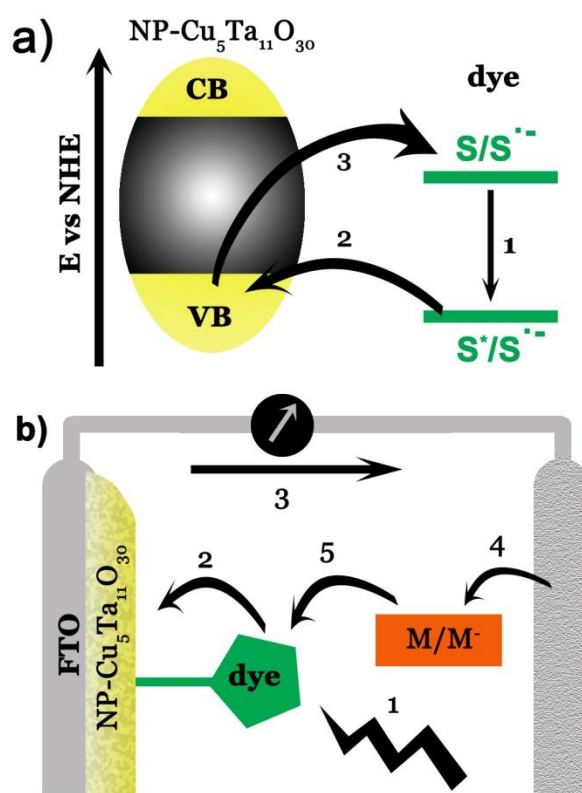
- (1) Rockstrom, J.; Steffen, W.; Noone, K.; Persson, A.; Chapin, F. S.; Lambin, E. F.; Lenton, T. M.; Scheffer, M.; Folke, C.; Schellnhuber, H. J.; Nykvist, B.; de Wit, C. A.; Hughes, T.; van der Leeuw, S.; Rodhe, H.; Sorlin, S.; Snyder, P. K.; Costanza, R.; Svedin, U.; Falkenmark, M.; Karlberg, L.; Corell, R. W.; Fabry, V. J.; Hansen, J.; Walker, B.; Liverman, D.; Richardson, K.; Crutzen, P.; Foley, J. A. *Nature* **2009**, *461*, 472.
- (2) Sherman, B. D.; Vaughn, M. D.; Bergkamp, J. J.; Gust, D.; Moore, A. L.; Moore, T. A. *Photosynth. Res.* **2014**, *120*, 59.
- (3) O'Regan, B.; Grätzel, M. *Nature* **1991**, *353*, 737.
- (4) Mathew, S.; Yella, A.; Gao, P.; Humphry-Baker, R.; Curchod, Basile, F. E.; Ashari-Astani, N.; Tavernelli, I.; Rothlisberger, U.; Nazeeruddin, Md, K.; Grätzel, M. *Nature Chem.* **2014**, *6*, 242.
- (5) Mercado, C. C.; Zakutayev, A.; Zhu, K.; Flynn, C. J.; Cahoon, J. F.; Nozik, A. J. *J. Phys. Chem. C* **2014**, *118*, 25340.
- (6) Odobel, F.; Pellegrin, Y. *The Journal of Physical Chemistry Letters* **2013**, *4*, 2551.
- (7) Youngblood, W. J.; Lee, S.-H. A.; Kobayashi, Y.; Hernandez-Pagan, E. A.; Hoertz, P. G.; Moore, T. A.; Moore, A. L.; Gust, D.; Mallouk, T. E. *J. Am. Chem. Soc.* **2009**, *131*, 926.
- (8) Sivula, K.; Gratzel, M. In *Photoelectrochemical Water Splitting: Materials, Processes and Architectures*; The Royal Society of Chemistry: 2013, p 83.
- (9) Tachibana, Y.; Vayssieres, L.; Durrant, J. R. *Nat. Photonics* **2012**, *6*, 511.
- (10) Kalyanasundaram, K.; Graetzel, M. *Curr. Opin. Biotechnol.* **2010**, *21*, 298.
- (11) Henry, C. H. *J. Appl. Phys.* **1980**, *51*, 4494.
- (12) Hanna, M. C.; Nozik, A. J. *J. Appl. Phys.* **2006**, *100*, 074510.
- (13) Odobel, F.; Pellegrin, Y.; Gibson, E. A.; Hagfeldt, A.; Smeigh, A. L.; Hammarström, L. *Coord. Chem. Rev.* **2012**, *256*, 2414.
- (14) Liao, L.; Yan, B.; Hao, Y. F.; Xing, G. Z.; Liu, J. P.; Zhao, B. C.; Shen, Z. X.; Wu, T.; Wang, L.; Thong, J. T. L.; Li, C. M.; Huang, W.; Yu, T. *Appl. Phys. Lett.* **2009**, *94*, 113106.
- (15) Joshi, U. A.; Maggard, P. A. *The Journal of Physical Chemistry Letters* **2012**, *3*, 1577.
- (16) Flynn, C. J.; Oh, E. E.; McCullough, S. M.; Call, R. W.; Donley, C. L.; Lopez, R.; Cahoon, J. F. *J. Phys. Chem. C* **2014**, *118*, 14177.

- (17) Gryko, D.; Lindsey, J. S. *J. Org. Chem.* **2000**, *65*, 2249.
- (18) Mitchell, D. R.; Schaffer, B. *Ultramicroscopy* **2005**, *103*, 319.
- (19) Malerba, C.; Biccari, F.; Leonor Azanza Ricardo, C.; D’Incau, M.; Scardi, P.; Mittiga, A. *Sol. Energy Mater. Sol. Cells* **2011**, *95*, 2848.
- (20) van Stokkum, I. H. M.; Larsen, D. S.; van Grondelle, R. *Biochim. Biophys. Acta* **2004**, *1657*, 82.
- (21) Choi, J.; King, N.; Maggard, P. A. *ACS Nano* **2013**, *7*, 1699.
- (22) Ullah, R.; Sun, H.; Ang, H. M.; Tadé, M. O.; Wang, S. *Ind. Eng. Chem. Res.* **2013**, *52*, 3320.
- (23) Zhang, X.; Song, J.; Jiao, J.; Mei, X. *Solid State Sci.* **2010**, *12*, 1215.
- (24) Boltersdorf, J.; King, N.; Maggard, P. A. *CrystEngComm* **2015**.
- (25) *Light Scattering from Polymer Solutions and Nanoparticle Dispersions*; Schärftl, W., Ed.; Springer Berlin, 2006.
- (26) Sartor, M. *Dinamic Light Scattering*, University of California, 2010.
- (27) Johnson, E. J. In *Optical Properties of III-V Compounds, Semiconductors and Semimetals*; R.K. Willardson, A. C. B., Ed.; Academic Press: New York, 1967; Vol. 3, p 153.
- (28) Fuoco, L.; Joshi, U. A.; Maggard, P. A. *J. Phys. Chem. C* **2012**, *116*, 10490.
- (29) Gomes, W. P.; Cardon, F. *Prog. Surf. Sci.* **1982**, *12*, 155.
- (30) Williams, R. F. X.; Hambright, P. *Bioinorganic Chemistry* **1978**, *9*, 537.
- (31) Worthington, P.; Hambright, P.; Williams, R. F. X.; Reid, J.; Burnham, C.; Shamim, A.; Turay, J.; Bell, D. M.; Kirkland, R.; Little, R. G.; Datta-Gupta, N.; Eisner, U. *J. Inorg. Biochem.* **1980**, *12*, 281.
- (32) Yu, M.; Natu, G.; Ji, Z.; Wu, Y. *The Journal of Physical Chemistry Letters* **2012**, *3*, 1074.
- (33) Powar, S.; Xiong, D.; Daeneke, T.; Ma, M. T.; Gupta, A.; Lee, G.; Makuta, S.; Tachibana, Y.; Chen, W.; Spiccia, L.; Cheng, Y.-B.; Götz, G.; Bäuerle, P.; Bach, U. *J. Phys. Chem. C* **2014**, *118*, 16375.

(34) Wang, H.; Zeng, X.; Huang, Z.; Zhang, W.; Qiao, X.; Hu, B.; Zou, X.; Wang, M.; Cheng, Y.-B.; Chen, W. *ACS Appl. Mater. Interfaces* **2014**, *6*, 12609.

Table 3.1. Short circuit current, open circuit potential, fill factor and light conversion efficiency of D1 and D2

Dye	I_{sc} ($\mu\text{A}/\text{cm}^2$)	V_{oc} (mV)	ff	η (%)
D1	5.28	200	0.260	$2.75 \cdot 10^{-4}$
D2	2.85	110	0.265	$8.31 \cdot 10^{-5}$



Scheme 3.1. a) Schematic of the processes involved in hole photo-injection in a system of a chromophore and a p-type semiconductor. The numbers on the arrows represent the order in which the processes occur; 1 – light absorption, 2 – hole injection, 3 – electron recombination. b) Schematic of a p-DSSC showing the electron transfer processes involved in the operation of the photoelectrochemical cell, as described in the text.

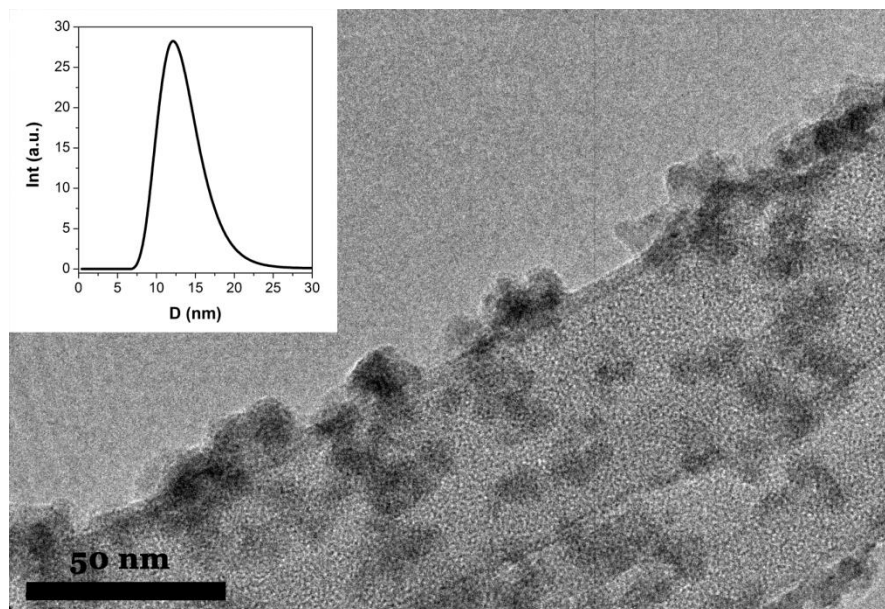


Figure 3.1. Representative HR-TEM of NP-Cu₅Ta₁₁O₃₀ where a quasi-spherical distribution of particles with sizes of (15 ± 5) nm can be observed. **Inset:** Size distribution obtained by DLS of NP-Cu₅Ta₁₁O₃₀ dispersed in an ethanol solution.

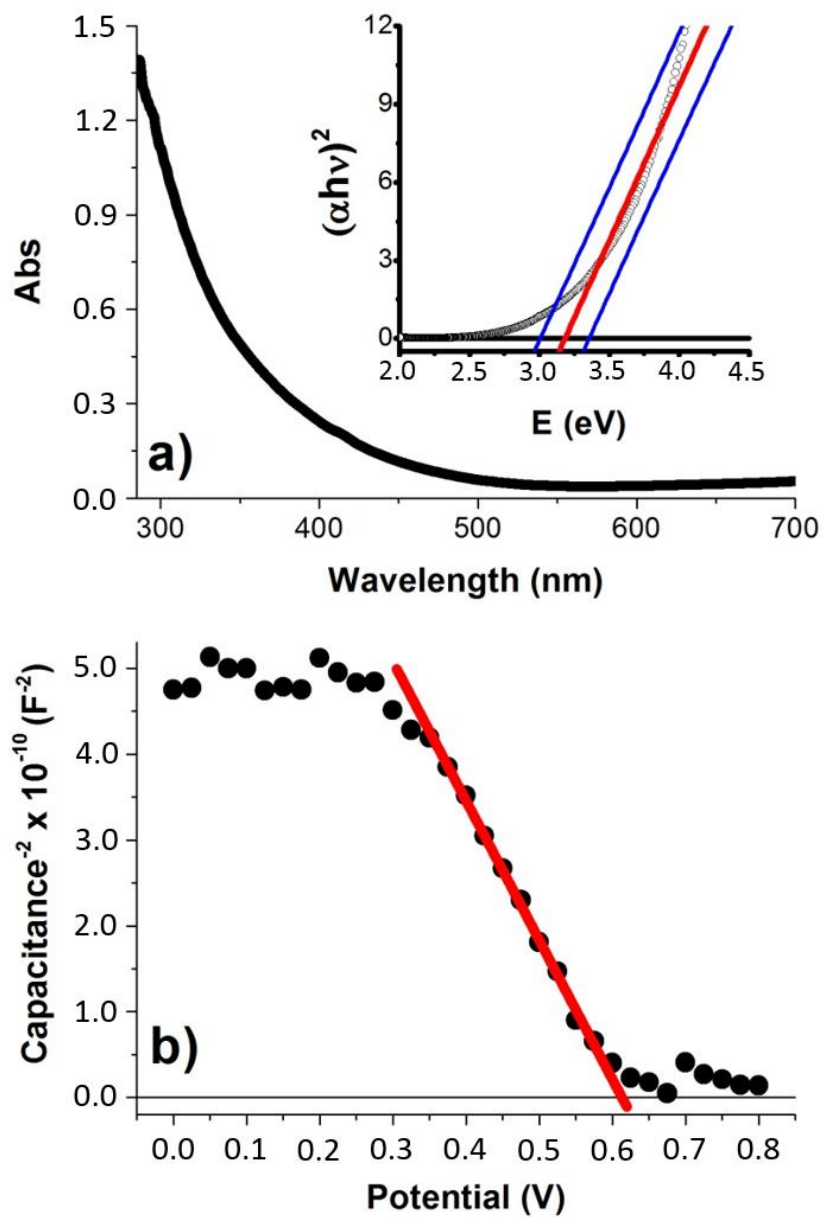


Figure 3.2. a) Absorption spectrum of NP-Cu₅Ta₁₁O₃₀ in ethanol at a concentration of 0.75 mg/mL. **Inset:** Absorption onset value of the first direct allowed transition for NP-Cu₅Ta₁₁O₃₀ (red line) and 99% confident bands (blue line). **b)** Mott-Schottky plot of NP-Cu₅Ta₁₁O₃₀.

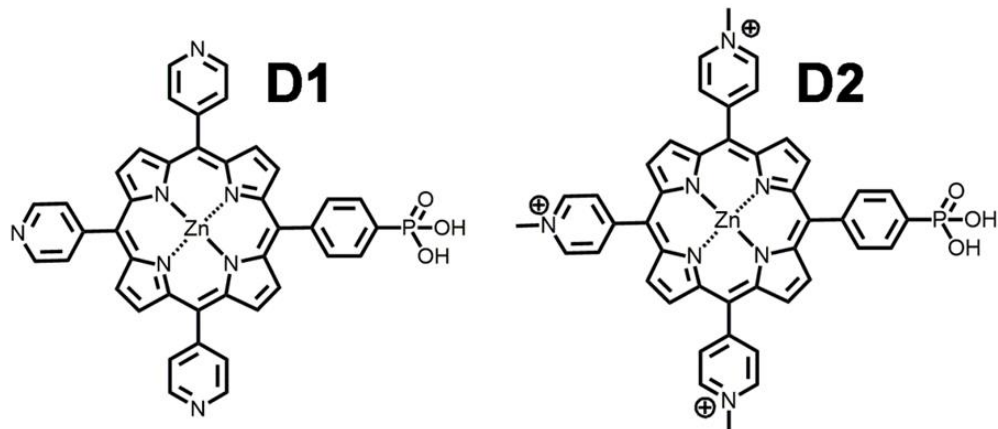


Figure 3.3. Molecular structures of the dyes **D1** and **D2** in their acid forms. Molecular structures of dyes **D1E** and **D2E**, in their ester forms, are shown in the Supporting Information.

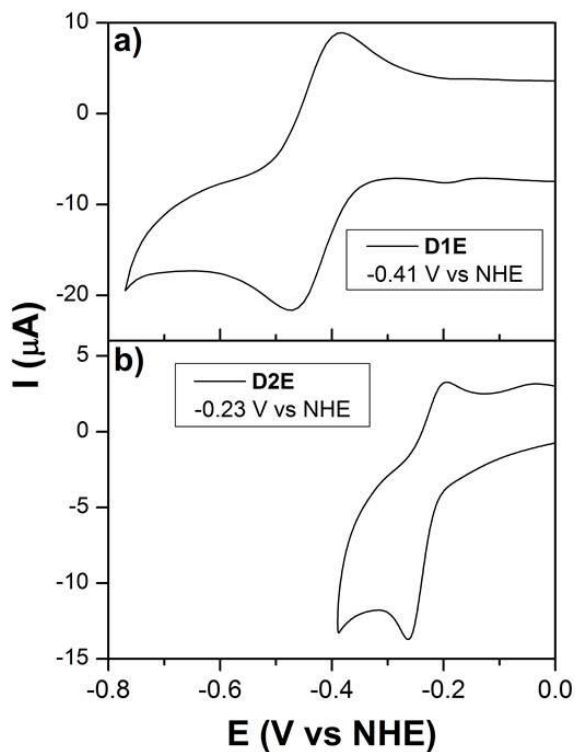


Figure 3.4. Cyclic voltammogram of **a) D1E** and **b) D2E** in DMF/ ClO_4TBA with a Pt working electrode, a Pt counter electrode and an Ag wire as the reference electrode.

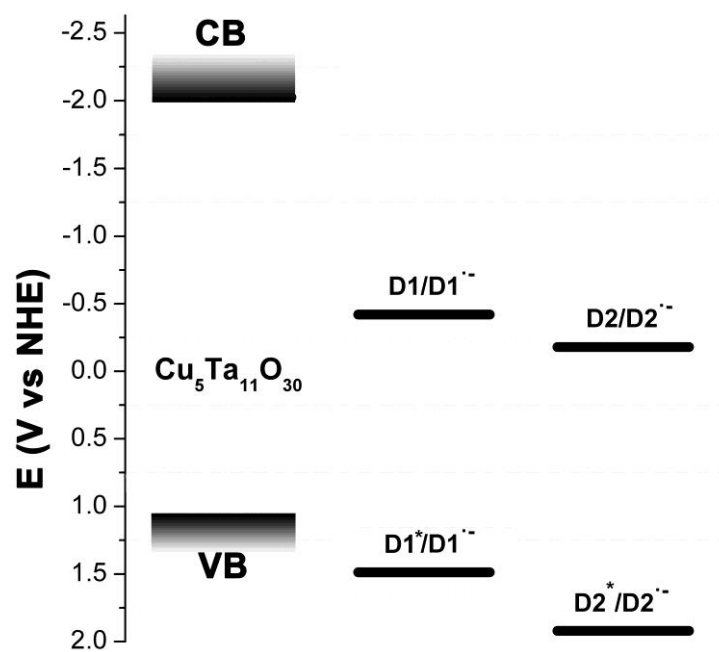


Figure 3.5. Diagram depicting the reduction potentials for the ground and the lowest excited singlet states of **D1** and **D2**, the NP-Cu₅Ta₁₁O₃₀ conduction band energy (CB), and the NP-Cu₅Ta₁₁O₃₀ valence band energy (VB).

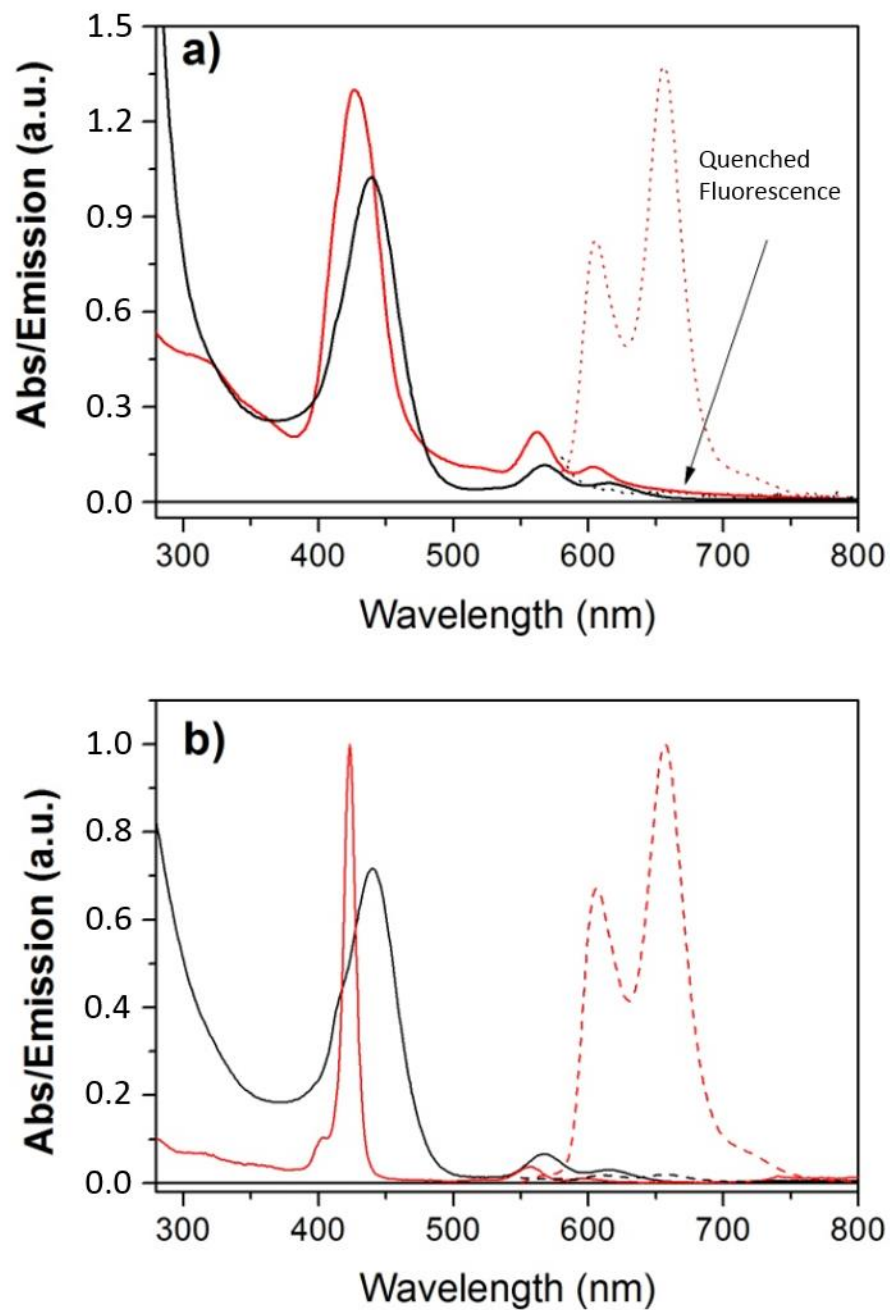


Figure 3.6. Absorption (solid lines) and emission (dashed lines) spectra of **D1** (panel a) and **D2** (panel b) before (red line) and after (black line) attachment to the NP-Cu₅Ta₁₁O₃₀ nanoparticles. Emission spectra were taken with excitation at 540 nm.

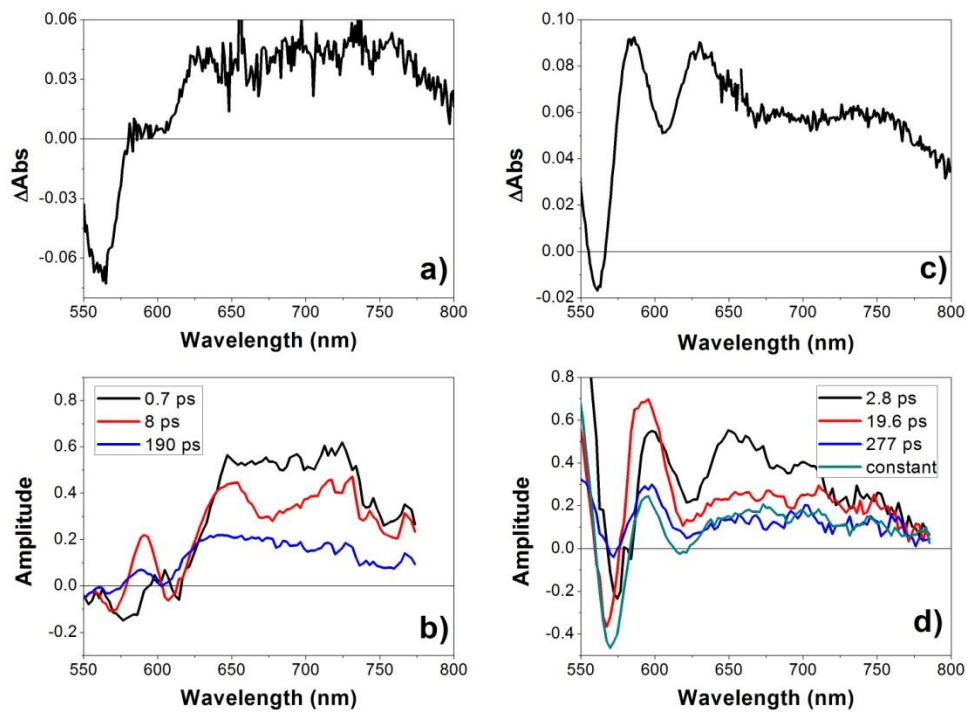


Figure 3.7. Difference absorption spectra **a)** ($\text{D1}^* - \text{D1}$) and **c)** ($\text{D2}^* - \text{D2}$) obtained by spectroelectrochemistry. Decay-associated-spectra in ethanol solution measured by fs transient absorption after excitation at 428 nm for **b)** $\text{D1-NP-Cu}_5\text{Ta}_{11}\text{O}_{30}$ and **d)** $\text{D2-NP-Cu}_5\text{Ta}_{11}\text{O}_{30}$.

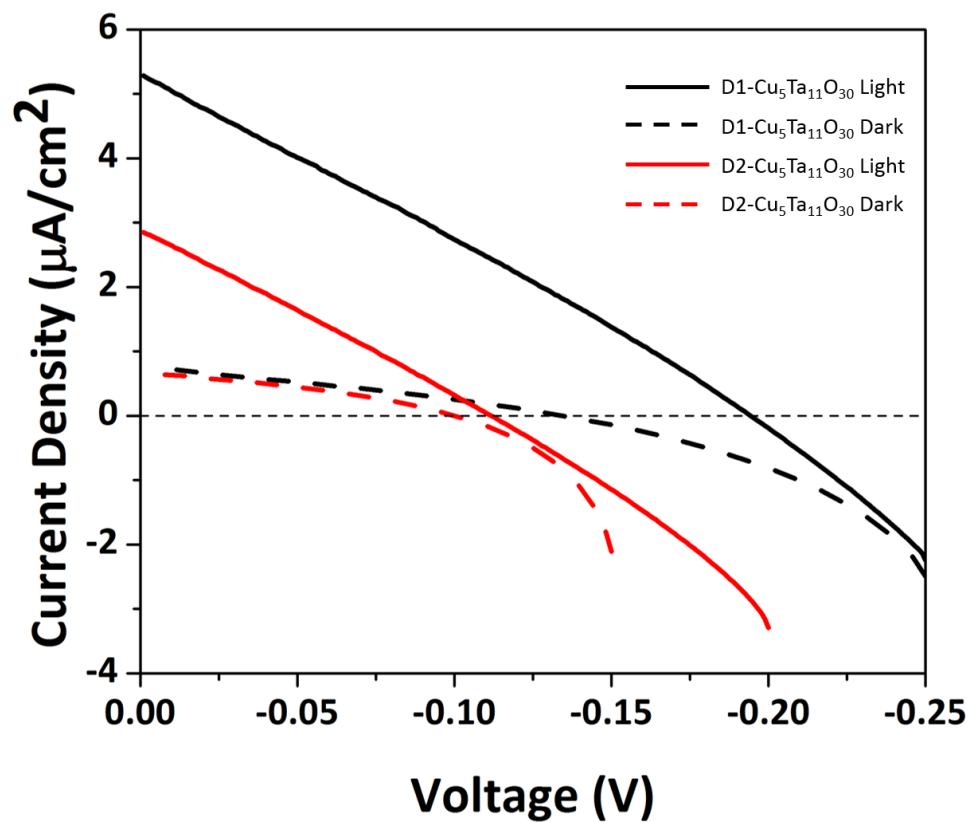


Figure 3.8. Linear sweep voltammograms of **D1** (black lines) and **D2** (red lines) in dark (dotted lines) and under AM 1.5 G irradiation (solid lines) with sweep rate of $10 \text{ mV}\cdot\text{s}^{-1}$.

CHAPTER 4: Flux-Mediated Syntheses, Structural Characterization, and Low-Temperature Polymorphism of the *p*-Type Semiconductor Cu₂Ta₄O₁₁

Based on a journal article published in the Journal of Solid State Chemistry

J. Solid State Chem., **2016**, 236, 10-18.

Nacole King,^a Ian Sullivan^a, Pilanda Watkins-Curry^{b,c} Julia Y. Chan,^c and Paul A. Maggard^{a,*}

^a*Department of Chemistry, North Carolina State University, Raleigh, NC USA 27695-8204.*

^b*Department of Chemistry, Louisiana State University, Baton Rouge, LA USA 70803*

^c*Department of Chemistry, The University of Texas at Dallas, Richardson, TX USA 75080-4551.*

The research presented here is a combination of work from all of the authors. The author of this dissertation contributed to the XRD measurements of polycrystalline films of Cu₂Ta₄O₁₁, and fabrication and photoelectrochemical measurements of polycrystalline Cu₂Ta₄O₁₁ photocathodes.

ABSTRACT

A new copper(I)-tantalate, α -Cu₂Ta₄O₁₁, has been synthesized via flux methods and characterized by a powder X-ray Rietveld refinement (space group *Cc*, (9), $a = 10.7337(14)$ Å, $b = 6.2506(3)$ Å, $c = 12.8869(14)$ Å, $\beta = 106.070(4)$ Å). The α -Cu₂Ta₄O₁₁ structure has been prepared in a molten CuCl flux at 665 °C for 1 h and is a low-temperature polymorph of the rhombohedral Cu₂Ta₄O₁₁ (β -Cu₂Ta₄O₁₁) (space group $R\bar{3}c$ $a = 6.2190(2)$ Å, $c = 37.107(1)$ Å) structure. The monoclinic α -Cu₂Ta₄O₁₁ structure is found at 223 K and 298 K in an inert atmosphere. The monoclinic α -Cu₂Ta₄O₁₁ is structurally similar to the rhombohedral β -Cu₂Ta₄O₁₁, and is composed of single layers of a distorted edge-shared TaO₇ and TaO₆ polyhedra alternating with layers of linearly coordinated Cu(I) cations and isolated TaO₆ octahedra. The symmetry-lowering distortions from the rhombohedral β -Cu₂Ta₄O₁₁

into the monoclinic α -Cu₂Ta₄O₁₁ are similar to second-order Jahn-Teller effects arising from the out-of-center displacement of Ta 5 d^0 cations in the edge-shared TaO₇ pentagonal bipyramid layer. The UV-vis diffuse reflectance spectra of the monoclinic α -Cu₂Ta₄O₁₁ shows a higher-energy direct band gap transition at ~2.71 eV and lower-energy indirect band gap transition at ~2.6 eV. Photoelectrochemical measurements on polycrystalline films of α -Cu₂Ta₄O₁₁ produced strong cathodic photocurrents ~1.5 mA/cm² under A.M. 1.5 G solar irradiation.

INTRODUCTION

The growth and design of metal-oxide semiconductors with intriguing properties is a vast area of research.¹⁻⁵ Synthetic optimization of complex oxides is a current challenge for a number of chemical systems, it is achievable using a combination of synthetic techniques such as hydrothermal synthesis, solid-state synthesis, and molten-salt flux synthesis methods, which are essential for the tailored crystal growth of metal-oxides.⁶⁻¹⁰ The flux synthesis method is a versatile and advantageous technique for the modification of particle characteristics, such as particle sizes, particle morphologies, surface features, and the high-purity synthesis of polycrystalline phases.¹¹ Further, the flux synthesis approach has been shown to yield lower reaction rates and temperatures, increased product homogeneity and lower the activation barrier for the growth of thermodynamically unstable phases.¹²⁻¹⁴ Synthetic modifications of metal-oxides can be used to alter the physical properties, such as the catalytic, optical, and electronic properties. For example, the Na_{2-x}Cu_xTa₄O₁₁ solid-solution displayed a significant redshift in the band gap energy from ~4.0 eV to ~2.65 eV as Cu(I) cations were inserted into the structure in place of the Na(I) cations.¹⁵

The Maggard research group has investigated the high-purity syntheses of several Cu(I)-M(V) (M = V, Nb, Ta) oxides using the solid state and molten-salt flux method, which includes Cu_3VO_4 ¹⁶, CuNb_3O_8 ¹⁷, $\text{Cu}_2\text{Nb}_8\text{O}_{21}$ ¹⁸, $\text{Cu}_3\text{Ta}_7\text{O}_{19}$ ¹⁹, and $\beta\text{-Cu}_2\text{Ta}_4\text{O}_{11}$ ²⁰. Although, the flux method is not required for the crystal growth of CuNb_3O_8 ; in the absence of CuCl as a molten salt, the solid-state reaction can take up to 48 h at a temperature of 750 °C with impurities from unreacted reagents.²¹ The introduction of a CuCl flux with a low melting point (~426 °C) has been reported to reduce the reaction time to 15 min at the same temperature and yields CuNb_3O_8 in high purity.¹⁷ The metastable $\text{Cu}_2\text{Nb}_8\text{O}_{21}$ phase requires the use of highly reactive and high-surface-area nanoparticle reactants in the presence of a CuCl flux at temperatures up to 550 °C.¹⁸ The rod-shaped multi-faceted single crystals can grow up to ~80 μm in the presence of a CuCl flux. Also, the high purity synthesis of the Cu(I)-tantalate phase, $\text{Cu}_3\text{Ta}_7\text{O}_{19}$, requires the use of a CuCl flux to facilitate crystal growth at 700 °C for 24 h, while the flux is not required for the growth of the high purity crystal growth of the $\text{Cu}_5\text{Ta}_{11}\text{O}_{30}$ phase.^{19,22} The Cu(I)-containing niobates and tantalate mentioned above have shown promise as visible light active *p*-type photoelectrodes for the conversion of solar energy into chemical fuels.²³ The reported band gap energy sizes of the Cu(I)-M(V) (M = V, Nb, Ta) oxides listed above are between ~1.1 eV to ~2.7 eV and polycrystalline films of the metal-oxides with increased *p*-type dopants have demonstrated cathodic photocurrents up to ~2.0 mA/cm².

The $\text{Cu}_2\text{Ta}_4\text{O}_{11}$ phase was first discovered in a very small quantity during a high resolution electron microscopy (HREM) investigation of the solid-state products for phases in the Cu_2O - Ta_2O_5 system in the temperature range of 700 °C to 1100 °C.^{24,25} Recently, the rhombohedral $\beta\text{-Cu}_2\text{Ta}_4\text{O}_{11}$ phase was prepared in high purity and, required the presence of a

CuCl flux in the temperature range of 625 °C to 700 °C.²⁰ The limited thermal stability of the rhombohedral β -Cu₂Ta₄O₁₁ has made the high-purity synthesis of the Cu(I)-tantarate challenging. This compound has been previously reported as a member of a family of related structures with the general composition $A^{m+}_{(n+1)/m}M_{3n+1}O_{(8n+3)}$ (e.g., A = Ag¹⁺, Na¹⁺, Cu¹⁺, Ca²⁺, Y³⁺; M = Ta, Nb), that contains single ($n = 1$) and/or double ($n = 2$) layers of MO₇ polyhedra alternating with a layer of isolated MO₆ polyhedra.^{26,27} Described herein is the structural characterization of the symmetry lowering distortion of Cu₂Ta₄O₁₁. The newest member in the Copper(I)-tantarate family, the monoclinic α -Cu₂Ta₄O₁₁, was prepared using a flux-mediated crystal growth technique, the thermal stability, optical and photoelectrochemical properties of the metal-oxide semiconductor were examined.

EXPERIMENTAL

A. Materials and Synthesis. The nanoparticle Cu₂O and Ta₂O₅ reactants were prepared according to previously reported procedures.^{28,29} The Ta₂O₅ (Alfa Aesar, 99.999%) reagents were used as received. Reactions targeting the monoclinic α -Cu₂Ta₄O₁₁ phase were performed by combining nanoparticle Cu₂O and Ta₂O₅ in a 2:1 molar ratio, respectively, and mixing with a CuCl flux in a 10:1 flux-to-reactant molar ratio. The reactants and flux were well-ground together inside a N₂-filled glovebox, sealed within an evacuated fused-silica tube, and heated at 665 °C for 1 h. The reaction vessel was then quenched in air immediately upon completion of the heating cycle. The products were repeatedly washed with concentrated ammonium hydroxide and deionized water in order to remove the CuCl flux. Minor impurities from the starting reagent Ta₂O₅ ($\leq 5\%$) were observed in the powder X-ray diffraction patterns of the obtained product.

B. Bulk Characterization Techniques. Powder X-ray diffraction data were collected on a Bruker D8 Advanced Powder diffractometer configured in Bragg Brentano

geometry with a Lynxeye XE detector and collected on an INEL diffractometer using Cu K_α ($\lambda = 1.54056 \text{ \AA}$). Data were collected in a 2θ range of $10\text{-}80^\circ$ in 0.01 steps with a dwell time of 4 s at each step. The Rietveld structure refinement of $\alpha\text{-Cu}_2\text{Ta}_4\text{O}_{11}$ at 298 K used single crystal data of $\alpha\text{-Cu}_2\text{Ta}_4\text{O}_{11}$ collected on a Bruker-Nonius X8 Apex2 diffractometer using Mo K_α radiation ($\lambda = 0.70926 \text{ \AA}$) (monoclinic crystal class Cc , 9) as the starting model in the Rietveld and lattice constant refinements for powder data collected at 223 K and 298 K , on the GSAS-II software program.³⁰ The reported rhombohedral $\beta\text{-Cu}_2\text{Ta}_4\text{O}_{11}$ structure was used as the calculated structures for the lattice constant refinements at temperatures 523 K to 723 K .²⁰ The refinement strategy was implemented as follows. The scale factor, background (Chebyshev function with 4 terms), sample displacement and sample transparency, and unit cell were independently refined. The atomic positions were refined in order of decreasing scattering length, followed by the refinement of isotropic temperature factors (U_{iso}). The U_{iso} values were fixed for O atoms, peak shape profile (Gaussian and Lorentzian terms) were refined. The occupancy factor for the Cu-sites were independently refined. The impurities of Ta_2O_5 were masked in the Rietveld refinements from 25.9° to 27.6° 2θ as indicated by the purple lines in the refinement profile. Selected data collection and refinement parameters for the refinement in the monoclinic $\alpha\text{-Cu}_2\text{Ta}_4\text{O}_{11}$ at 298 K is listed in Table 4.1 and interatomic distances are given in Table 4.2. A complete list of refined structural and atomic parameters, as well as a crystallographic information file, are included in Supporting Information, Table C1. The UV-Vis diffuse reflectance spectra of $\alpha\text{-Cu}_2\text{Ta}_4\text{O}_{11}$ were collected on a Shimadzu UV-Vis-NIR Spectrophotometer (UV-3600) equipped with an integrating sphere. The data were plotted as the remission function $F(R_\infty) = (1-R_\infty)^2/(2R_\infty)$, where R is the diffuse reflectance based on the Kubelka-Munk theory.^{31,32} The reflectance data were analyzed in

the form of Tauc plots as $[F(R) \times hv]^n$ versus hv , where $n = 2$ for direct allowed transitions and $n = 1/2$ for indirect allowed transitions.^{33,34} The optical bandgap sizes were estimated from the onset of absorption, as extrapolated from the linear section of the curve that intersects with the baseline.

C. Photoelectrochemical Investigation. Polycrystalline films of α -Cu₂Ta₄O₁₁ were prepared on TEC-15 fluorine doped tin oxide (FTO) slides (Hartford Glass Inc.). First, FTO slides are sonicated in de-ionized water, followed by ethanol and acetone for 30 min each and dried in air in an oven set to 80 °C. A 1 cm² area was taped off using Scotch tape on the conducting side of the FTO, and a slurry of Cu₂Ta₄O₁₁ in a water/tert-butanol solution was deposited using the doctor blade method. The films were annealed under dynamic vacuum ($P < 50$ mTorr) at 500 °C for 3 h to allow particles to sinter. After the annealing process, films were heated to various temperatures for 3 h each. The polycrystalline films were examined as photoelectrodes in a photoelectrochemical cell. The linear sweep voltammetry (LSV) measurements were taken on a CH-Instruments CH620a potentiostat under chopped simulated AM 1.5 G irradiation at 100 mW/cm² (Oriel) using a scan rate of 0.0250 Vs⁻¹. Chronoamperometric measurements were taken at the short circuit condition ($V = 0.0$) for 1000 s each. The polycrystalline films served as the working electrodes, Pt foil as the counter electrode and an SCE (sat. KCl) electrode served as the reference electrode during the measurements. A 0.5 M Na₂SO₄ solution adjusted to pH 6.5 using diluted H₂SO₄ was prepared for each photoelectrochemical measurement. This solution was purged with N₂ gas for 30 min prior to, and during photoelectrochemical measurements to remove any dissolved O₂ in the electrolyte solution.

D. Electronic Structure Calculations. Electronic structure calculations were performed on the geometry-optimized α -Cu₂Ta₄O₁₁ monoclinic crystal structure using plane-wave density functional theory (DFT) within the Vienna Ab initio Simulation Package (VASP; ver. 4.6).^{35–38} The band-structure diagram and the densities-of-states calculations were performed using the Perdew-Burke-Ernzerhof (PBE) functional in the generalized gradient approximation (GGA), using the projector augmented wave (PAW) method and automatic sampling of the Brillouin-zone was performed using a $2 \times 2 \times 1$ Monkhorst-Pack grid.³⁹ The Cu deficiencies were simulated by the random distribution of Cu-site vacancies throughout the unit cell. The band structure calculation followed the standard k -path of special k -points through the Brillouin group for a monoclinic unit cell.⁴⁰

RESULTS AND DISCUSSION

A. Synthesis and Structure. The monoclinic α -Cu₂Ta₄O₁₁ phase has been synthesized using nanoparticle precursor reactants in a 2:1 (Cu₂O:Ta₂O₅) molar ratio at 665 °C for 1 h in a molten CuCl flux (10:1 flux-to-reactant molar ratio) and immediately quenched in air upon completion of reaction. The flux was removed using concentrated NH₄OH and, the resulting products were washed with deionized water and dried overnight at 80 °C. High-surface-area nanoparticle Cu₂O and Ta₂O₅ precursors were required for the flux synthesis of α -Cu₂Ta₄O₁₁. In the absence of the nanoparticle precursors, impurities of Ta₂O₅ ~20% resulted therefore, the highly reactive reagent powders are necessary in order to stabilize the monoclinic α -Cu₂Ta₄O₁₁ phase and minimize impurities. The crystallization of β -Cu₂Ta₄O₁₁ in the rhombohedral space group, $R\bar{3}c$, requires an additional heating cycle of synthesized products at 665 °C for 1 h in excess Cu₂O and a CuCl flux. A powder X-ray data set collected at room temperature was refined in a monoclinic space group with unit cell parameters of ($a = 10.7337(14) \text{ \AA}$, $b = 6.2506(3) \text{ \AA}$, $c = 12.8869(14) \text{ \AA}$, $\beta = 106.070(4)^\circ$) at

298 K, as shown in Figure 4.1. The refinement of the data was unsuccessful in the monoclinic space group $C2/c$ where a goodness-of-fit and W_R resulted as 15.2 and 25%. Thus, the monoclinic Cc space group was employed and 2.5 goodness-of-fit and 5.4% W_R values resulted. Data collection, refinement parameters, and selected interatomic distances are listed in Tables 4.1 and 4.2, and are consistent with the previously reported Cu(I)-tantalate structures. A Rietveld Refinement analysis of the monoclinic α - $\text{Cu}_2\text{Ta}_4\text{O}_{11}$ at 223 K is included in the Supporting Information, Figure C1. The monoclinic crystal structure of α - $\text{Cu}_2\text{Ta}_4\text{O}_{11}$ is composed of alternating layers of linearly coordinated Cu atoms, isolated TaO_6 octahedra that are apically bridged to O atoms in a single layer of a distorted edge-shared layers of TaO_6 and TaO_7 polyhedra, as shown in Figure 4.2. The apical oxygen atoms of the TaO_7 pentagonal bipyramids construct the isolated TaO_6 octahedra with interatomic distances from 1.91(7) Å to 2.11(8) Å as shown in the Supporting Information, Figure C2. The monoclinic α - $\text{Cu}_2\text{Ta}_4\text{O}_{11}$ phase consists of three symmetry unique Ta sites (Ta1, Ta2, Ta3) with interatomic distances in the range of 1.92(8) Å to 2.45(8) Å, and are consistent with the bond distances observed for the rhombohedral β - $\text{Cu}_2\text{Ta}_4\text{O}_{11}$, as shown in Figure 4.3. The three symmetrically inequivalent Cu-sites in the monoclinic α - $\text{Cu}_2\text{Ta}_4\text{O}_{11}$ unit cell (Cu1, Cu2, Cu3) have bond distances that are in the range of 1.71(8) Å to 2.01(9) Å. A crystal structure of a layer of isolated TaO_6 octahedra bridged to linearly coordinated Cu(I) cations is shown in the Supporting Information, Figure C3.

The $\text{Cu}_2\text{Ta}_4\text{O}_{11}$ structure is a member in a family of previously reported Cu(I)-tantalates that are constructed with α - U_3O_8 type layers. These structures contain single ($n = 1$) and/or double ($n = 2$) layers of edge-shared TaO_7 pentagonal bipyramids that alternate with layers of isolated TaO_6 octahedra surrounded by the A-site cations. The occupancy of

the Cu-site is 66.7% for the rhombohedral β -Cu₂Ta₄O₁₁, where ($n = 1$) is occupied in order to satisfy the charge-balancing requirements of the desired neutral composition, as full occupation of this site would result in the undesired Cu₃Ta₄O₁₁ composition. Higher Cu-site occupancies are found in the related Copper(I)-tantarate structures of Cu₅Ta₁₁O₃₀ (83%) where ($n = 1.5$) and Cu₃Ta₇O₁₉ (100%) where ($n = 2$). The symmetry-lowering distortion of the rhombohedral β -Cu₂Ta₄O₁₁ into the monoclinic α -Cu₂Ta₄O₁₁ has not been observed in the related Copper(I)-tantarate mentioned above however, this transition has been reported for a related member of the α -U₃O₈-layer type of structures, Na₂Nb₄O₁₁.⁴¹

B. Symmetry-Lowering Distortions in Cu₂Ta₄O₁₁. The relationship between the structural transformation observed for the monoclinic and hexagonal-rhombohedral unit cells has been reported previously, and are illustrated in the Supporting Information, Figure C3.^{27,41,42} Masó et. al reported the layered niobates, Ag₂Nb₄O₁₁ and Na₂Nb₄O₁₁, as the only structures to exhibit a phase transition within the family of related structures in arrangement of alternating single layers of edge-shared pentagonal bipyramids and octahedra.⁴³ Furthermore, they comment on the tendency for niobates rather than tantalates to exhibit ferroelectric polymorphism, due to the differences in the unit cell volumes, octahedron sizes and interatomic distances. For example, the c lattice parameter, unit cell volume, and Ta-O interatomic distances of Ag₂Ta₄O₁₁ were shorter in comparison to Ag₂Nb₄O₁₁. The Ag₂Nb₄O₁₁ displays a polar non-centrosymmetric phase transition from a structure in the rhombohedral space $R\bar{3}c$ to $R3c$ upon cooling. The driving force for the symmetry-lowering polar distortion observed in Ag₂Nb₄O₁₁ can be attributed to atomic displacements of the Nb cations in NbO₇ pentagonal bipyramids towards apical O atoms, and the Ag cations in AgO₆ octahedra toward octahedral faces along the c direction of the rhombohedral unit cell.

By contrast, $\text{Na}_2\text{Nb}_4\text{O}_{11}$ exhibits a non-polar centrosymmetric distortion from the $R\bar{3}c$ to $C2/c$ space group upon cooling due to the smaller unit cell dimensions and shorter Na-O1 interatomic distances (2.510(3) Å) in a NaO_7 polyhedron comparatively, the Ag cation in $\text{Ag}_2\text{Nb}_4\text{O}_{11}$ is coordinated to three O1 atoms at a longer distance (2.6503(14) Å) in the octahedron. A comparison of the c lattice parameter, unit cell volumes and Nb/Ta-O interatomic distances of the $\text{Na}_2\text{Nb}_4\text{O}_{11}$, $\text{Ag}_2\text{Nb}_4\text{O}_{11}$, $\text{Ag}_2\text{Ta}_4\text{O}_{11}$, and $\text{Cu}_2\text{Ta}_4\text{O}_{11}$ rhombohedral structures indicate striking similarities between $\text{Na}_2\text{Nb}_4\text{O}_{11}$, $\text{Ag}_2\text{Nb}_4\text{O}_{11}$, and $\text{Cu}_2\text{Ta}_4\text{O}_{11}$. The Cu-(I) cation in $\text{Cu}_2\text{Ta}_4\text{O}_{11}$ adopts a linear coordination owing to the smaller crystal radius ~ 0.6 Å with significantly shorter Cu-O interatomic distances (1.71(8) Å to 2.01(9) Å). The rhombohedral β - $\text{Cu}_2\text{Ta}_4\text{O}_{11}$ structure displays an out-of-center displacement of the Ta $5d^0$ cation in the edge-shared TaO_7 pentagonal bipyramid layer, and is shown in Figure 4.4. The symmetry transformation of the atoms in $\text{Cu}_2\text{Ta}_4\text{O}_{11}$ from the rhombohedral $R\bar{3}c$ to a monoclinic Cc unit cell are as follows: Cu1 \rightarrow Cu1, Cu2, Cu3; Ta1 \rightarrow Ta1, Ta2, Ta3; Ta2 \rightarrow Ta4; O1 \rightarrow O1, O11; O2 \rightarrow O4, O5, O7, O8, O9, O10; O3 \rightarrow O2, O3, O6.

The tendency for symmetry-lowering transitions of d^0 cations in an octahedral coordination are known to occur as a result of a second-order Jahn-Teller effects.⁴⁴ The driving force for a second-order Jahn-Teller distortion is expected to increase as the energy separation between the t_{2g} orbitals and the non-bonding O $2p$ states in the HOMO and LUMO decrease.⁴⁵ The second order Jahn-Teller distortions have typically been reported and observed for octahedral d^0 cations with high valency and the magnitude of the distortion increases in the following sequence: $\text{Zr}^{4+} < \text{Ta}^{5+} < \text{Nb}^{5+} < \text{W}^{6+} < \text{V}^{5+} < \text{Mo}^{6+}$.⁴⁵ To the best of our knowledge, there are not any examples in the literature of a second-order Jahn-Teller effect of Ta $5d^0$ in an arrangement of alternating layers of pentagonal bipyramid and

octahedral environments therefore, $\text{Cu}_2\text{Ta}_4\text{O}_{11}$ is the first case of a Cu(I)-containing tantalate which displays a symmetry-lowering structural distortion. A possible explanation for the uncommon phase transition observed in $\text{Cu}_2\text{Ta}_4\text{O}_{11}$ can be observed in the Ta-O bond lengths. The Ta-O bond distance in the TaO_6 octahedron are slightly larger, in the range of 1.92(7) to 2.20(6) Å, than in $\text{Ag}_2\text{Ta}_4\text{O}_{11}$, of 1.9845(5). Also, the longer distance in the equatorial plane of edge-shared pentagonal bipyramids is also slightly larger for Ta1-O3 in $\text{Cu}_2\text{Ta}_4\text{O}_{11}$ as compared to $\text{Ag}_2\text{Ta}_4\text{O}_{11}$ of 2.45(8) Å and 2.3983(18) Å, respectively. The orbital interactions between a metal-oxygen bond with shorter distances are stronger, thus less likely to distort out of place and displace the cation as observed for $\text{Ag}_2\text{Ta}_4\text{O}_{11}$. The longer Ta-O interatomic distances observed in TaO_6 and TaO_7 polyhedra in $\text{Cu}_2\text{Ta}_4\text{O}_{11}$ are comparable to the Nb-O bond distances in $\text{Na}_2\text{Nb}_4\text{O}_{11}$ and $\text{Ag}_2\text{Nb}_4\text{O}_{11}$, thus a distorted environment is likely to occur due to the out-of-center displacement of the Ta/Nb cations. Goodenough and Longo described the displacement of a d^0 cation in an octahedral coordination environment may occur rhombohedrally along the C_3 axis.⁴⁶ Kunz and Brown reported the direction of the displacement of the d^0 cation is not determined from the electronic second-order Jahn-Teller effect.⁴⁷ By using bond-valence arguments, they were able to conclude the preferential direction of out-of-center cation displacement is influenced by bond network stresses (e.g. asymmetry in the bond network from nearest neighbors) and cation-cation repulsions from near neighbor cations that share edges or faces. For example, the tendency of V^{5+} to favor a distorted environment is observed in the ZnV_2O_6 structure, an asymmetrical bond network, leading to the displacement of the V d^0 cation and contributing to the effects of the second-order Jahn-Teller distortion. In the rhombohedral β - $\text{Cu}_2\text{Ta}_4\text{O}_{11}$ structure, effects from cation-cation repulsion cause the nearest neighbor Ta $5d^0$

cation in the edge-shared TaO₇ pentagonal bipyramid layer to move out of the center of the polyhedron. Furthermore, the preferential direction of the out-of-center displacement of the Ta cations is towards the vertex of the polyhedron not shared by a neighboring Ta cations, and is shown in Figure 4.5. Thus, the repulsion from nearest neighbor cations is shown to direct the out-of-center displacement of Ta d^0 cations towards an edge of the polyhedron that is not shared by a neighboring Ta cation in the rhombohedral β -Cu₂Ta₄O₁₁ structure.

The distortion of the rhombohedral β -Cu₂Ta₄O₁₁ has also been reported to occur after exposing a powder sample to room temperature conditions for ~ 6 weeks.²⁰ The effects of the cation-cation repulsions in the TaO₇ pentagonal bipyramid layer direct the displacement of the Ta $5d^0$ cation towards an edge that is not shared. As a result of the out-of-center displacement, the rhombohedral β -Cu₂Ta₄O₁₁ structure transformation into the monoclinic α -Cu₂Ta₄O₁₁ occurs. The TaO₇ pentagonal bipyramid layer distorts into a layer containing TaO₆ and TaO₇ polyhedra where Ta₃ and Ta₁ maintains the TaO₇ pentagonal bipyramid coordination environment, and Ta₂ distorts into a TaO₆ octahedron. In the monoclinic α -Cu₂Ta₄O₁₁ structure fewer edges are shared as the Ta₂ and O₂ interatomic distance lengthens to 2.55(3) Å, an increase of ~0.13 Å as compared to the rhombohedral β -Cu₂Ta₄O₁₁ structures as shown in Figures 4.3 and 4.4, respectively. The interatomic distances change in the isolated TaO₆ octahedron and linearly coordinated Cu(I)-cations are also listed in Table 4.2.

C. Thermal Decomposition of α -Cu₂Ta₄O₁₁. The phase transformation of the monoclinic α -Cu₂Ta₄O₁₁ into the rhombohedral phase β -Cu₂Ta₄O₁₁ was investigated in the temperature range of 223 K to 723 K in an inert atmosphere. A powder XRD analysis of the phase transformation the monoclinic α -Cu₂Ta₄O₁₁ shown in Figure 4.6, and indicates the

transformation of the monoclinic α -Cu₂Ta₄O₁₁ into the rhombohedral β -Cu₂Ta₄O₁₁ by at least 523 K. At temperatures above 523 K, the powder XRD analysis indicates the rhombohedral β -Cu₂Ta₄O₁₁ structure is stable. The lattice constants of the monoclinic α -Cu₂Ta₄O₁₁ as it transforms into the rhombohedral β -Cu₂Ta₄O₁₁ are listed in the Supporting Information, Table C2. The lattice constant refinements were analyzed in order to give new insights of the phase transition of the monoclinic α -Cu₂Ta₄O₁₁ into the rhombohedral β -Cu₂Ta₄O₁₁ at increasing temperatures. At temperatures 223 K and 298 K the monoclinic the a , b , c , and β , lattice constants and unit cell volume decreases as the temperature increase from 223 K to 298 K. The trend is further observed for the lattice constant refinements and the unit cell volume of the rhombohedral β -Cu₂Ta₄O₁₁ as the temperature increases from 523 K to 723 K. Upon heating α -Cu₂Ta₄O₁₁ from 523 K to 623 K, a change in color results from a yellowish to a tannish. This observation is consistent with the change in color observed after the in air heating of Cu₅Ta₁₁O₃₀, and the formation of Cu-deficient structure, Cu_{5-x}Ta₁₁O₃₀.⁴⁵ Previous investigations of the thermal instability of Cu₅Ta₁₁O₃₀ and CuNb₃O₈ reported the extrusion of Cu(I) and the formation of CuO nanoparticles on the surfaces of the particles heated at temperatures of 450 °C and 550 °C for 3 h.^{17,48} Further, the extrusion of Cu(I) at the temperatures of 550 °C leads to increased Cu-site vacancies in the unit cell and the emergence of an ‘O–’ species at the heated surface. Ongoing efforts and studies are underway to determine if the formation of CuO occurs after the transition of α -Cu₂Ta₄O₁₁ into β -Cu₂Ta₄O₁₁.

D. Optical and Photoelectrochemical Properties. The optical band gap and photoelectrochemical properties of the monoclinic α -Cu₂Ta₄O₁₁ semiconductor were examined in order to establish and compare the cathodic photocurrent of Cu₂Ta₄O₁₁ to the

previously known members of the Cu(I)-tantalate family, $\text{Cu}_5\text{Ta}_{11}\text{O}_{30}$ and $\text{Cu}_3\text{Ta}_7\text{O}_{19}$. The visible-light absorbing *p*-type semiconductors $\text{Cu}_5\text{Ta}_{11}\text{O}_{30}$ and $\text{Cu}_3\text{Ta}_7\text{O}_{19}$, have reported band gap energies of ~ 2.6 eV and ~ 2.5 eV, respectively. The UV-visible diffuse reflectance data for the monoclinic $\alpha\text{-Cu}_2\text{Ta}_4\text{O}_{11}$ were calculated and analyzed as Tauc plots of $(F(R)h\nu)^n$ versus $h\nu$ ($h\nu$ = photon energy), as shown in Figure 4.6. A direct band gap transition of ~ 2.71 eV and indirect band gap transitions ($n = 1/2$) of ~ 2.61 eV were observed. The observed band gap energies of $\alpha\text{-Cu}_2\text{Ta}_4\text{O}_{11}$ are comparable to the reported bandgap energies of the rhombohedral $\beta\text{-Cu}_2\text{Ta}_4\text{O}_{11}$ phase.

The photoelectrochemical properties of $\text{Cu}_2\text{Ta}_4\text{O}_{11}$ were investigated in order to confirm the cathodic nature of the semiconductor under simulated A.M. 1.5 G solar irradiation. The polycrystalline films of $\alpha\text{-Cu}_2\text{Ta}_4\text{O}_{11}$ were annealed under vacuum at 550 °C for 3 h and heated in air at temperatures of 250 °C and 350 °C. The post-annealing heat treatments of Copper(I)-tantalates $\text{Cu}_5\text{Ta}_{11}\text{O}_{30}$ and $\text{Cu}_3\text{Ta}_7\text{O}_{19}$ have shown to increase *p*-type dopant concentration of the semiconductor, thus improved conductivity and enhanced cathodic photocurrents have been observed. The linear sweep voltammetry and chronoamperometric measurements of the polycrystalline films of $\text{Cu}_2\text{Ta}_4\text{O}_{11}$ before heating and after heating at 250 °C and 350 °C for 3 h are shown in Figure 4.7 and in the Supporting Information, S5. The cathodic photocurrent density of $\alpha\text{-Cu}_2\text{Ta}_4\text{O}_{11}$ were increased from -0.25 mA/cm² up to -1.5 mA/cm² before and after heating in air, respectively. This has been previously reported for $\text{Cu}_5\text{Ta}_{11}\text{O}_{30}$ polycrystalline films and, has been attributed to CuO formation at the surface of these materials. To determine whether the enhanced photocurrents occur from the phase change of monoclinic $\alpha\text{-Cu}_2\text{Ta}_4\text{O}_{11}$ into rhombohedral $\beta\text{-Cu}_2\text{Ta}_4\text{O}_{11}$, the increase in *p*-type deficiencies or a combination of both, CuO was added to

the surface of a polycrystalline α -Cu₂Ta₄O₁₁ film by soaking the film in an ethanolic solution of Cu(NO₃)₂ and heating to 250 °C for 20 min. A control was also performed by heating a film at the same conditions, without adding CuO to the surface. Increased photocurrents were observed as CuO is added to the surface, however; the photocurrent densities were not as significant as observed for films heated to 350 °C as shown in Figure 4.8. This large difference in photocurrent may be due to the phase change of the material. Powder X-ray diffraction was used to characterize the solid powders after photoelectrochemical measurements and is shown in the Supporting Information, Figure C6.

E. Electronic Structure Calculations. The electronic structure calculations were performed using density-functional-theory methods for the refined α -Cu₂Ta₄O₁₁ structure using the crystal structure from the powder X-ray Rietveld refinement at 298 K. The band structure diagram for the monoclinic α -Cu₂Ta₄O₁₁ was calculated using density functional theory (DFT), and the special *k*-path for the monoclinic unit cell was evaluated with the Fermi level outlined as a dashed line, as shown in the Supporting Information, S7. The band structure diagram indicates a direct band gap transition along the Γ point and two lower-energy indirect band gap transitions occur from the Γ point to the E, X, and M points. The electron densities are plotted within the range of 0.75 eV of the uppermost region the valence band and 0.1 eV the lowermost region of the conduction band, as shown in Figure 4.9. The highest-energy valence band states arise from the filled Cu 3*d*¹⁰ orbital contributions, while the lowest-energy conduction band states are composed of empty Ta 5*d*⁰ orbital contributions. The plots of electron density in the valence band as shown in Figure 4.9 indicate the delocalization of electron density over the Cu atoms with some contributions of electron density from the O 2*p* orbitals within the layer. The electron density within the

lower-energy states of the conduction band in Figure 4.9 are composed of orbital contributions from the empty Ta $5d$ orbitals found in the two layers containing isolated TaO₆ octahedra and TaO₇ pentagonal bipyramid layers and small contributions from the O $2p$ orbitals located on TaO₆ octahedra. The calculated densities-of-states, with the Fermi level (E_f) indicated by a dashed line, further support the origins of the projected electron densities from the uppermost valence band states and the lower-most conduction band states that arise from the filled Cu $3d^{10}$ and empty Ta $5d^0$ orbitals, respectively (supporting information, Figures C8).

CONCLUSIONS

The α -Cu₂Ta₄O₁₁ phase was prepared with highly reactive Cu₂O and Ta₂O₅ nanoparticles in a CuCl flux at 665 °C for 1 h and characterized by Rietveld refinement. The structure is composed of alternating layers of distorted edge-shared TaO₆ and TaO₇ polyhedra coordinated to layers of linearly coordinated Cu(I) atoms and isolated TaO₆ octahedra. The Cu₂Ta₄O₁₁ structure distorts from a rhombohedral $R\bar{3}c$ space group and crystallizes in a polar non-centrosymmetric monoclinic Cc space group. The Cu₂Ta₄O₁₁ is the first case of a Ta $5d^0$ cation arranged in alternating layers of pentagonal bipyramids and octahedra to exhibit a symmetry lowering distortion. The structural distortion is similar to a second-order Jahn-Teller effect, and the origin of the distortion is due to an out-of-center displacement of the nearest-neighbor Ta cations in the layer of edge-shared TaO₇ polyhedra. The α -Cu₂Ta₄O₁₁ phase is thermally unstable by at least 523 K and transforms into the rhombohedral β -Cu₂Ta₄O₁₁. The UV-vis diffuse reflectance spectra of α -Cu₂Ta₄O₁₁ exhibits a direct band gap transition of ~2.7 eV and a lower-energy indirect band gap transitions at ~2.6 eV. The visible light absorbing semiconductor is p -type, and produces cathodic

photocurrents up to ~ 1.5 mA/cm² under A.M. 1.5 G irradiation. Thus, these new results may provide insights for the stabilization of metastable Cu(I)-containing compositions, and the out-of-center displacements of Ta 5 d^0 cations in a rhombohedral unit cell.

SUPPORTING INFORMATION. The crystallographic information file of α -Cu₂Ta₄O₁₁ at 298 K are included in the Supporting Information. The crystal structure of the relationship between the monoclinic and hexagonal-rhombohedral unit cell transformation, and the local coordination view of the out-of-center displacement of Ta cations as the monoclinic α -Cu₂Ta₄O₁₁ 298 K are available. Photoelectrochemical measurements of Cu₂Ta₄O₁₁ are included as well.

ACKNOWLEDGEMENTS. The authors would like to thank Dr. Roger D. Sommer at North Carolina State University for the single crystal data collection of the monoclinic α -Cu₂Ta₄O₁₁.

REFERENCES

- (1) Cheng, X. H.; Xu, H. F.; Wang, Z. Z.; Zhu, K. R.; Li, G.; Jin, S. *Mater. Res. Bull.* **2013**, *48*, 3383–3388.
- (2) Rao Popuri, S.; Artemenko, A.; Labrugere, C.; Miclau, M.; Villesuzanne, A.; Pollet, M. *J. Solid State Chem.* **2014**, *213*, 79–86.
- (3) Cui, Y. L. C. Y. J.; Cheng, Y. Z. C. H. *J. Supercond. Nov. Magn.* **2013**, *26*, 327–332.
- (4) Chen, H.; Leng, W.; Xu, Y. *J. Phys. Chem. C.* **2014**, *118*, 9982–9989.
- (5) Montanari, E.; Righi, L.; Calestani, G.; Migliori, A.; Gilioli, E.; Bolzoni, F.; Area, P. *Chem. Mater.* **2005**, *17*, 1765–1773.
- (6) Li, W.; Kong, D.; Cui, X.; Du, D.; Yan, T.; You, J. *Mater. Res. Bull.* **2014**, *51*, 69–73.
- (7) Wei, W.; Yue, X.; Cui, H.; Lü, X.; Xie, J. *J. Mater. Res.* **2013**, *28*, 3408–3416.
- (8) Boltersdorf, J.; Wong, T.; Maggard, P. A. *ACS Catal.* **2013**, *3*, 2943–2953.
- (9) Mclamb, N.; Sahoo, P. P.; Fuoco, L.; Maggard, P. A. *Cryst. Growth Des.* **2013**, *13*, 2322–2326.
- (10) Arney, D.; Maggard, P. A. *ACS Catal.* **2012**, *2*, 1711–1717.
- (11) Boltersdorf, J.; King, N.; Maggard, P. A. *CrystEngComm* **2015**, *17*, 2225–2241.
- (12) Arney, D.; Fuoco, L.; Boltersdorf, J.; Maggard, P. A. *J. Am. Ceram. Soc.* **2013**, *96*, 1158–1162.
- (13) Brazhkin, V. V. *Physics-USpekhi* **2006**, *49*, 719–724.
- (14) Kumar, V.; Gupta, A.; Uma, S. *Dalton Trans.* **2013**, *42*, 14992–14998.
- (15) Palasyuk, O.; Palasyuk, A.; Maggard, P. A. *Inorg. Chem.* **2010**, *49*, 10571–10578.
- (16) Sahoo, P. P.; Zoellner, B.; Maggard, P. A. *J. Mater. Chem. A* **2015**, *3*, 4501–4509.
- (17) King, N.; Sahoo, P. P.; Fuoco, L.; Stuart, S.; Dougherty, D.; Liu, Y.; Maggard, P. A. *Chem. Mater.* **2014**, *26*, 2095–2104.
- (18) Choi, J.; King, N.; Maggard, P. A. *ACS Nano* **2013**, *7*(2), 1699–1708.
- (19) Palasyuk, O.; Palasyuk, A.; Maggard, P. A. *J. Solid State Chem.* **2010**, *183*, 814–822.

- (20) Growth, C.; King, N.; Sommer, R. D.; Watkins-Curry, P.; Chan, J. Y.; Maggard, P. A. *Cryst. Growth Des.* **2015**, *15*, 552-558.
- (21) Joshi, U.; Maggard, P. A. *J. Phys. Chem. Lett.* **2012**, *3*, 1577–1581.
- (22) Fuoco, L.; Joshi, U. A.; Maggard, P. A. *J. Phys. Chem. C* **2012**, *116*, 10490–10497.
- (23) Joshi, U. A. **2014**, *174*, 97–112.
- (24) Jahnberg, L. Sundberg, M. *J. Solid State Chem.* **1992**, *100*, 212–219.
- (25) Jahnberg, L. *Acta Chem. Scand. A* **1987**, *41*, 527–532.
- (26) Jahnberg, L. *Mat. Res. Bull* **1981**, *16*, 513–518.
- (27) Jahnberg, L. *Chem. Comm.* **1971**, 1–41.
- (28) Zhang, X.; Song, J.; Jiao, J.; Mei, X. *Solid State Sci.* **2010**, *12*, 1215–1219.
- (29) Uekawa, N.; Kudo, T.; Mori, F.; Wu, Y. J.; Kakegawa, K. *J. Colloid. Interface Sci.* **2003**, *264*, 378–384.
- (30) Toby, B. H.; Von Dreele, R. B. *J. Appl. Cryst.* **2013**, *46*, 544–549.
- (31) Kortum, G. *Reflectance Spectroscopy*; Springer-Verlag: New York, NY, 1969.
- (32) Weckhuysen, B.M. Schoonhedt, R. A. *Catal. Today* **1999**, *49*, 441–451.
- (33) Tauc, J. *Mat. Res. Bull.* **1968**, *3*, 37–46.
- (34) Buchholz, D. B.; Liu, J.; Marks, T. J.; Zhang, M.; Chang, R. P. H. *ACS Appl. Mater. Interfaces* **2009**, *1*, 2147–2153.
- (35) Kresse, G. Hafner, J. *Phys. Rev. B.* **1994**, *49*, 14251–14269.
- (36) Kresse, G. Furthmuller, J. *Phys. Rev. B.* **1996**, *6*, 11169–11186.
- (37) Kresse, G. Furthmuller, J. *Comput. Mater. Sci.* **1996**, *6*, 6–15.
- (38) Kresse, G. Joubert, D. *Phys. Rev. B.* **1999**, *59*, 1758–1775.
- (39) Perdew, J.P. Burke, L. Ernzerhof, M. *Phys. Rev. Lett.* **1996**, *77*, 3865–3868.
- (40) Setyawan, W.; Curtarolo, S. *Comput. Mater. Sci.* **2010**, *49*, 299–312.

- (41) Masó, N.; Woodward, D. I.; Várez, A.; West, A. R. *J. Mater. Chem.* **2011**, *21*, 12096–12102.
- (42) Ercit, T. S. *Bull. Mineral.*, **1985**, *108*, 541-549.
- (43) Masó, N.; Woodward, D. I.; Thomas, P. a.; Várez, A.; West, A. R. *J. Mater. Chem.* **2011**, *21*, 2715–2722.
- (44) Halasyamani, P. S.; Poepelmeier, K. R. *Chem. Mater.* **1998**, *10*, 2753–2769.
- (45) Woodward, P. M.; Mizoguchi, H.; Kim, Y. I.; Stoltzfus, M. W. In *Metal Oxides: Chemistry and Applications*; 2005; Vol. 108, pp. 133–194.
- (46) Goodenough, J.B., Longo, J. M. *Crystallographic and magnetic properties of perovskite and perovskite-related compounds*; Hellewege, K.H., Hellewedge, A. M., Ed.; 4th ed.; Springer-Verlag: Berlin, 1970; pp. 126–314.
- (47) Kunz, M.; Brown, I. D. Out-of-Center Distortions around Octahedrally Coordinated d0 Transition Metals. *Journal of Solid State Chemistry*, 1995, *115*, 395–406.
- (48) Sullivan, I.; Sahoo, P. P.; Fuoco, L.; Hewitt, A. S.; Stuart, S.; Dougherty, D.; Maggard, P. A. *Chem. Mater.* **2014**, *16*, 6711-6721.

Table 4.1. Selected Rietveld Refinement Data for α -Cu₂Ta₄O₁₁.

Refined Formula	Cu ₂ Ta ₄ O ₁₁
Formula Weight (g/mol)	1030.69
Space Group, Z	<i>Cc</i> (9), 4
Crystal System	Monoclinic
Temperature (K)	298
Unit Cell (Å), <i>a</i>	10.7337 (14)
<i>b</i>	6.2506(3)
<i>c</i>	12.8869(14)
β	106.070
V (Å) ³	830.82(12)
No. of unique data collected	7005
No. of variables residuals ^a	R ₁ , [F _o >4 σ (F _o)], 0.0431
	wR = 0.09653
	wR _{exp} = 0.05447
Goodness-of-Fit	2.517
$R1 = [\sum F_o - F_c / \sum F_o \quad wR2 = [\sum [w(F_o - F_o^2)^2] / \sum wF_o^4]^{1/2}$ $w^{-1} = [\sigma(F_o^2) + (Ap)^2 + Bp] \quad p = [\max(F_o^2, 0) + 2F_c^2] / 3$	

Table 4.2. Selected Interatomic Distances for the Symmetry-Inequivalent Metal Sites in α - $\text{Cu}_2\text{Ta}_4\text{O}_{11}$ from the powder Rietveld refinement at 298 K.

Atom	Atom pair	Distance (Å)	$\Delta_{\text{dist}}^{\text{a}}$ (Å)	Atom	Atom pair	Distance (Å)	$\Delta_{\text{dist}}^{\text{a}}$ (Å)
Ta1, pentagonal bipyramid				Ta4, octahedron			
	Ta1-O1	2.10(8)	+0.106		Ta4-O4	2.20(4)	+0.21
	Ta1-O2	2.07(8)	+0.077		Ta4-O5	1.98(7)	-0.01
	Ta1-O3	2.12(6)	+0.092		Ta4-O7	1.99(8)	0.0
	Ta1-O4	1.98(7)	+0.006		Ta4-O8	2.08(10)	+0.09
	Ta1-O5	2.08(9)	+0.086		Ta4-O9	1.92(7)	-0.07
			+0.169		Ta4-O10	2.16(7)	+0.17
	Ta1-O6	2.19(5)		bvs	4.319		
	Ta1-O11	1.96(8)	-0.48				
bvs⁺	4.743						
Ta2, octahedron *							
	Ta2-O1	2.08 (7)	+0.059	Cu1, linear	Cu1-O5	1.96(9)	+0.055
	Ta2-O2	1.92(8)	-0.074		Cu1-O9	1.77(7)	-0.19
			+0.156	bvs	1.037		
	Ta2-O6	2.15(8)					
	Ta2-O9	2.11(8)	+0.138				
	Ta2-O10	1.91(7)	+0.068				
	Ta2-O11	2.06(8)	+0.034				
bvs	4.496						
				Cu2, linear	Cu2-O7	1.71(8)	-0.195
					Cu2-O8	1.78(9)	+0.105
Ta3, pentagonal bipyramid				bvs	1.114		
	Ta3-O1	2.12(7)	+0.099				
	Ta3-O2	2.45(4)	+0.01				
	Ta3-O3	2.07(5)	+0.077				
	Ta3-O6	1.98(7)	-0.013				
	Ta3-O7	1.95(8)	-0.22	Cu3, linear	Cu3-O4	1.71(8)	-0.195
			+0.108		Cu3-O10	2.01(9)	+0.105
	Ta3-O8	2.07(10)					

Table 4.2 Continued

bvs	Ta3-O11	1.99(8)	-0.031	bvs	1.102
	4.755				

*The Ta2-O2 atom pair is not bonded at 298 K in the monoclinic Cc space group, Ta2 distorts to an octahedron
^a Δ_{dist} (Å) is the difference between the interatomic distance as compared to the α -Cu₂Ta₄O₁₁ structure from the single crystal XRD structure refinement at 298 K for the rhombohedral $R\bar{3}c$.

[†]The bvs is the calculated bond valence sum

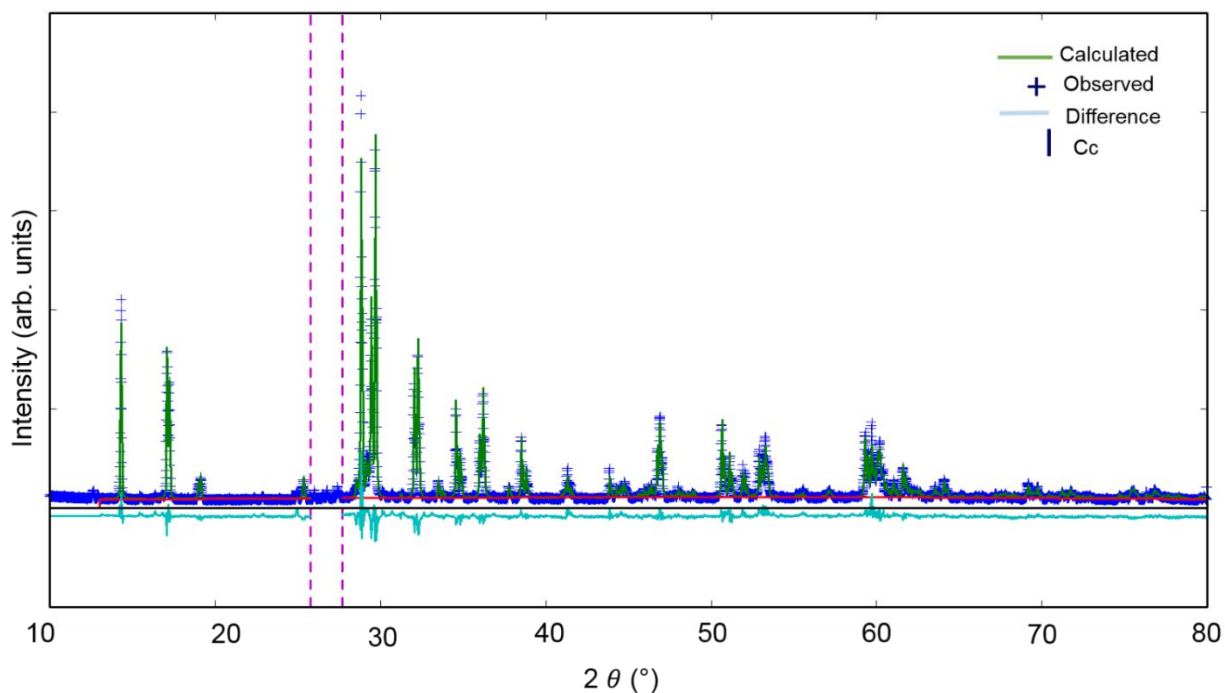


Figure 4.1. The Rietveld refinement pattern of the monoclinic α -Cu₂Ta₄O₁₁ at 298 K under flowing nitrogen. The observed intensities are indicated in blue (+), calculated intensities in green, the difference pattern is indicated by light blue, and the peak positions of α -Cu₂Ta₄O₁₁ in the monoclinic Cc space group are indicated by the blue tick marks. Impurities of Ta₂O₅ were masked as indicated by the purple lines.

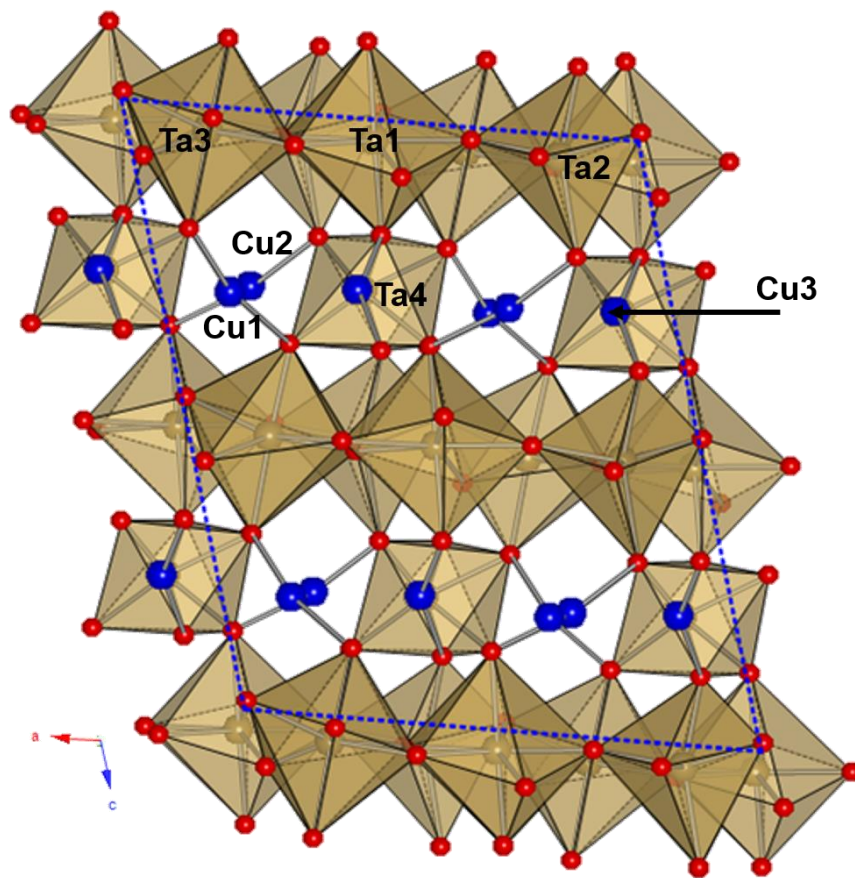


Figure 4.2. A crystal structure of α - $\text{Cu}_2\text{Ta}_4\text{O}_{11}$ at 298 K in the monoclinic Cc space group along the ac direction of the unit cell, outline in blue. The Cu and O atoms are in blue and red, respectively. The Ta cation and polyhedra are shown in tan.

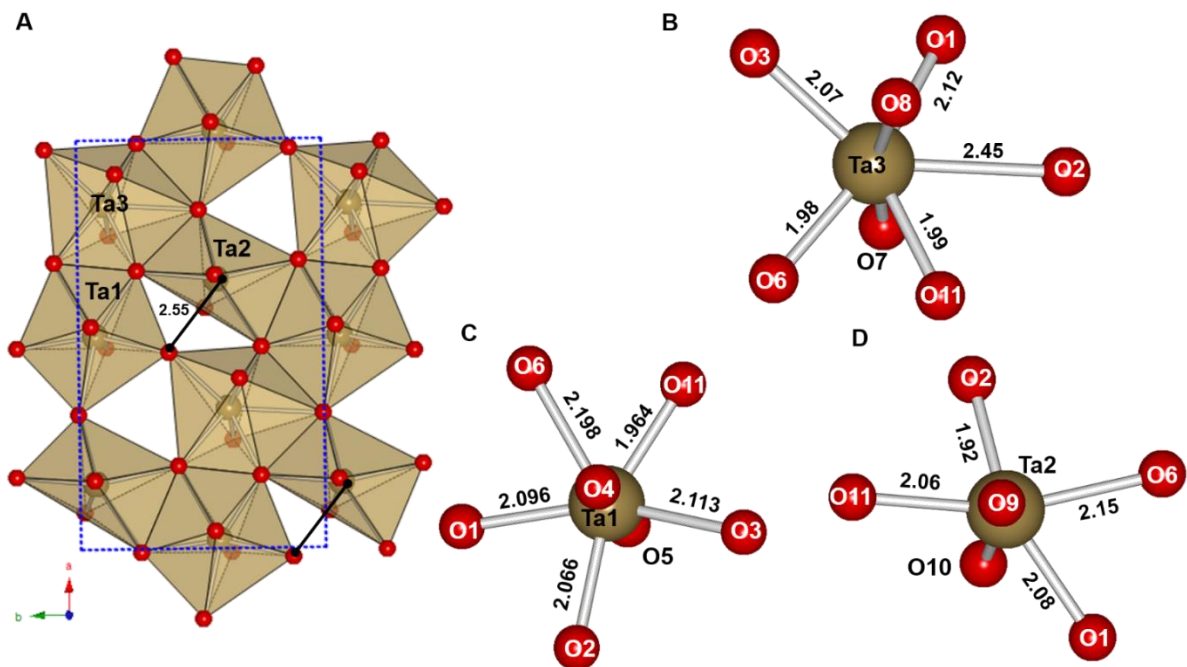


Figure 4.3. A crystal structure of a layer of edge-sharing TaO₇ in the pentagonal bipyramid layer of the monoclinic α -Cu₂Ta₄O₁₁ a) a view of the edge sharing of Ta cations along the ab plane with the unit cell outline in a blue dashed line, black line indicates the distortion of Ta2 into an octahedra in the edge-shared tantalate layer b-d) the local coordination environment of Ta3, Ta1 and Ta2, respectively.

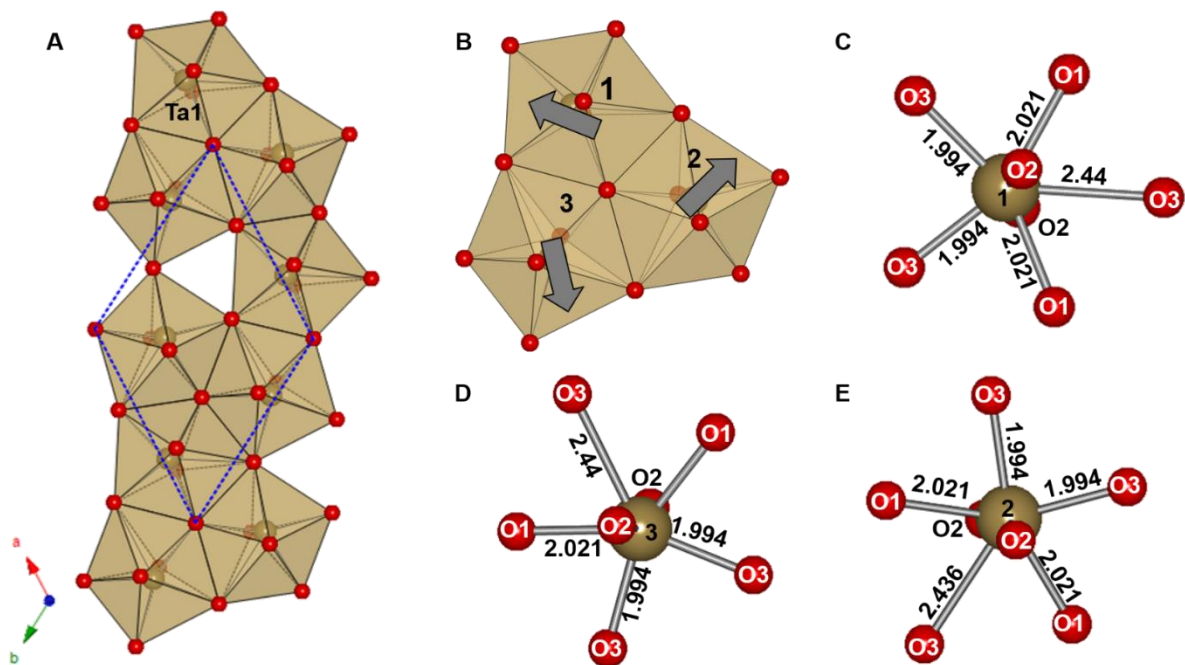


Figure 4.4. A crystal structure of a layer of edge-sharing TaO₇ in the pentagonal bipyramid layer of the rhombohedral β -Cu₂Ta₄O₁₁ a) a view of the edge sharing of Ta cations along the ab plane with the unit cell outline in a blue dashed line b) a smaller segment from the uppermost three Ta cations, the grey arrows indicate the out-of-center displacement of Ta due to repulsions from nearest neighbor cations a local view of the Ta cations from the small segments (c-e) for Ta cations labeled 1, 2, and 3 respectively.

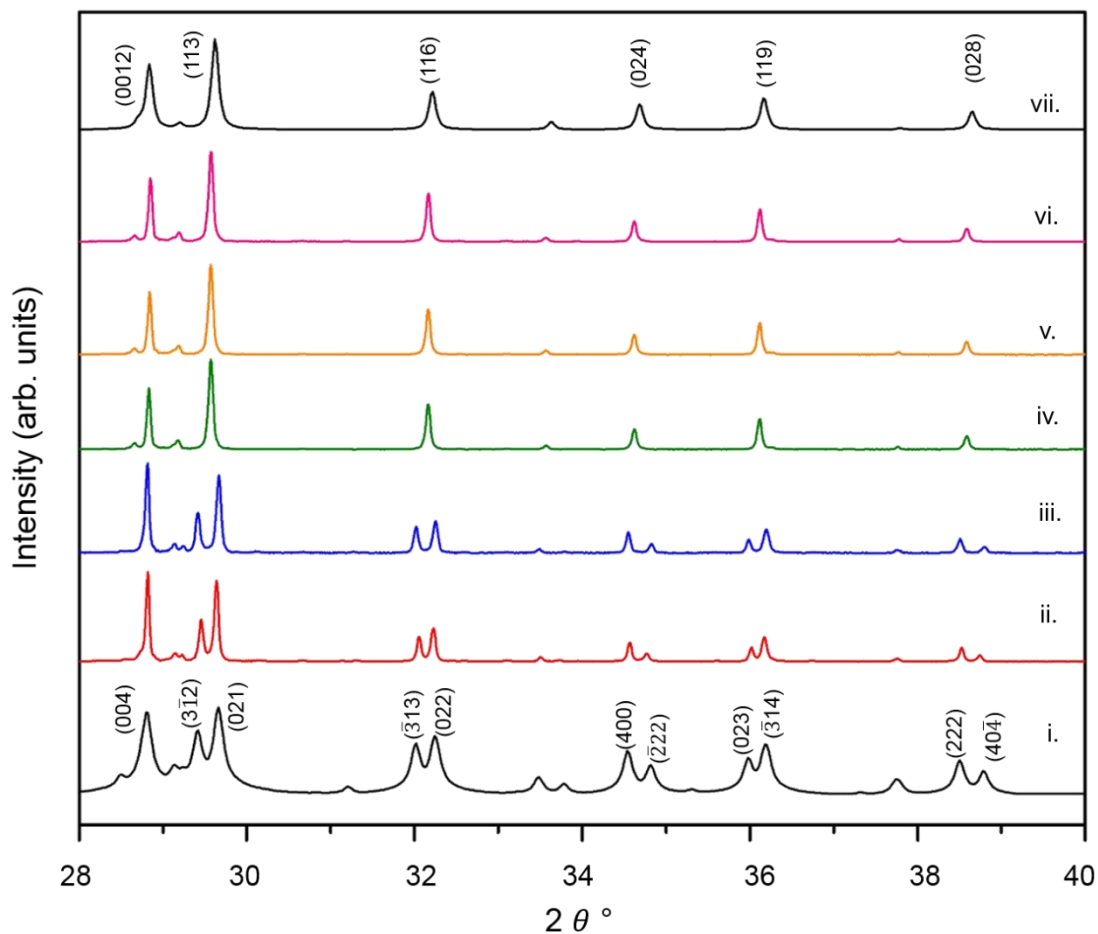


Figure 4.5. The powder X-ray diffraction patterns of α - $\text{Cu}_2\text{Ta}_4\text{O}_{11}$ in an inert atmosphere with i) the simulated XRD of α - $\text{Cu}_2\text{Ta}_4\text{O}_{11}$ from the Rietveld refinement, ii-vi) the experimental powder XRD patterns heated at 223 K, 273 K, 523 K, 623 K, and 723 K, and vii) the simulated XRD pattern of β - $\text{Cu}_2\text{Ta}_4\text{O}_{11}$ at room temperature.

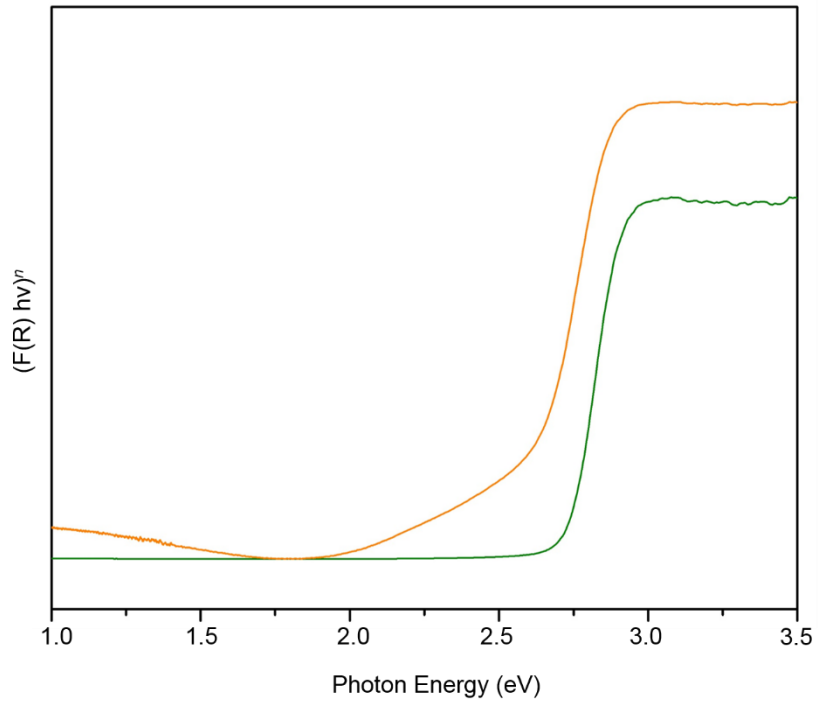


Figure 4.6. The Tauc plots of the UV-vis diffuse reflectance data for the monoclinic α - $\text{Cu}_2\text{Ta}_4\text{O}_{11}$ showing indirect ($n = 1/2$; orange) and direct ($n = 2$; green) band gap transitions.

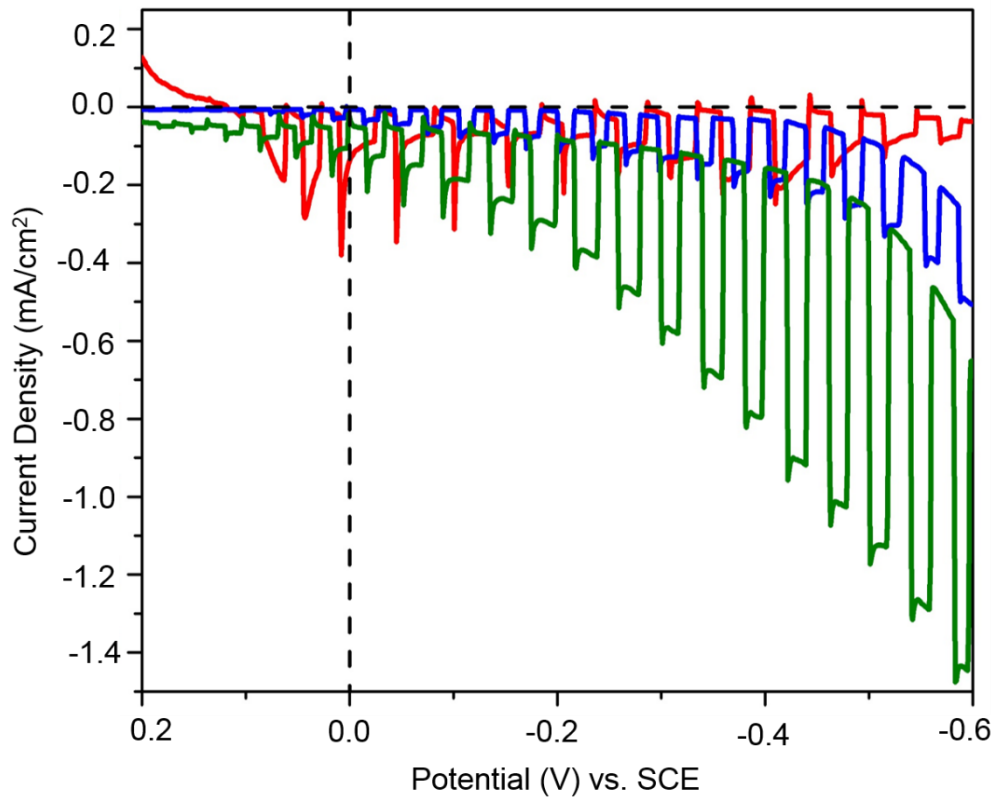


Figure 4.7. The linear sweep voltammetry scans of the polycrystalline monoclinic α - $\text{Cu}_2\text{Ta}_4\text{O}_{11}$ films annealed under vacuum at 773 K for 3 h (red), and heated in air to 523 K (blue), and 623 K (green) for 3 h each.

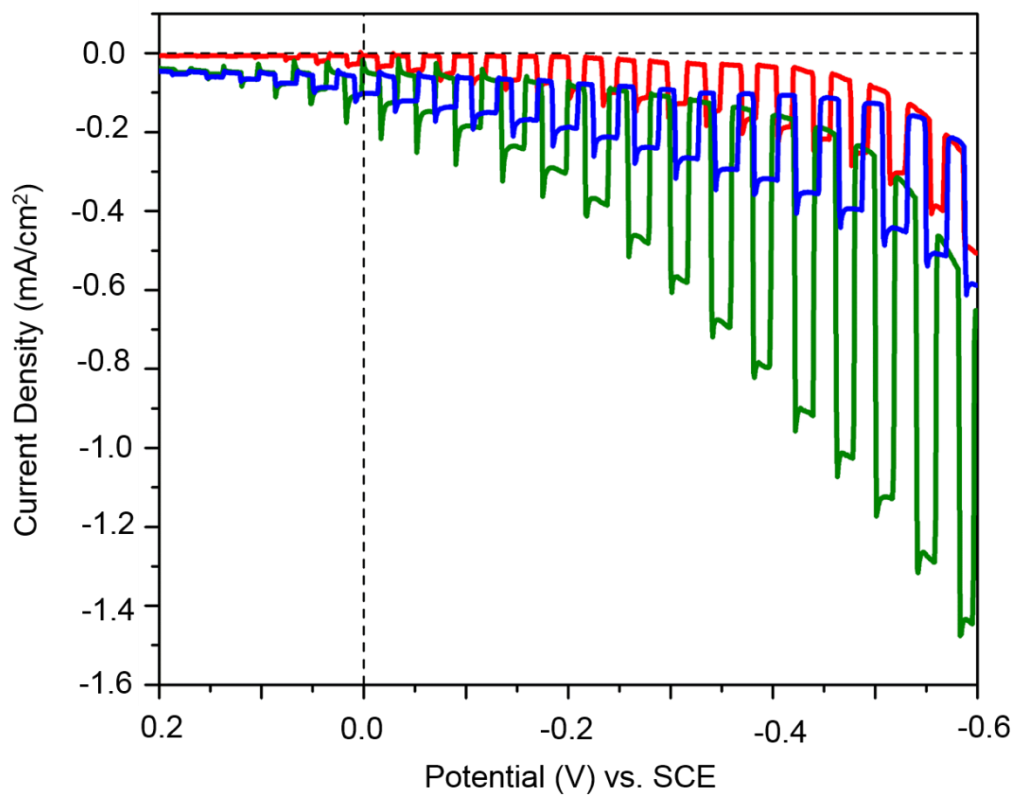


Figure 4.8. The linear sweep voltammetry scans of the polycrystalline monoclinic α - $\text{Cu}_2\text{Ta}_4\text{O}_{11}$ films heated to 523 K for 3 h (red), 523 K with CuO on surface (blue), and 623 K for 3 h.

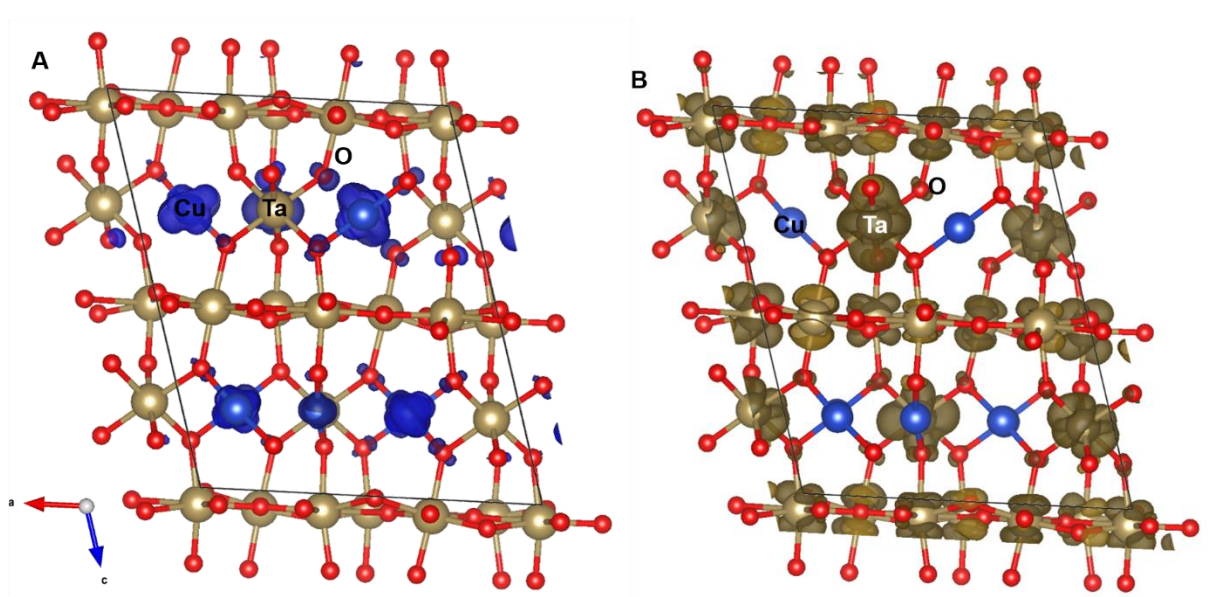


Figure 4.9. The plots of electron density for the monoclinic α - $\text{Cu}_2\text{Ta}_4\text{O}_{11}$ with the orbital contributions in the A) valence band with electron density contributions in blue shading and in the B) conduction band with electron density contributions in tan shading.

CHAPTER 5: Conclusions

This chapter has been adapted from a manuscript prepared for publication.

Ian Sullivan, Brandon Zoellner and Paul A. Maggard

Department of Chemistry, North Carolina State University, Raleigh, NC USA 27695-8204.

I. Optical and Structural Relationships between the Ternary Cu(I) Oxides

As described in the preceding chapters, it has been found that the Cu(I)-based oxides have a wide range of bandgap sizes owing to their different structures and compositions. The reported bandgap sizes and copper coordination environments of several Cu(I) oxides are listed in Table 5.1. Their bandgap sizes are governed mainly by the energy of the conduction band states, and in some cases, owing to their differences in the coordination of copper. Highly representative examples are found in the group-V metal oxide systems, such as the copper(I) vanadates, niobates and tantalates. Generally, the vanadates have the lowest band gap sizes (1.2-1.4 eV), followed by the niobates (1.26-2.0 eV), and then the tantalates (2.4-2.7 eV). The higher energy conduction band states of Ta > Nb > V yield a larger band gap size. By comparison, the delafossites have a more complex electronic structure, with several computational reports regarding orbital mixing in the conduction and valence bands.^{1,2} However, in general, the Cu(I) delafossites follow a similar trend. The *s*-based conduction bands of UV-band gap CuBO₂, CuAlO₂, CuGaO₂ and CuInO₂ all are higher in energy than the lower lying *d*-based bands of the visible-light absorbing CuFeO₂ and CuRhO₂.^{3,4}

The Cu(I) coordination environment also has been found to have a significant impact on the bandgap size as well, with higher coordinated Cu(I) leading to smaller band gaps, as listed in Table 5.1. For example, the Cu(I) niobates show a large variation in bandgap size, ranging from 1.26 to 2.0 eV, owing in large part to the coordination of Cu(I) in the different

structures. The smallest bandgap size of ~ 1.26 eV for CuNb_3O_8 is due to the relatively uncommon octahedrally-coordinated Cu(I). Next, $\text{Cu}_2\text{Nb}_8\text{O}_{21}$ follows with a band gap of ~ 1.6 eV, with tetrahedrally-coordinated Cu(I). Finally, CuNbO_3 has the largest band gap of ~ 2.0 eV, and has linearly coordinated Cu(I). This trend is also apparent in CuGaO_2 . The α - CuGaO_2 phase has a band gap of ~ 3.6 eV⁵ owing to higher lying Ga 4s conduction band states; however, Omata *et al.* have reported a β - CuGaO_2 phase which has a band gap of 1.47 eV with a mainly Cu 3d-based valence band, and a Ga 4s-based conduction band.⁵ Again, the coordination of Cu(I) is a key factor, as the delafossite type α - CuGaO_2 has a linearly coordinated Cu(I), while the wurtzite type β - CuGaO_2 phase has tetrahedrally-coordinated Cu(I). Similarly, the copper tantalates all have very similar structure types and linearly coordinated Cu(I), all with very similar bandgap sizes (~ 2.5 - 2.6 eV).^{6,7}

II. Surface Modification, Copper Migration and Decomposition in the Cu(I) Oxides

The extrusion of Cu(I) to the surfaces of the group-V Cu(I) oxides (*i.e.* copper vanadates, niobates, and tantalates) to form Cu(II)-based oxides has previously been observed by the Maggard group, as shown in the SEM/HRTEM images in Figure 5.1. The extrusion of Cu(I) was first reported by King *et al.* in the *p*-type semiconductor CuNb_3O_8 . Using experimental techniques including XRD, HR-TEM, elemental mapping, and electron diffraction, it was shown that CuO formed on the surface of the materials as its particles were heated in air.⁸ Sahoo *et al.* have also found nanostructure growth of CuO and $\text{Cu}_2\text{V}_3\text{O}_8$ from surfaces of Cu_3VO_4 under heating in air as well.⁹ Both, CuNb_3O_8 and Cu_3VO_4 , compounds were found to have Cu(II) based oxides at all surfaces, shown in Figure 5.1. As described in Chapter 2, a similar effect in $\text{Cu}_5\text{Ta}_{11}\text{O}_{30}$ was observed, found by SEM to arise from the preferential growth of CuO to the surfaces.¹⁰ This preferential growth is due to high Cu(I)

mobility in the *ab* plane of the $\text{Cu}_5\text{Ta}_{11}\text{O}_{30}$ crystal structure, as shown in Figure 5.2a. Migration pathways for Cu(I) along the [100] and [010] directions allow for the preferential migration to specific crystal facets, as shown in Figure 5.2b.

It has been reported that photocurrent densities were increased after heating polycrystalline films of the group-V copper oxides in air. This is attributed to the process of Cu(I) being oxidized to Cu(II), inducing *p*-type defects and increasing conductivity of the material. However, the Maggard group has shown that the addition of CuO nanoparticles to the surfaces of $\text{Cu}_5\text{Ta}_{11}\text{O}_{30}$ (i.e., Chapter 2) and Cu_3VO_4 , with relatively little oxidation of Cu(I) within the structure, results in increased photocurrents as well. This is postulated to arise from a favorable type-I or type-II band offset in the heterojunction of the parent material and Cu(II) oxide at the surface (*i.e.* CuO or $\text{Cu}_2\text{V}_3\text{O}_8$), allowing for increased charge transport at the interfaces and increased photocurrents.^{10,11} Another advantage is increased visible light absorption, especially for the larger band gap copper tantalates (E_g : 2.5-2.7 eV). As CuO forms on the surface, the color of the material darkens from yellow to black, and sub-bandgap absorption is observed by UV-Vis diffuse-reflectance spectroscopy, allowing for absorption as low as ~1.5 eV for $\text{Cu}_3\text{Ta}_7\text{O}_{19}$, ~1.3 eV for $\text{Cu}_5\text{Ta}_{11}\text{O}_{30}$, and < 1.0 eV for Cu_3VO_4 . Similar insights could be utilized in investigating the optical and photoelectrochemical properties of some of the wide band gap delafossites. Simply heating these materials to an intermediate state of CuO and $\text{Cu}_{1-x}\text{MO}_2$ may also provide a favorable heterojunction, as well as a red-shifted absorption into the visible-light range.

Amrute *et al.* have reported on the synthesis and thermal decomposition of various copper delafossites (CuMO_2 , M = Fe, Al, Mn, Cr and Ga).¹² Synthesis of these materials were performed by combining stoichiometric ratios of Cu_2O and the corresponding M_2O_3 and

heating in air at temperatures of 800-1210 °C. The two step synthesis first involves the reaction of Cu₂O reacted with O₂ and M₂O₃ to form CuO and CuM₂O₄. Next, CuM₂O₄ and CuO then react to form the final CuMO₂ phases. When these delafossites are heated in air, they decompose to the corresponding spinel phase and CuO according to the equation $2\text{CuMO}_2 + \frac{1}{2}\text{O}_2 \rightarrow \text{CuM}_2\text{O}_4 + \text{CuO}$.¹² Lalanne *et al.* investigated the solid solution CuFe_{1-x}Cr_xO₂ for use as a transparent conducting oxide. It was found that up to half of the Cu(I) ions in the structure migrate to the surface and are oxidized to CuO as the delafossite phase is oxidized to the spinel phase. The copper ions from CuO can also re-enter the spinel to form the delafossites phase.¹³

Concluding Remarks

While a large amount of research has been focused on *n*-type metal-oxide semiconductors, new research on the *p*-type metal oxides is rapidly growing. Many new copper(I) oxide systems are similar in their characteristics of 1) *p*-type semiconducting behavior, 2) a Cu 3*d*¹⁰ based valence band, and 3) thermal decomposition into CuO and/or another Cu(II) metal oxide. The mixed-metal copper(I) oxides show increased stability in aqueous solution, owing to different metal based conduction bands (either *d*-or *s*-based on the metal), and diminished self-reducing effects as seen in Cu₂O. A majority of the Cu(I)-metal oxides absorb within the visible-wavelengths spectrum, ranging from as low as ~1.2 up to ~2.6 eV. This is dependent on the energy level of the conduction band, as well as structural differences, such as the coordination of Cu in the structure. The ternary Cu(I) oxides also have the benefit of band gap tuning, allowing for the absorption of a broader range of wavelengths in the solar spectrum. These are based on the relative energy of the conduction band, as well as the coordination of Cu in the structure. The graphic in Figure 5.3 illustrates

some of the band positions relative to water redox couples for several Cu(I) oxides, clearly showing that most have band positions thermodynamically favorable for overall water splitting.

From the research described in this dissertation, several similar structural and optical are apparent in several of the Cu(I) oxides. As seen with the copper tantalates ($\text{Cu}_5\text{Ta}_{11}\text{O}_{30}$ and $\text{Cu}_2\text{Ta}_4\text{O}_{11}$), as well as other Cu(I) oxides through literature searches, Cu migration occurs to the surface of the material under heating in air, and oxidizes to either CuO, or other Cu(II) based oxides such as the general spinel phase, CuM_2O_4 , in the copper delafossites. Oxidation of these materials forms a type-II heterojunction with CuO or the other Cu(II) oxides at the surface, allowing for a more efficient charge separation, increasing the photocurrents.^{6,7,10,12}

Future research in this area will be needed to address the optimization of heterojunctions and dye-sensitization of these materials. Several investigations have shown that heterojunctions of *p*-type Cu(I) oxides with other *n*-type metal oxides can effectively separate charge carriers and result in large photocurrents.¹⁵⁻¹⁷ As an additional effect, this can also result in a protective layer, as seen with Cu_2O .¹⁸ Currently, Cu_2O based heterojunctions have yielded the largest photocurrents and open circuit potentials. However, the mixed-metal Cu(I) oxides have yet to be investigated in these types of configurations. With varying valence and conduction band energies, mixed-metal Cu(I) oxides could be highly useful in increasing the open circuit voltage of PV devices, leading to an increase in efficiency. While much research has been performed on Cu(I)-based DSSCs, there remains to be a *p*-type DSSC with an efficiency great than 1.5%. While other *p*-type semiconductors such as NiO or CaFe_2O_4 have been under investigation,¹⁹ Cu(I)-based materials show promise as they exhibit

wide absorption ranges (~1.3-4.0 eV), high current densities when used for proton reduction, and larger open circuit potentials when used in DSSCs (~200-400 mV). The relative abundance and non-toxicity of copper based materials also make them advantageous for solar energy harvesting.

REFERENCES

- (1) Godinho, K. G.; Morgan, B. J.; Allen, J. P.; Scanlon, D. O.; Watson, G. W. Chemical Bonding in Copper-Based Transparent Conducting Oxides: CuMO_2 ($M = \text{In, Ga, Sc}$). *J. Phys. Condens. Matter* **2011**, *23*, 334201-334209.
- (2) Gillen, R.; Robertson, J. Band Structure Calculations of CuAlO_2 , CuGaO_2 , CuInO_2 , and CuCrO_2 by Screened Exchange. *Phys. Rev. B* **2011**, *84*, 035125-035129.
- (3) Gu, J.; Wuttig, A.; Krizan, J. W.; Hu, Y.; Detweiler, Z. M.; Cava, R. J.; Bocarsly, A. B. Mg-Doped CuFeO_2 Photocathodes for Photoelectrochemical Reduction of Carbon Dioxide. *J. Phys. Chem. C* **2013**, *117*, 12415-12422.
- (4) Gu, J.; Yan, Y.; Krizan, J. W.; Gibson, Q. D.; Detweiler, Z. M.; Cava, R. J.; Bocarsly, A. B. P-Type CuRhO_2 as a Self-Healing Photoelectrode for Water Reduction under Visible Light. *J. Am. Chem. Soc.* **2014**, *136*, 830–833.
- (5) Yu, M.; Natu, G.; Ji, Z.; Wu, Y. P-Type Dye-Sensitized Solar Cells Based on Delafossite CuGaO_2 Nanoplates with Saturation Photovoltages Exceeding 460 mV. *J. Phys. Chem. Lett.* **2012**, *3*, 1074–1078.
- (6) King, N.; Sommer, R. D.; Watkins-Curry, P.; Chan, J. Y.; Maggard, P. A. Synthesis, Structure, and Thermal Instability of the $\text{Cu}_2\text{Ta}_4\text{O}_{11}$ Phase. *Cryst. Growth Des.* **2015**, *15*, 552–558.
- (7) Fuoco, L.; Joshi, U. A.; Maggard, P. A. Preparation and Photoelectrochemical Properties of P-Type $\text{Cu}_5\text{Ta}_{11}\text{O}_{30}$ and $\text{Cu}_3\text{Ta}_7\text{O}_{19}$ Semiconducting Polycrystalline Films. *J. Phys. Chem. C* **2012**, *116*, 10490–10497.
- (8) Septina, W.; Ikeda, S.; Khan, M. A.; Hirai, T.; Harada, T.; Matsumura, M.; Peter, L. M. Potentiostatic Electrodeposition of Cuprous Oxide Thin Films for Photovoltaic Applications. *Electrochim. Acta* **2011**, *56*, 4882–4888.
- (9) Minami, T.; Nishi, Y.; Miyata, T.; Nomoto, J. High-Efficiency Oxide Solar Cells with $\text{ZnO}/\text{Cu}_2\text{O}$ Heterojunction Fabricated on Thermally Oxidized Cu_2O Sheets. *Appl. Phys. Express* **2011**, *4*, 062301-062307.
- (10) Sullivan, I.; Sahoo, P. P.; Fuoco, L.; Hewitt, A. S.; Stuart, S.; Dougherty, D.; Maggard, P. A. Cu-Deficiency in the P-Type Semiconductor $\text{Cu}_{5-x}\text{Ta}_{11}\text{O}_{30}$: Impact on Its Crystalline Structure, Surfaces, and Photoelectrochemical Properties. *Chem. Mater.* **2014**, *26*, 6711–6721.
- (11) Paracchino, A.; Laporte, V.; Sivula, K.; Grätzel, M.; Thimsen, E. Highly Active Oxide Photocathode for Photoelectrochemical Water Reduction. *Nat. Mater.* **2011**, *10*, 456–461.
- (12) Amrute, A. P.; Łodziana, Z.; Mondelli, C.; Krumeich, F.; Pérez-Ramírez, J. Solid-State

Chemistry of Cuprous Delafossites: Synthesis and Stability Aspects. *Chem. Mater.* **2013**, 25, 4423–4435.

(13) Lalanne, M.; Barnabé, A.; Mathieu, F.; Tailhades, P. Synthesis and Thermostructural Studies of a $\text{CuFe}_{(1-x)}\text{Cr}_{(x)}\text{O}_{(2)}$ Delafossite Solid Solution with $0 \leq X \leq 1$. *Inorg. Chem.* **2009**, 48, 6065–6071.

(14) Nishi, Y.; Miyata, T.; Minami, T. Effect of Inserting a Thin Buffer Layer on the Efficiency in n-ZnO/p-Cu₂O Heterojunction Solar Cells. *J. Vac. Sci. Technol. A Vacuum, Surfaces, Film.* **2012**, 30, 140-145.

(15) Katayama, J.; Ito, K.; Matsuoka, M.; Tamaki, J. Performance of Cu₂O/ZnO Solar Cell Prepared By Two-Step Electrodeposition. *J. Appl. Electrochem.* **2004**, 34, 687–692.

(16) Minami, T.; Nishi, Y.; Miyata, T.; Nomoto, J. High-Efficiency Oxide Solar Cells with ZnO/Cu₂O Heterojunction Fabricated on Thermally Oxidized Cu₂O Sheets. *Appl. Phys. Express* **2011**, 4, 301-310.

(17) Paracchino, A.; Laporte, V.; Sivula, K.; Grätzel, M.; Thimsen, E. Highly Active Oxide Photocathode for Photoelectrochemical Water Reduction. *Nat. Mater.* **2011**, 10, 456–461.

(18) Morales-Guio, C. G.; Tilley, S. D.; Vrubel, H.; Grätzel, M.; Hu, X. Hydrogen Evolution from a Copper(I) Oxide Photocathode Coated with an Amorphous Molybdenum Sulphide Catalyst. *Nat. Commun.* **2014**, 5, 3059-3067.

(19) Ida, S.; Yamada, K.; Matsunaga, T.; Hagiwara, H. Preparation of P-Type CaFe_2O_4 Photocathodes for Producing Hydrogen from Water. *J. Am. Chem. Soc.* **2010**, 132, 17343–17345.

Table 5.1. Reported Bandgap Sizes, Photocurrents, Stability, and Coordination of Cu(I) in the Cu(I) Oxides

Material	Band Gap (eV)	Maximum Photocurrent (mA/cm ²); Potential (V)	Cu Coordination	PEC Cell and Conditions	Stability J/J ₀ (%); Time
Cu ₂ O	2.00	-7.6; 0.0 (vs. Ag/AgCl)	Linear	From LSV measurements; Layered film with AZO, TiO ₂ and Pt; Ref. 39	78%; 20 min
		-5.7; 0.0 (vs. Ag/AgCl)		From LSV measurements; Layered film with AZO and MoS _{2-x} ; Ref. 57	99%; 10 h
		-5; 0.0 (vs. Ag/AgCl)		Short circuit current; Layered film with AZO, TiO ₂ and RuO ₂ Ref. 55	94%; 8 h
		4.3; 0.0 (vs. Ag/AgCl)		From LSV measurements; Layered with CuO and Ni nanoparticles Ref. 56	87.7%; 20 min
		-1.54; 0.0 (vs. Ag/AgCl)		Short circuit current; Cu/Cu ₂ O/CuO layered Ref. 43	74.4%; 20 min
		-0.18; -0.38 (vs. SCE)		From LSV measurements; Thin film in aqueous media; Ref. 36	N/A
		2.08-10; 0.0 (two electrode)		From I _{sc} condition; photovoltaic cells Cu ₂ O/ZnO, Highest efficiency 4%; Ref. 45-47, 50-52	N/A
Cu ₃ VO ₄	1.20	-0.25; -0.2 (vs. SCE)	Tetrahedral	From LSV measurements; Oxidized film electrode; Ref. 68	20%; 4000 s
CuNb ₃ O ₈	1.26	-0.85; -0.38 (vs. SCE)	Octahedral	From LSV measurements; Oxidized film electrode Ref. 64	80%; 5000 s
Cu ₂ Nb ₈ O ₂₁	1.43	-1.3; -0.6 (vs. SCE)	Tetrahedral	From LSV measurements; Oxidized film electrode; Ref. 67	N/A

Table 5.1 Continued

CuNbO ₃	2.00	-0.45; -0.6 (vs. SCE)	Linear	From LSV measurements; Oxidized film electrode; Ref. 74	95%; 11,000 s
α -Cu ₂ Ta ₄ O ₁₁	2.65	-0.5; -0.6 (vs. SCE)	Linear	From LSV measurements; Oxidized film electrode; Ref. 85	50%; 1000 s
β -Cu ₂ Ta ₄ O ₁₁	2.65	-1.5; -0.6 (vs. SCE)	Linear	From LSV measurements; Film electrode; Oxidized; Ref. 85	47%; 1000 s
Cu ₃ Ta ₇ O ₁₉	2.60	-2.6; -0.6 (vs. SCE)	Linear	From LSV measurements; Oxidized film electrode; Ref. 87	N/A
Cu ₅ Ta ₁₁ O ₃₀	2.55	-2.5; -0.6 (vs. SCE)	Linear	From LSV measurements; Oxidized film electrode; Ref. 87	25-50%; 1000 s
CuFeO ₂	1.36	-1.5; -1.6 (vs. SCE)	Linear	From LSV measurements; Pellet electrode; Ref. 81	N/A
CuRhO ₂	1.90	-7.0; -1.6 (vs. SCE)	Linear	From LSV measurements; Pellet electrode; Ref. 103	60%; 10 h
CuAlO ₂	3.00	0.3; 0.0 (two electrode)	Linear	From I _{sc} condition; 0.04% efficiency; DSSC; Ref. 108	N/A
		0.954; 0.0 (two electrode)		From I _{sc} condition; 0.04% efficiency; DSSC; Ref. 109	N/A
α -CuGaO ₂	3.00	0.384; 0.0 (two electrode)	Linear	From I _{sc} condition; 0.026% efficiency; DSSC; Ref. 110	N/A
		0.415; 0.0 (two electrode)		From I _{sc} condition; 0.045% efficiency; 1% Mg doped; DSSC; Ref. 111	N/A
		2.05; 0.0 (two electrode)		From I _{sc} condition; 0.182% efficiency; DSSC; Ref. 112	N/A
β -CuGaO ₂	1.50	N/A	Tetrahedral	Wurtzite structure; Ref. 106-107	N/A

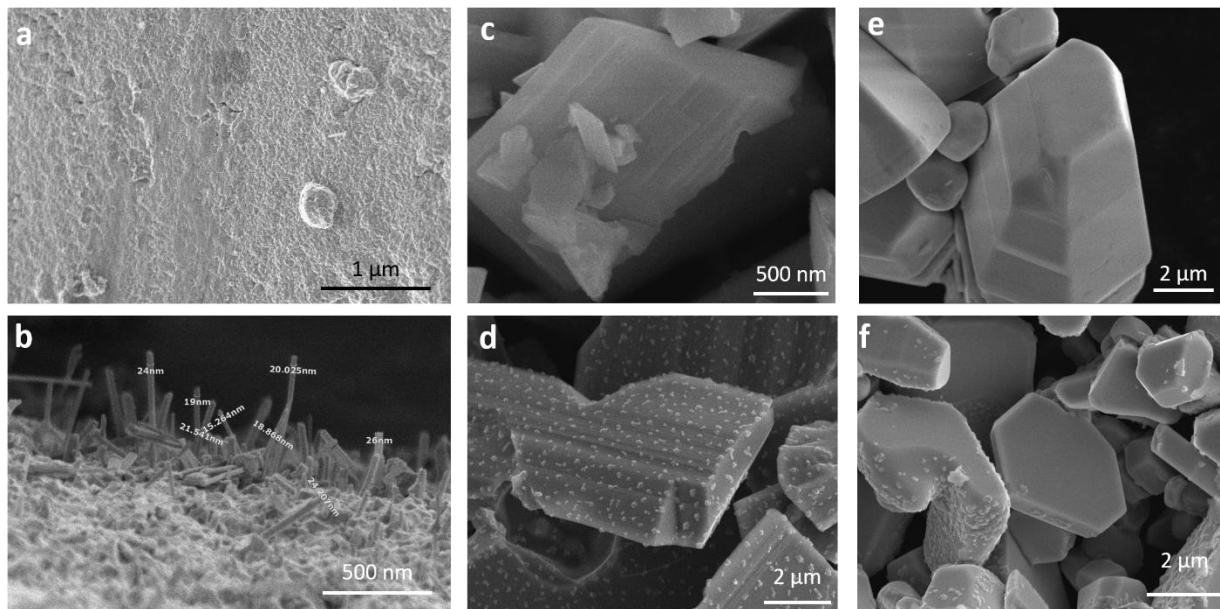


Figure 5.1. SEM images of copper oxide extrusion in (a,b) Cu_3VO_4 , (c,d) CuNb_3O_8 , and (e,f) $\text{Cu}_5\text{Ta}_{11}\text{O}_{30}$. Figures (a,b) adapted from ref. 68 with permission of The Royal Society of Chemistry. Figures (c,d) and (e,f) reprinted with permission from refs. 65 and 87. Copyright 2014 American Chemical Society.

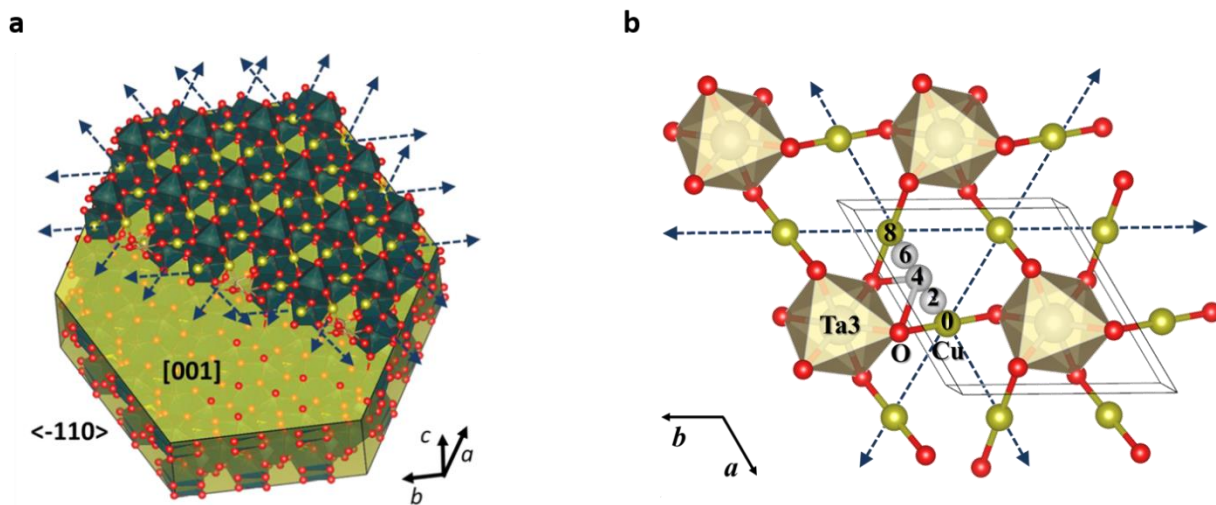


Figure 5.2. Preferential copper migration through the crystallites of $\text{Cu}_5\text{Ta}_{11}\text{O}_{30}$ (a), and copper migration within the channels along the [100] and [010] directions (b). Reprinted with permission from ref. 87. Copyright 2014 American Chemical Society.

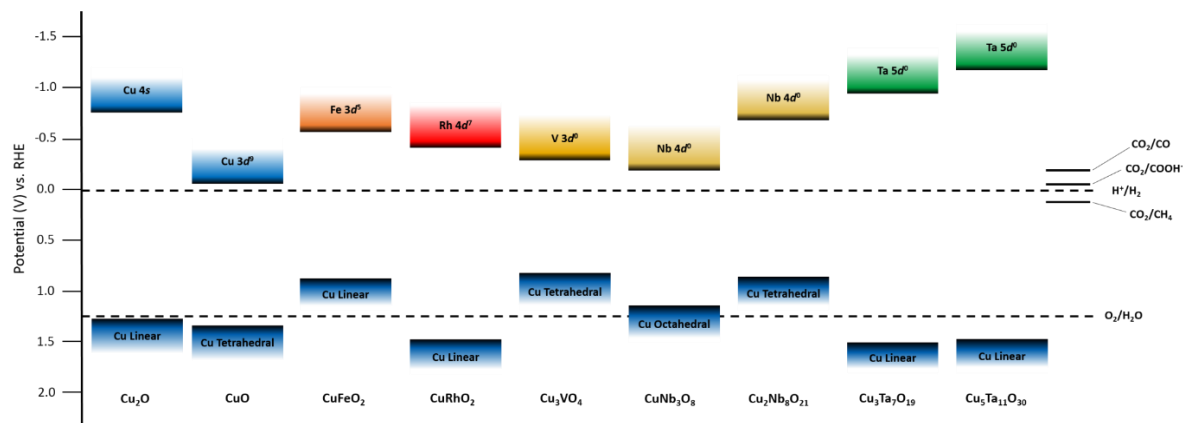


Figure 5.3. Band positions of various copper oxides compared to the redox potentials of water and CO₂. Bands have been shifted to reflect positions at pH 0 for comparison.

APPENDICES

APPENDIX A

Supporting Information

“Cu-Deficiency in the *p*-Type Semiconductor Cu_{5-x}Ta₁₁O₃₀: Impact on its Crystalline Structure, Surfaces, and Photoelectrochemical Properties”

Ian Sullivan,^a Prangya P. Sahoo,^a Lindsay Fuoco,^a Andy S. Hewitt,^b Sean Stuart,^b Daniel Dougherty^b and Paul A. Maggard^a

^a Department of Chemistry, North Carolina State University, Raleigh, NC 27695-8204.

^b Department of Physics, North Carolina State University, Raleigh, NC 27695-8204.

Table A1. Unit cell volumes calculated from lattice parameters of heated films of Cu_{5-x}Ta₁₁O₃₀.

Cu₅Ta₁₁O₃₀ heated to 350 °C			
Time (min)	a (Å)	c (Å)	Volume (Å³)
15	6.2460(9)	32.54(1)	1099.3(4)
30	6.2425(7)	32.51(1)	1097.0(3)
60	6.243(1)	32.46(2)	1095.8(5)

Cu₅Ta₁₁O₃₀ heated to 450 °C			
Time (min)	a (Å)	c (Å)	Volume (Å³)
15	6.2401(8)	32.397(7)	1092.5(3)
30	6.246(1)	32.30(1)	1091.2(5)
60	6.244(1)	32.30(1)	1090.4(5)

Cu₅Ta₁₁O₃₀ heated to 550 °C			
Time (min)	a (Å)	c (Å)	Volume (Å³)
15	6.2396(9)	32.437(7)	1093.7(3)
30	6.242(1)	32.338(9)	1091.2(4)
60	6.246(1)	32.41(1)	1094.7(4)

Table A2. Refined atomic coordinates and isotropic displacement parameters (\AA^2) and site shifts in the atomic positions (Δ_{pos}) of $\text{Cu}_{3.1(1)}\text{Ta}_{11}\text{O}_{30}$, compared to the previously reported $\text{Cu}_5\text{Ta}_{11}\text{O}_{30}$.

Atom and Wyckoff position		x	y	z	U_{eq} (\AA^2)	Δ_{pos}^a (\AA)
Cu1	12i	0.342(5)	0.166(6)	0.0932(8)	0.0594	0.076
Ta1	6g	0.357(1)	0	0	0.028(2)	0.034
Ta2	12i	0.670(1)	0.9725(8)	0.1913(1)	0.027(1)	0.025
Ta3	4f	0.333333	0.666667	0.0973(4)	0.040(3)	0
O1	6g	0.737(10)	0	0	0.018	0.094
O2	4f	0.333333	0.666667	0.986(3)	0.018	0.106
O3	12i	0.418(9)	0.969(1)	0.058(1)	0.018	0.283
O4	12i	0.447(9)	0.052(9)	0.181(1)	0.018	0.472
O5	4f	0.333333	0.666667	0.191(3)	0.018	0.164
O6	4e	0	0	0.182(3)	0.018	0.039
O7	6h	0.722(11)	0.048(11)	0.25	0.018	0.484
O8	12i	0.633(10)	0.922(8)	0.131(1)	0.018	0.121

^a The calculated shift in the atomic position compared to the previously reported $\text{Cu}_5\text{Ta}_{11}\text{O}_{30}$.

^b The occupancy of the Cu site refined as 0.53(1).

Table A3. The results of Curie-Weiss fits to magnetic susceptibility measurements for $\text{Cu}_5\text{Ta}_{11}\text{O}_{30}$ and the Cu-deficient $\text{Cu}_{5-x}\text{Ta}_{11}\text{O}_{30}$ after heating to 250 °C, 350 °C and 450 °C.

Oxidation Temperature	Θ (K)	C (emu/mol·K)	TIP (emu/mol)	R^2	μ_{eff} per Cu (B.M.)
$\text{Cu}_5\text{Ta}_{11}\text{O}_{30}$ (R.T.)	-0.149	0.0299	5.3×10^{-4} (60-281 K)	0.9779	0.0978
$\text{Cu}_{5-x}\text{Ta}_{11}\text{O}_{30}$ (250°C)	-3.95	0.0510	5.2×10^{-4} (59-271 K)	0.9940	0.1278
$\text{Cu}_{5-x}\text{Ta}_{11}\text{O}_{30}$ (350°C)	0.0516	0.1990	1.4×10^{-3} (60-140 K)	0.9983	0.2523
$\text{Cu}_{5-x}\text{Ta}_{11}\text{O}_{30}$ (450°C)	-1.23	0.6091	1.6×10^{-3} (50-300 K)	0.9997	0.4410

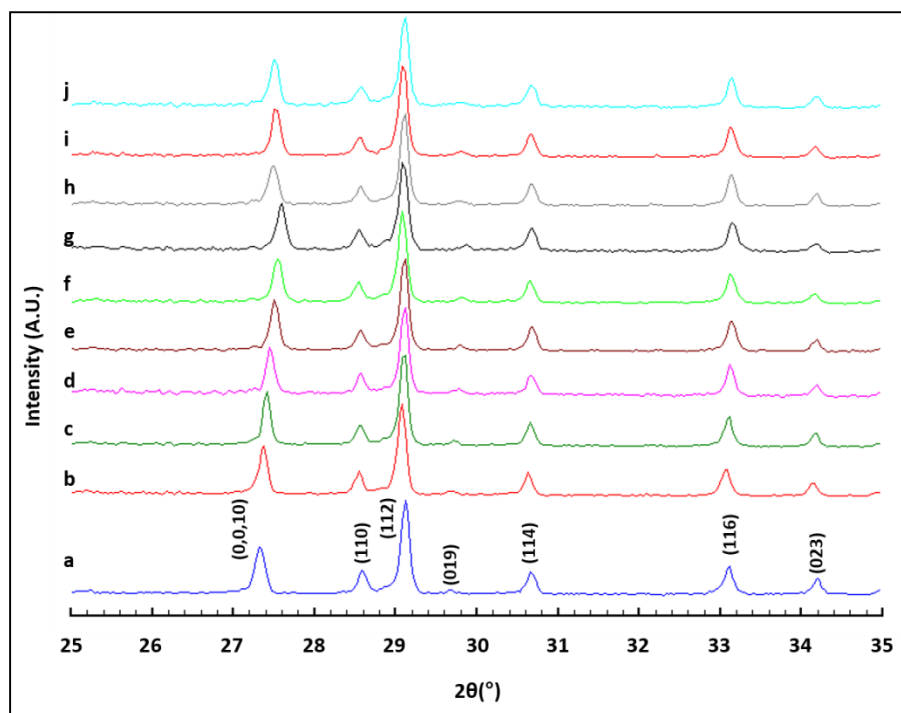


Figure A1. Powder XRD patterns of $\text{Cu}_5\text{Ta}_{11}\text{O}_{30}$ films before heating (a), heated to 350 °C for 15 min (b), 30 min (c) and 60 min (d); heated to 450 °C for 15 min (e), 30 min (f) and 60 min (g); and heated to 550 °C for 15 min (h), 30 min (i) and 60 min (j).

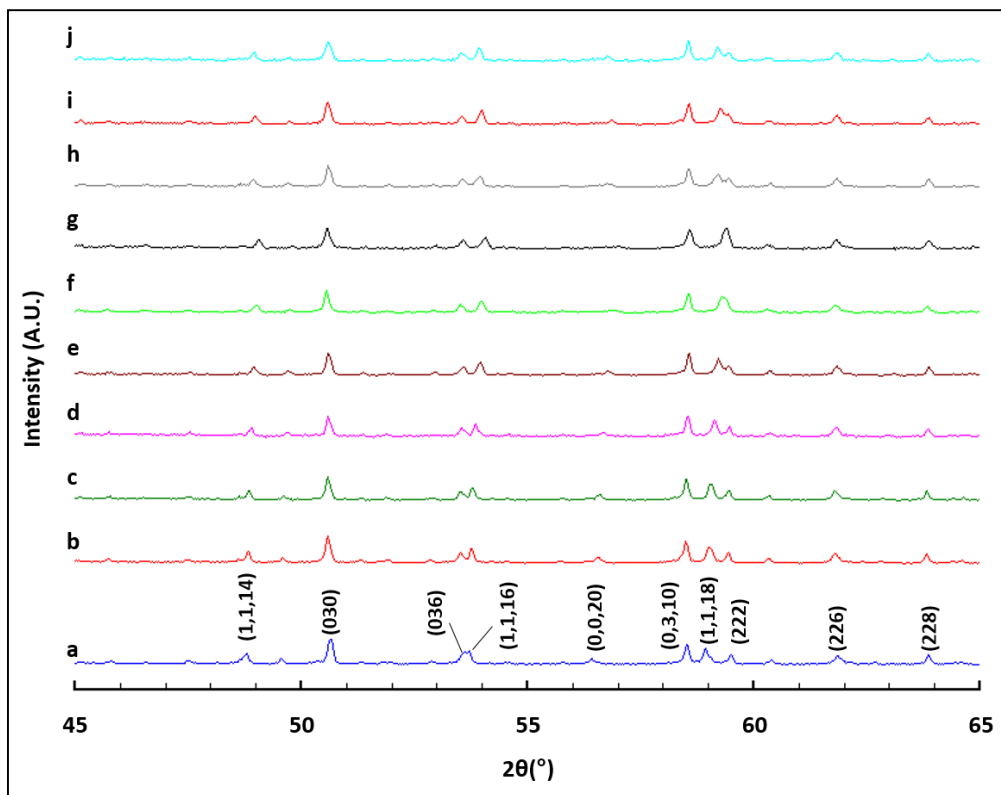


Figure A2. Powder XRD patterns of $\text{Cu}_5\text{Ta}_{11}\text{O}_{30}$ films before heating (a), heated to 350 °C for 15 min (b), 30 min (c) and 60 min (d); heated to 450 °C for 15 min (e), 30 min (f) and 60 min (g); and heated to 550 °C for 15 min (h), 30 min (i) and 60 min (j).

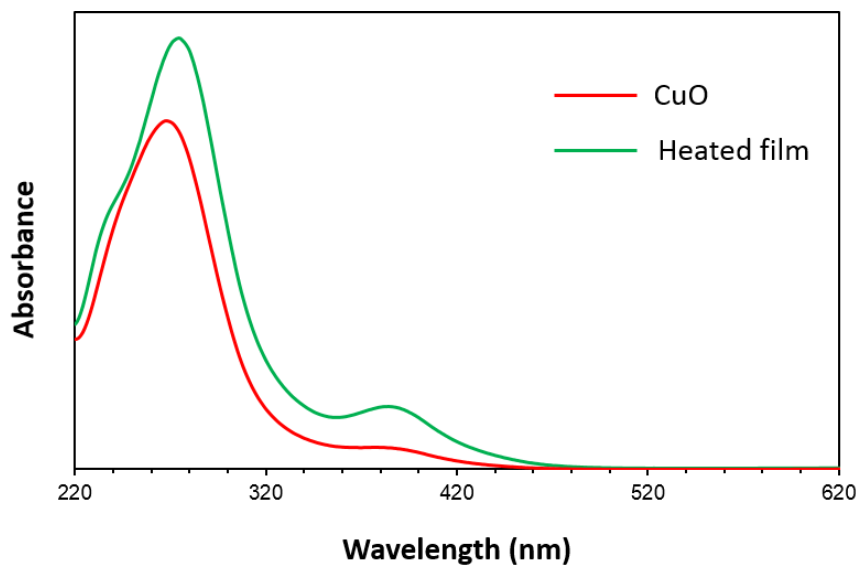


Figure A3. UV-Vis absorption of CuO dissolved in HCl/H₂O solution and a heated film of Cu₅Ta₁₁O₃₀ with CuO surface islands soaked in a similarly prepared solution.

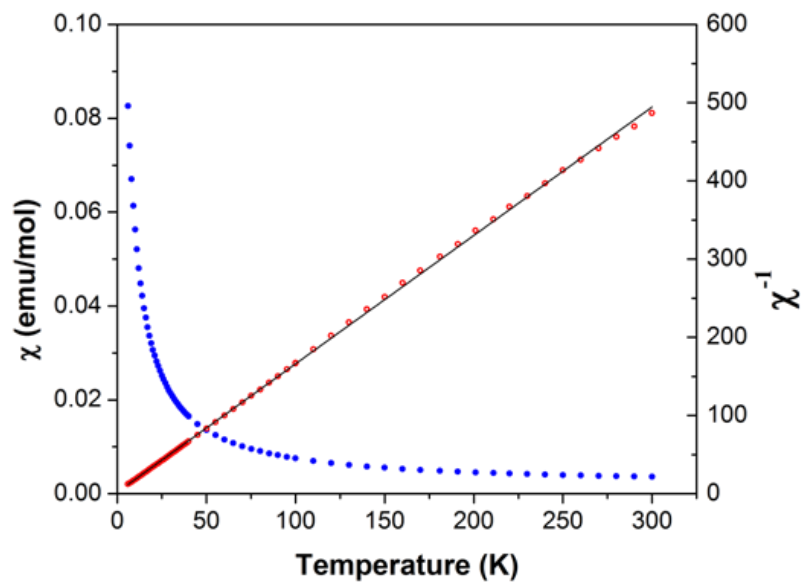


Figure A4. Temperature-dependent magnetic susceptibility of $\text{Cu}_5\text{Ta}_{11}\text{O}_{30}$ that was heated in air at 450 °C for 3 h.

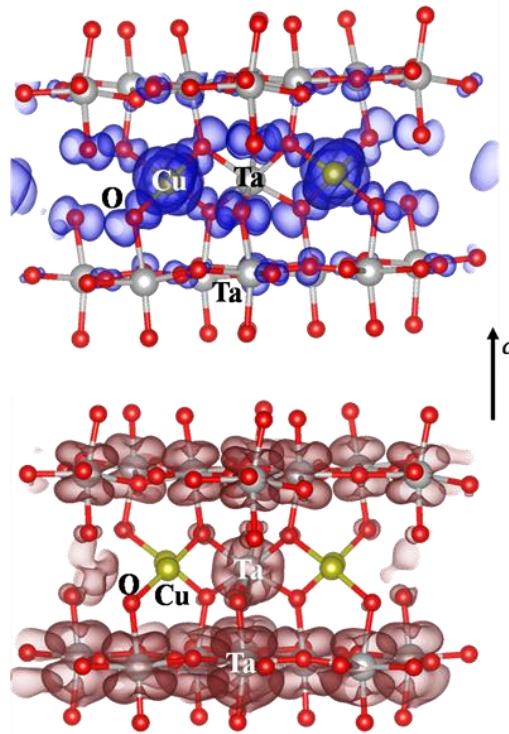


Figure A5. Calculated electron-density plots for $\text{Cu}_{3.2(1)}\text{Ta}_{11}\text{O}_{30}$ (~50% Cu vacancies) at the highest energies of the valence band edge (upper; blue shading) and lowest energies of the conduction band edge (lower; red shading). Atom types are labeled.

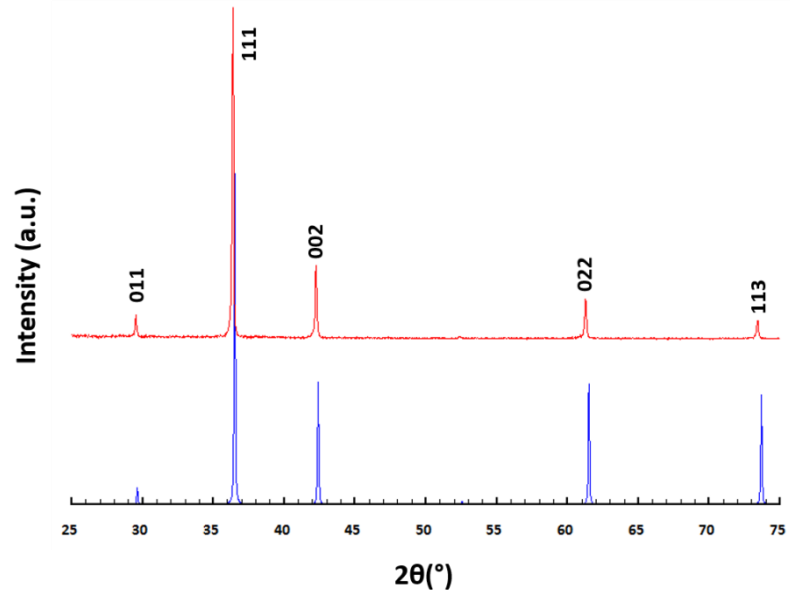


Figure A6. Powder XRD pattern of the electrodeposited Cu₂O polycrystalline film (upper), and the calculated theoretical pattern (lower) with Miller indices labeled.

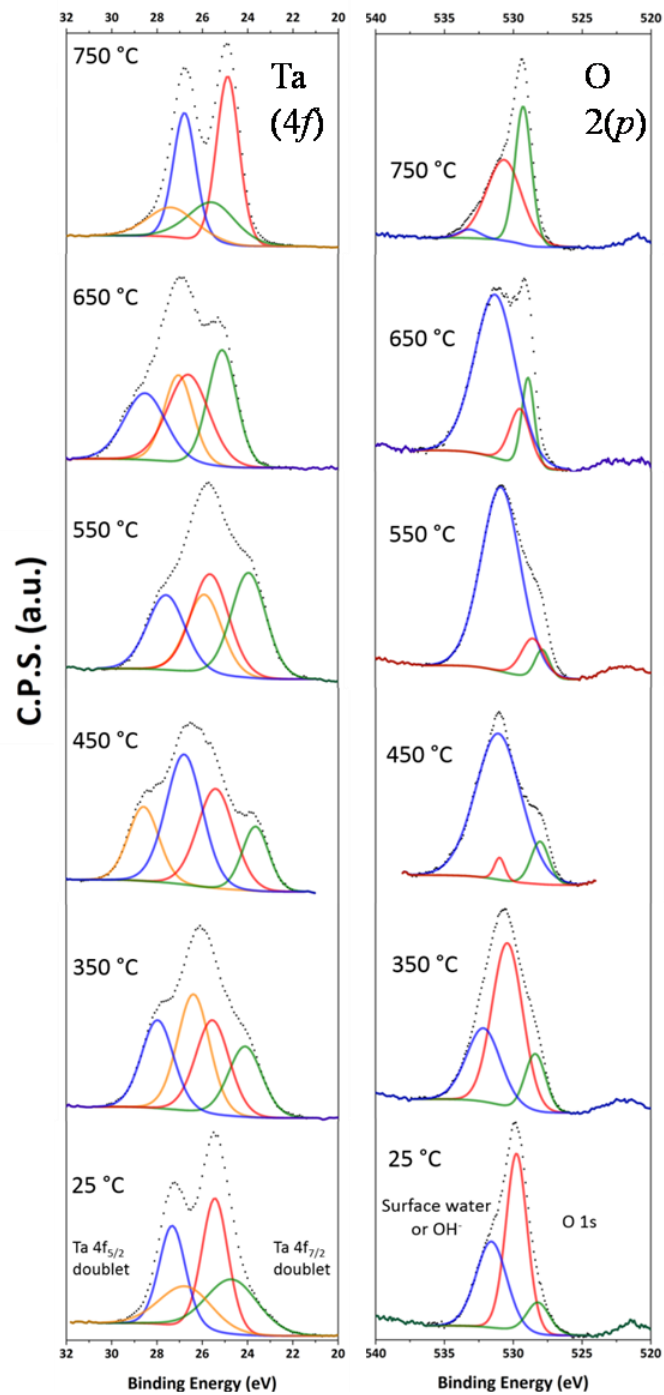


Figure A7. Detailed XPS scans of Ta 4*f* (left) and O 2*p* (right) core levels for $\text{Cu}_5\text{Ta}_{11}\text{O}_{30}$ heated to increasing temperatures. The Ta 4*f*_{7/2} doublet is the red and green fit and the 4*f*_{5/2} doublet is the blue and yellow fit (right).

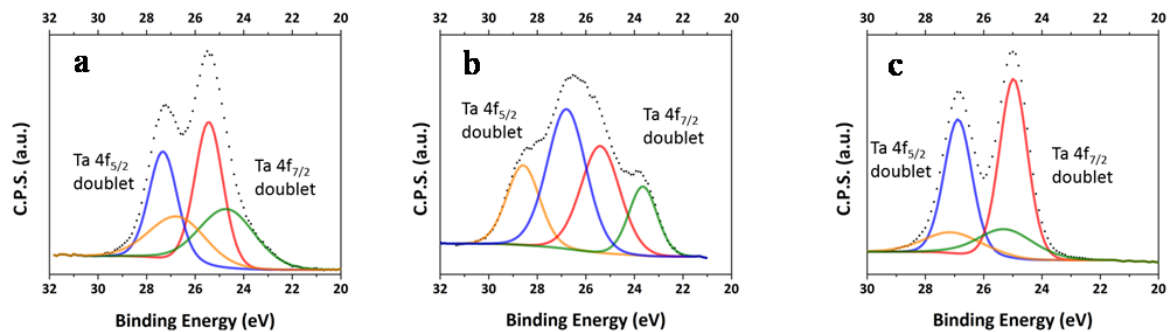


Figure A8. Detailed XPS scans of the Ta 4f core levels for $\text{Cu}_5\text{Ta}_{11}\text{O}_{30}$ with no heat treatment (a), after heating to 450 °C for 1 h in air (b), and after chronoamperometry measurements for 1000 s (c). The Ta 4f_{7/2} doublet is the red and green fit and the 4f_{5/2} doublet is the blue and yellow fit.

APPENDIX B

Supporting Information

Photo-Injection of High Potential Holes into $\text{Cu}_5\text{Ta}_{11}\text{O}_{30}$ Nanoparticles by Porphyrin Dyes

Ian Sullivan,[†] Chelsea Brown,[‡] Manuel J. Llansola-Portoles,[‡] Miguel Gervaldo,[§] Gerdenis Kodis,[‡] Thomas Moore,[‡] Devens Gust,[‡] Ana Moore,[‡] Paul Maggard[†]

[†] *Department of Chemistry, North Carolina State University, Raleigh, NC 27695-8204.*

[‡] *Department of Chemistry and Biochemistry, Arizona State University, Tempe, AZ 85287*

USA

[§] *Department of Chemistry, Universidad Nacional de Río Cuarto. Agencia Postal Nro. 3,*

X5804BYA Río Cuarto, Córdoba, Argentina

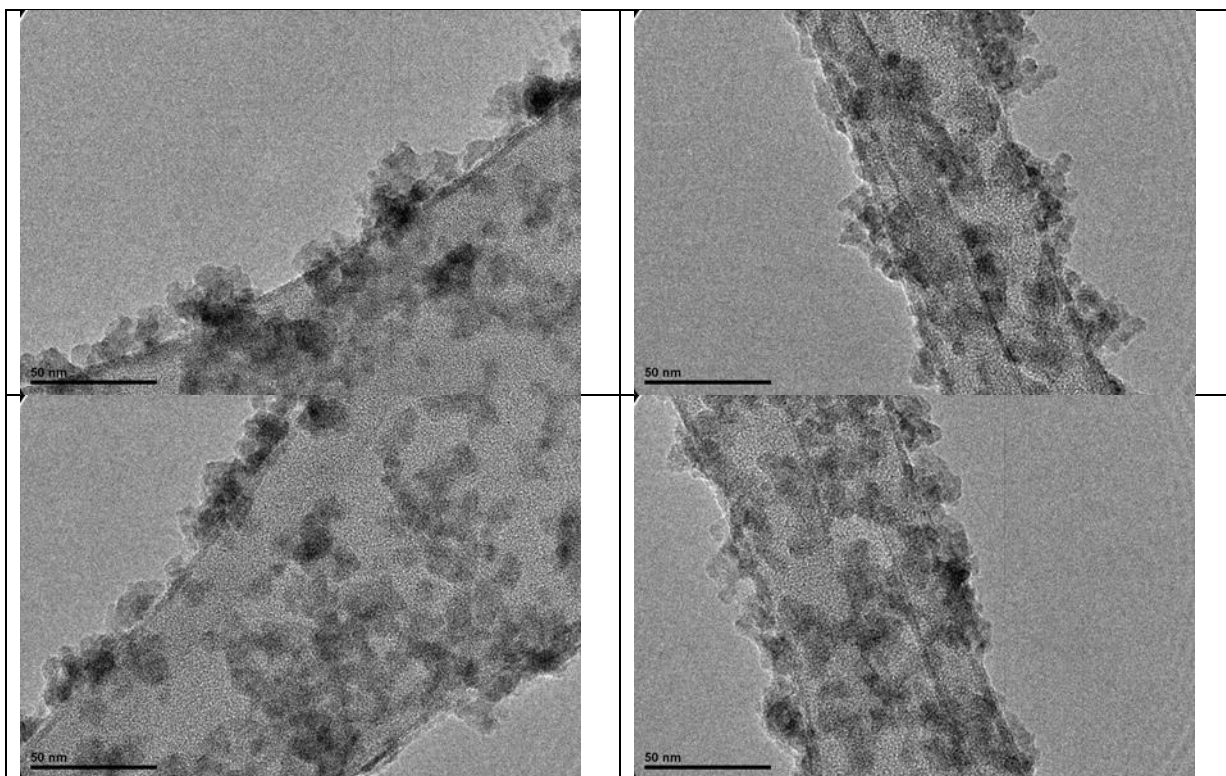
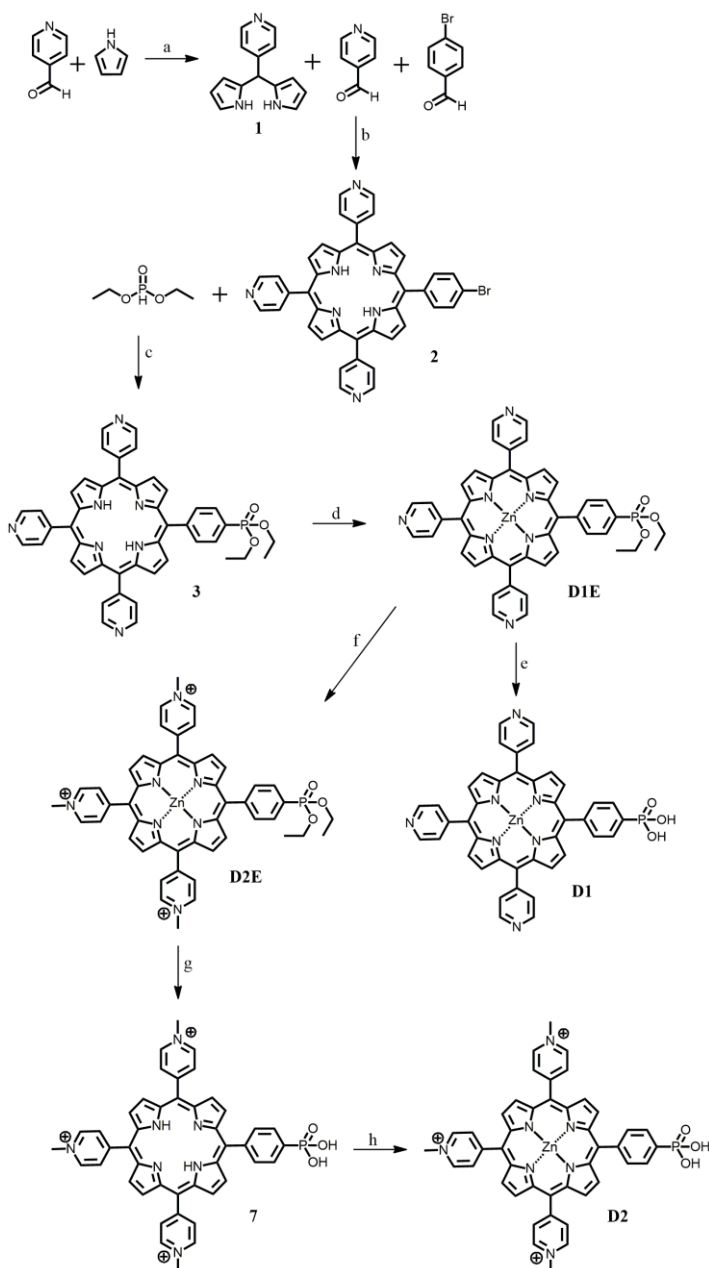


Figure B1. Representative HR-TEM images of NP-Cu₅Ta₁₁O₃₀.

Dye synthesis



Scheme B1. Reagents and conditions: (a) Ar/85 °C/24 h, 53% yield; (b) propionic acid, reflux/45 min, 5.5% yield; (c) diethyl phosphite/Pd(PPh₃)₄/toluene/TEA, Ar/80 °C/18 h, 23% yield; (d) ZnOAc•2H₂O/THF/DCM, 60 °C/12 h, 32 % yield; (e) TMS-Br/CHCl₃/TEA, 60 °C/18 h, 100% yield; (f) MeI/DMF, Ar/100 °C/1 h then room temperature/12 h, 100% yield; (g) TMS-Br/ACN/TEA, 65 °C/12 h, 100 % yield; (h) ZnOAc•2H₂O/THF/H₂O, 60 °C/2 h, 100% yield.

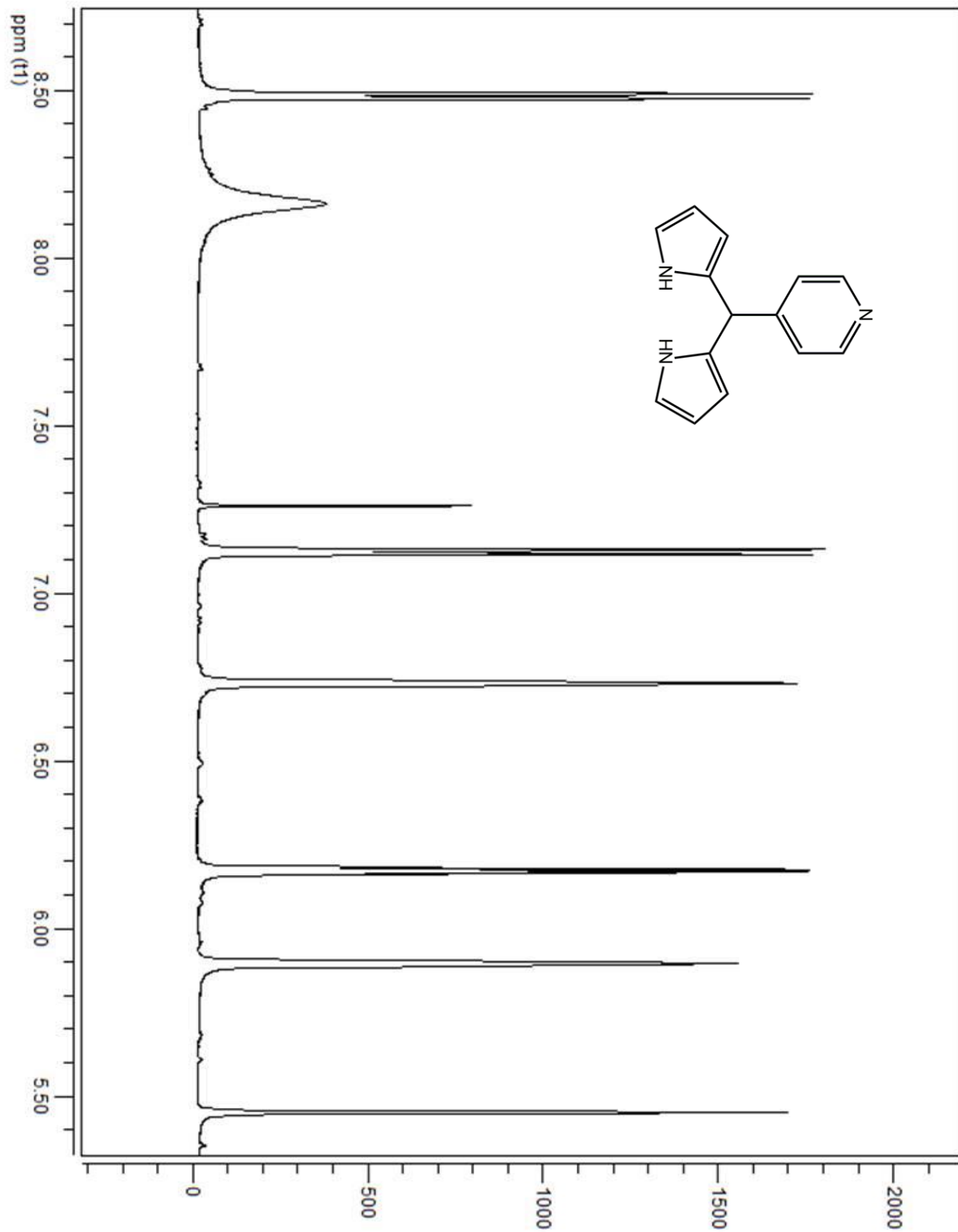


Figure B2. $^1\text{H-NMR}$ of 1 in CDCl_3 .

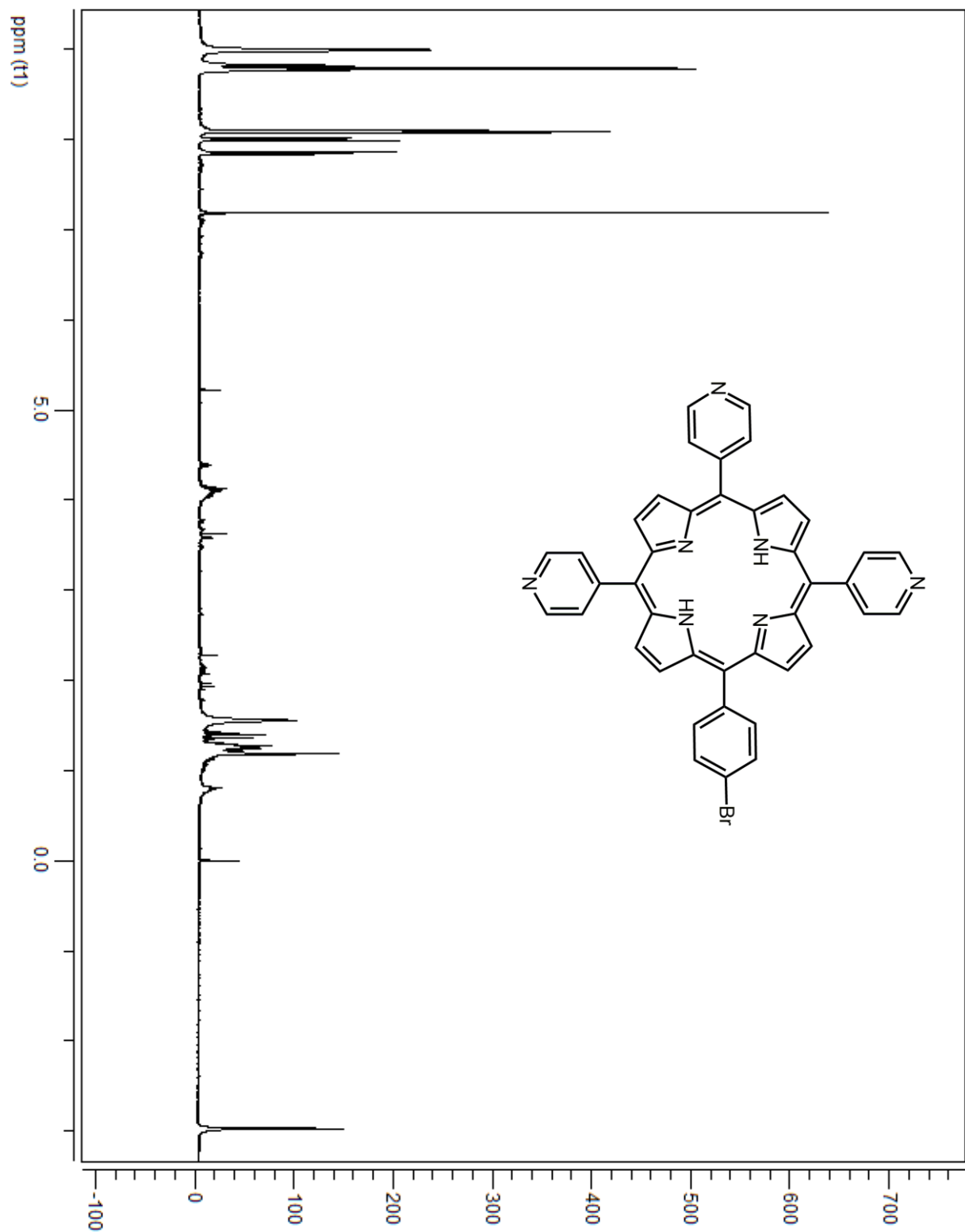


Figure B3. ¹H-NMR of 2 in CDCl₃.

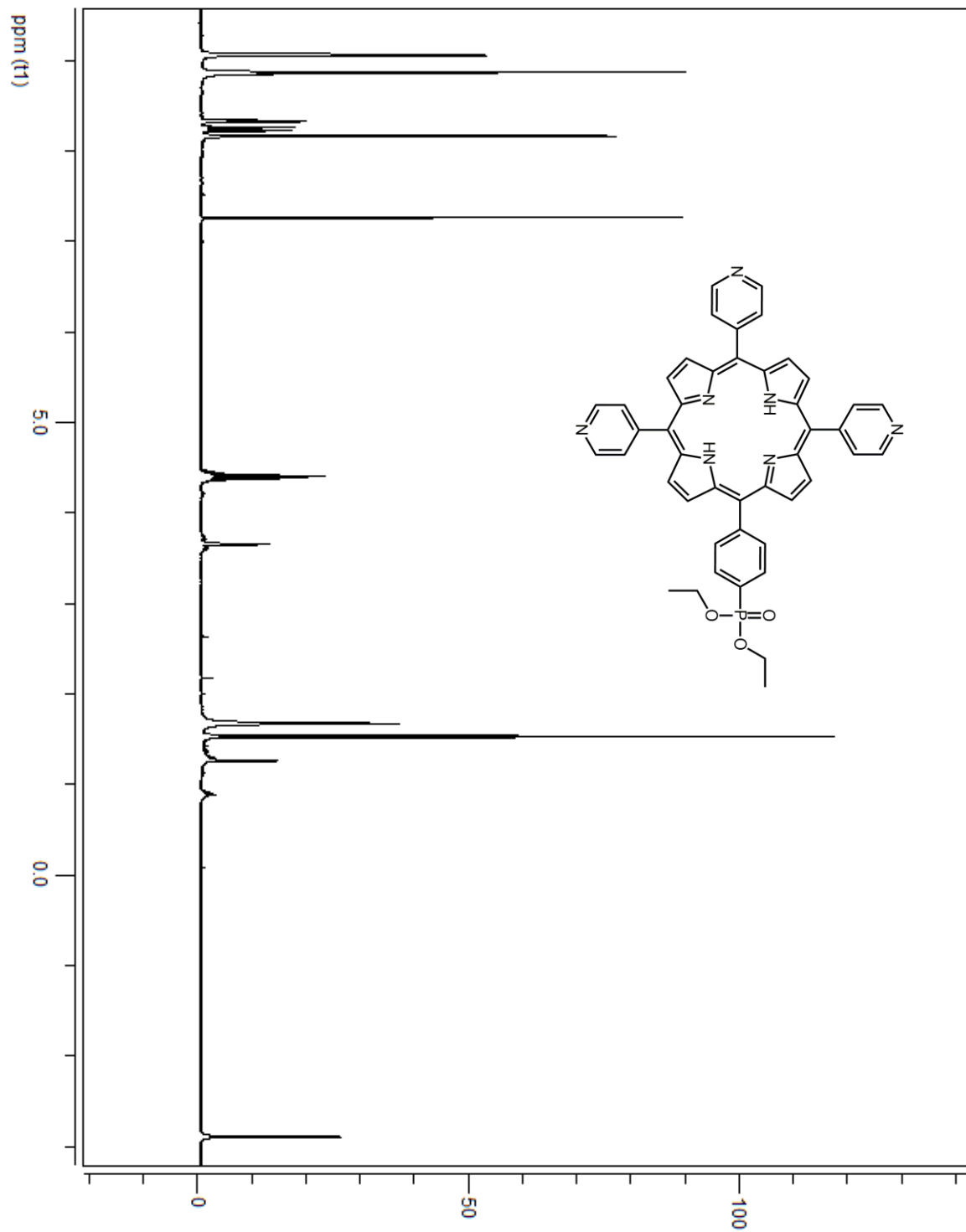


Figure B4. $^1\text{H-NMR}$ of 3 in CDCl_3 .

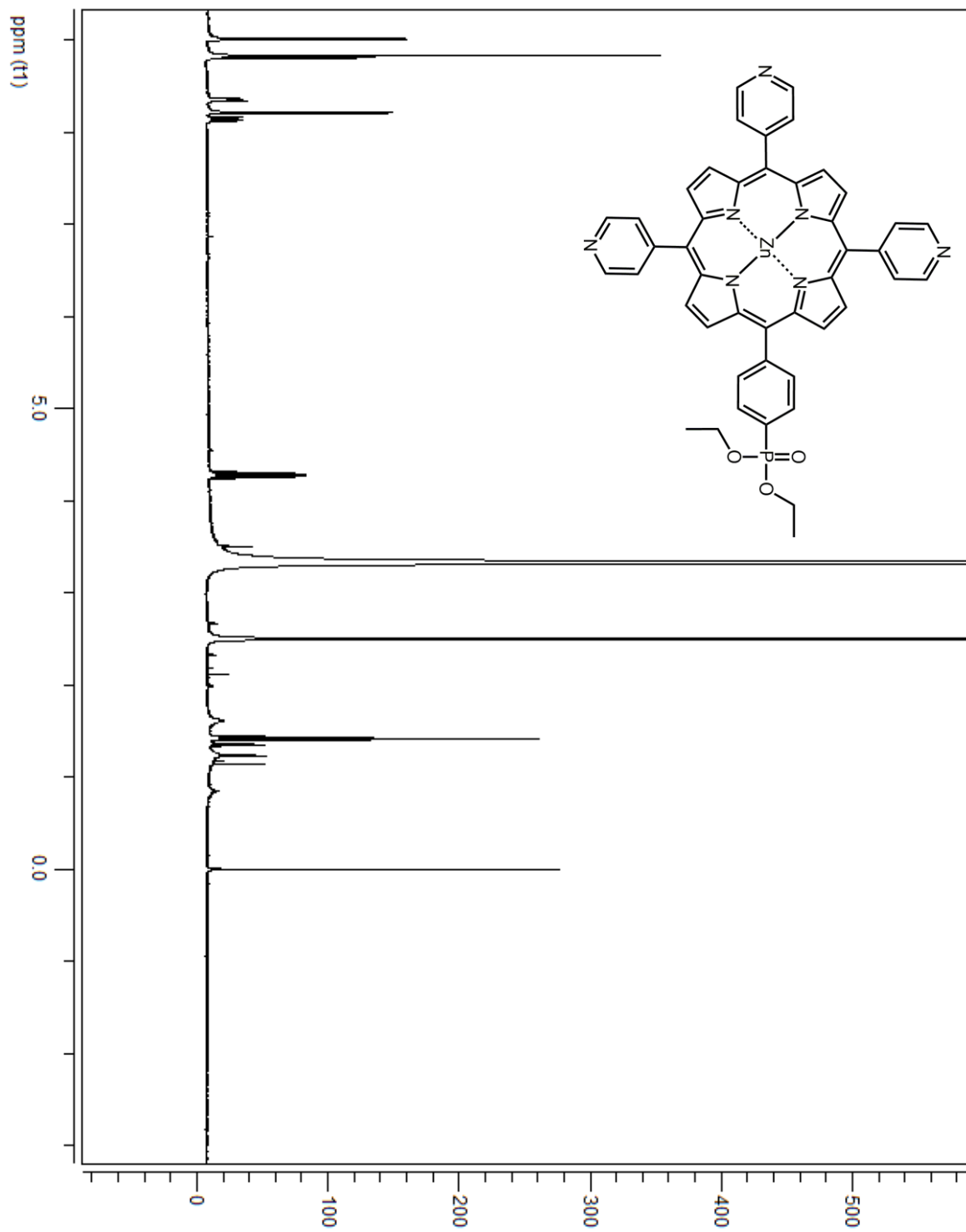


Figure B5. $^1\text{H-NMR}$ of D1E in DMSO-d_6 .

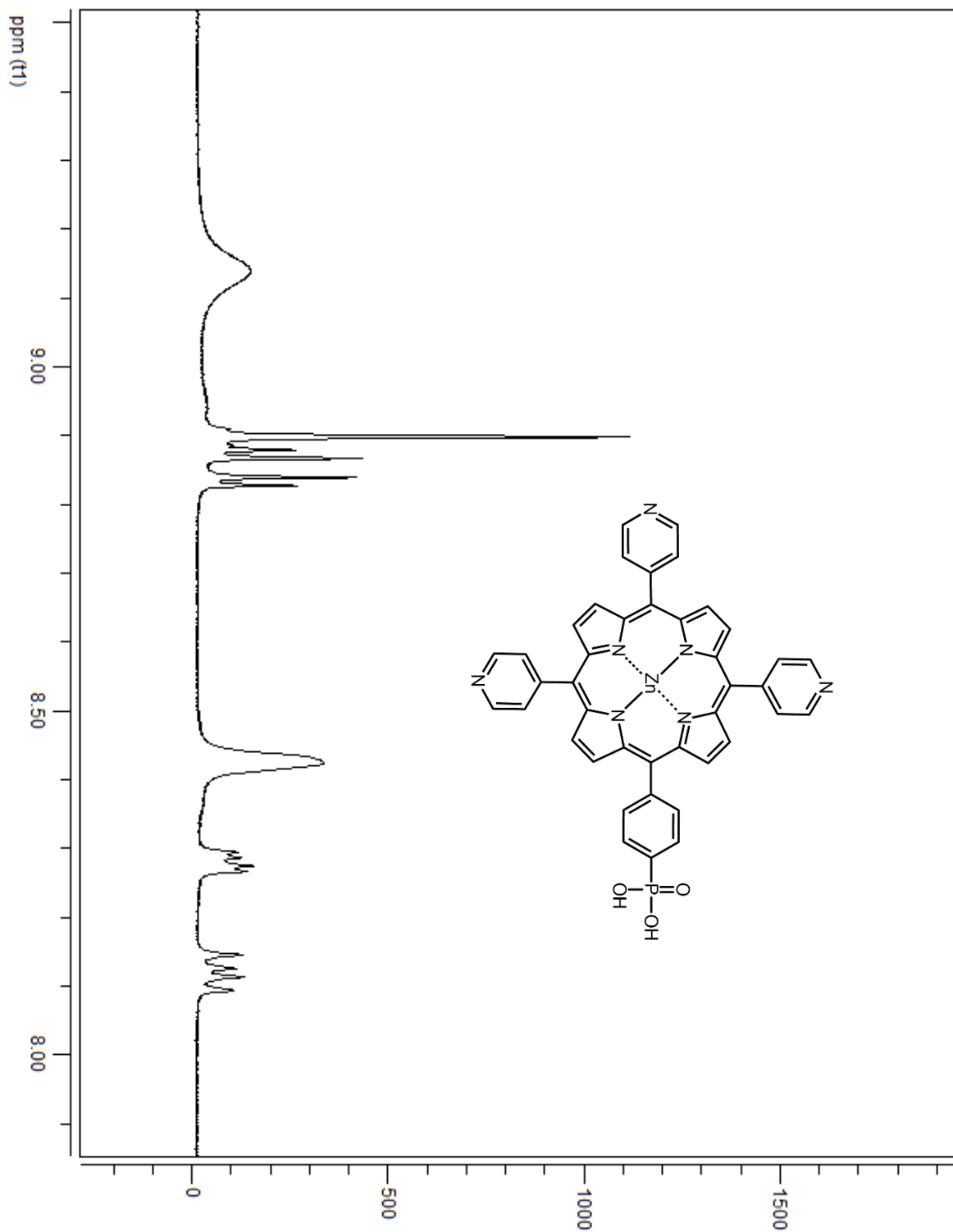


Figure B6. ¹H-NMR of D1 in DMSO-d₆.

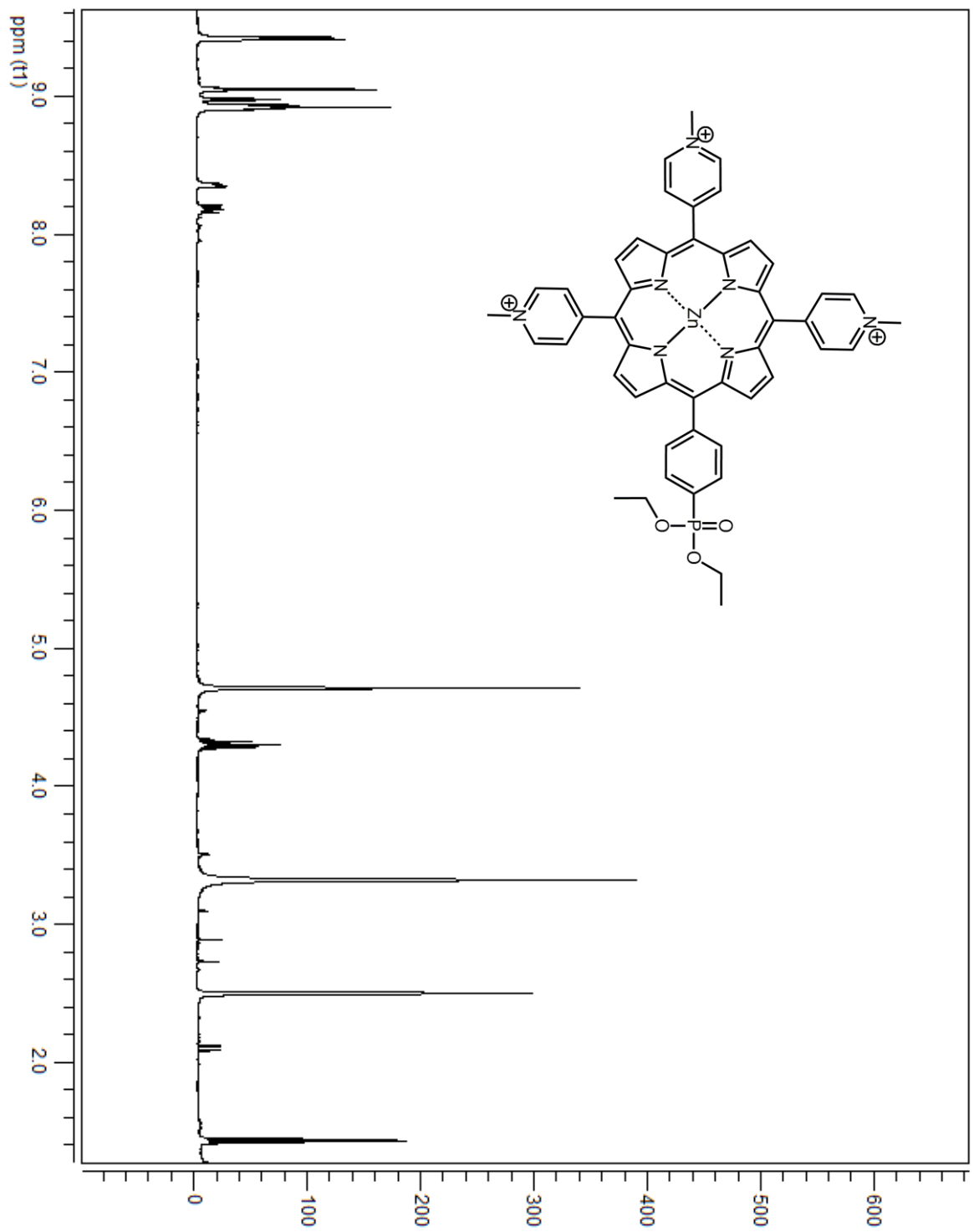


Figure B7. ¹H-NMR of D2E in DMSO-d₆.

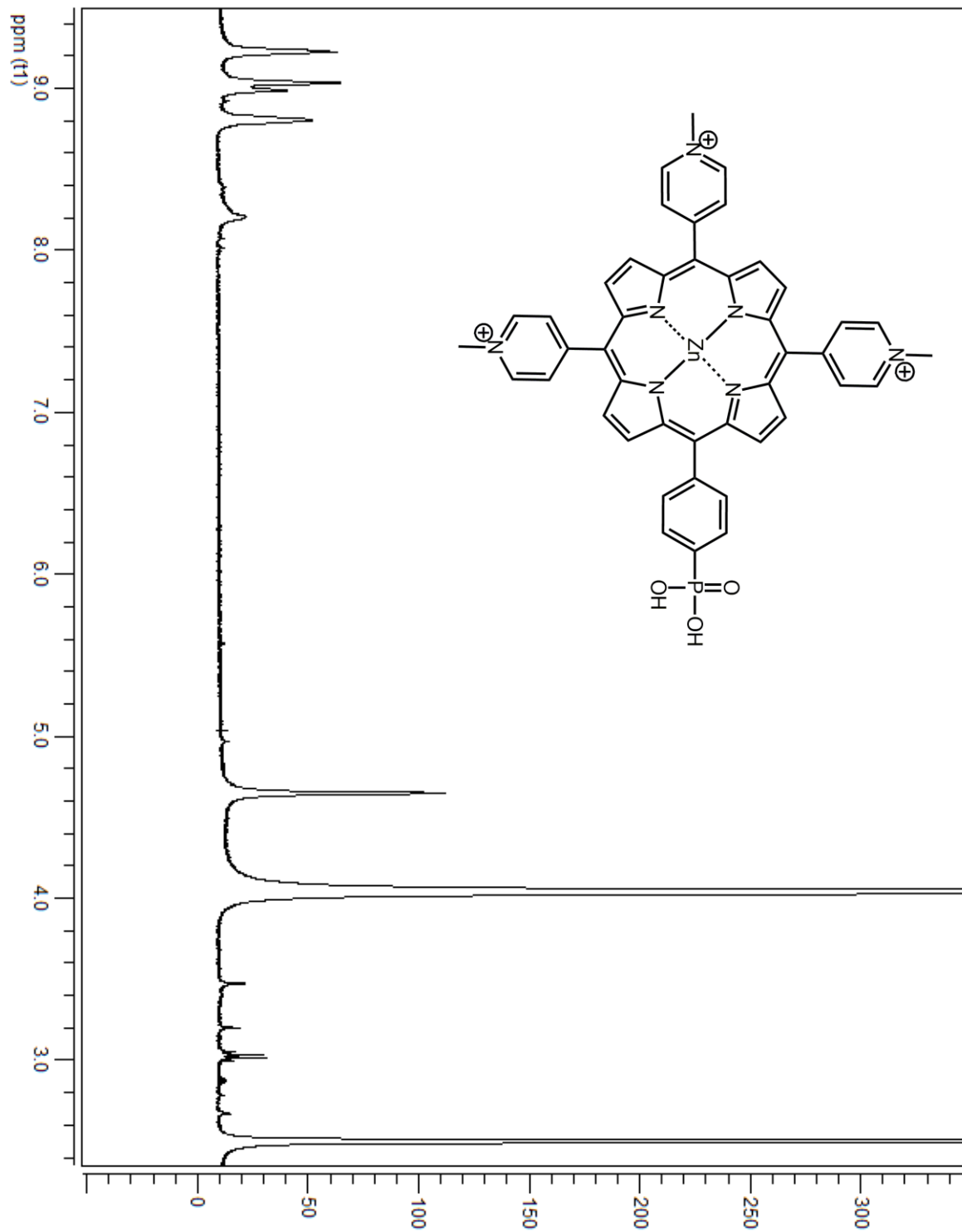


Figure B8. $^1\text{H-NMR}$ of D2 in $\text{DMSO-}d_6/\text{D}_2\text{O}$.

Determination of E_{00} of D1 and D2

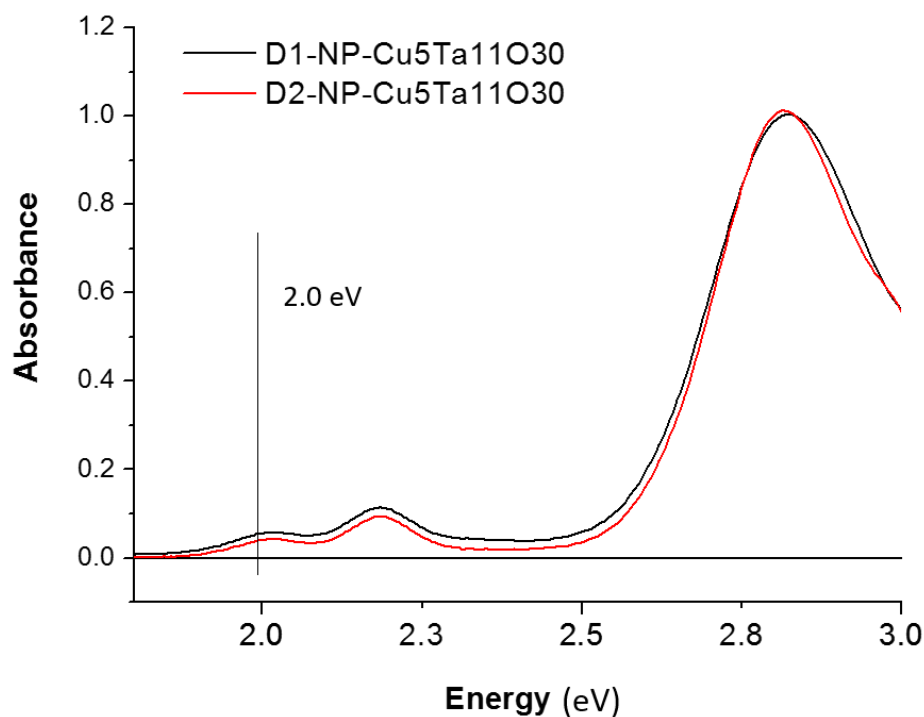


Figure B9. Absorption spectra in ethanol for: a) D1-Cu₅Ta₁₁O₃₀ (black line) and b) D2-NP-Cu₅Ta₁₁O₃₀ (red line).

Photophysics of D1 in its ester form attached to NP-Cu₅Ta₁₁O₃₀.

Following the same procedure described on the main manuscript, D1 in ester form (D1E) was attached to NP-Cu₅Ta₁₁O₃₀. Figure S3 shows how the Soret Q bands of attached D1E shift toward the red and the emission of the dye is completely quenched presumably because the hole injection into the semiconductor.

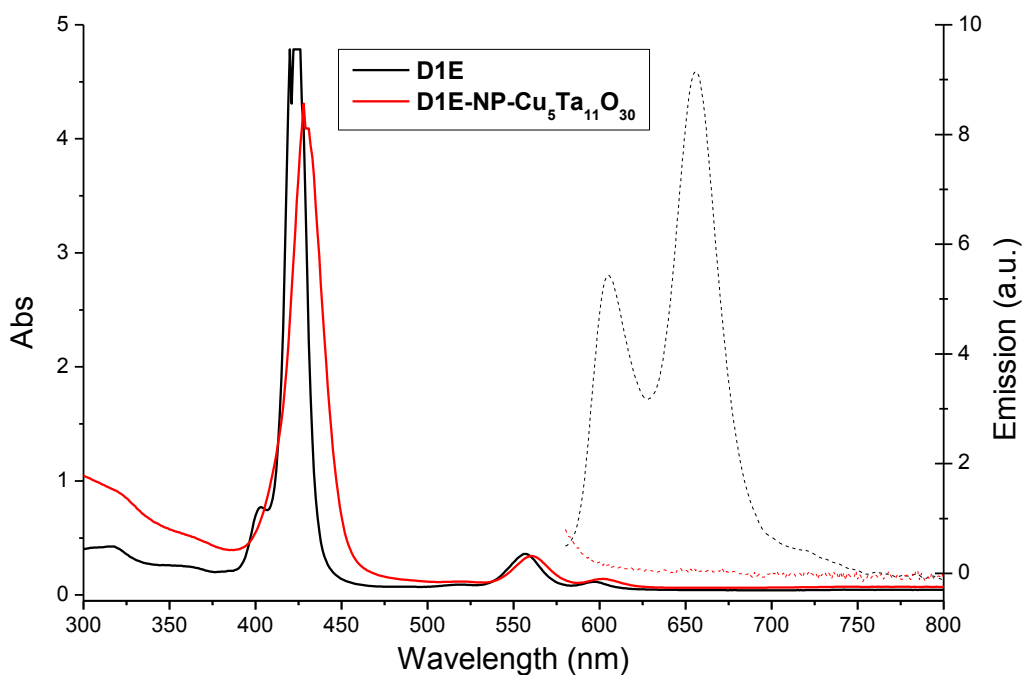


Figure B10. Absorption spectra (solid lines) and emission spectra upon 560 nm excitation (dash lines) in ethanol for D1E–NP–Cu₅Ta₁₁O₃₀ (red) and D1E (black).

Femtosecond transient absorption experiments were performed to establish the kinetics of the photoinduced hole transfer reactions in D1E–NP–Cu₅Ta₁₁O₃₀, in ethanol solution. Global analysis of the transient absorption data for D1E–NP–Cu₅Ta₁₁O₃₀ (Fig. S11) reveals three lifetimes of 800 fs, 15.6 ps, 758 ps and a nondecaying component (not shown) upon excitation at 426 nm (Fig. S4a) and 560 nm (Fig S4b). Since some NP–Cu₅Ta₁₁O₃₀ band gap absorption can be registered at 426 nm, spectra with excitation at 560 nm excitation were recorded finding the same overall features and confirming that the small band gap absorption at 426 nm can be neglected in front of the huge Soret band absorption. The 800 fs DAS can be attributed to the recombination of the charge separated state of the D1E⁺–NP–Cu₅Ta₁₁O₃₀(e⁻) (inverted kinetics), showing ground state bleaching around 560 and 610 nm and induced absorption associated with D1E⁺ between 620 nm and 700 nm. The 15.6 ps DAS can be attributed to the hole injection from D1E* to the valence band of the Cu₅Ta₁₁O₃₀ showing ground state bleaching around 560 and 610 nm and decay of the stimulated emission around 620 and 670 nm. The 758 ps DAS can be attributed to decay of the singlet excited state of the non-attached(physisorbed)/aggregated dye, which is not involved in the hole injection process, ground state bleaching and stimulated emission bands are slightly blue shifted. Due to the high nonhomogeneity (heterogeneity) of the system, obtained lifetimes do not correspond to single species. These lifetimes represent an average of the decay of several slightly different species. For D1E–NP–Cu₅Ta₁₁O₃₀ there is likely some population with very fast formation of charge separate state (<100 fs), this would explain high amplitude of 0.8 ps DAS in such inverted kinetics case, but overall the rate of decay of the charge-separated species is greater than the average effective rate of formation.

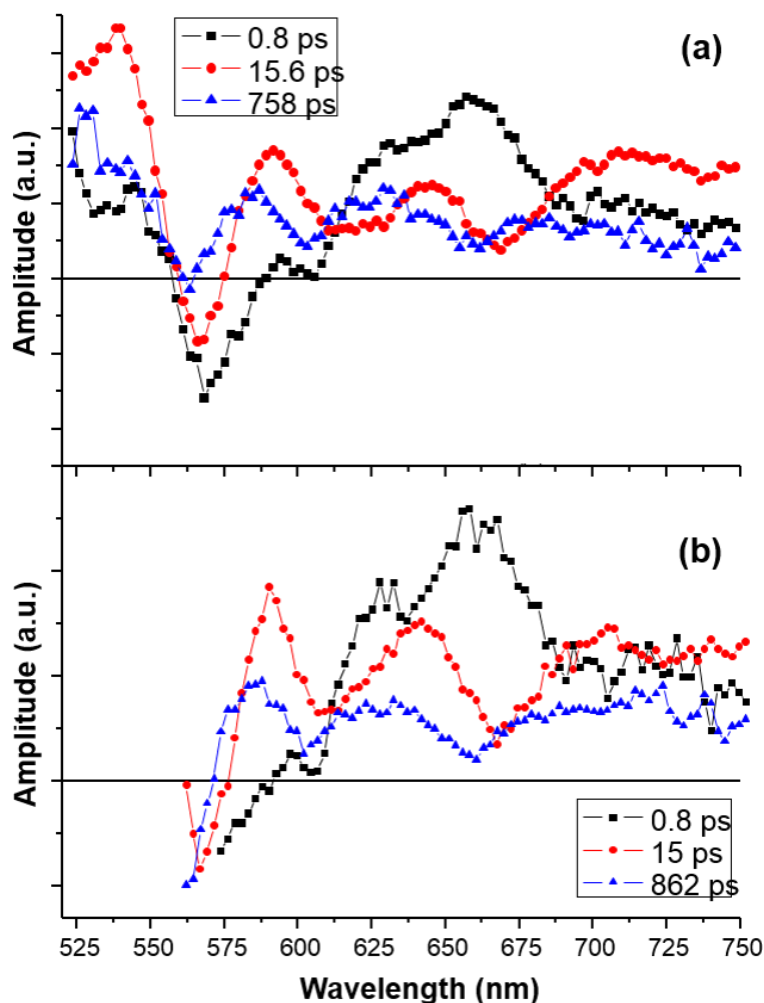


Figure B11. Decay-associated-spectra in ethanol measured by fs transient absorption upon excitation at a) 426 nm and b) 560 nm for D1E–NP–Cu₅Ta₁₁O₃₀.

DSSC Efficiency Calculations

Fill factor and efficiency for the DSSCs were calculated by using Equations S1 and S2:

$$ff = \frac{I_{mp}V_{mp}}{I_{sc}V_{oc}} = \frac{Area\ B}{Area\ A} \quad (S1)$$

$$\eta = I_{sc}V_{oc} \left(\frac{ff}{I_c} \right) \quad (S2)$$

Where ff is the fill factor, I_{mp} is maximum power current, V_{mp} is maximum power voltage, I_{sc} is the short circuit current, V_{oc} is the open circuit potential, I_c is incident power from the light source (100 mW/cm²) and η is the photo-conversion efficiency (PCE)¹ and is graphically shown in Figure S5. Current-potential scans were performed on a CH-Instruments CH-620a potentiostat under simulated solar irradiance using an AM 1.5 G filter (Oriel). Scans were started near the open circuit voltage and scanned towards the short circuit condition (0.0 V) at a scan rate of 10 mV s⁻¹. The semiconducting film served as the working electrode, while

the Pt deposited FTO served as the counter and reference electrode. Power curves were made by multiplying the voltage and currents obtained and plotting against the voltage range used, shown in Figure S5. Shown in Figure S6 are the i-v curves for the control experiments in the absence of sensitizing dye. Currents from the control are negligible and do not show any large changes between dark and light conditions, indicating that the dye must be present for any photoinjection to occur.

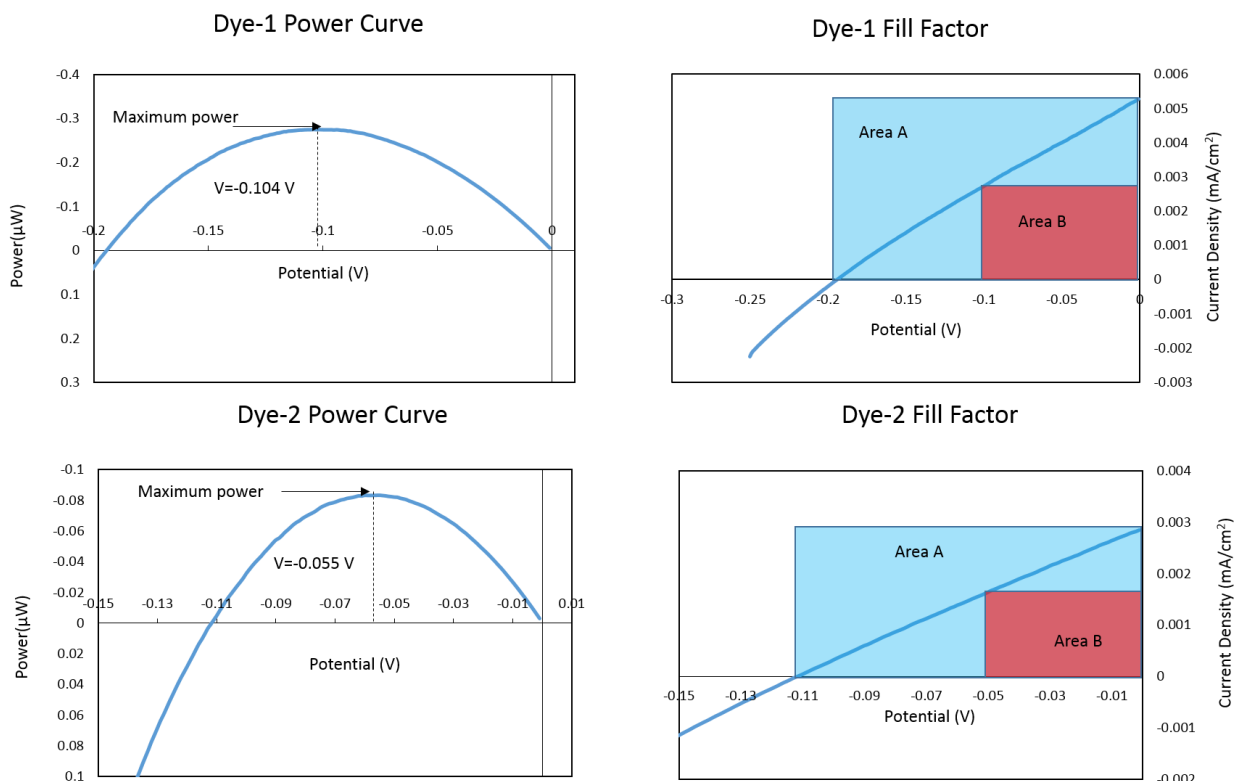


Figure B12: Power-voltage (P-V) curves and fill factor (ff) plots for Dye-1 (top) and Dye-2 (bottom) on nanoparticle $\text{Cu}_5\text{Ta}_{11}\text{O}_{30}$ films.

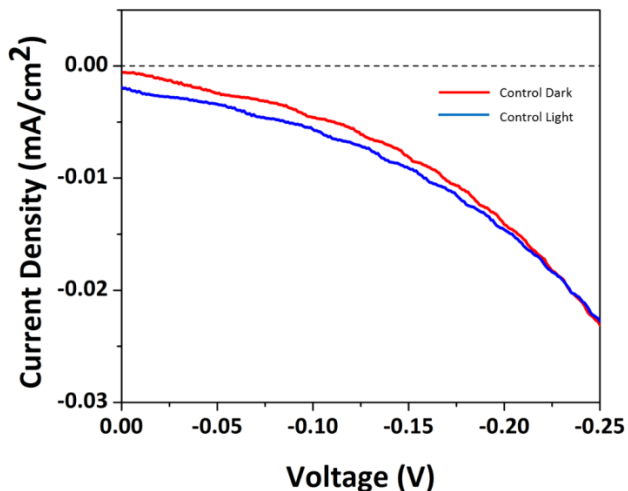


Figure B13. Control i-v curves for $\text{Cu}_5\text{Ta}_{11}\text{O}_{30}$ nanoparticle films without dye.

	<u>Dye-1</u>	<u>Dye-2</u>
V_{oc} (V)	0.2	0.11
I_{sc} (A)	5.28E-06	2.85E-06
I_{mp}	2.64E-06	1.51E-06
V_{mp}	0.104	0.055
FF	2.60E-01	2.65E-01
η	2.75E-04	8.31E-05

Table B1. Table of Parameters Determined in the Efficiency Calculations.

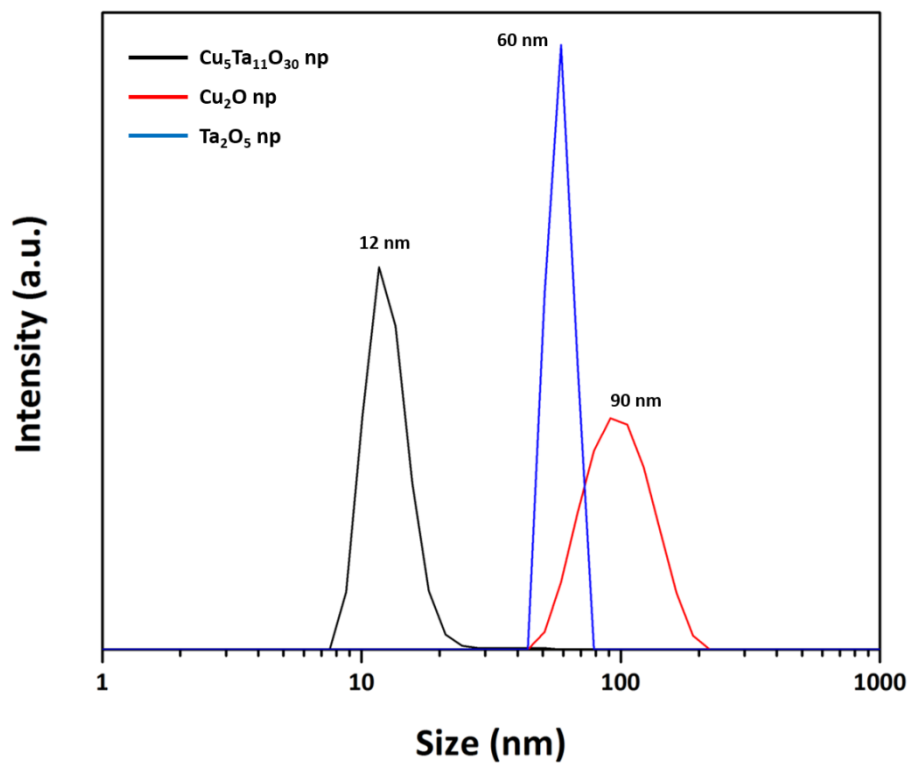


Figure B14. Particle size distributions of Cu_2O (red) and Ta_2O_5 (blue) nanoparticle precursors and $Cu_5Ta_{11}O_{30}$ nanoparticle product (black).

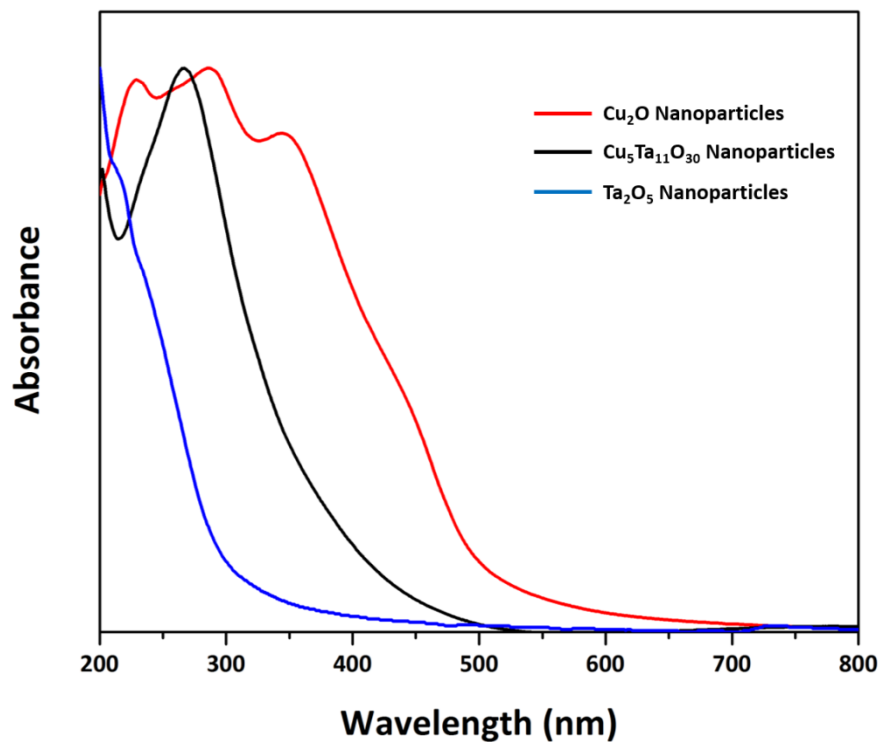


Figure B15. UV-Vis of suspended Cu₂O (red), Ta₂O₅ (green) and Cu₅Ta₁₁O₃₀ (black) nanoparticles.

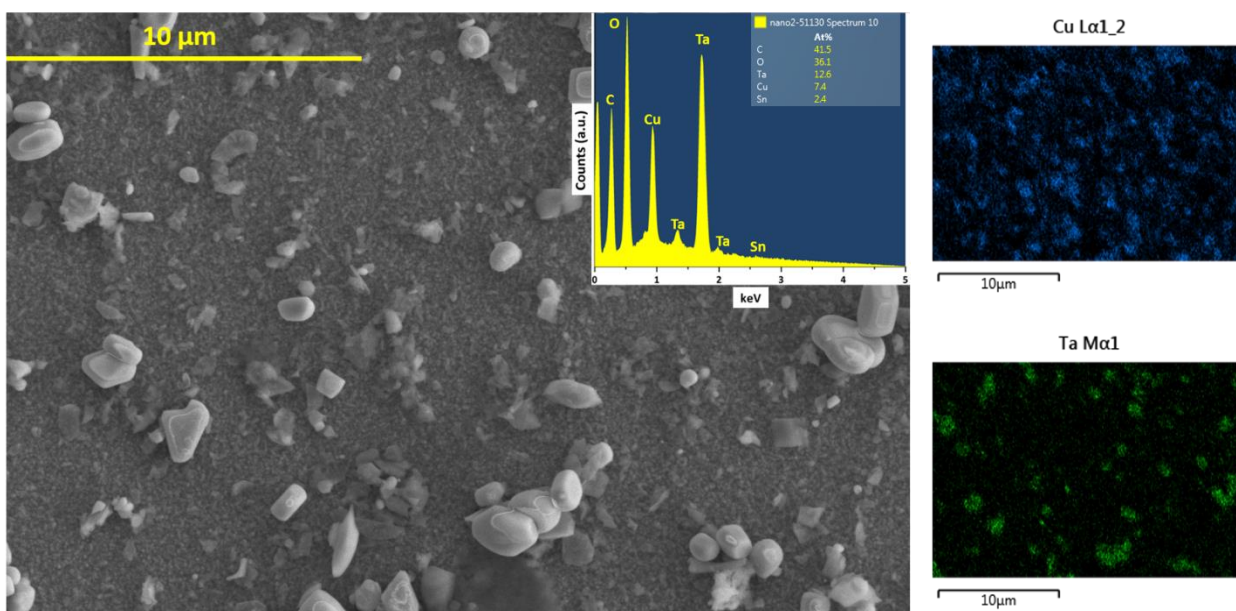


Figure B16. FESEM image of an annealed film of $\text{Cu}_5\text{Ta}_{11}\text{O}_{30}$ nanoparticles in solution with elemental mapping of Cu and Ta (right). Inset: EDS spectrum of the area.

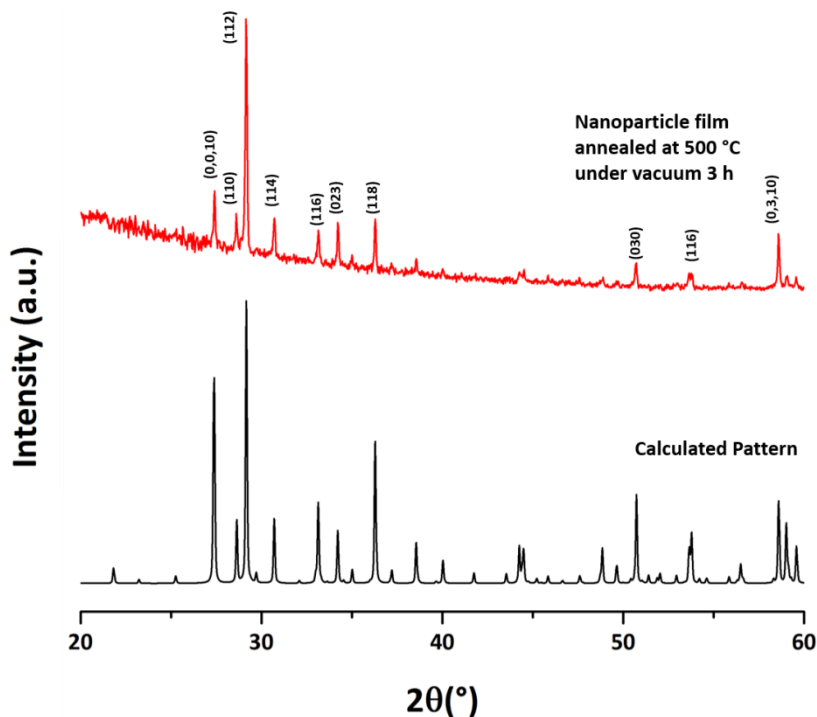


Figure B17. Powder X-ray diffraction pattern of the $\text{Cu}_5\text{Ta}_{11}\text{O}_{30}$ film (upper), and comparison to a calculated pattern based on the known crystalline structure of $\text{Cu}_5\text{Ta}_{11}\text{O}_{30}$ (lower).

EXPERIMENTAL SECTION

Materials. For the $\text{Cu}_5\text{Ta}_{11}\text{O}_{30}$ nanoparticles: copper sulfate (anhydrous, 99%), tantalum pentachloride (99.9%), ascorbic acid (anhydrous, 99.9%), sodium hydroxide (99%) and copper(I) chloride (anhydrous, 99.9%) were all purchased from Alfa Aesar. 200 proof anhydrous ethanol was purchased from Koptek.

High Resolution Transmission Electron Microscopy. TEM micrographs were collected using a Philips CM200 TEM at 200kV, Cs 1.2 mm, PTP Resolution: 0.25nm Focused Probe: 0.5nm and Imaging Modes: TEM/STEM. TEM micrographs were analyzed using *Digital Micrograph*TM software.²

Powder X-ray Diffraction. The $\text{Cu}_5\text{Ta}_{11}\text{O}_{30}$ products were characterized by powder X-ray diffraction using an Inel X-ray diffractometer and $\text{Cu K}\alpha_1$ radiation ($\lambda=1.54056 \text{ \AA}$) from a sealed tube X-ray generator (30 mA, 35 kV). A curved position sensitive detector (CPS-120) was used in transmission mode.

Steady State Absorption and Fluorescence. Spectra were recorded in 1 cm path length cuvettes with the following spectrophotometers: diode array HP 8452, Shimadzu - UV-IR (2041PC), and Hitachi double beam UV/Vis spectrophotometer (U-2800). Steady-state fluorescence spectra were measured using a Photon Technology International MP-1 spectrometer and corrected for detection system response and excitation source intensity as a function of wavelength. Excitation was provided by a 75 W xenon-arc lamp and single-grating monochromator. Fluorescence was detected at 90° to the excitation beam via a single-grating monochromator and an R928 photomultiplier tube having S-20 spectral response and operating in the single photon counting mode.

Time Resolved Absorption. Femtosecond to nanosecond transient absorption measurements were acquired with a kilohertz pulsed laser source and a pump-probe optical setup. Laser pulses of 100 fs at 800 nm were generated from an amplified, mode-locked titanium sapphire kilohertz laser system (Millennia/Tsunami/Spitfire, Spectra Physics). Part of the laser pulse energy was sent through an optical delay line and focused onto a 3 mm sapphire plate to generate a white light continuum for the probe beam. The remainder of the pulse energy was used to pump an optical parametric amplifier (Spectra Physics) to generate excitation pulses, which were selected using a mechanical chopper. The white light generated was then compressed by prism pairs (CVI) before passing through the sample. The polarization of the pump beam was set to the magic angle (54.7°) relative to the probe beam and its intensity was adjusted using a continuously variable neutral density filter. The white light probe was dispersed by a spectrograph (300 line grating) onto a charge-coupled device (CCD) camera (DU420, Andor Tech.). The final spectral resolution was about 2.3 nm for over a nearly 300 nm spectral region. The instrument response function was ca. 100 fs. The decay-associated spectra (DAS) were obtained by fitting globally the transient absorption kinetic traces over a selected wavelength region simultaneously as described by equation (1) (parallel kinetic model).³

$$\Delta A(\lambda, t) = \sum_{i=1}^n A_i(\lambda) \exp(-t / \tau_i) \quad (1)$$

where $\Delta A(\lambda, t)$ is the observed absorption change at a given wavelength at time delay t and n is the number of kinetic components used in the fitting. A plot of $A_i(\lambda)$ versus wavelength is called a DAS and represents the amplitude spectrum of the i^{th} kinetic component, which has a lifetime of τ_i . Random errors associated with the reported lifetimes obtained from transient absorption measurements were typically $\leq 5\%$. Rigorous analysis of time resolved emission and absorption data in a non-homogeneous system requires the use of a model which considers a distribution of multi-exponential decays to describe the kinetics of each transient species and thus accounts for the distribution of available environments in the heterogeneous system. In our analysis we used the minimum number of exponential components that adequately fitted the experimental data within the experimental error. Thus it is likely that the reported decay components correspond to a weighted mean value of the actual distribution of constants associated with each species.

Dynamic Light Scattering Measurements. Dynamic light scattering measurements were performed on a Malvern Zetasizer Nano S with detector 173° from the incident beam and a laser wavelength of 633 nm. Nanoparticles of $\text{Cu}_5\text{Ta}_{11}\text{O}_{30}$, Cu_2O and Ta_2O_5 were separately suspended in ethanol and measurements were taken at a temperature of 25° C, with single size distributions observed for each sample. Ta_2O_5 and Cu_2O precursor nanoparticles have size distributions centered around 60 nm and 90 nm, respectively, with $\text{Cu}_5\text{Ta}_{11}\text{O}_{30}$ nanoparticles having a lower size distribution centered around 12 nm. This is due to the dissolution of the precursors in the CuCl flux and then re-crystallization at a smaller size.

Electronic Absorption Spectroscopy of Nanoparticle Solutions. Electronic absorption spectra were taken of suspended particles in ethanol using a Shimadzu UV 3600. The suspensions of Cu_2O , Ta_2O_5 and $\text{Cu}_5\text{Ta}_{11}\text{O}_{30}$ show different absorption profiles shown in Figure S8. Cu_2O absorbs around 2.3 eV, Ta_2O_5 absorbs around 4.0 eV and $\text{Cu}_5\text{Ta}_{11}\text{O}_{30}$ absorbs around 3.0 eV.

Field Emission Scanning Electron Microscopy and Energy Dispersive Spectroscopy (FESEM/EDS). FESEM/EDS measurements were taken on an FEI Verios 460L field emission scanning electron microscope. Nanoparticle films were deposited from an ethanol solution, then annealed at 200 °C for 2 h under dynamic vacuum. Images show nanoparticle films on fluorine doped tin oxide (FTO) with a Cu-Ta ratio of 2:1, in agreement with the Cu-Ta ratio in $\text{Cu}_5\text{Ta}_{11}\text{O}_{30}$. Small amounts of Sn are also detected from the FTO substrate. Elemental mapping shows the coverage of Cu and Ta across the entire area of the film.

X-ray Diffraction of Annealed Films. Suspended nanoparticles in ethanol were deposited on fluorine doped tin oxide (FTO) and allowed to dry in air leaving a film of the nanoparticles. The film was heated to 500 °C for 3 h under dynamic vacuum and allowed to cool to room temperature before removing from the tube furnace. Scotch tape was then used to remove the film from the FTO and taken for X-ray diffraction (XRD). Diffraction patterns of the material match the calculated pattern for $\text{Cu}_5\text{Ta}_{11}\text{O}_{30}$, with peaks indexed in Figure S17. Preferential orientation is observed for the thin films with dominant diffraction on the (112) reflection.

REFERENCES

- (1) Odobel, F.; Pellegrin, Y. Recent Advances in the Sensitization of Wide-Band-Gap Nanostructured p-Type Semiconductors. Photovoltaic and Photocatalytic Applications. *J. Phys. Chem. Lett.* 2013, 4(15), 2551-2564.
- (2). Mitchell, D.R.; Schaffer, B. Scripting-customized microscopy tools for Digital Micrograph. *Ultramicrosc.* 2005, 103(4), 319-332.
- (3) Van Stokkum, I.H.M.; Larsen, D.S.; Van Grondelle, R. Global and target analysis of time-resolved spectra. *Biochim. Biophys. Acta* 2004, 1657, 82-104.

APPENDIX C

Supporting Information

Flux-mediated Syntheses, Structural Characterization, and Polymorphism of the *p*-Type Semiconductor Cu₂Ta₄O₁₁

Nacole King,^a Ian Sullivan^a, Pilanda Watkins-Curry,^{b,c} Julia Y. Chan^c and Paul A. Maggard^{a,*}

^a*Department of Chemistry, North Carolina State University, Raleigh, NC 27695-8204.*

^b*Department of Chemistry, Louisiana State University, Baton Rouge, LA*

^c*Department of Chemistry, The University of Texas at Dallas, Richardson, TX 75080-4551.*

Table C1. The atomic positions, Isotropic Displacement Parameters (Å), and Wyckoff sites for the refined structure of α -Cu₂Ta₄O₁₁ at 298 K.

α-Cu₂Ta₄O₁₁ Rietveld Refinement 298 K								
Refined Chemical Formula	Space Group	Atom	Wyckoff Site	<i>x</i>	<i>y</i>	<i>z</i>	U _{iso}	Occ. \neq 1 ^a
Cu ₂ Ta ₄ O ₁₁	<i>Cc</i>	Ta1	4	0.521(6)	0.0694(17)	0.634(3)	0.022(3)	
		Ta2	4	0.160(6)	0.0671(13)	0.535(4)	0.019(3)	
		Ta3	4	0.343(6)	0.6092(6)	0.540(4)	0.0229(17)	
		Ta4	4	0.603(6)	0.243(2)	0.286(4)	0.0305(15)	
		Cu1	4	0.820(7)	0.501(6)	0.294(4)	0.068(2)	0.67
		Cu2	4	0.363(7)	0.482(5)	0.305(4)	0.024(15)	0.67
		Cu3	4	0.611(7)	0.240(5)	0.786(4)	0.012(8)	0.67
		O1	4	0.493(9)	-0.251(12)	0.485(5)	0.02	
		O2	4	0.329(9)	-0.001(6)	0.520(6)	0.02	
		O3	4	0.480(7)	0.371(8)	0.591(5)	0.02	
		O4	4	0.544(8)	0.050(11)	0.691(6)	0.02	
		O5	4	0.492(9)	0.116(10)	0.369(8)	0.02	
		O6	4	0.203(8)	0.403(12)	0.539(9)	0.02	
		O7	4	0.266(9)	0.628(11)	0.384(7)	0.02	
		O8	4	0.417(9)	0.343(12)	0.205(7)	0.02	
		O9	4	0.669(8)	0.441(10)	0.201(7)	0.02	
		O10	4	0.590(8)	0.481(11)	0.883(7)	0.02	
O11	4	0.179(9)	0.741(13)	0.553(5)	0.02			

^a The U_{iso} for the Cu sites in the structure were refined as 0.67(5) and were not statistically different.

Table C2. Lattice Constant Refinements $\text{Cu}_2\text{Ta}_4\text{O}_{11}$ in the temperature range of 223 K to 723 K. The lattice constants of powder X-ray samples at the temperature 223 K and 298 K were refined and indexed using a monoclinic Cc unit cell, powder samples at 523 K, 623 K, and 723 K were refined and indexed using a rhombohedral $R\bar{3}c$ unit cell.

Temperature (K)	a (Å)	b (Å)	c (Å)	β (°)	Volume (Å ³)
223 K	10.7349(15)	6.2512(3)	12.8882(15)	106.071(4)	831.08(12)
298 K	10.7337(14)	6.2506(3)	12.8869(14)	106.070(4)	830.82(12)
523 K	6.2322(1)	6.2322	37.1745(4)	90	1250.46(3)
623 K	6.2299(1)	6.2299	37.1471(4)	90	1248.61(3)
723 K	6.2285(2)	6.2285	37.1297(6)	90	1247.46(4)

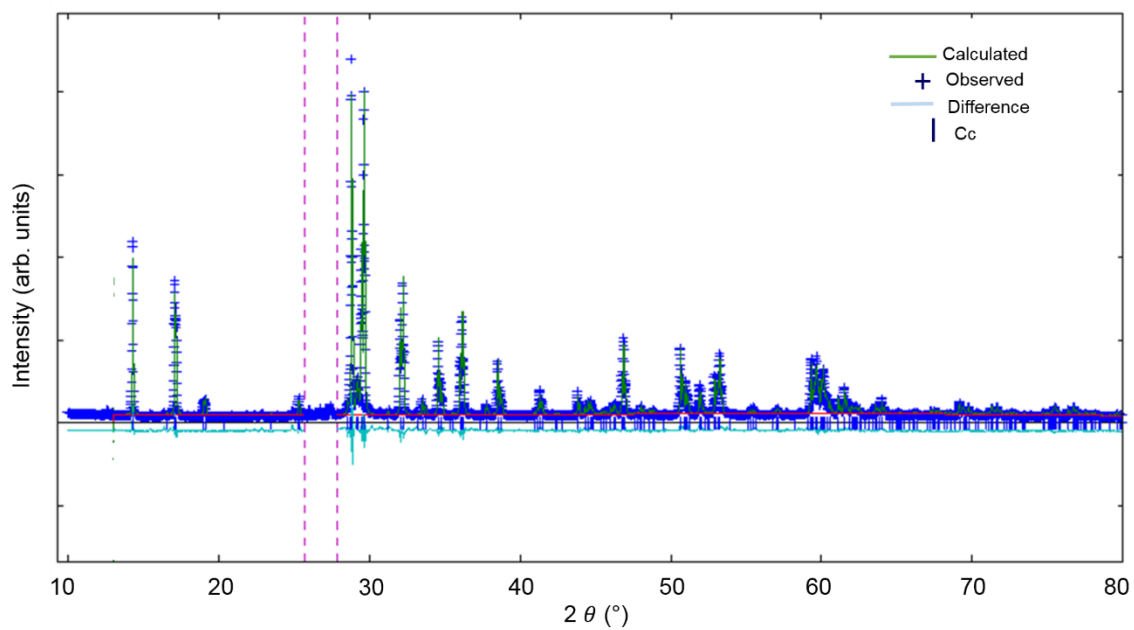


Figure C1. The Rietveld refinement pattern of the monoclinic α - $\text{Cu}_2\text{Ta}_4\text{O}_{11}$ at 223 K under flowing nitrogen. The observed intensities are indicated in blue (+), calculated intensities in green, the difference pattern is indicated by light blue, and the peak positions of α - $\text{Cu}_2\text{Ta}_4\text{O}_{11}$ in the monoclinic Cc space group are indicated by the blue tick marks. Impurities of Ta_2O_5 were masked as indicated by the purple lines.

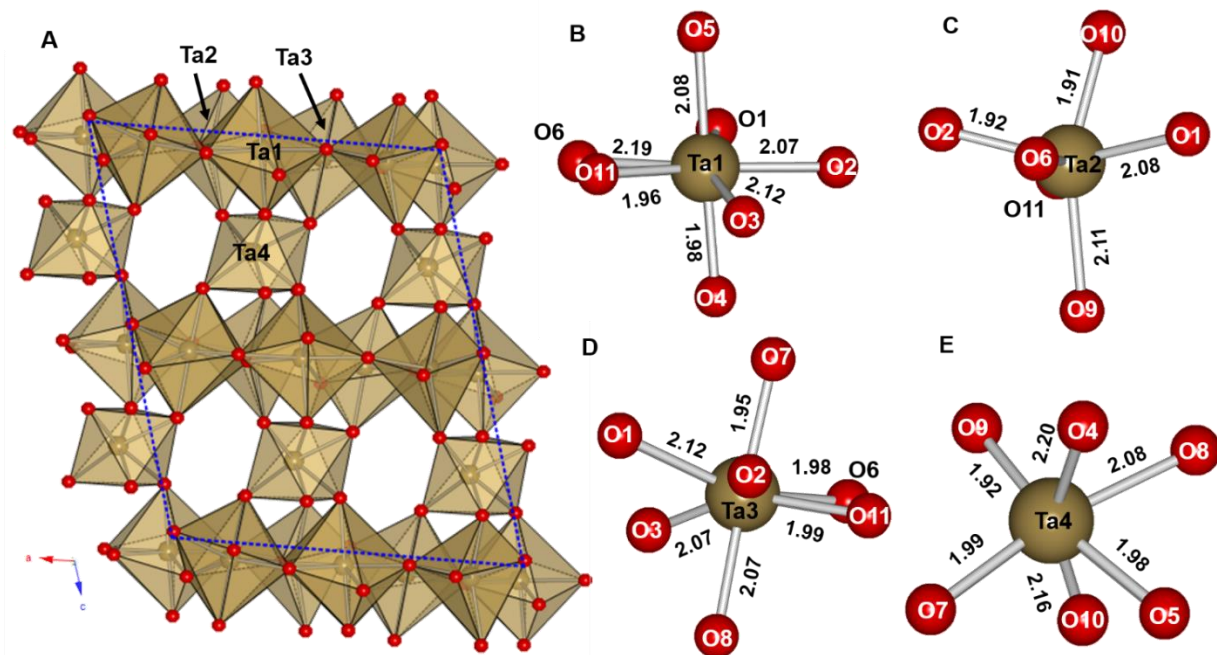


Figure C2. A) The crystal structure of a unit cell of $\alpha\text{-Cu}_2\text{Ta}_4\text{O}_{11}$ along the ac direction showing the coordination of TaO₆ and TaO₇ polyhedra in the distorted tantalate layer to the TaO₆ octahedra in the alternating layer with the unit cell outlined in dashed blue line. B-E) Local coordination environment of Ta1, Ta2, Ta3, and Ta4 cations with the interatomic distances shown. The Ta cations and polyhedra are shown in tan, and the O atoms are shown in red.

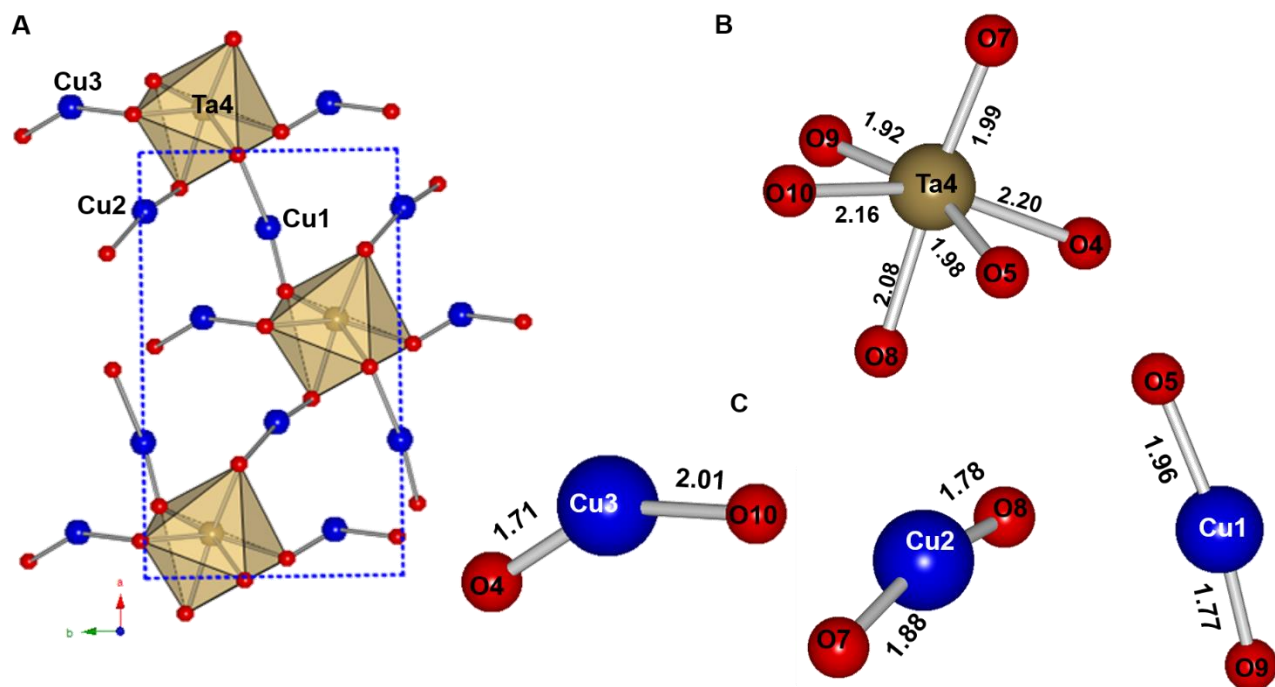


Figure C3. A) The crystal structure of α - $\text{Cu}_2\text{Ta}_4\text{O}_{11}$ along the ab direction of the layer of linearly coordinated Cu cations bridged to the TaO₆ octahedra with the unit cell outlined in a blue dashed line. B-C) The local coordination environments of Ta4 and the symmetry inequivalent Cu(I) cations are shown with the interatomic distances displayed. The Ta cations and polyhedra are shown in tan, the Cu and O atoms are shown in blue and red, respectively.

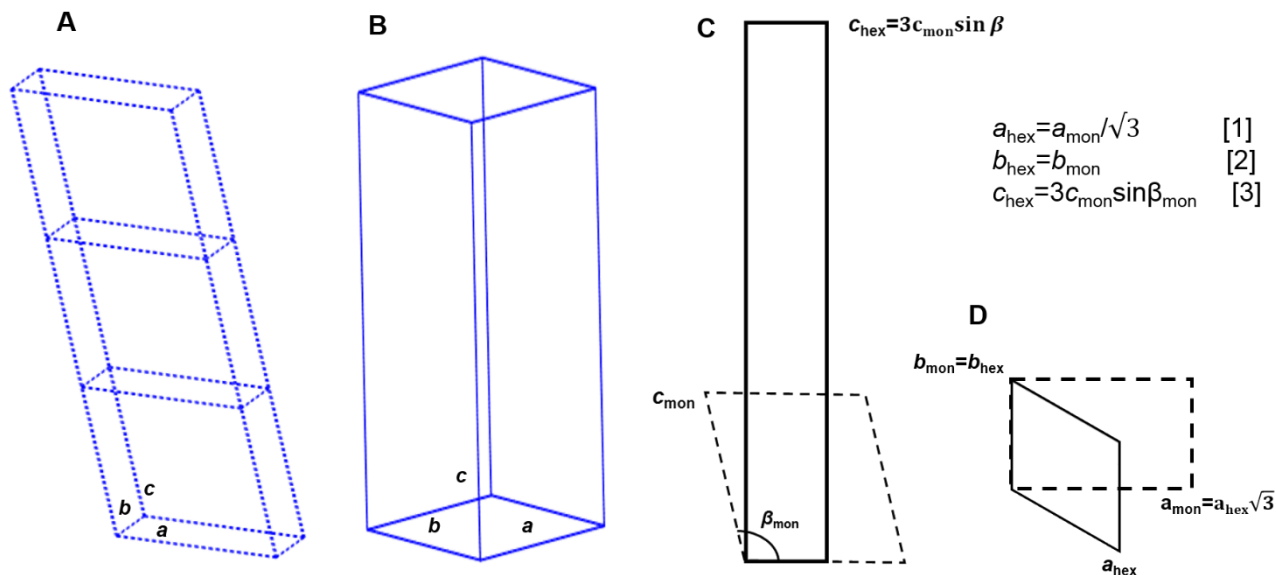


Figure C4. Figures adapted from Jahnberg indicating the relationship between the phase transition from a monoclinic to a rhombohedral unit cells A) 3 monoclinic unit cells stacked on top of each other outlined in the dashed line along the ab plane and B) the hexagonal unit cell outlined in the solid line. C) a single monoclinic unit cell outlined in a dashed line along the bc plane with the β angle shown in relation to the [001] of the rhombohedral unit cell. D) the ab plane of the monoclinic unit cell outlined in a dashed line in relation to the [100] direction of a hexagonal unit cell outlined in a solid line. The equations [1] to [3] reported from Ercit et. al.³⁸

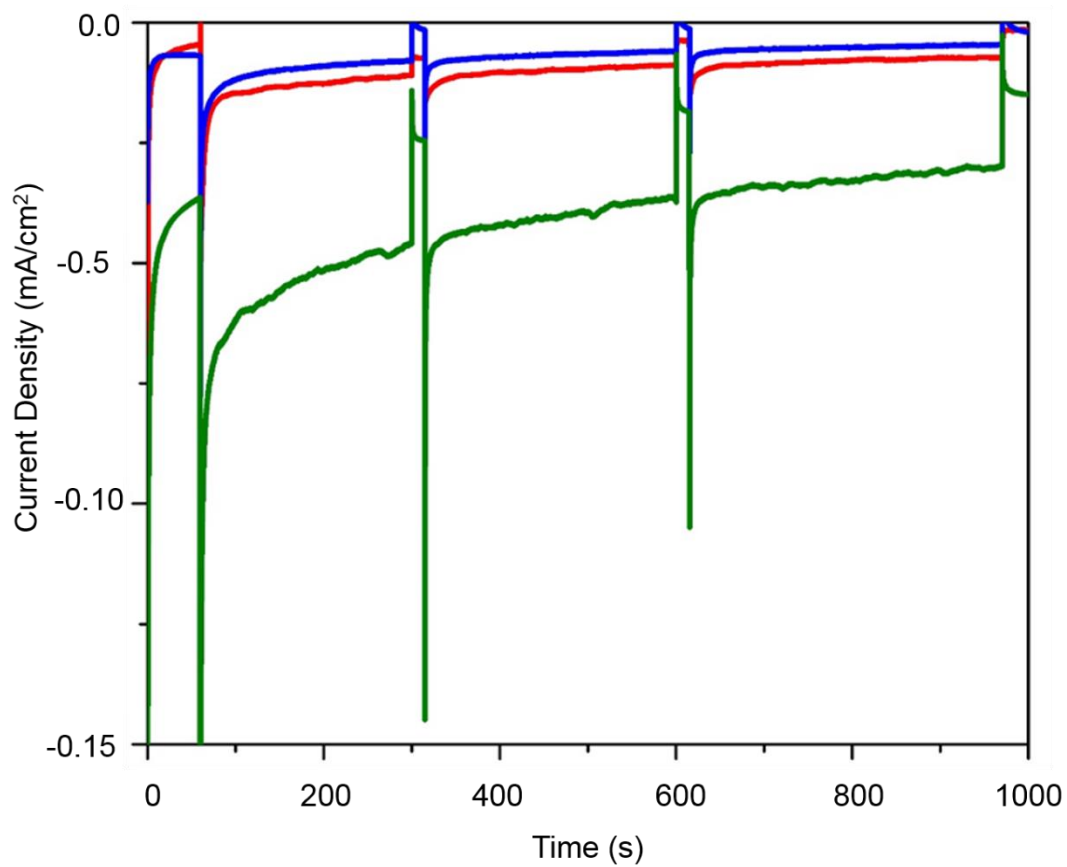


Figure C5. Chronoamperometric scans of the monoclinic α - $\text{Cu}_2\text{Ta}_4\text{O}_{11}$ polycrystalline films that were annealed under vacuum at 500 °C for 3 h a) not heated in air b) heated in air at 250 °C for 3 h, c) heated in air 350 °C.

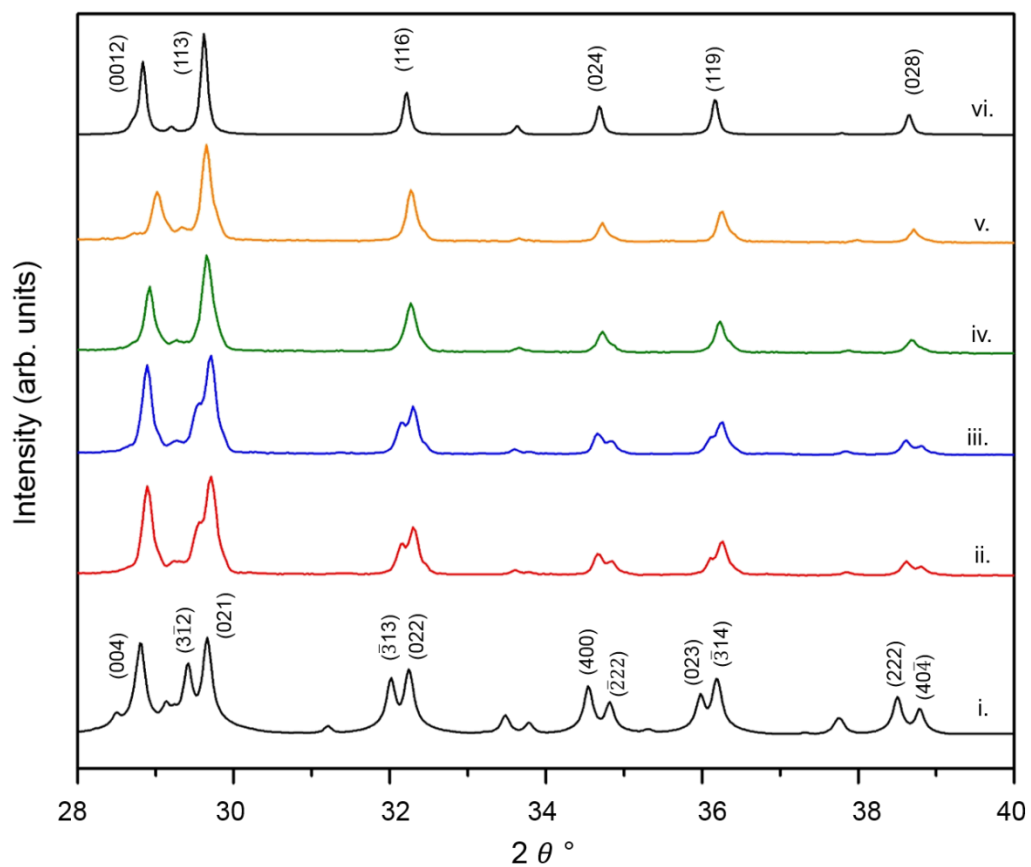


Figure C6. The powder X-ray diffraction patterns of $\text{Cu}_2\text{Ta}_4\text{O}_{11}$ before and after heating in air after photoelectrochemical measurements i) simulated XRD of $\alpha\text{-Cu}_2\text{Ta}_4\text{O}_{11}$ ii) before heating iii) after heating at 250 °C, iv) after heating at 350 °C, v) after heating at 450 °C vi) simulated XRD of the rhombohedral $\beta\text{-Cu}_2\text{Ta}_4\text{O}_{11}$.

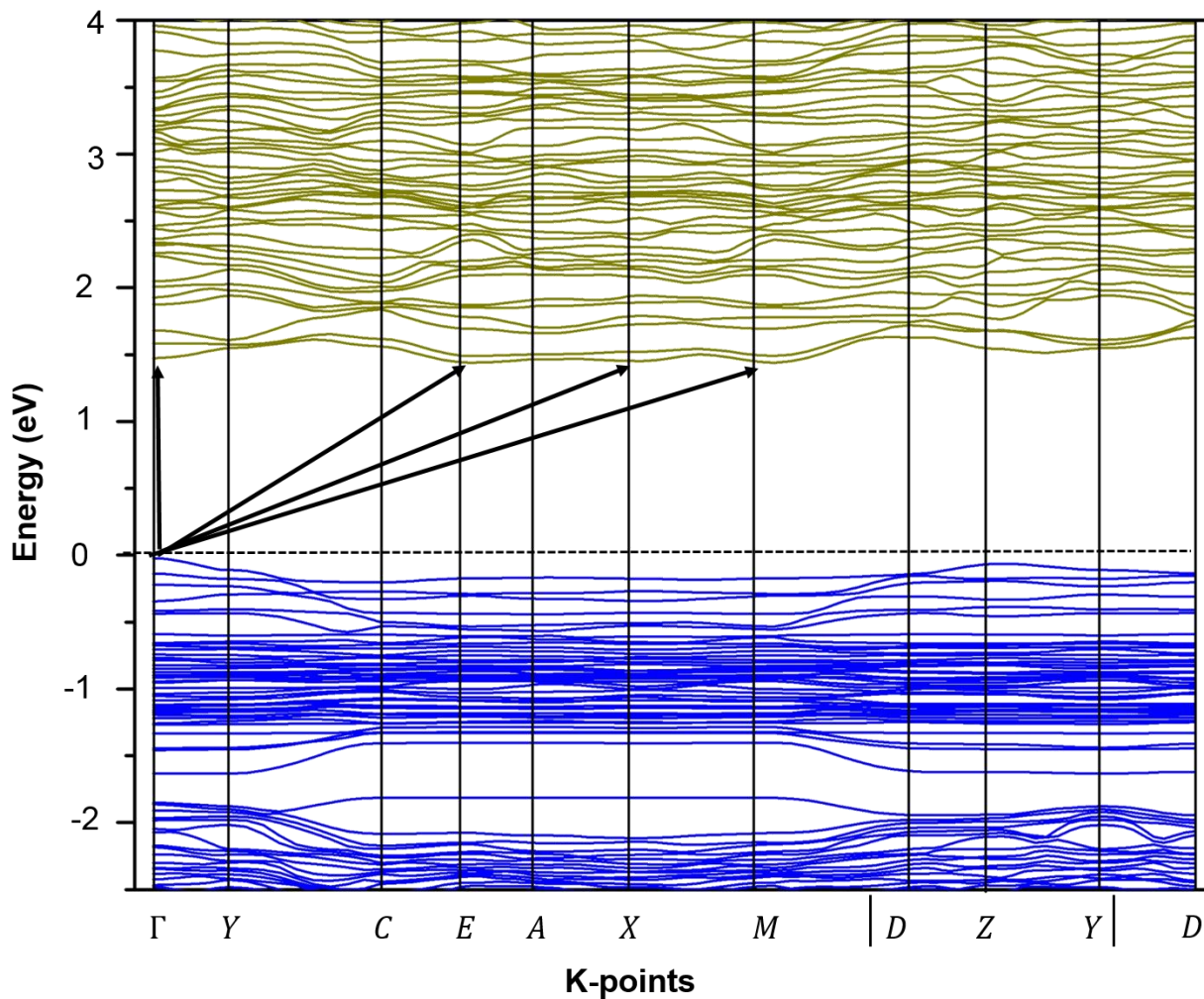


Figure C7. The calculated band structure diagram of $\alpha\text{-Cu}_2\text{Ta}_4\text{O}_{11}$ with contributions from the valence and conduction band in blue and tan respectively. The indirect and direct band gap transitions are indicated with a black arrow.

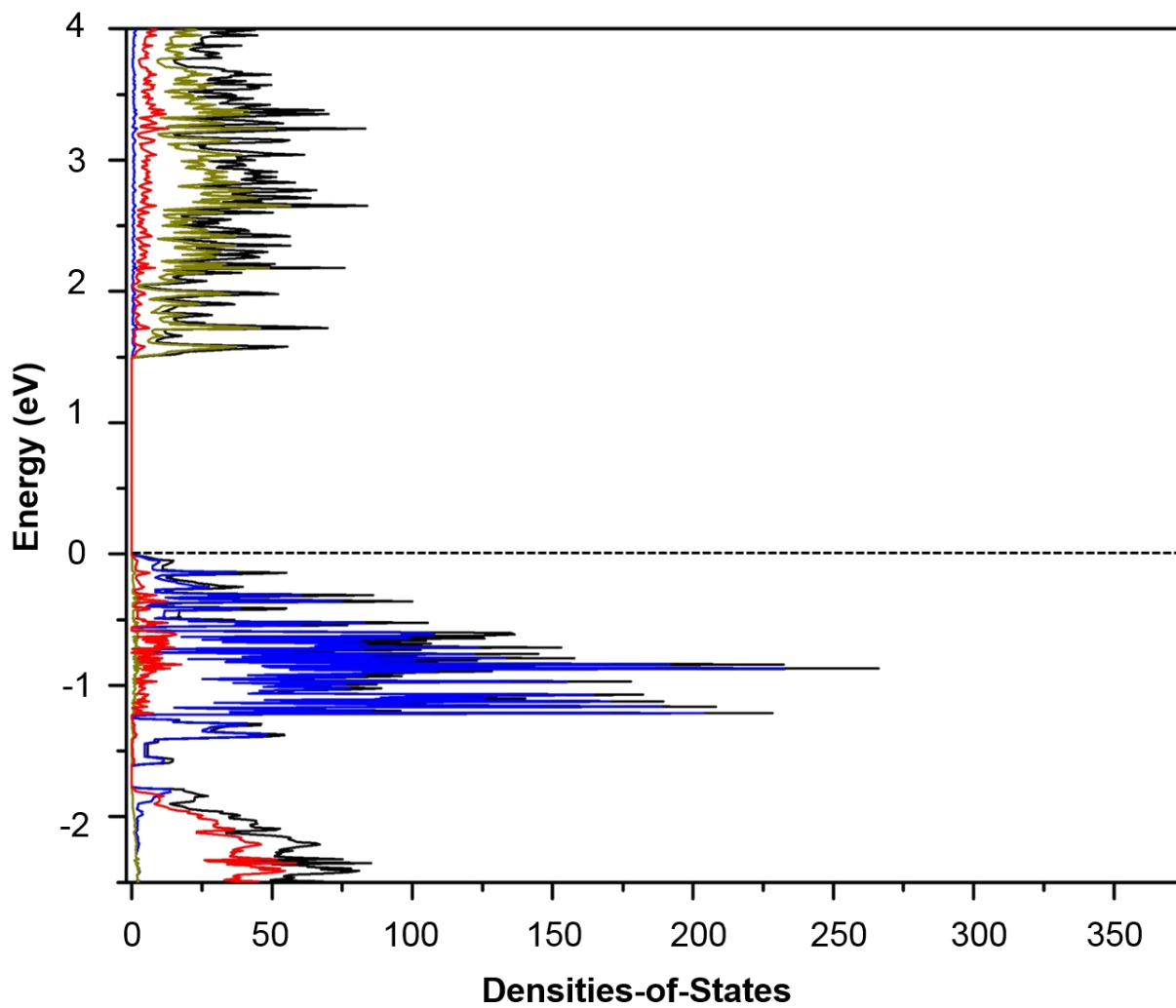


Figure C8. The calculated densities-of-states for α -) with the partial densities-of-states from Cu, Ta, and O indicated in blue, tan, and red. The total densities of states are indicated in black. ..